Quelques études de la physique des écoulements d'une mousse et dans une mousse

Florence Rouyer

▶ To cite this version:

Florence Rouyer. Quelques études de la physique des écoulements d'une mousse et dans une mousse. Matière Molle [cond-mat.soft]. Université Paris-Est, 2011. tel-00682720
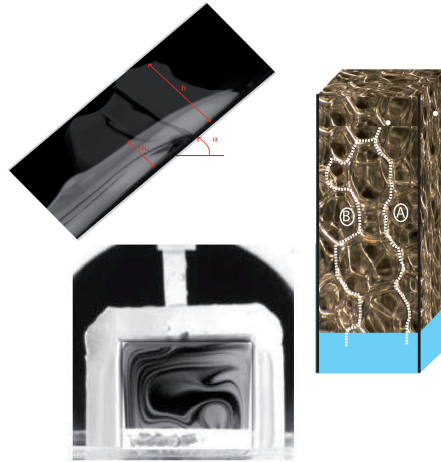
Quelques études de la physique des écoulements d'une mousse et dans une mousse

Présenté par : Florence Rouyer

le 7 décembre 2011 devant le jury composé de :

Michel Cloitre	Examinateur
Annie Colin	Présidente
François Graner	Rapporteur
Elisabeth Guazzelli	Rapportrice
Pierre Mills	Examinateur
Marc Rabaud	Rapporteur

Table des Matières

Remerciements

Tout d'abord, je remercie l'ensemble des membres du jury pour leur présence et leurs questions le jour de la soutenance et tout particulièrement les rapporteurs pour avoir accepté cette tâche.

Ensuite, je tiens à remercier Pierre Mills et Michèle Adler qui, en tant que directeurs du LPMDI, ont permis mon recrutement à l'université de Marne-La-Vallée, et qui m'ont fait part de leurs conseils avisés. Je suis reconnaissante envers Sylvie Cohen-Addad et Reinhard Hohler qui m'ont soutenue et initiée aux " mousses " et à la rhéologie.

Je remercie Olivier Pitois et Elise Lorenceau qui m'ont proposé de les rejoindre sur le projet de l'ANR microfluidique particulaire. C'est un vrai plaisir que de travailler avec eux, et j'espère que cela continuera encore longtemps... même si l'environnement est différent ! Un grand merci à Navier et à l'équipe Rhéophysique qui nous a tous accueilli avec Yacine.

Enfin, je remercie mon collaborateur de ces trois dernières années, Franck Pigeonneau qui m'a permis de découvrir quelques secrets du verre fondu, en espérant en découvrir d'autres secrets dans les prochaines années...

" And last but not least " ! Merci à Nicolas Louvet et Helena Kocarkova qui ont fait un excellent travail en thèse et qui, plus est, ont supporté mes remarques sans trop rechigner. Je n'oublie pas les sympathiques et efficaces stagiaires de Master : Sébastien, Sophie, Julien, Jamal, Salahedine et Benoît.

Mais pour finir, merci à ma petite famille, car sans son soutien moral et logistique et leur patience, je n'aurais jamais écrit ce manuscrit.

Préambule

Depuis mes " premiers pas " dans le monde de la recherche, je me suis intéressée à la physique des milieux divisés. J'entends par milieu divisé un milieu homogène à grande échelle formé d'une phase continue et d'une phase dispersée. En thèse à l'université d'Orsay, j'ai étudié les suspensions macroscopiques fluidisées (grains solides dans un liquide visqueux). Pendant mon post-doctorat à l'Université du Massachusetts, j'ai étudié les gaz granulaires (grains solides dans un gaz). Enfin, depuis mon arrivée au L.P.M.D.I. à l'université de Marne-la-Vallée à l'automne 2000 j'ai étudié les mousses aqueuses (bulle d'air dans un liquide). À l'origine expérimentatrice, j'ai développé depuis 2007 des simulations numériques "simples" sous Surface Evolver ou Comsol comme outil d'aide à la compréhension ou à l'exploitation de résultats expérimentaux.

Ce manuscript d'Habilitation à Diriger des Recherches présente mes travaux de recherche pour la période 2000-2011, pendant laquelle je me suis intéressée à la description et à la compréhension de la dynamique d'écoulement des mousses aqueuses ainsi qu' à l'écoulement de liquide et de particules dans un tel milieu. Une brève introduction aux mousses aqueuses définit le matériau et ses propriétés caractéristiques ainsi qu'un vocabulaire parfois spécifique à la communauté "mousse". Les problèmatiques et leur contexte sont présentés plus précisément au début de chaque chapitre ou sous-chapitre.

Bien évidemment, ces résultats sont le fruit d'un travail en equipes avec des chercheurs, enseignants chercheurs et doctorants du laboratoire L.P.M.D.I.. Une petite partie des résultats présentés est issue d'une collaboration avec Saint Gobain Recherche et le laboratoire S.V.I. d'Aubervilliers.
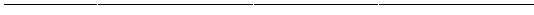
Brève présentation des mousses aqueuses

Une mousse aqueuse est un empilement de bulles de savon qui perdent leur forme sphérique lorqu'elles sont mises en contact les unes avec les autres. Elles se facettent, et partagent avec chacune de leurs voisines un film de savon.

Les principaux paramètres physiques régissant les propriétés d'une mousse sont : la tension de surface des interfaces liquide/air, la taille des bulles et la fraction liquide ϕ_l égale au rapport du volume de liquide sur le volume total de mousse : $\phi_l = \frac{volume_{liquide}}{volume_{total}}$ ($= 1 - \phi_g$ où ϕ_g est la fraction de gaz). Un empilement de sphères dures monodisperse est compact pour un fraction de vide égale à 0.36. Ainsi, pour des fractions liquides supérieures à 0.36 environ, il est plus approprié de parler de suspension de bulles que de mousse car en moyenne les bulles ne sont plus en contact les unes aux autres et l'essentiel des propriétés physiques caractéristiques d'une mousse ne sont plus vérifiées.

Pour des fractions liquides inférieures à 0.36, trois bulles voisines ont leur trois films communs qui se joignent pour former un petit canal appelé bord de Plateau du nom de Mr Joseph Plateau, comme illustrée sur le schéma de la figure 1. La junction entre quatres bords de Plateau appartenant à quatres bulles voisines s'appelle vertex ou noeud. Pour des fractions liquides tendant vers zéro, on parle de mousse sèche. Dans cette limite, la géométrie d'une mousse à l'équilibre suit les lois de Plateau :
  - l'angle entre chaque film est de 120°
  - l'angle entre les bord de Plateau est égale à $109,471^o$ ($\arccos(-1/3)$), égale à l'angle au centre d'un tétraèdre régulier.

Les films de savon qui joignent les bulles entre elles "rigidifient" l'empilement. On dit qu'une mousse est un matériau à seuil dont le comportement peut être solide ou liquide en
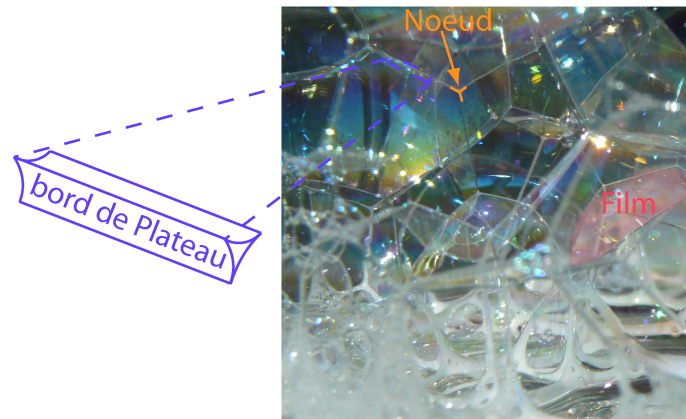
FIGURE 1 – Image couleur d'une mousse reposant sur une bain de liquide. Les bulles sont sphériques en bas et polyhédriques en haut. Les canaux sont d'autant plus fins qu'ils sont loin du réservoir de liquide. N.B : l'irisation des films illustrent leur épaisseur.

fonction de la contrainte qui lui est appliquée. Pour des contraintes inférieures à une contrainte seuil σ_y, la mousse se déforme élastiquement (toute transformation est réversible). Pour des contraintes appliquées supérieures à σ_y, la mousse présente des régions où la déformation est plastique du fait de réarrangements topologique entre bulles (changement de premier voisin) identifiables par la disparition et apparition de film (cf. figure 2).

La loi rhéologique classiquement utilisée pour décrire la relation contrainte (σ)- vitesse de déformation ($\dot{\varepsilon}$) d'une mousse est la loi d'Herschel-Bulkley :

$$\sigma = \sigma_y + \eta_p \dot{\varepsilon}^{\beta} \quad \text{si} \quad \sigma > \sigma_y \tag{0.0.1}$$

où η_p est un paramètre physique relatif à la viscosité et β un paramètre d'ajustement (variable entre 0.2 et 0.8 et dépendant de la rhéologie interfaciale). Cette loi permet de décrire la plupart des résultats de l'écoulement d'une mousse à l'échelle macroscopique. Cependant, le lien avec les mécasnismes observés à l'échelle microscopique : réarrangment de films entre bulles et mésoscopique : écoulement non-uniforme ne fait pas encore l'unanimité dans la communauté scientifique à l'heure actuelle.

Une mousse aqueuse soumise à une contrainte inférieure à son seuil d'écoulement n'est pas pour autant dans un état figé. En effet, une mousse vieillit suivant des mécanismes propres

les bulles 1 et 3 sont proches voisines

Suite au retrecissement du film entre les bulles 1 et 3, l'instant où 4 films se joignent est instable. Un film dans une direction transverse s'étire.

les bulles 4 et 2 deviennent proches voisines

FIGURE 2 – Succession d'images illustrant un réarrangement T1 de bulles dans une mousse 3D.

à la fluidité de ces constituants élémentaires (liquide et gaz), la vie d'une mousse est bien souvent éphémère même si elle parait tenace lorsqu'on veut s'en débarasser (rinçage d'un vêtement !). On distingue trois mécanismes de vieillissement : le mûrissement, le drainage et la coalescence. Ces mécanismes agissent généralement simultanément cependant on cherche à les étudier séparemment au laboratoire. Décrivons brièvement un à un chacun de ces mécanismes.

Le mûrissement : La tension de surface entre gaz et liquide moussant entraine un saut de pression entre la phase gazeuse et liquide d'autant plus importante que l'interface est courbée (loi de Laplace). Il en résulte une différence de pression entre les bulles de différentes tailles constituant une mousse : la pression, et par conséquent la concentration en gaz, est plus grande dans les petites bulles que dans les grosses bulles. Les petites bulles sont donc amenées à disparaître au détriment des plus grosses qui grandissent par diffusion du gaz des petites bulles vers les grosses bulles. Au laboratoire, afin de minimiser l'effet du mûrissement, on travaille soit sur des intervalles de temps court, soit avec une assemblée de bulles monodisperses, soit encore avec un gaz dont la solubilité dans la phase liquide est faible (les films entre les bulles deviennent alors des frontières plus difficilement franchissables).

Le drainage : Sous l'effet de gradient de pression induit par la gravité ou la capillarité, la phase liquide est mise en écoulement : on parle de drainage. La mousse peut alors être vue comme un milieu poreux à géométrie variable.
Sous l'effet de la pesanteur, le liquide plus dense que les bulles s'écoule vers le bas du récipient alors que les bulles se concentrent en haut de celui-ci : à l'équilibre il existe donc un très fort gradient vertical de fraction liquide (figure 3).
Le drainage capillaire (ou succion capillaire), est le moteur de l'amincissement d'un film entre
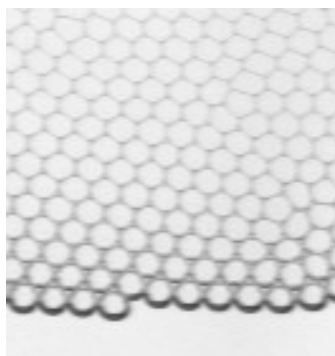
FIGURE 3 – Image d'une mousse 2D reposant sur une bain de liquide. Les bulles sont sphériques en bas et polyhédriques en haut. Les canaux sont d'autant plus fins qu'ils sont loin du réservoir de liquide.

bulle. En effet du fait de la courbure plus importante dans les bords de Plateau que dans un film quasi plat, la pression du liquide est plus importante dans la région des bords de plateau qu'à l'intérieur d'un film. Le liquide s'écoule ainsi vers les bords de Plateau et le film s'amincit ainsi jusqu'à se rompre sauf si d'autres forces s'y opposent.

La coalescence ou rupture de film : La présence de surfactants aux interfaces permet de stabiliser un film plat par l'action de forces répulsives entre les deux interfaces du film, ces forces peuvent avoir diverses origines : électrostatiques ou stériques par exemple. Cependant un film de savon n'atteint jamais un état d'équilibre stable. La moindre fluctuation d'épaisseur qui équivaut à des variations locales de la courbure de l'interface engendre l'écoulement du liquide et l'amincissement localisé du film . Le film rompt localement et se retracte vers sa périphérie. La disparation de ce film crée des réarrangements topologiques dans son voisinage (quelques bulles).

Au-delà de l'effet de stabilisation des films fins, les surfactants ont un effet sur la mobilité des interfaces. Cet effet différencie de manière quantitative les propriétés physiques des mousses, aussi bien en ce qui concerne leur stabilité : drainage, fraction liquide minimale avant la rupture que dans leur comportement rhéologique. En effet, la structure d'une mousse reste rarement figée, chaque restructuration provoque la disparition et apparition d'un film et donc l'écoulement de liquide dans un espace confiné par des interfaces liquide/air.

Chapitre 1

Rhéologie des mousses aqueuses

Collaborations : Michèle Adler (DR), Sylvie Cohen-Addad (MCF), Reinhard Höhler (PROF), Sébastien Vincent-Bonnieu (étudiant DEA), Sophie Berthet (étudiante Maîtrise).

Connaître la rhéologie des mousses aqueuses est bien évidemment crucial dans la mise en place et la modélisation de procédés industriels mais cela représente également un enjeu plus fondamental. Depuis une quinzaine d'années une nouvelle dénomination de matériau est apparue : les matériaux mous vitreux. Ce sont des matériaux qui ont pour caractéristique de s'écouler lorsqu'ils sont soumis à une contrainte supérieure à une contrainte seuil et dont l'origine microscopique est liée à l'existence de réarrangements plastiques localisés (dans des zones mésoscopiques où la contrainte est supérieure à une contrainte seuil).

La mousse peut être vue comme un tel matériau dont la sollicitation mécanique à grande déformation entraîne des réarrangements de bulles voisines les unes par rapport aux autres facilement identifiable par la disparition et apparition de films. Ce changement topologique est habituellement dénommé T1. La figure 2 illustre un réarrangement de bulles dans une mousse 3D cisaillée parallèlement à l'axe horizontal de l'image. Comprendre les liens entre les mécanismes observés à l'échelle microscopique et les comportements mécaniques à l'échelle macroscopique d'une mousse est un enjeu scientifique de grande ampleur auquel prennent part les physiciens, les chimistes et les mécaniciens qu'ils soient expérimentateurs ou numériciens ...

Les paramètres physiques identifiés dont dépend l'état de blocage de la mousse (Jamming-figure 1.1) sont la contrainte (load) et la fraction volumique de gaz (1/densité), cependant au début des années 2000 la dépendance de la contrainte seuil en fonction de la fraction volumique de gaz ne semblait pas être bien définie. Par ailleurs, de même que pour d'autres
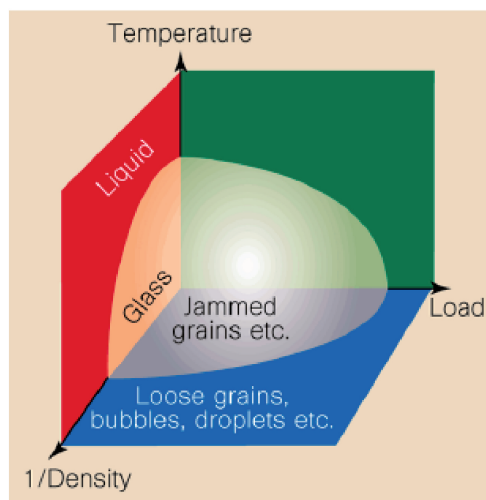
FIGURE 1.1 – Diagramme de phase de transition quasi-solide / liquide d'après A. Liu [1] : la région grisée proche de l'origine décrit un état quasi-solide ou bloqué (jammed)

systèmes athermiques, la question d'une pseudo-température dont dépendrait la fréquence des réarrangements microscopiques et leur seuil reste ouverte ...

Je présente ici les résultats de travaux expérimentaux sur la rhéologie des mousses aqueuses sèches proche de leur mise en écoulement : dynamique des prémices de l'écoulement ; contrainte seuil d'écoulement ; non-linéarité et localisation du cisaillement au-delà du seuil d'écoulement.

1.1 Seuil d'écoulement d'une mousse : existe-t-il une valeur bien définie ?

Publications : Colsua 2005.

Il est important de comparer des mesures rhéologiques obtenues dans différentes géométries car bien souvent le rhéometre est une "boite noire" dans laquelle les déformations et contraintes ne sont pas nécessairement homogènes (localisation, glissement ...). Ainsi les lois macroscopiques obtenues reliant contrainte et déformation peuvent être dépendantes du dispotif expérimental ! Cependant, si les contraintes et déformations locales sont connues (imagerie confocale ou IRM), une loi de comportement fiable peut alors être établie pour le matériau

13
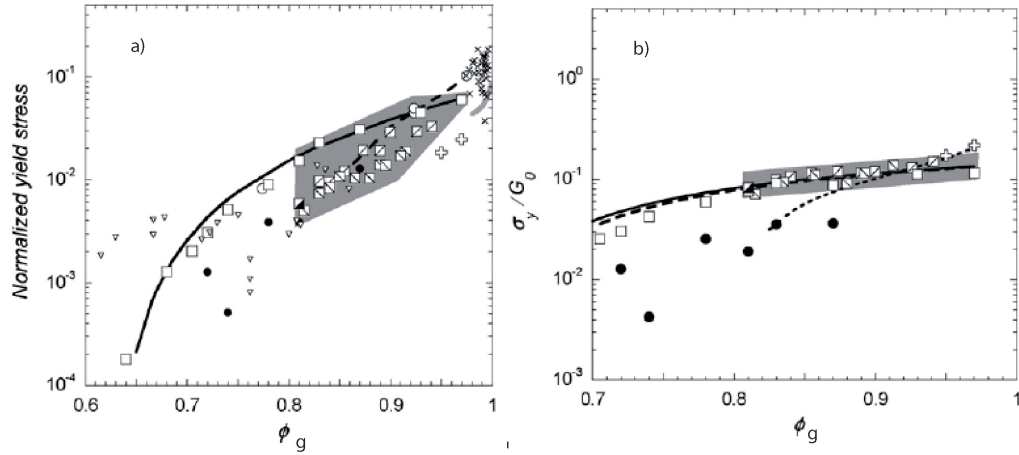
FIGURE 1.2 – Diagramme d'état quasi-solide/ quasi-liquide

[2].

Dans un premier temps, nous avons testé la robustesse de la détermination de la contrainte seuil d'écoulement de mousses aqueuses par différentes méthodes expérimentales. Nous avons montré une bonne adéquation entre des résultats obtenus à partir d'écoulement sur plan incliné ou d'expérience en mode oscillatoire dans une géométrie Couette cylindrique (faible gap) à contrainte ou déformation imposée.

Dans un deuxième temps, nous avons comparé nos résultats à ceux de la littérature, ces résultats correspondant à différentes fractions volumiques de liquide, différentes tailles de bulles et différentes solutions moussantes. L'élasticité d'une mousse étant conditionnée par la déformation des interfaces des bulles, nous nous attendons à ce que la contrainte seuil d'écoulement (de même que le module élastique, cf. [3]) soit proportionnelle à γ/R_{32}. γ est la tension de surface liquide/air et R_{32} est le rayon de Sauter égal au rapport du troisième et deuxième moment de la distribution des rayons des bulles constituant la mousse et réprésente la surface moyenne des interfaces par unité de volume. Cependant cette dernière valeur est rarement connue pour l'ensemble des expériences que nous avons pu collecter, et pour lesquels nous avons uniquement une estimation du rayon moyen R des bulles.

La représentation graphique de la variation de la contrainte seuil normalisée par γ/R en fonction de la fraction volumique de gaz (ϕ_g) montre une très grande dispersion des points (figure 1.2a). Cette dispersion est fortement réduite si nous normalisons la contrainte seuil par

le module élastique de la mousse (figure 1.2b). Rappellons que le module élastique est aussi proportionnel à γ/R_{32} [3]. La dispersion de la contrainte seuil normalisée par γ/R s'expliquerai alors par une mauvaise connaissance de R et/ou une différence entre R et R_{32} en raison de la polydispersité des mousses utilisées.

Cette étude expérimentale et comparative nous permet de conlure que, si on s'affranchit des incertitudes concernant la distribution en taille des bulles qui constituent la mousse, la contrainte seuil d'écoulement d'une mousse aqueuse est bien définie et que, sur une large gamme de fraction volumique de gaz [0.7-1], elle peut être décrite par la loi : $\Sigma_y/G_0 = 0.39 \times (\phi_g - 0.64)/\phi_g$ où G_0 est le module élastique aux petites déformations. Notons, que cette loi vérifie bien que lorsque les bulles n'ont plus de films en commun ($\phi_g = 0.64$) alors la contrainte seuil s'annule.

1.2   Dynamique du seuil d'écoulement

Publications : PRE 2003.

L'observation du réseau de bord de Plateau à l'intérieur d'une mousse sèche ($\Phi_l < 0.01\%$) par microscopie confocale permet d'identifier un T1 induit par des cycles de cisaillement à taux de déformation constant dans une géométrie Couette plan dans une mousse à 3 dimensions .

L'étude de l'apparition des premiers réarrangments induits par cisaillement a permis d'apporter quelques conclusions significatives :
   - aux petites déformation ces évènements sont irréversibles, et locaux et sont donc bien des évènements plastiques à une échelle mésoscopique ; la déformation à laquelle apparaissent ces évènements dépend de l'histoire de l'échantillon, elle augmente après un cycle de cisaillement à grande amplitude.
   - la vitesse de cisaillement augmente la déformation seuil à laquelle le premier T1 apparait.
.

La dépendance de la déformation seuil avec la vitesse de déformation peut être décrite par une fonction linéaire : $\gamma_c = \gamma_{c0} + T\dot{\gamma}$ où dans le cas de la mousse utilisée (SDS + PEO + dodecanol + butanol) $\gamma_{c0} = 0.05 \pm 0.05$ (déformation quasistatique) et $T = 1.08 \pm 0.14s$. Ce temps caractéristique est de l'ordre de grandeur du temps pendant lequel un réarrangement est observable pendant l'expérience autrement dit temps de relaxation d'un T1.

Ce travail expérimental a mis en évidence l'augmentation de la déformation à laquelle apparait le premier réarrangement induit par cisaillement avec la vitesse de cisaillement et suggère que cet effet est dépendant du temps de relaxation d'un T1.

1.3   Localisation au-delà du seuil d'écoulement

Publications : PRE 2003, EPJE 2008.

Afin de sonder l'homogénéité des déformations, nous avons cherché à mesurer les profils de vitesse pour chacun des montages expérimentaux.

Nous avons conclu que aussi bien en géométrie Couette plan que en géométrie Couette cylindrique (faible gap), les profils de vitesses mesurés dans l'entrefer sont linéaires aux faibles déformations et peuvent dévier d'un profil linéaire pour des déformations très supérieures au seuil d'écoulement.

Dans le cas de cisaillement à taux de déformation constant dans le temps en partant d'une situation au repos dans une géométrie Couette plan, nous n'observons aucun profil type (déviation par rapport au profil linéaire non reproductible). A l'inverse, nous observons de manière systématique une déviation plus marquée proche du centre de l'entrefer dans le cas d'une géométrie Couette cylindrique en mode oscillant.

Les observations de ces expériences ne sont pas en contradiction avec d'autres expériences récentes sur les mousses ne présentant pas de localisation [4]. En effet, la localisation observée est peut-etre due au fait que le cisaillement se fait à partir d'un état au repos et non à partir d'un état fortement cisaillé et nous pourrions invoquer des profils de vitesse transitoire [5]. Enfin la non reproductibilité des profils est également cohérente avec un mécanisme d'instabilités [6].

1.4   Au-delà du seuil : non-linéarité en mode oscillatoire

Publications : EPJE 2008.

Nous avons montré qu'au-delà du seuil d'écoulement la rhéologie d'une mousse, mesurée au premier ordre harmonique (module complexe $G^* = G' + iG''$, où G' est le module élastique et G'' est le module visqueux ou de perte), est indépendante de la physico-chimie une fois pris en

compte l'élasticité et la déformation seuil. Cette rhéologie linéaire aux grandes déformations est très bien décrite par un modèle élasto-plastique. Notons que la rhéologie linéaire aux plus faibles déformation peut être décrite par un modèle viso-élasto-plastique permettant de décrire la dissipation visqueuse aux faibles déformations [7].

Cependant la rhéologie non-linéaire peut correspondre à près de 10% de l'amplitude du signal mesuré et est essentiellement décrite par l'harmonique 3. La variation de l'amplitude non-linéaire (résidu) en fonction de l'amplitude des déformations présente une signature différente pour chaque mousse étudiée. La rhéologie non-linéaire aux grandes déformations peut donc être un test utile pour distinguer des mousses entre elles et tester des modèles théoriques ou numériques.

L'augmentation du résidu avec l'amplitude des déformations est moins importante que l'augmentation attendue par un modèle élasto-plastique et d'autant moins importante que la mousse est humide. Nos résultats expérimentaux sont également comparés à un modèle de milieux mous vitreux dont les données des harmoniques d'ordre supérieur à 1 ont précédemment été publiées, mais l'accord est moyennement satisfaisant.

D'autres résultats expérimentaux mériteraient d'être obtenus afin de tester la réponse rhéologique non-linéaire en fonction des différents paramètres physico-chimique, (fraction liquide, mobilité des interfaces et temps de relaxation des réarrangements), ces expériences sont actuellement en cours dans l'équipe de S. Cohen-Addad et R. Hohler. Ces expériences sur les mousses pourront alors être confronter de manière plus systématique à d'autres systèmes complexes et d'autres modèles théoriques et numériques.

Bibliographie

[1] A. J. Liu and S. R. Nagel, *Nature* **396**, 6706, 21 (1998).

[2] G. Ovarlez, S. Rodts, P. Coussot, J. Goyon, A. Colin, *Phys. Rev. E* **78**, 036307 (2008)

[3] H.M. Princen, A. D. Kiss, *Journal of Colloid and Interface Science*, **128**, 176 -187 (1989).

[4] G. Ovarlez, K. Krishan, and S. Cohen-Addad, *EPL* **91** 68005 (2010).

[5] T. Divoux, D. Tamarii, C. Barentin, and S. Manneville, *Phys. Rev. Lett.*,**104**,208301,(2010).

[6] R. Besseling, L. Isa, P. Ballesta, G. Petekidis, M.E. Cates, W.C.K. Poon, *Phys. Rev. Lett.*, **105**, 268301, (2010).

[7] P. Marmottant and F. Graner, *Eur. Phys. J. E* **23**, 337-347 (2007)

ROUYER *et al.*

Dynamics of yielding observed in a three-dimensional aqueous dry foam

Florence Rouyer, Sylvie Cohen-Addad, Michèle Vignes-Adler, and Reinhard Höhler
Laboratoire de Physique des Matériaux Divisés et des Interfaces, UMR 8108 du CNRS, Université de Marne-la-Vallée,
5 Boulevard Descartes, 77454 Marne-la-Vallée cedex 2, France

We study the onset of yielding in stable three-dimensional dry foams following the start up of steady shear flow. By means of a charge-coupled device camera equipped with a small depth-of-field objective, we visualize the Plateau border network in the bulk of the foam. We show that γ_c is independent of shear rate $\dot\gamma$ in a quasistatic regime whereas at high strain rates, a rapid increase of γ_c with $\dot\gamma$ is observed, in qualitative agreement with theoretical models. Moreover, spatiotemporal image analyses are used to determine the velocity profile in the gap. We find that this profile remains linear up to strains far beyond γ_c. Moreover, we have studied the strain history dependence of γ_c.

DOI: 10.1103/PhysRevE.67.021405   PACS number(s): 82.70.−y, 62.20.Fe, 83.80.Iz

I. INTRODUCTION

Aqueous foams are concentrated dispersions of gas bubbles in a surfactant solution. Even though they are only made of fluids, foams behave elastically under small applied stresses, whereas when subjected to large stresses they flow like viscous non-Newtonian liquids. The crossover between these two types of behavior is called yielding. In the context of macroscopic rheological measurements, the yield strain is usually defined as the strain corresponding to the maximum of stress obtained in a strain growth experiment [1]. At the scale of the individual bubbles, yielding may be defined as the crossover from reversible elastic behavior to a regime where the deformation involves topological changes of the bubble packing [1,2].

The first theoretical analysis of yielding in foams and concentrated emulsions is due to Princen [3]. Based on the observation that this rheological behavior is common to a large class of complex fluids, recent theoretical models have attempted to identify a general framework providing a link between the macroscopic rheological response and the local structural changes that accompany the yielding process under quasistatic conditions [4]. In these models, the strength of the coupling between the rearrangements in neighboring "mesoscopic regions" plays an important role. Numerical simulations of steady shear flow in foam often rely on simplified descriptions of the structure and the interactions between bubbles: Simulations based on the vertex model exhibit avalanches of rearrangements [5], whereas using the bubble model local rearrangements are predicted [6]. The surface evolver software, allows to carry out highly accurate three-dimensional (3D) simulations, but only in the quasistatic regime [2,7]. Concerning the dynamics of yielding, several 2D theoretical studies and simulations have shown that under large strain rates, viscous forces in the foam strongly affect yielding behavior [8–11]. Since the pioneering work of Khan *et al.*, yielding of 3D foams has been studied on the macroscopic scale by rheological measurements [12–15]. The dynamics of bubble rearrangements in wet foams that undergo yielding have been studied using diffusing-wave spectroscopy. This work has confirmed the crucial role
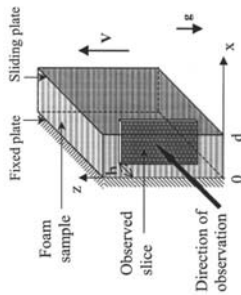
played by these rearrangements for the rheological behavior [16,17]. Moreover, recent theoretical studies have shown how yielding can be interpreted as a generic jamming phenomenon [18,19].

In this paper, we present direct observations of the local structural changes that accompany the onset of yielding in a 3D dry foam. We report the first measurement of the strain at which shear-induced rearrangements set in a strain growth experiment. These data are compared to theoretical predictions concerning the influence of the strain rate on yielding.

II. MATERIALS AND METHODS

We have developed a formulation based on well-characterized chemicals allowing to obtain highly stable foams that do not exhibit coalescence under shear. The foaming liquid is an aqueous solution containing a mixture of sodium dodecyl sulfate (SDS), polyethylene oxide (PEO, $M_w = 3 \times 10^5\ \text{g mol}^{-1}$), dodecanol, and butanol. The products were all purchased from Aldrich and used as received. The solution is prepared using pure water (MilliQ) as follows: First, 0.02 g of PEO is dissolved in 100 ml of water and subjected to a gentle mechanical agitation for 1 h. Then, 0.006 g of dodecanol is diluted in 5 ml of butanol. This alcoholic solution is added to the PEO solution, and further gently agitated for 15 min. Besides, 0.2 g of SDS is dissolved in 40 ml of water. The final foaming solution is obtained by mixing the PEO solution with the SDS solution and completing with water up to 200 ml. It is gently agitated for 15 min. The final concentrations are SDS 0.1% g/g, PEO 0.01% g/g, dodecanol 0.003% g/g, butanol 2% g/g. To avoid aging effects, the solution is prepared no more than 24 h before use. The surface tension of the foaming solution, σ, was measured by the de Noüy method and found to be equal to 23 mN m^{-1} at 20 °C. Its viscosity was determined using an Ostwald capillary viscometer tube at 20 °C, $\mu = 1.08$ mPa s.

The foam is generated by mixing nitrogen gas and the foaming solution using a setup inspired by the one described by Khan [12]. In our device, the gas and the solution are injected at constant flow rates (28 and 2.3 ml/min, respec-

tively) at the entrance of a Plexiglass tube (200 mm long, 20 mm inside diameter) filled with compacted glass beads (1.5 mm diameter). The porosity of the bead packing is about 36%. Under these conditions, the gas volume fraction of the generated foam is 92% and the average bubble radius is of the order of 0.1 mm. The output of the generator is connected to a flexible tube, allowing to fill directly a sliding plate cell (cf. Fig. 1). The air in contact with the sample is saturated with humidity. After injection, the foam drains *in situ* for 75 min before the shearing experiment is started. To determine a typical gas volume fraction of the foam at this time, a sample is prepared and injected into a cell whose geometry corresponds to that of the sliding plate cell and which is weighted after 75 min. We also measure the foam volume and thus obtain an average gas volume fraction for the entire sample, it is larger than 99%. The liquid content in the foam sample will be highest near the bottom due to drainage and we expect the gas volume fraction at midheight, where we study the foam, to be above 99%. All the experiments have been carried out at a temperature of (20 ± 1) °C.

A charge-coupled device camera equipped with a very thin depth-of-field objective allows to observe the structure inside the foam. Since it is very dry, the films are so thin that they are almost totally transparent and the only visible elements are the Plateau borders that appear as black lines on the images (cf. Fig. 2). The camera is focused on a region 10 mm inside the foam and captures images of a foam "slice." It is 2.5 mm deep, the width is equal to the gap between the plates and the height is chosen such that the volume of observation, denoted V_{obs}, is equal to 430 mm^3 for all of the experiments at different gap widths. Before applying the shear, the disordered and polydispersed foam structure is inspected: the bubble size is estimated from the bubble contours drawn by the Plateau borders visible on the images [cf. Fig. 2(a)]. This procedure yields an average bubble radius $R = 0.8$ mm with a standard deviation of 0.4 mm, the minimum and the maximum radii are equal to 0.2 and 2 mm, respectively. The average bubble size remains constant during the shearing experiment. No film rupture is observed,

FIG. 1. Experimental setup. The sliding plate cell consists of two parallel plates (100×80 mm^2). The observed slice is situated at a depth ($h = 10$ mm) at the midheight of the foam sample and is 2.5 mm thick. The arrows V and g show the directions of the velocity of the moving plate and of gravity, respectively.
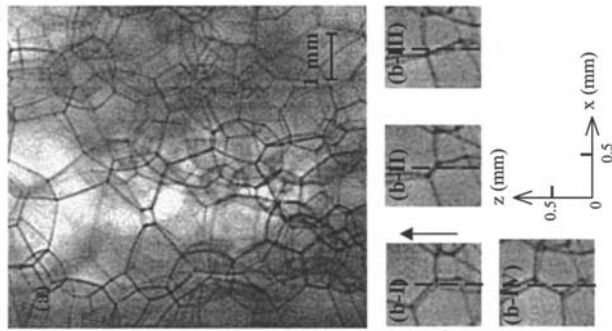
FIG. 2. (a) Part of the image of a quiescent foam slice observed at a depth $h = 10$ mm inside the sample. (b) Four successive images showing a topological $T1$ transformation: (b-I) and (b-II) before the $T1$, (b-III) instant of $T1$, (b-IV) after the $T1$. The dotted line indicates a typical pixel line used for constructing spatiotemporal plots.

even during the shearing. The rate of coarsening induced bubble rearrangements slows down considerably during the first 75 min of the foams existence. Indeed, observations on static foam show that right after the production of the sample, of the order of 1% of the bubbles in the observed volume participate in rearrangements during one second, suggesting that the rearranged bulk volume fraction per second is of the order of 10^{-2} s^{-1}. At a foam age of 75 min, this parameter is more than 60 times smaller. Besides the chemical composition and the bubble size distribution described in this paragraph, the rheological response of foams, generally, also depends on strain history [15,17,20]. During foam injection into the sliding plate cell, a complex flow occurs which leads to trapped strains and stresses. We expect coarsening to relax at least partially such macroscopic stresses, [21] in agreement with numerical simulations by Kermode reported in Ref. [2], as well as in recent experiment [22]. In addition to relaxing slowly macroscopic stresses, coarsening also creates stresses on the bubble scale which are intermittently released upon bubble rearrangements. Such stresses can be relaxed by controlled preshearing of the

DYNAMICS OF YIELDING OBSERVED IN A THREE-... PHYSICAL REVIEW E **67**, 021405 (2003)

The sliding plate cell (plane Couette geometry) consists of two vertical parallel glass plates (100×80 mm²). To prevent wall slip, we use plates that are rough on the scale of about 1 mm and rendered hydrophobic using a chemical treatment. One plate is fixed, while the other can be moved in the z direction at a constant velocity V (cf. Fig. 1). This velocity can be chosen in the range from 0.02 to 3 mm/s. The gap width between the plates, d, can be set to either 11.5 or 16.0 mm. The shear rate is defined as $\dot{\gamma}=V/d$. During a strain growth experiment, successive images of the deformed structure are recorded as the strain grows from 0 up to a maximum value 1.7. The image grabbing rate can be adjusted between 5 and 25 images per second. Such movies enable us to detect the onset of yielding in the sample, as well as to measure the velocity profile in the gap.
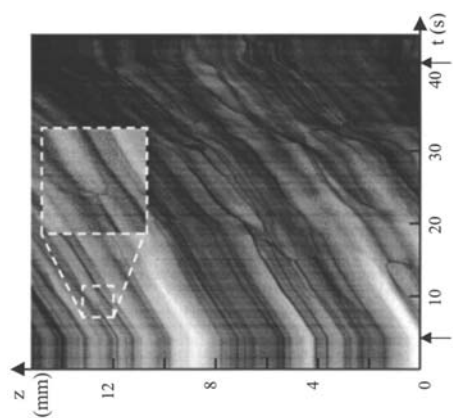
To measure the velocity in the z direction, we generate spatiotemporal plots; pixel lines corresponding to a given value of x are extracted from successive images, and then juxtaposed to form the new plot (cf. Fig. 3). For immobile foam, one expects horizontal lines of constant brightness. If the evolution of the foam structure under steadily increasing shear were affine, one would expect space-time plots containing tilted straight lines of constant brightness with a slope equal to the local and instantaneous velocity $v_z(x,z,t)$. Nonaffine deformation of the foam structure leads to deviations from such a pattern. In particular, strain in-

FIG. 3. Spatiotemporal plot generated for a pixel line located at x=11.5 mm and the shear rate is equal to 0.043 s⁻¹. The vertical and horizontal axes correspond, respectively, to the position in the shear direction z and to time t. The two arrows on the horizontal axis indicate the beginning and the end of shear. The inset shows a zoom on a kink due to a rearrangement.

duced bubble rearrangements give rise to marked irregularities in the space-time plots that occur over a brief time interval (cf. Fig. 3).

To quantify the bubble flow induced by shearing, we determine a mean velocity in the z direction, $\bar{v}(x)$, averaged over a pixel line for a given value of x and over a time interval. Let us denote $I(x,z,t)$ the intensity of a pixel at a position (x, z) and at a time t in a spatiotemporal plot. We quantify the extent to which the evolution of a pixel line for a given value of x, during a time interval Δt, can be described as a translation Δz of the pixels in the z direction by calculating the correlation function $\langle I(x,z,t)I(x,z,t+\Delta t)\rangle_z$. The distance Δz corresponding to the strongest correlation is called $\Delta z_m(x,t)$. For each experiment, Δt has to be sufficiently short to resolve rapid structural changes such as rearrangements and long enough to obtain good precision in the measurement of Δz_m. As a compromise between these criteria, we choose $\Delta t=R/(2V)$. We thus obtain an estimate $\Delta z_m(x,t)/\Delta t$ of the instantaneous mean velocity. The time evolution of this quantity is studied by calculating its temporal average, denoted $\bar{v}(x)$, and the corresponding standard deviation. Using this procedure, we are able to establish the average foam velocity profile $\bar{v}(x)$, throughout the gap using a set of spatiotemporal plots for values of x ranging from 0 to d.

Moreover, in the aim to study the effect of strain history on the onset of yielding, we perform strain cycling experiments; upon each cycle, the sample is subjected to a strain that rises at a fixed rate $\dot{\gamma}$ up to a maximum value, denoted γ_{max}, then stays constant for 1 s and finally comes back to zero strain. Up to three such cycles of equal maximum strain were applied successively to the sample, with strain rates ranging from 0.04 to 0.18 s⁻¹. We choose a fixed time interval of 1 min between the instants where the maximum strain is reached in successive cycles, whatever the maximum strain and the strain rate. This choice ensures that the total duration and, thus, the influence of coarsening is the same for all of the experiments. Before and after each cycle, images of the initial and final foam structures are recorded. They do not differ significantly in average and variance of intensity. Therefore, we quantify the extent of the irreversible structural changes induced by shearing using a correlation factor defined as follows:

$$C=\frac{\langle\langle(A_i(x,z)-\langle A_i\rangle)(A_f(x,z)-\langle A_f\rangle)\rangle\rangle}{\langle\langle(A_i(x,z)-\langle A_i\rangle)^2\rangle\rangle}. \quad (1)$$

$A_i(x,z)$ and $A_f(x,z)$ are the intensities of pixels at the position (x, z) and the indices i and f distinguish between initial and final images. The angular brackets represent averages over the pixels. The correlation factor is 1 for identical initial and final images and it decreases as irreversible structural changes occur during the cycle.

To detect quantitatively the onset of yielding of the foam, corresponding to the passage from the first to the second regime defined above, we analyze spatiotemporal plots for a closely spaced set of x values ranging from 0 to d. To define the first rearrangement, we identify it with the strain at which the first rearrangement appears in these plots for a given experiment. Let us relate this parameter to the number of strain induced rearrangements per total sample volume, denoted ρ, which is

III. RESULTS AND DISCUSSION

Figure 3 is a typical spatiotemporal plot obtained for a strain growth experiment. Up to the beginning of the shear deformation, the lines of constant brightness are horizontal

and continuous, indicating a static structure. Following the start of the strain growth, we observe a first regime where the lines are all tilted, continuous and parallel. Thus, the strain in the foam sample is to a good approximation homogeneous and there are not any topological changes of the bubble packing. Note that the nonaffine deformation that is known to exist at the scale of the individual films [7] is beyond the resolution of our experimental technique. Beyond a characteristic strain denoted γ_c, a second regime can be identified where kinks appear on the lines, indicating that the Plateau border displacement is no longer a smooth function of time; the kinks correspond to sudden topological transformations of the Plateau border network, as illustrated in Fig. 2(b). In principle, kinks in the spatiotemporal plots could also arise due to motions of bubbles in the x or y directions that are not directly related to topological rearrangements. We have verified experimentally that such effects are rare by comparing unprocessed images and spatiotemporal plots. Beyond a characteristic strain denoted by γ^* which is significantly larger than γ_c, a third regime progressively appears where the lines are neither continuous nor parallel, and their slopes differ from the one observed in the previous regimes, indicating nonaffine bubble motion that strongly fluctuates in space and time. γ^* presents extremely large fluctuations: In 30% of the experiments, it exceeded 1.7, the maximum strain applied to the samples. We choose not to extend the range of applied strains further, since due to the free lateral boundary conditions of the sample, a sliding plate configuration is intrinsically inadequate for applying very large fully homogeneous strains.

Figure 4 shows typical velocity profiles $\bar{v}(x)$ obtained for shear strain values in the three regimes. In all cases, the velocities of the bubbles in contact with the glass plates at x=0 and x=d correspond to those of the respective plates, allowing to exclude artifacts related to wall slip. In the range of investigated shear rates, $\bar{v}(x)$ remains globally linear up to the strain value γ^*. This observation implies that for $\gamma_c<\gamma<\gamma^*$, the rearrangements are localized and randomly distributed in the sample. A direct study of the spatiotemporal plots such as Fig. 3 confirms this finding. Indeed, the signature of avalanchelike, large scale collective rearrangements would be kinks that simultaneously appear for a wide range of z. Visual inspection of the foam images shows that the extent in the x direction of bubble clusters undergoing rearrangements is comparable to that in the z direction. For strains beyond γ^*, the strain rate is no longer homogeneous throughout the foam. In this regime, we observe temporal fluctuations of the velocity $\bar{v}(x)$ that are much larger than for $\gamma<\gamma^*$. The profile and its fluctuation do not present any systematic variations with strain rate and gap size, within the investigated range of parameters.

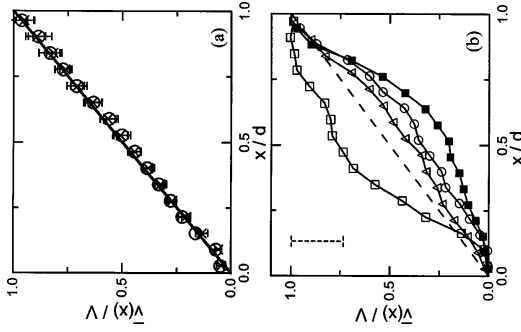ROUYER et al. PHYSICAL REVIEW E **67**, 021405 (2003)

FIG. 4. Normalized velocity profiles $\bar{v}(x)/V$ for different shear strains and strain rates. (a) The symbols indicate the strain interval over which the data have been averaged; (○) $0<\gamma<\gamma_c$, (×) $\gamma_c<\gamma<\gamma^*$. The standard deviation of the strain dependent fluctuations of $\bar{v}(x)/V$ is indicated by the error bars. It is of the order of the experimental resolution. The straight line corresponds to the curve expected for uniform strain. The strain rate is 0.04 s⁻¹. Comparable results are obtained in the entire range of strain rates. (b) Velocity profiles averaged over the strain interval $\gamma^*<\gamma<1.7$. The symbols correspond to experiments with the following parameters: (○) $\dot{\gamma}=0.22$ s⁻¹ and $\gamma^*=0.85$, (△) $\dot{\gamma}=0.14$ s⁻¹ and $\gamma^*=0.76$, (□) $\dot{\gamma}=0.04$ s⁻¹ and $\gamma^*=1$, (■) $\dot{\gamma}=0.03$ s⁻¹ and $\gamma^*=0.60$. The gap width d is equal to 11.5 mm in all experiments except the one for $\gamma=0.03$ s⁻¹, where $d=16$ mm. The dashed straight line corresponds to uniform strain. Typical strain dependent fluctuation of $\bar{v}(x)/V$ is illustrated by an error bar drawn in the top left corner.

an increasing function of the applied strain and which we expect to be a bulk property of the foam for $\gamma<\gamma^*$. A simple statistical argument given in the Appendix allows to relate ρ to the probability p that no rearrangement occurs in the observed volume V_{obs} for strains up to γ: $\rho=-\ln(p)/V_{obs}$. We estimate the strain γ for which $p=0.5$ as the average of γ_c, obtained in a set of experiments for a given strain rate $\dot{\gamma}$. In our experiments, we thus obtain a bulk density of rearrangements ρ equal to 1.7 cm⁻³. To summarize this analysis, we note that the average of strain that induces the onset of rearrangements, detected with a level of sensitivity of 1.7 rearrangements per cm³.

In the previous discussion, we assumed that the first rearrangement observed during a shear start-up experiment is induced by the applied strain. However, this hypothesis is

Left page

FIG. 5. Onset of yielding γ_c as a function of strain rate $\dot\gamma$. Open circles and disks correspond to experiments with a gap width equal to 11.5 mm and 16.0 mm, respectively. The continuous line corresponds to the fit explained in the text. Error bars indicate the measurement errors due to the finite image grabbing rate.

valid only if rearrangements due to the coarsening process are sufficiently rare; the number of such rearrangements detected in the observed volume per unit time, multiplied by $\gamma_c/\dot\gamma$ must be much smaller than one. This argument, based on the assumption that coarsening and strain induced rearrangements are independent phenomena, implies that we must restrict our study to strain rates much larger than 10^{-3} s^{-1}. To rule out artifacts related to the finite size of the sample, the measurements have been performed for two different gap widths; results are indeed independent of this parameter for a fixed amount of observed volume.

The data shown in Fig. 5 indicate that γ_c is nearly constant for low strain rates ranging from 0.002 to 0.07 s^{-1}. At higher strain rates, the onset of yielding occurs at strains γ_c that strongly increase with $\dot\gamma$. This evolution of the yield stress with strain rate can be understood qualitatively by noting that in the quasistatic limit, the stress is dominated by surface tension forces whereas at high strain rates, viscous stresses play an important role. We expect on dimensional grounds that the limit of the quasistatic regime should be governed by a characteristic capillary number Ca$=\mu R\dot\gamma/\sigma$. This criterion should allow to compare yielding in foams of different liquid viscosity, surface tension, and bubble radius for a gas volume fraction comparable to that of our samples. Our experiments cover the range $7\times10^{-8}<$Ca$<7\times10^{-6}$ with a crossover at a capillary number of the order of 2×10^{-6}. Previous rheological determinations of yield stresses and strains at well defined strain rates have generally been carried out at much lower capillary numbers, corresponding to the quasistatic regime [12]. This is consistent with the fact that yield strains and stresses have been reported to be independent of strain rate.

More insight is provided by the theoretical analyses by Khan and Armstrong [8] and Kraynik and Hansen [9] who used a model of film-level viscous flow to study simple shearing flow of perfectly ordered two-dimensional foams. They showed that the effect of viscous forces under steady shear is governed by a modified capillary number Ca'

$=\alpha\mu a(1-\phi)\dot\gamma/\sigma$, where a is the initial length of a cell side, ϕ the gas volume fraction, and α a geometrical prefactor of the order of 1. They further predicted that the most significant effect of the viscous forces consists in slowing down any length changes of the films separating bubbles. Thus, for high shear rates, bubbles will rearrange only after having reached very strong deformations. The yield strain γ_c is predicted to be independent of Ca' up to a characteristic value above which a rapid increase of γ_c with Ca' is expected. Furthermore, the cited theoretical studies present numerical values of $\gamma_c($Ca'$)$ that may be described by a relation of the form $\gamma_c=\gamma_{c,o}+A$Ca'$,$ where $\gamma_{c,o}$ is the quasistatic limit of γ_c and $A\approx20$ is a dimensionless parameter. This expression is equivalent to $\gamma_c=\gamma_{c,o}+T\dot\gamma,$ where T is a characteristic time. The fit in Fig. 5 shows that our data is in agreement with the expected functional relation with $\gamma_{c,o}=0.05\pm0.02$ and $T=1.08\pm0.14$ s. However, the prefactor A deduced from our experimental data exceeds the theoretical value by at least five orders of magnitude. This may partly be due to the fact that the theoretical model describes ordered 2D foam. In this context, new theoretical work taking into account mechanisms related to fluid flow in the vicinity of the Plateau borders [10], viscous flow along the Plateau borders which is specific to 3D foams as well as interfacial viscoelastic effects [24] would be of great interest. A better understanding of the maximum strain rate where yielding behavior is quasistatic is crucial for the comparison of experimental data with simulations obtained using the surface evolver software. Indeed, the results of this much used tool for theoretical investigations are only valid in the quasistatic regime [2,7]. Moreover, in applications of flowing foam such as mineral flotation [25], bubbles are of the order of a millimeter, and thus flow behavior at capillary numbers beyond the quasistatic regime is of great practical interest.

The quantitative comparison of our results concerning γ_c with rheological yield strain data is not straightforward, since there is at present no proven theory relating quantitatively the onset of structural changes to macroscopic rheological behavior. Yield strains for dry foams reported in the literature [8,14] strongly vary according to the experimental technique and yield criterion used, the values are in the range from 0.18 to 0.5. Surface evolver simulations of the yielding of dry 3D foams also give values in this range [26], even though systematic statistical studies to our knowledge have not yet been published in the literature. A fundamental problem for experimental as well as for numerical studies of yielding is the great variety of microstructures possible for a random foam. Surface evolver simulations of sheared 3D dry foams have recently shown that an "annealed" structure of decreased energy can be obtained by strain cycling of an amplitude large enough to provoke many rearrangements but small enough to prevent the buildup of residual stress [27]. We expect that prolonged coarsening can be considered as another way to obtain a statistically well defined distribution of internal strains that naturally appears in any sufficiently stable foam. The onset of yielding should be observed at much higher strains if annealed rather than coarsened foams are studied. To verify this prediction, we have carried out successive strain cycle experiments as described in Sec. II.

Right page

FIG. 6. The image correlation factor C [cf. Eq. (1)] is represented as a function of the maximum strain γ_{max} applied in a strain cycling experiment. C is measured for the first (disks), a second, and a third shear cycle. The first cycle leads to irreversible rearrangements starting at deformation amplitudes in the range 0.1–0.15. Remarkably, the second as well as the third cycles do not induce a significant amount of further rearrangements below strain amplitudes of the order of 0.25. At larger strain amplitudes, all three cycles induce rearrangements. These findings concerning the interplay of strain history and yielding will help to guide the future development of mesoscopic foam rheology models.

Figure 6 shows image correlation factors that allow to compare the onset of irreversible changes induced by a first, a second, and a third shear cycle. The first cycle leads to irreversible rearrangements starting at deformation amplitudes in the range 0.1–0.15. Remarkably, the second as well as the third cycles do not induce a significant amount of further rearrangements below strain amplitudes of the order of 0.25. At larger strain amplitudes, all three cycles induce rearrangements. These findings concerning the interplay of strain history and yielding will help to guide the future development of mesoscopic foam rheology models.

IV. SUMMARY AND CONCLUSION

Using video observation of dry aqueous foams combined with spatiotemporal image analysis, we have studied the onset of yielding at the start up of a steady shear flow as a function of strain rate $\dot\gamma$. We have shown by direct observa-

tion in the bulk that the strain induced rearrangements that occur at small strains are distinct, localized events. In a range of strains extending well beyond the onset of yielding, we have explicitly verified that the bubble velocity profile in the gap is linear. For very large strains, fluctuating nonlinear profiles are found. Furthermore, we have observed a transition from a quasistatic regime at low $\dot\gamma$ to a regime where the onset of yielding occurs at strains that rapidly increase with $\dot\gamma$. These findings are in qualitative agreement with previous theoretical studies of viscous effects in 2D dry foams even though the underlying physical mechanism may not yet be well understood. Moreover, we have performed strain cycling experiments showing that the onset of rearrangements in a shear start-up flow strongly depends on strain history. Experimentally, reproducible histories may be obtained either by prolonged coarsening or by shear cycling, leading to onsets of yielding at widely differing strains.

APPENDIX

Let us call δV a small element of the foam sample volume corresponding to the typical extent of structural changes observed upon a shear induced rearrangement and ρ the number of such rearrangements per volume. Since here, we are interested only in the onset of yielding, we restrict our discussion to the case ρ $\delta V\ll1$. Our observations show that ρ is independent of the position in the sample and we therefore describe shear induced rearrangements using a Poisson process in space. As a consequence, the probability x of not finding a rearrangement in the observed part of the sample volume V_{obs} is: $x=(1-\rho\ \delta V)^{V_{obs}/\delta V}$. Since $V_{obs}\gg\delta V$, we obtain to a good approximation, $x=e^{-\rho V_{obs}}$.

[1] R. G. Larson, *The Structure and Rheology of Complex Fluids* (Oxford University Press, Oxford, 1999), Chaps. 1 and 9.
[2] D. Weaire and S. Hutzler, *The Physics of Foams* (Clarendon Press, Oxford, 1999), Chaps. 1 and 8.
[3] H. M. Princen, J. Colloid Interface Sci. **91**, 160 (1983).
[4] P. Sollich, F. Lequeux, P. Hébraud, and M. E. Cates, Phys. Rev. Lett. **78**, 2020 (1997); P. Hébraud and F. Lequeux, *ibid.* **81**, 2934 (1998).
[5] T. Okuzono and K. Kawasaki, Phys. Rev. E **51**, 1246 (1995).
[6] D. J. Durian, Phys. Rev. E **55**, 1739 (1997); S. Tewari *et al.*, *ibid.* **60**, 4385 (1999).
[7] D. A. Reinelt and A. M. Kraynik, J. Fluid Mech. **311**, 327 (1996); J. Rheol. **44**, 453 (2000).
[8] S. A. Khan and R. C. Armstrong, J. Non-Newtonian Fluid Mech. **22**, 1 (1986); **25**, 61 (1987).
[9] A. M. Kraynik and M. G. Hansen, J. Rheol. **31**, 175 (1987).
[10] L. W. Schwartz and H. M. Princen, J. Colloid Interface Sci. **118**, 201 (1987).
[11] T. Okuzono, K. Kawasaki, and T. Nagai, J. Rheol. **37**, 571 (1993).
[12] S. A. Kahn, C. A. Schnepper, and R. C. Armstrong, J. Rheol. **32**, 69 (1988).
[13] B. S. Gardiner, B. Z. Dlugogorski, and G. J. Jameson, J. Rheol. **42**, 1437 (1998).
[14] A. Saint-Jalmes and D. J. Durian, J. Rheol. **43**, 1411 (1999).
[15] R. Höhler, S. Cohen-Addad, and A. Asnacios, Europhys. Lett. **48**, 93 (1999).
[16] A. D. Gopal and D. J. Durian, J. Colloid Interface Sci. **213**, 169 (1999).
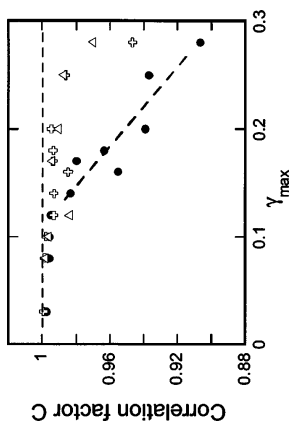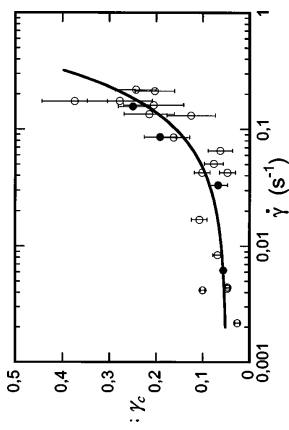[17] S. Cohen-Addad and R. Höhler, Phys. Rev. Lett. **86**, 4700 (2001).

Is the yield stress of aqueous foam a well-defined quantity?

Florence Rouyer*, Sylvie Cohen-Addad, Reinhard Höhler

Université de Marne-la-Vallée, Laboratoire de Physique des Matériaux Divisés et des Interfaces, UMR 8108 du CNRS, 5 Boulevard Descartes, 77454 Marne-la-Vallée Cedex 2, France

Abstract

Dimensional arguments suggest that the yield stress of aqueous foams and emulsions, for a given volume fraction of the dispersed phase, should scale as the ratio of surface tension and a length scale, such as the mean bubble radius. We show that yield stress data from the literature and from our experiments follow this scaling only in a very rough approximation. We present new experimental evidence that clarifies the role of shear banding in this context and we discuss the robustness of the yield stress with respect to changes of flow geometry and experimental technique. Finally, we show that scaling oscillatory yield stress data by the elastic shear modulus at small amplitude provides a master curve when plotted versus the volume fraction of the dispersed phase.
© 2005 Elsevier B.V. All rights reserved.

Keywords: Foam; Emulsion; Rheology; Yield stress; Yield strain

1. Introduction

Aqueous foam is a two-phase fluid–fluid mixture with a complex rheological behavior that is similar in many respects to concentrated emulsions and soft pastes. Subjected to small stresses, these materials behave as viscoelastic solids whereas beyond a yield stress, viscoplastic flow is observed [1–3]. In flowing foams or emulsions the bubbles or droplets are progressively deformed and the corresponding local stresses are released by intermittent structural rearrangements at a mesoscopic scale. Dimensional arguments suggest that the elasticity as well as the yield stress of foam and emulsion should scale as surface tension Γ divided by a length scale that many authors have supposed to be equal to the mean bubble radius R. Moreover, the yield stress has been found to increase with the volume fraction of the dispersed phase [4–6]. At a fraction close to 0.64, it falls to zero.

Various experimental studies of yielding as a function of the dispersed volume fraction have been conducted for foams and emulsions, using different experimental techniques, based on steady, transient or oscillatory flows [4–13]. Comparing the yield stress data, normalized by Γ/R, shows much scatter and only an order of magnitude agreement, suggesting that parameters other than Γ/R may have an influence on the yield stress. The samples used in the cited studies differ by their bubble polydispersity, but according to Saint-Jalmes and Durian [6], moderate polydispersity has no effect on yield stress. Mason et al. [4] have shown that the detected yield stress can strongly depend on the experimental technique used. For the same emulsion, yield stress values obtained from oscillatory and steady shear experiments differed by a factor of three at gas volume fractions above 0.7. This difference is attributed to shear banding observed in steady flow of the sample. Several recent experimental studies [14–17] have provided further direct evidence for such heterogeneous flow in 2D and 3D foams as well as 3D emulsions. Thus, in situ visualization of foam flow is of crucial importance for the interpretation of yield stress measurements. Moreover, recent work on yield strain fluids suggests that the behavior observed under controlled stress may significantly differ from the behavior under controlled strain rate [18]. We have therefore performed measurements under both conditions.

DYNAMICS OF YIELDING OBSERVED IN A THREE-...

[18] I. K. Ono, C. S. O'Hern, D. J. Durian, S. A. Langer, A. J. Liu, and S. R. Nagel, Phys. Rev. Lett. **89**, 095703 (2002).

[19] L. Cipelletti and L. Ramos, Curr. Opin. Colloid Interface Sci. **7**, 228 (2002).

[20] F. da Cruz, F. Chevoir, D. Bonn, and P. Coussot, Phys. Rev. E **66**, 051305 (2002).

[21] A. D. Gopal and D. J. Durian, e-print cond-mat/0208181.

[22] Y. Khidas, S. Cohen-Addad, and R. Höhler (unpublished).

[23] A. D. Gopal and D. J. Durian, Phys. Rev. Lett. **75**, 2610 (1995).

[24] D. M. A. Buzza, C.-Y. D. Lu, and M. E. Cates, J. Phys. II **5**, 37 (1995).

[25] See for instance, www.mimpt.com.au/jamesoncell-advantages.html

[26] A. M. Kraynik, D. A. Reinelt, and F. van Swol, in *Proceedings of the 3rd EuroConference on Foams, Emulsions and Applications*, edited by L. J. Z. Pacelli, J. Banhart, and G. L. M. M. Verbist (Verlag MIT, Bremen, 2000), p. 191.

[27] A. M. Kraynik, D. A. Reinelt, and F. van Swol (unpublished).

The aim of the present study is to clarify whether the yield stress of aqueous foam is a well-defined quantity that can be specified independently of a specific flow geometry and experimental setup. To answer this question and to rule out artifacts related to inaccurate sample characterization, we compare results obtained using different techniques for the same kind of foam. In all of these experiments, the flow of the sample is directly observed, which allows detecting the onset of heterogeneous flow. The results are discussed and compared to the data in the literature using two ways of scaling. The standard one which consists in dividing yield stress by Γ/R and a new one using the elastic shear modulus measured at small deformation. This latter approach has the advantage of being robust with respect to inaccurate physico-chemical sample characterization.

2. Experiments

2.1. Foam samples

The samples consisted of either Gillette shaving cream [19] or a foam that we will refer to as TTAB foam. The latter is produced by mixing nitrogen saturated with perfluorohexane vapor and an aqueous solution containing a cationic surfactant tetradecyltrimethylammonium bromide, usually noted TTAB (0.936%, g/g), dodecanol (6.24 × 10⁻⁴%, g/g) and glycerol (50%, g/g). All the chemicals were purchased from Aldrich and used as received. The concentrations are expressed as the weight of chemicals divided by the total weight of the solution. This formulation was chosen to ensure slow coarsening and drainage, thereby enhancing foam stability [20]. The gas and liquid were injected at the bottom of a vertical cylindrical column (2 cm i.d. and 15 cm high) in which a rotating plate mixes the two phases. The foam gas volume fraction can be adjusted in the range 83–94%, by varying the gas and liquid flow rates. The foam flows from the top of the column through a tube which allows filling directly the rheometer. Using the Wilhelmy plate method, the surface tension of the foaming solution was found to be $\Gamma = 37.5 \pm 0.5$ mN/m at a temperature of 21 °C. The arithmetic mean bubble radius R deduced from observations of the sample surface is 21 ± 4 µm at an age of 5 min.

For Gillette foam, we measured a liquid surface tension $\Gamma = 30 \pm 1$ mN/m using the Wilhelmy plate method. We found that gas volume fraction upon production of Gillette foam decreases progressively as the bottle is emptied. Using this fact, we were able to obtain samples with gas volume fractions ϕ from 94% to 83%. For $\phi = 92\%$, we found a mean bubble radius $R \cong 10$ µm at an age of 5 min and $R \cong 15$ µm at an age of 30 min. In all cases, ϕ is measured upon foam production to a precision better than 2% by weighing a known volume of foam. Using this
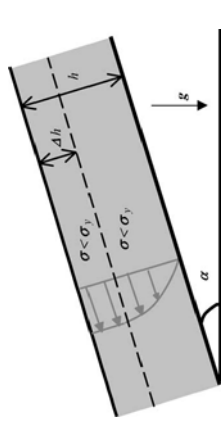
volume fraction progressively introduced by drainage. Such an effect would have a much stronger influence on h_f than on the earliest measurements of Δh. For Gillette foam, the precision of the measure of σ_y is of the order of 3 Pa, due to the uncertainties on gas volume fraction and foam thickness. Note that Δh and h_f are determined up to an uncertainty of ±1 mm.

The inclined plane method is not well adapted for studying the yielding of very dry foams where extremely large sample thicknesses would be required to induce yielding and flow, even if the plane is vertical. All rheological measurements are difficult at very low gas volume fractions because of drainage occurring during the experiment and the beginning of the experiment or even during the experiment. In the present study, we have only studied samples with gas volume fractions ranging from 78% to 83%. The interest of inclined plane measurements is that it is very easy to detect wall slip in this configuration. Moreover, the sample is simultaneously subjected to shear stresses ranging from zero (on top of the foam) up to a maximum value (at the plate). In other types of experiments where a homogeneous progressively increasing stress is applied, the question arises to what extent strain history and aging effects have an influence on the measurement.

2.2. Inclined plane set-up

The yield stress of a complex fluid can be measured by visualizing its flow on an inclined plane, due to its own weight [21,22]. Assuming steady laminar flow and homogeneous sample thickness, it has been shown that shear stress due to gravity increases linearly with the depth, measured from the upper free surface towards the inclined plane (Fig. 1). The characteristic depth Δh at which the shear stress reaches the yield stress σ_y is given by: $\sigma_y = \rho g \Delta h \sin(\alpha)$, where ρ, g and α are respectively the foam density, gravity acceleration and inclination angle [22]. The lower part of the foam yields and flows whereas the upper part remains solid-like and is carried away by translation. As a consequence, the thickness h of a finite sized sample decreases with time. The sample stops flowing when its thickness reaches a value h_f, equal to the solid-like layer depth Δh [21].

In our set-up, the foam is introduced in a parallelepipedic frame (7 cm long, 5 cm wide, 2.5 cm high), placed on an initially horizontal plane. Right after the filling, the plane is inclined to an angle α that can be fixed between 10° and 90°. The surface of the plane is covered with sand paper to avoid wall slip. Temperature is fixed at 21 ± 1 °C. About 5 min after foam production (the time necessary to install the sample in a reproducible way), the frame is withdrawn without perturbing the sample shape, and the set-up covered by a large transparent box filled with air saturated with humidity to avoid evaporation of the foam liquid content. This box does not touch the foam sample. To visualize the flow, a black stripe is painted on the vertical free sample surface. Its time evolution as well as the thickness of the sample are recorded using a CCD camera, oriented towards the vertical lateral free surface (cf. Fig. 1). We determine the yield stress from these data by measuring the quantities Δh at any time during the flow and h_f when foam stops flowing. Both analyses gave the same results and were independent of α. This agreement strongly argues against significant artifacts in the yield stress determination related to the heterogeneity of sample gas

Fig. 1. Schematic sketch of a foam sample of thickness h flowing on a plane inclined by an angle α with respect to the horizontal direction. The gray curve represents a typical velocity profile. The dashed line separates two regions: In the upper region, of thickness Δh, foam behaves as an elastic solid and its motion is a homogeneous translation. In the lower region, the foam flows and the velocity increases with the distance from the plane. The vector g describes acceleration due to gravity.

Fig. 2. Evolution of the elastic G' and loss G'' shear moduli, normalized by the elastic modulus G_0 (obtained in the limit of small amplitude, vs.: (a) stress amplitude σ normalized by the yield stress σ_y, (b) strain amplitude γ normalized by the yield strain γ_Y. Empty symbols correspond to controlled stress experiments, full symbols to controlled strain experiments. Hatched areas correspond to the observed onset of strain localization. Dashed lines represent power law fits to G'/G_0 at small and large amplitudes. The sample consists of Gillette foam with gas volume fraction equal to 92% at an age of 30 min. The frequency is 0.3 Hz.

2.3. Cylindrical Couette rheometer

Right after its production, the foam is injected into the gap of a cylindrical Couette rheometer (Bohlin CVOR150). The inner and outer radii are respectively equal to 21 and 25 mm, and the height of the inner rotating cylinder is 48 mm. The surfaces in contact with the foam are grooved to prevent wall slip, and the air in contact with the samples is saturated with humidity to avoid evaporation. All the experiments were carried out at a temperature of 21 ± 1 °C. The samples were sheared using either controlled oscillatory strain or controlled oscillatory stress. Moreover, frequency was varied between 0.3 and 3 Hz. The complex shear modulus, denoted $G^* = G' + iG''$, is obtained from the amplitudes and phases of the first harmonic shear stress and strain signals. Close to the yield strain, the rheological response is nonlinear so that for a complete study of the behavior the full spectrum of strain or stress harmonics has to be considered. Such results will be presented in a separate publication [23]. The complex shear modulus was measured as a function of controlled strain or controlled stress amplitude.

or strain amplitude was reproducible. Results obtained with controlled stress or controlled strain do not present any significant difference in the explored range of parameters (cf. Fig. 2). There is no unique and rigorously motivated criterion allowing a yield stress to be determined from oscillatory data. A possibility consists in representing G' versus stress amplitude σ in a log–log plot. The behavior well above and well below the yield stress is well described by power laws corresponding to straight lines in such a plot. Their intersection provides an empirical definition of a yield stress σ_Y. This construction is illustrated in Fig. 2a. We use an analogous approach to determine the yield strain γ_Y using a log–log plot of G' versus strain amplitude γ (cf. Fig. 2b). In the literature, the yield stress has been deduced from oscillatory data by plotting the stress amplitude as a function of strain amplitude. σ_Y is obtained from the intersection of lines fitted to data at low and high strain amplitudes in a log–log plot [4,6]. We compare results obtained from all these procedures in Fig. 3 where yield stress is plotted as a function of frequency. Yield strains are converted in yield stresses by the relation $\sigma_y = |G^*|\gamma_Y$, where G^* is measured for a strain amplitude γ_Y. Manifestly, all these data are consistent. To check whether the yielding deduced from oscillatory data is affected by heterogeneous flow phenomena, we have observed the deformation of a black stripe painted on the free surface of the foam samples in the Couette cell, using a video camera. Using this

3. Results and discussion

3.1. Robustness of the determination of yielding by oscillatory experiments

In this section, we present measurements on Gillette foam at an age of 30 min and a gas volume fraction of 92%. The measured variation of the complex shear modulus with stress
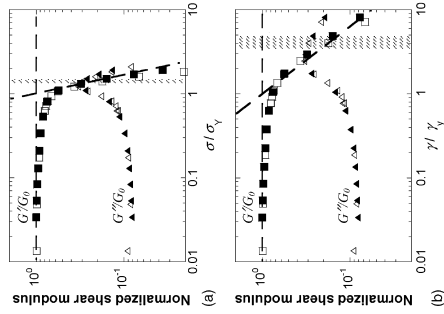
DTD 5

F. Rouyer et al. / Colloids and Surfaces A: Physicochem. Eng. Aspects xxx (2005) xxx–xxx · 4

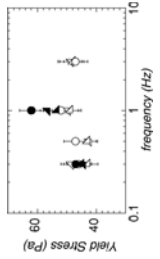F. Rouyer et al. / Colloids and Surfaces A: Physicochem. Eng. Aspects xxx (2005) xxx–xxx · 5

Page 4

Fig. 3. Yield stress vs. frequency measured for Gillette foam with gas volume fraction equal to 92% at an age of 30 min. Empty and full symbols correspond to controlled stress and controlled strain experiments, respectively. Yield stress values are measured using the three different methods explained in details in the text. For ($\triangle$) and ($\blacktriangle$) σ_y is deduced from plots of G' vs. σ; for ($\triangle$) and ($\blacktriangle$) σ_y is deduced from the relation $\sigma_y = \gamma_y |G^*|$ where γ_y is measured from plots of G' vs. γ and G^* is measured for a strain amplitude γ_y; for ($\bigcirc$) and ($\bullet$), σ_y is measured from plots of σ vs. γ.

method, we did indeed detect marked strain localization under controlled strain as well as under controlled stress. The onset of this phenomenon is indicated by the hatched area in Fig. 2. Since it occurs at stresses far above σ_y, we conclude that the yield stress determined in our samples by an oscillatory experiment may indeed be considered as a well-defined bulk property of the foam. The frequency independence over a decade of the measured yield stress with frequency strongly suggests that experiments are done in a quasi-static regime.

3.2. Comparison between inclined plane and oscillatory experiments

In Fig. 4, we compare yield stresses measured using the inclined plane method and the cylindrical Couette rheometer as a function of volume fraction ϕ for Gillette foam. The foam age is fixed at 5 min, to avoid drainage effects at small gas volume fraction. Within the explored range of volume fractions, the results are in good agreement. Moreover, the data can be fitted by the empirical law $\sigma_y = A(\phi - 0.64)^2$ as proposed in the literature [4,6]. Our results show that the present determinations of yield stress for Gillette foam are robust with respect to a change of flow geometry and boundary conditions.
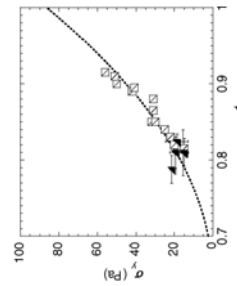
Fig. 4. Yield stress measured by the inclined plane method ($\blacktriangle$) compared to oscillatory measurement ($\boxtimes$) vs. volume fraction ϕ. The samples consist of Gillette foam at an age equal to 5 min. The dotted line represents the fit to the data of the equation: $\sigma_y = A(\phi - 0.64)^2$, with $A = 667$ Pa.
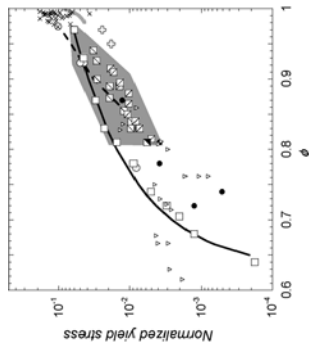
3.3. Normalization and comparison with the literature

In Fig. 5, we compare the yield stress of Gillette foam and TTAB foam measured by oscillatory experiments as a function of volume fraction to previous experimental data that we have found in the literature. All results are normalized by Γ/R, except those obtained by [8,11] that are normalized by Γ/R_{32} where R_{32} is the Sauter mean radius, defined as the ratio of the third and second moments of the bubble radius distribution. The data clearly do not form a well-defined master plot. This disagreement cannot be attributed to the use of different experimental techniques, as previously pointed out in the literature [5]. Even if we only consider oscillatory measurements reported here and in previous studies of emulsions and foams [4,6], results obtained at a given dispersed volume fraction can vary by more than a factor of 3. It seems improbable that such a discrepancy is due to experimental errors of the measured surface tension or average bubble radius. Part of the scatter of the results may be due to differences in the frequencies used by the investigators. G^* has been shown to vary considerably at very low frequencies [24,25]. However, our yield stress data measured in the range of frequencies typically used for oscillatory σ_y measurements did not show any significant frequency dependence (cf. Fig. 3). To explain the large scatter of the data in Fig. 5, we recall the conjecture by Princen and Kiss [11] that the yield stress should scale as $1/R_{32}$ rather than $1/R$. Note that the physical origin of elastic stress in foam is the surface tension of the gas–liquid interfaces and $1/R_{32}$ is proportional to the amount of interfacial area per unit volume. Unfortunately, for most

Fig. 5. Yield stress normalized by Γ/R vs. volume fraction. Our data are compared to previous results: Princen and Kiss (steady shear) [11] (dashed line), Gardiner et al. (pendulum technique) [5] (continuous gray line), Saint-Jalmes and Durian (oscillatory) [6] (continuous black line), Wenzel et al. (steady shear) [7] ($\times$), Yoshimura et al. (steady shear) [8] ($\bigcirc$), Calvert and Nezhati (steady shear) [9] ($\triangledown$), Khan et al. (stress relaxation technique) [10] ($\oplus$), Mason et al. [4]: oscillatory ($\square$) and steady shear ($\bullet$) experiments. Present study: Gillette foam for oscillatory ($\boxtimes$) and inclined plane methods ($\blacktriangle$), and TTAB foam (oscillatory) ($\boxdot$). The gray area is a guide to the eye highlighting the scatter of oscillatory measurements reported by different authors.

Page 5

experiments published in the literature the Sauter mean radius is not known. Studies of the bubble size distributions at the surface of our samples show that R_{32}/R can vary between 1.5 and 2, and that this ratio can be volume fraction and time dependent. Note that it is indeed difficult to deduce rigorously bulk bubble size distributions of 3D foams from surface observations. Therefore, a scaling using the Sauter mean radius would strongly reduce the discrepancy between normalized data for monodispersed emulsions [4] where $R_{32}/R = 1$ and our data.

To test the conjecture that scaling by Γ/R_{32} provides a much better master plot of the yield stress data, we normalize yield stress by the elastic shear modulus at small amplitude, denoted G_0. According to early work as well as recent numerical simulations G_0 scales as Γ/R_{32} [26,27], so that the ratio of σ_y/G_0 should not depend on surface tension and bubble size distribution if σ_y indeed depends on the Sauter mean radius. Fig. 6 shows that with such a normalisation, there is good agreement between all yield stresses obtained using the oscillatory method, reported in the literature as well as here. These results collapse on the same curve: $\sigma_y/G_0 = C(\phi - 0.64)\phi$ with $C \cong 0.39$, suggesting that the yield stress is a well-defined quantity in the context of oscillatory flows. This result implies that polydispersity has an effect on yielding. The differences between oscillatory data and the yield stresses deduced from steady shear experiments [4,10,11] may be due to shear banding as previously suggested by [4]. Recent magnetic resonance imaging studies of flowing foams [17] and concentrated emulsions [15] strongly argue in favor of this interpretation.

4. Conclusion

We have subjected foam samples to oscillatory flows and to flows on an inclined plane. We have visualized in situ the flow profile at the free sample surface in order to check for strain localization. In oscillatory experiments, yielding occurs for strain or stress amplitudes clearly below the onset of localization. Our results obtained using oscillatory experiments are robust with respect to different choices of the yield criterion and coincide with measurements using the inclined plane method. Moreover, we compare our data to previous oscillatory yield stress data for foams and emulsions. These results, plotted versus volume fraction of the dispersed phase, can be collapsed onto a master curve provided the yield stress is normalized by the elastic shear modulus at small amplitude. Such a consistent picture is not obtained using a normalization using the ratio of surface tension and mean radius. Since the shear modulus has been predicted to scale as the inverse of the Sauter mean radius, this suggests that the yield stress follows the same scaling. The remaining discrepancies observed between oscillatory yield stress data and data obtained by other experimental techniques might be due to strain history effects or shear-banding phenomena.

References

[1] A.M. Kraynik, Ann. Rev. Fluid Mech. 20 (1988) 327.
[2] D. Weaire, S. Hutzler, The Physics of Foams, Clarendon Press, Oxford, 1999.
[3] R.G. Larson, The Structure and Rheology of Complex Fluids, Oxford University Press, New York, 1999.
[4] T.G. Mason, J. Bibette, D.A. Weitz, J. Colloid Interface Sci. 179 (1996) 439.
[5] B.S. Gardiner, B.Z. Dlugogorski, G.J. Jameson, R.P. Chhabra, J. Rheol. 42 (1998) 1437.
[6] A. Saint-Jalmes, D.J. Durian, J. Rheol. 43 (1999) 1411.
[7] H.G. Wenzel, R.J. Brungraber, T.E. Stelson, J. Mater. 5 (1970) 396.
[8] A.S. Yoshimura, R.K. Prud'Homme, H.M. Princen, A.D. Kiss, J. Rheol. 31 (1987) 699.
[9] J.R. Calvert, K. Nezhati, Heat Fluid Flow 8 (1987) 102.
[10] S.A. Kahn, C.A. Schnepper, R.C. Armstrong, J. Rheol. 32 (1988) 69.
[11] H.M. Princen, A.D. Kiss, J. Colloid Interface Sci. 128 (1989) 176.
[12] A.D. Gopal, D.J. Durian, Phys. Rev. Lett. 75 (1995) 2610–2613.
[13] F. Rouyer, S. Cohen-Addad, M. Vignes-Adler, R. Höhler, Phys. Rev. E 67 (2003) 021405.
[14] G. Debregeas, H. Tabuteau, J.-M. di Meglio, Phys. Rev. Lett. 87 (2001) 8305.
[15] P. Coussot, et al., Phys. Rev. Lett. 88 (2002) 218301.
[16] J. Lauridsen, G. Chanan, M. Dennin, Phys. Rev. Lett. 93 (2004) 018303.
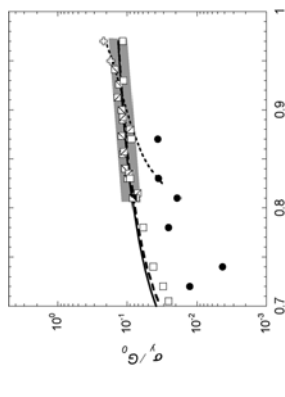
Fig. 6. Yield stress normalized by elastic shear modulus vs. volume fraction. Our data are compared to previous results: Princen and Kiss [11,26] (dotted line), Saint-Jalmes and Durian (oscillatory) [6] (continuous black line), Khan et al. [10] ($\oplus$), Mason et al. [4]: oscillatory ($\square$) and steady shear ($\bullet$) experiments. Present study: Gillette foam for oscillatory ($\boxtimes$) and inclined plane ($\blacktriangle$) measurements, TTAB foam (oscillatory) ($\boxdot$). The dashed line corresponds to the curve: $\sigma_y/G_0 = 0.39(\phi - \phi_c)/\phi$. The gray area is a guide to the eye to highlight the consistency between oscillatory measurements.

The large amplitude oscillatory strain response of aqueous foam: Strain localization and full stress Fourier spectrum

F. Rouyer[1,a], S. Cohen-Addad[1], R. Höhler[1], P. Sollich[2], and S.M. Fielding[3]

[1] Université Paris-Est, Laboratoire de Physique des Matériaux Divisés et des Interfaces, UMR 8108 du CNRS, 5 Boulevard Descartes, 77 454 Marne-la-Vallée cedex 2, France
[2] King's College London, Department of Mathematics, Strand, London WC2R 2LS, UK
[3] Manchester Centre for Nonlinear Dynamics and School of Mathematics, University of Manchester, Manchester M13 9EP, UK

Abstract. We study the low frequency stress response of aqueous foams, subjected to oscillatory strain. As the strain amplitude is progressively increased starting from zero, the initially linear viscoelastic response becomes nonlinear as yielding sets in. To characterize this crossover from solid-like to liquid-like behaviour quantitatively, the full harmonic spectrum of the stress is measured. These results are compared to the soft glassy rheology model as well as to elastoplastic models. Moreover, to check for strain localization, we monitor the displacement profile of the bubbles at the free surface of the foam sample in a Couette cell using video microscopy. These observations indicate that strain localisation occurs close to the middle of the gap, but only at strain amplitudes well above the yield strain.

PACS. 83.80.Iz Rheology: Emulsions and foams – 47.57.Bc Fluids dynamics: Foams and emulsions – 83.60.La Viscoplasticity; yield stress

1 Introduction

Aqueous foam is a metastable disordered complex fluid, made up of gas bubbles closely packed in a surfactant solution. It behaves like a viscoelastic solid or like a non-Newtonian liquid, depending on gas volume fraction and applied stress [1–3]. In the work reported here, we focus on the nonlinear viscous, elastic and plastic response of 3D foams at the shear-induced transition between solid-like and liquid-like behaviour. Non-Newtonian steady flow has been probed experimentally and interpreted in terms of interactions on the bubble scale [4–7]. Insight into the physical processes explaining the transient dynamics that accompany the onset of yielding requires additional experiments. Such information can be gained by applying oscillatory strain so that the sample switches back and forth between solid-like and liquid-like behaviour on well-defined scales of time and strain amplitude. Previous studies of the oscillatory foam response as a function of strain amplitude were focussed on the fundamental harmonic components of stress and strain [8,9] and discussed in terms of a strain amplitude dependent complex shear modulus. However, much additional information is contained in the spectrum of harmonics, or equivalently in the Lissajous representation showing the evolution of stress *versus* strain with the time as a parameter [10]. Indeed, for a fixed strain amplitude and frequency, the complex shear modulus alone

does not allow to distinguish whether the dissipation of a predominantly elastic sample is of viscous or plastic origin. In contrast, a Lissajous plot does directly allow such a distinction since it exhibits a characteristic signature of the nonlinear response. It has the shape of an ellipse for viscous dissipation or of a parallelogram for plastic dissipation. Therefore, Lissajous data provide the opportunity to test physical foam rheology models predicting the onset of plastic response with increasing strain amplitude, corresponding on the local scale to the onset of strain-induced irreversible bubble rearrangements. The evolution of the complex shear modulus with strain amplitude also provides information about the mechanisms involved in the sample deformation, but the following example shows that such evidence alone can be misleading. In a recent experimental study of a biological yield stress fluid [11] the complex shear modulus was found to be almost independent of strain amplitude up to the yield strain so that one might have expected that the rheological response is linear in this entire range. Remarkably, a Lissajous plot revealed that this is not true: strong strain hardening is observed within each strain cycle. Motivated by this context, we study in the present paper the oscillatory response of 3D foam at the transition from solid-like to liquid-like behaviour, detecting for the first time the full stress harmonics spectrum.

Rheological studies of flowing foam, at a macroscopic scale, require great care, because the engineering strain,

DTD 5

6   F. Rouyer et al. / Colloids and Surfaces A: Physicochem. Eng. Aspects xxx (2005) xxx–xxx

ARTICLE IN PRESS

[17] S. Rodts, J.C. Baudez, P. Coussot, Europhys. Lett. 69 (4) (2005) 636.
[18] F. Da Cruz, F. Chevoir, D. Bonn, P. Coussot, Phys. Rev. E 66 (2002) 051305.
[19] The Gillette Company, Gillette UK Ltd., London.
[20] M. Safouane, M. Durand, A. Saint-Jalmes, D. Langevin, V. Bergeron, J. Phys. IV (France) 11 (2001) Pr6-275.
[21] P. Coussot, S. Proust, C. Ancey, J. Non-Newton. Fluid Mech. 66 (1996) 55.
[22] V. Di Frederico, Fluid Dynam. Res. 24 (1999) 23.

[23] F. Rouyer, S. Cohen-Addad, R. Höhler, in preparation.
[24] A.D. Gopal, D.J. Durian, Phys. Rev. Lett. 91 (2003) 188303.
[25] S. Cohen-Addad, R. Höhler, Y. Khidas, Phys. Rev. Lett. 93 (2004) 028302.
[26] H.M. Princen, A.D. Kiss, J. Colloid Interface Sci. 112 (1986) 427.
[27] A.M. Kraynik, D.A. Reinelt, Microrheology of random polydisperse foam, in: Proceedings of the XIVth International Congress on Rheology, 2004.

[a] e-mail: florence.rouyer@univ-mlv.fr

deduced from the relative motion of the sample boundaries, can be different from the local strain relevant for physical models, and it is possible that a solid-like region and a liquid-like region coexist in the same sample. This phenomenon is known as flow localization [7,12]. Since the conditions under which the flow of foam is localized are not yet clear [4,5,7,8,12-14], a reliable interpretation of engineering strain in terms of local strain requires *in situ* observation of the sample deformation during the rheological experiment. We follow this approach and identify the limits of the range of strains where the flow is homogeneous.

The paper is organized as follows: In Section 2.1, we first provide a brief overview of nonlinear rheological data for foams and concentrated emulsions. In Section 2.2, we present theoretical models and we focus on those where, in addition to conventional rheological characteristics, the full harmonics spectrum of the oscillatory stress response has been predicted. So far, the soft glassy rheology (SGR) model and a simple elastoplastic model fulfil this criterion. Section 3 describes the sample preparation and the experimental procedures are given in Sections 4 and 5. In Section 6, experimental and theoretical results are presented and discussed in the framework of other recent experiments. On this basis, directions for further development of foam rheology models are pointed out.

2 Previous nonlinear rheological experiments and models

2.1 Experiments probing nonlinear rheology of 3D foams and concentrated emulsions

Experiments probing the solid-liquid transition

Experimentally, the nonlinear rheological response of 3D foam at the transition from solid-like to liquid-like behaviour has been studied by measurements of the stress response to a steady applied shear rate [4-6,15], and to strain steps superimposed to such a constant strain rate [13]. These data alone do not fully characterize the nonlinear response. As the sample passes from solid-like to liquid-like behaviour, there is transient behaviour, evidenced by viscosity bifurcation dynamics [16] and the stress overshoot reported in shear start-up experiments [15]. Transient dynamics have also been found by applying oscillatory strain [8,12,17]. At amplitudes far below the yield strain, the stress is sinusoidal and its amplitude scales linearly with strain amplitude. When the strain amplitude is increased nonlinear response such as shear-induced normal stresses sets in [18]. Beyond the yield strain, there is a crossover of the real and imaginary parts of the complex shear modulus as a function of strain amplitude. This feature is often used as a criterion to determine the yield strain [8]. Moreover, oscillatory experiments probing how soft disordered materials yield as a function of strain rate amplitude have recently shown that frequency and strain amplitude dependence can be explained in terms of a structural relaxation time which depends on strain amplitude [9]. However none of these oscillatory experiments make use of the information contained in the harmonics spectrum of the stress response, which provides the signature of the physical processes involved in dissipation, as explained in the introduction.

Flow localization

Flow localization of a yield stress fluid can occur as a direct consequence of stress heterogeneity. For example, if a steady torque is applied in a cylindrical Couette geometry, the stress increases with decreasing distance from the inner cylinder. If the stress remains larger than the yield stress only in the vicinity of this cylinder, localized flow sets in. Previous authors have ruled out other forms of localized flow because they obtained compatible results in different rheological geometries [4,8]. Multiple light scattering studies of the flow profile in Couette experiments [4] and observation of the bubble motion at the free sample surface for samples obtained with a variety of foaming solutions in the plate-plate geometry [5] provided additional evidence in favour of this conclusion. However, other experiments with 3D foams have evidenced flow localization [14]. Moreover, MRI observations of the flow in the cylindrical Couette geometry have shown that steady flow is impossible below a critical strain rate $\dot{\gamma}_c$ [7]. This means that for an engineering strain rate smaller than $\dot{\gamma}_c$, part of the sample must remain solid-like whereas another part flows at a shear rate $\dot{\gamma}_c$. At strain rates $\dot{\gamma}$ larger than $\dot{\gamma}_c$, the stress was found to scale with $\dot{\gamma}$ following a power law. In oscillatory shear experiments, shear localization in the *middle* of the gap has been observed [12]. This is an unexpected form of flow localization because the stress is highest in the vicinity of the inner cylinder. Let us note that the flow of 2D foams has recently been studied by many authors, but we will not discuss this work in the present paper focussed on 3D foams.

The flow profile at the free surface of concentrated emulsions has been studied in steady-shear experiments using a Couette cell [19]. For emulsions with dispersed volume fractions well above 0.7, localized flow is reported whereas in more dilute emulsions, the flow was found to be homogeneous [19]. In other recent steady-flow experiments with emulsions, strain localization was found only in the presence of attractive interactions between the droplets [20].

2.2 Models for the rheology of soft disordered materials

Fluidity models are based on a scalar measure of the "degree of jamming" or structural relaxation time, coupled to the flow history of the material: Flow breaks up the jammed structure and reduces the viscosity. In contrast, aging re-establishes the jammed structure and enhances the viscosity [21-23]. The most detailed approach of this kind is based on a Maxwell equation $\partial_t \sigma = -a\sigma + G\dot{\gamma}$, where the parameter a is the fluidity [22]. Aging and shear rejuvenation are expressed by a nonlinear differential equation that describes the spatial and temporal evolution of a, as well as its coupling to stress and strain rate. This model predicts flow heterogeneities reminiscent of shear banding, but which are not intrinsic to the sample in the sense that they are dependent on the boundary conditions for the fluidity at the walls confining the sample.

The SGR Model

The soft glassy rheology (SGR) model is motivated by the strikingly similar rheology of foams, emulsions, pastes and other close packings of small soft units, suggesting that a generic mechanism may be involved. The model explains the rheological behaviour in terms of the dynamics of mesoscopic elements [24,25]. They are chosen sufficiently large compared to the bubbles, grains or droplets so that the local packing structure is not resolved in detail and so that the local strain, stress and yield stress of an element are well-defined quantities. At the same time, the mesoscopic length scale is chosen small enough to capture spatial variations of local strain, stress and yield stress. The SGR model uses a simple mean-field coupling between mesoscopic and macroscopic stress and it describes interactions between mesoscopic regions in terms of an effective noise temperature, denoted x.

In more detail, the SGR model describes an ensemble of mesoscopic elements of the material, each of which is characterized by its local yield energy density E and strain l, the latter being measured relative to a local equilibrium configuration. Elements are assumed to deform elastically, with l incrementing in step with the global strain γ, until their local elastic energy reaches values of order E; they then yield stochastically. The elastic energy is taken to be of the simple quadratic form $kl^2/2$, with k a local elastic constant that is assumed to be uniform across the material for simplicity. The yield rate is the product of a microscopic inverse attempt time $1/\tau_0$, and an activation factor determined by the difference of the actual elastic energy to the yield value. After a yield, elements are taken to have zero local strain ($l=0$) relative to a new local equilibrium configuration, as well as a new yield energy drawn randomly from some fixed distribution $\rho(E)$. This distribution one presumes to be of exponential form, $\rho(E) = (1/E_0)\exp(-E/E_0)$, for $E > 0$. The mean E_0 of this is used to make the effective temperature parameter x dimensionless, *i.e.* the energy (density) available for activation is written as xE_0.

Mathematically, the above assumptions are summarized in the master equation for the probability $P(E, l, t)$ of a given element having yield energy E and strain l at time t:

$$\frac{\partial P}{\partial t} = -\dot{\gamma}(t)\frac{\partial P}{\partial l} - \frac{1}{\tau_0}\exp\left(-\frac{E - kl^2/2}{xE_0}\right)P + Y(t)\delta(l)\rho(E).$$

(1)

The first term on the right corresponds to the uniform increment in the local strains of all elements that do not yield, according to $\dot{l} = \dot{\gamma}$; The second gives the decrease in probability due to yielding, and the third the corresponding increase in probability when elements are "reborn" after a yield; the factor $Y(t)$ can be found from the requirement of conservation of probability.

Once $P(E, l, t)$ has been determined, the global stress Σ is taken as the average of all local stresses kl across this distribution. It is possible, in fact, to solve for $P(E, l, t)$ analytically for a given strain history $\gamma(t)$, and this leads to two coupled constitutive integral equations for $\Sigma(t)$ and $Y(t)$ [24].

One can show that a glass (or jamming) transition takes place in the SGR model at $x = 1$ [25,26]. For smaller x and in the absence of steady shear, the system continues to evolve without ever reaching equilibrium: it ages. We will see, however, that the experimental data presented below can be reasonably fitted using optimal values of x greater than unity. Consequently we will focus on the steady-state predictions of the model. For oscillatory strain, in particular, the amplitude and frequency dependent complex shear modulus $G^*(\Gamma_0, \omega)$ and the residual stress q (see Sect. 4 for definitions) can be found by solving the constitutive equation numerically as outlined in reference [26].

We briefly discuss which parameters appear when fitting predictions of the SGR model to experimental data. The elastic (G') and viscous (G'') components of the complex modulus $G^* = G' + iG''$ both scale with the local elastic constant k; this can be eliminated by normalizing by the linear response limit value (denoted G' below) of G' at each given angular frequency ω. The dependence on frequency of the SGR predictions is through the dimensionless combination $\Omega = \omega\tau_0$. Similarly, the dependence on the strain amplitude Γ_0 is through a scaled strain $\Gamma_0/\Gamma_{\text{SGR}}$; the relevant scale is set by $\Gamma_{\text{SGR}} = \sqrt{E_0/k}$. The fitting procedure therefore involves finding optimal values for x, Ω and Γ_{SGR}. The result cannot be cast in any simple explicit form but examples of the variation of G^* with amplitude can be found in Section 6.4 below.

Viscoelastoplastic models

Several constitutive laws [1,26-29], based on the association of springs, sliders and viscous elements, have been proposed to describe phenomenologically the homogeneous flow of complex strain fluids similar to foams. If the deformation is quasistatic, viscous effects vanish and elastoplastic behaviour is expected to be dominant. In this case, foam may be mimicked by a spring connected in series with a slider. The spring represents the static elastic response, characterized by a shear modulus G, whereas the slider schematically describes the yielding (cf. Fig. 1a). It behaves as a rigid link when subjected to a force whose magnitude is below a threshold and it slides freely for forces of larger magnitude (cf. Fig. 1b). In a material, the force and its threshold value, respectively, correspond to the stress Σ and the yield stress Σ_y where plastic flow sets in. To our knowledge, the first analytical prediction of the stress response to an oscillatory strain of an elastoplastic material is presented in [28]. The complex modulus and the stress harmonic spectrum are given in Appendix A.
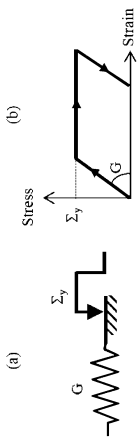
Fig. 1. (a) Schematic model of elastoplastic behaviour based on a spring and a slider, representing, respectively, an elastic modulus G and a yield stress Σ_y. (b) Stress-strain relationship of such an elastoplastic element.

Fig. 2. Stress residual q defined in equation (7) and odd harmonics from $n = 3$ to 9 versus normalised strain amplitude, for AOK foam at 1 Hz. The harmonics are normalized in the same way as the stress residual.

Fig. 3. Top view of the Couette cell illustrating the coordinates used in the analysis. The dashed line represents the tracer position before shear, and the continuous thick line shows its position after rotation of the inner cylinder. The thick arrow represents the amplitude of the curvilinear tracer displacement $s_0(r)$, measured at a time t when $\Gamma(t)$ reaches its maximum value Γ_0.

4 Rheological experiments and data analysis

Immediately after its production, the foam is injected into the cylindrical Couette cell of a rheometer (Bohlin CVOR-150) with an inner radius $r_1 = 21$ mm, an outer radius $r_0 = 25$ mm and a rotor height $H = 48$ mm. To prevent wall slip, closely spaced 0.2 mm deep grooves parallel to the axis of the cylinders are carved into the surfaces in contact with the foam. The air in contact with the samples is saturated with humidity to avoid evaporation. When the sample has aged as described in the previous section, we apply a sinusoidal shear strain by rotating the inner cylinder. The frequency $\nu = \omega/2\pi$, is fixed either to 1 Hz or 0.3 Hz and the strain amplitude Γ_0 is increased from 10^{-3} to 3. This sweep is divided into steps where the amplitude is constant, lasting 5 seconds for 1 Hz and 10 seconds for 0.3 Hz. The rheometer is operating in a controled strain mode. During the experiment it records as a function of time the engineering strain $\Gamma(t) = \Gamma_0 \mathrm{Re}[\exp(-i\omega t)]$, which is deduced from the angle of rotation of the inner cylinder $\theta(t)$ as

$$\Gamma(t) = \frac{8r_1^2 r_0^2 \theta(t)}{(r_1 + r_0)^3 (r_1 - r_0)}. \tag{2}$$

Note that for linear elastic or Newtonian materials, this macroscopic quantity is equal to the strain in the middle of the gap. The rheometer also records the shear stress $\Sigma(t)$ which is deduced from the torque $M(t)$ applied to the inner cylinder

$$\Sigma(t) = \frac{2M(t)}{\pi H (r_0 + r_1)^2}. \tag{3}$$

To first order in $(r_0 - r_1)/r_1$, this stress is equal to the spatially averaged stress in the sample, and in the following, we will neglect the distinction between these two stresses. To analyze the stress data, we decompose them as follows:

$$\Sigma(t) = \Gamma_0 \mathrm{Re}\left[G^*(\Gamma_0, \omega) e^{i\omega t}\right] + \Delta\Sigma(t). \tag{4}$$

The first term is the fundamental harmonic component. It is related to the applied strain via $G^*(\Gamma_0, \omega)$, defined as the ratio of the fundamental harmonic components of shear stress and strain. Note that in the limit of small strain amplitude, $G^*(\Gamma_0, \omega)$ does not depend on Γ_0 and converges to the usual linear complex shear modulus. The second term in equation (4), $\Delta\Sigma(t)$, contains the contributions of all the higher stress harmonics

$$\Delta\Sigma(t) = \sum_{n=2}^{\infty} h_n \cos(n\omega t + \varphi_n), \tag{5}$$

where

$$h_n = \frac{\pi}{\omega} \left| \int_0^{2\pi/\omega} e^{-in\omega t} \Sigma(t) dt \right|. \tag{6}$$

As shown in Figure 2 the third harmonic ($n = 3$) provides the dominant part of the nonlinear response, and contributions from harmonics where n is even or greater than 9
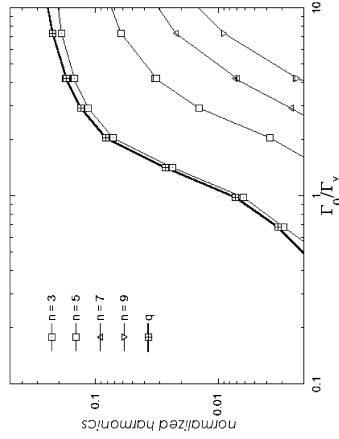
are found to be insignificant. To quantify the nonlinearity of the rheological response in a global way, we define the stress residual q as the dimensionless root-mean-square variation of $\Delta\Sigma(t)$

$$q = \sqrt{\frac{\int [\Delta\Sigma^2(t)] dt}{\int \Sigma^2(t) dt}} = \sqrt{\frac{\sum_{i=1}^{4} h_{2i+1}^2}{h_1^2 + \sum_{i=1}^{4} h_{2i+1}^2}}. \tag{7}$$

In our experiments, q is almost equal to the amplitude of the third harmonic. We nevertheless discuss our data in terms of q to provide a connection with the SGR model. We also analyse the Fourier spectrum of the recorded strain signal $\Gamma(t)$ which should yield be perfectly sinusoidal. Its anharmonic residual, defined in analogy with q, is found to be smaller than 0.002. Therefore, we conclude that nonlinear stress response with q well above 0.002 is due only to the nonlinear rheological response of the foam.

5 Measurement of the local strain and stress

Before the shear experiment we draw a black radial line on the free foam surface between the two cylinders, using a suspension made of carbon black particles dispersed in the foaming solution. When oscillatory shear is applied by rotating the inner cylinder, the bubbles move to a good approximation on trajectories whose radial coordinate r is constant (cf. Fig. 3). The black line is used as a tracer and we record its deformed shape as a function of time using a CCD camera. The curvilinear displacement of tracer points along their circular trajectories is observed as a function of r and time t. For $r = r_1$, the bubbles move within experimental accuracy at the same velocity as the inner cylinder and at $r = r_0$ they are immobile. This observation excludes any wall slip.

To introduce schematically viscoelastic behaviour at low strain amplitudes and to fit the yielding transition more accurately, an additional viscous element and a phenomenological yield function have been introduced [26, 27]. A similar model has also recently been proposed in the context of complex polymeric fluids [30]. To summarize, these viscoelastoplastic models involving springs, sliders and viscous elements do not explain the physical mechanisms involved in foam rheology on the bubble or mesoscopic scale, but they have the merit of providing simple constitutive laws where the information contained in experimental data is reduced to a relatively small number of parameters. However, they are restricted to flow regimes where strain localization does not occur.

3 Samples

We use stable foams for which drainage, coarsening and bubble coalescence are negligible over the duration of a rheological measurement. We study Gillette shaving cream which has been used in many rheological experiments published in the literature [2]. Its measured gas volume fraction is $92.5 \pm 0.5\%$. We also investigate a second kind of foam that will be called AOK. It is generated by injecting a gas and a polymer surfactant based aqueous solution into a column filled with glass beads, as described elsewhere [14]. This solution contains 1.5% g/g sodium α-olefin sulfonate (AOK, Witco Chemicals), 0.2% g/g Polyethylene-oxide ($M_w = 3 \times 10^5$ g mol^{-1}, Aldrich) and 0.4% g/g dodecanol (Aldrich). Its surface tension and viscosity are similar to those of the Gillette foaming solution. The gas is nitrogen containing perfluorohexane vapour. The measured gas volume fraction of the AOK foam samples is $97.0 \pm 0.3\%$. All experiments are performed at a temperature of $21 \pm 1\,°C$. To minimize the rheological memory of the flow history due to sample injection into the rheometer, Gillette samples are allowed to coarsen for either 30 or 60 minutes before the experiment is started. This leads to average bubble diameters equal to $28\,\mu m$ and $36\,\mu m$, respectively. For AOK foam, the experiments are done 20 minutes after sample injection when the average bubble diameter is $50\,\mu m$. Note that AOK foams coarsen much more slowly than Gillette foams.

We focus next on the amplitude of the bubble displacements during one oscillation period. The amplitude of the curvilinear bubble displacement at a radius r is denoted $s_0(r)$. The local shear strain amplitude $\gamma_0(r)$ is extracted from this function by the following expression, applied for a closely spaced set of radii, covering the range $r_1 < r < r_0$:

$$\gamma_0(r) = \frac{\partial s_0(r)}{\partial r} - \frac{s_0(r)}{r}. \tag{8}$$

The derivative in this expression is evaluated approximately by constructing a tangent to the experimental $s_0(r)$ curve. Due to the imperfection of the tracer, this construction is not accurate for r very close to either r_0 or r_1 and the corresponding points are omitted. The second term that is subtracted on the right-hand side represents the change of s_0 with r expected for a rigid rotation without any strain.

Similarly, we can look at stress amplitudes, denoting Σ_0 and $\sigma_0(r)$ the amplitudes of the fundamental harmonic components of the shear stress $\Sigma(t)$ and of the local stress σ at a radius r. Since inertial forces acting on the foam are negligible in the investigated range of frequencies and strain amplitudes, and in view of equation (3), they are related as follows [31]:

$$\sigma_0(r) = \Sigma_0 \frac{(r_0 + r_1)^2}{4r^2}. \tag{9}$$

6 Results and discussion

6.1 Onset of strain localization

To monitor flow homogeneity, we observe the bubble motion at the free surface of Gillette samples as described in

F. Rouyer *et al.*: Large amplitude oscillatory strain response of aqueous foam

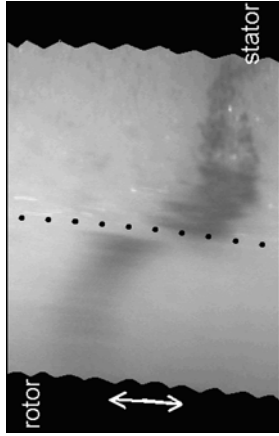**Fig. 7.** a) Parametric plots of stress $\Sigma(t)$ *versus* strain $\Gamma(t)$ for applied strain amplitudes $\Gamma_0 = 0.055, 0.15, 0.25, 0.43, 0.72$ and 1.2 corresponding to contours of increasing thicknesses. The frequency is equal to 1 Hz. The sample is Gillette foam (bubble size 28 μm). Panels b) and c) schematically illustrate the response expected for viscoelastic and elastoplastic response, respectively.

duced by the stress variation in the gap. Moreover, it is consistent with the coexistence of liquid-like and solid-like regions reported in [32]. This finding is robust with respect to changes of bubble size in the investigated range.

6.3 Nonlinear rheological response

A typical Lissajous plot showing $\Gamma(t)$ *versus* $\Sigma(t)$ is shown in Figure 7a for a Gillette sample. The same qualitative behaviour is found for all investigated samples. At small amplitudes, the plot has an elliptic shape (Fig. 7b), as expected for linear viscoelastic behaviour. With increasing strain amplitude, a crossover to a parallelogram-shaped Lissajous plot is observed, as expected for elastoplastic materials (Fig. 7b) (for further details see App. A), and in qualitative agreement with Lissajous plots predicted in the framework of the SGR model [24]. A variety of complex fluids showing similar behaviour have been classified in a phenomenological survey of large amplitude oscillatory strain responses [10]. These materials typically present a yield stress, and the flat and steep parts of the Lissajous diagram for large strain amplitudes correspond to liquid-like and solid-like response which alternately predominate during the oscillations. To analyze this behaviour quantitatively, we first focus on the fundamental frequency components of stress and strain from which we deduce the amplitude dependent complex shear modulus $G^*(\Gamma_0, \omega) = G'(\Gamma_0, \omega) + iG''(\Gamma_0, \omega)$ defined in equation (4). The insert of Figure 8a shows the typical evolution of $G'(\Gamma_0, \omega)$ with stress amplitude Σ_0. There is a linear regime at small Σ_0, characterized by a constant modulus that will be denoted G, and followed by the nonlinear regime where $G'(\Gamma_0, \omega)$ decreases following a power law. The intersection between these two asymptotic regimes is used to estimate the yield stress Σ_y as illustrated by the geometrical construction. Similar criteria have been used in many previous studies to detect yielding [8,10,19]. The criterion that we use here has been shown to be consistent

Fig. 6. Comparison of local and macroscopic normalised stress amplitudes *versus* strain amplitude. The lines correspond to the macroscopic stress amplitude Σ_0 / Σ_y *versus* engineering strain amplitude Γ_0. The symbols represent the local stress amplitude normalized by the yield stress, $\sigma_0(r)/\Sigma_y$ *versus* local strain amplitude $\gamma_0(r)$. These data are deduced from Figure 4. Typical error bars for $\gamma_0(r)$ and $\sigma_0(r)/\Sigma_y$ are drawn. The sample is Gillette foam (average bubble size = 28 μm) and the frequency is 1 Hz.

6.2 Local constitutive relation

We now use equation (8) and equation (9) to deduce from our observations the constitutive law relating local stress amplitude $\sigma_0(r)$ and strain amplitude $\gamma_0(r)$. In Figure 6, this relation is compared to the one between Σ_0 and Γ_0. Here stresses are normalized by the yield stress Σ_y which is determined as explained in Section 6.3. For $\Gamma_0 < 0.6$, all the data are consistent, showing that in our case the continuum description of foam flow is indeed valid. This verification is necessary, since it has been suggested on the basis of previous MRI measurements of Gillette foams steadily flowing in a Couette geometry that in regions of the order of 25 bubble diameters, the continuum description can break down [7]. In our experiments this would correspond to a significant fraction of the gap.

At strain amplitudes Γ_0 larger than 0.6 there are clearly deviations between local and macroscopic rheological behaviours. Indeed, a narrow range of $\sigma_0(r)$ corresponds to a wide range of $\gamma_0(r)$. This local rheological behaviour confirms that the observed strain localization is not in-

---

The European Physical Journal E

Fig. 5. Image of the free top surface of Gillette foam in the Couette cell. The applied strain amplitude Γ_0 is 0.9 and the picture is taken close to an instant where $\Gamma(t) \cong 0$. The rotor and the stator appear in black. A dotted line is drawn at the radius where the local strain is maximum.

ever, for the largest amplitude $\Gamma_0 = 0.7$ there are deviations larger than the error bar. These results are further analyzed in Figure 4b where the local strain amplitude $\gamma_0(r)$ is derived from the measured values of $s_0(r)$ using equation (8). For a linearly elastic material or a Newtonian fluid, $\gamma_0(r)$ is expected to scale with $1/r^2$, as the stress. In our geometry, this implies $\gamma_0(r_1) \cong 1.20\Gamma_0$ and $\gamma_0(r_o) \cong 0.85\Gamma_0$, in rough agreement with our data for $\Gamma_0 = 0.3$ and 0.5. However, for $\Gamma_0 = 0.7$ the deformation has a maximum near the middle of the gap where the local strain reaches $2\Gamma_0$. This is the signature of strain localization, setting in above $\Gamma_0 = 0.6 \pm 0.1$ as reported previously [12]. Moreover, above a strain amplitude of 0.9 ± 0.1, we systematically observe a sharp discontinuity in the displacement profile, indicating a strongly localized strain as shown in Figure 5. The picture is blurred close to the rotor because in this region the bubbles motion is faster than close to the stator. The quantitative analysis presented in Figure 4 was carried out only for one type of foam sample but, qualitatively, strain localization only close to the middle of the gap for strain amplitudes larger than about 0.6 is observed for all of the investigated foams and frequencies. Since in cylindrical Couette geometry the stress increases with decreasing distance from the axis of the cylinders, localization would *a priori* be expected close to the inner cylinder as mentioned in Section 2.1. Thus, we can exclude stress heterogeneity as the direct origin of the observed localization. Moreover, at least in simple shear and steady flow, the fluidity model outlined in Section 2.2 predicts flow that is localized in the vicinity of boundaries, contrary to our observations.

These features demonstrate that for the foams investigated here, there exists a regime of localized oscillatory flow which is explained neither by stress heterogeneity, nor by fluidity models. Our results also show that this localized flow only sets in at strain amplitudes well above the yield strain. As a consequence, there is a well-defined regime where it is legitimate to compare our data to models of yielding that do not predict flow localization.
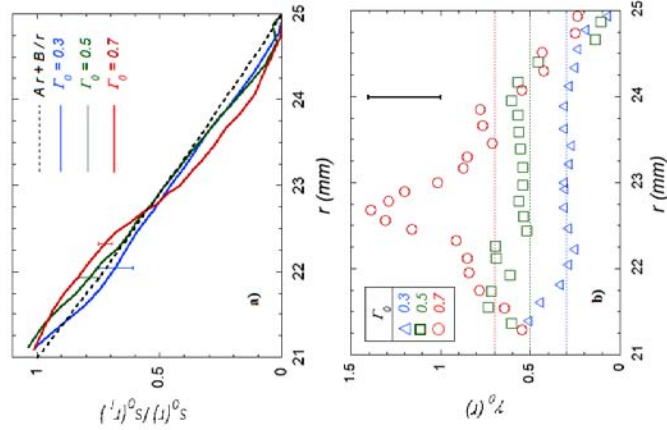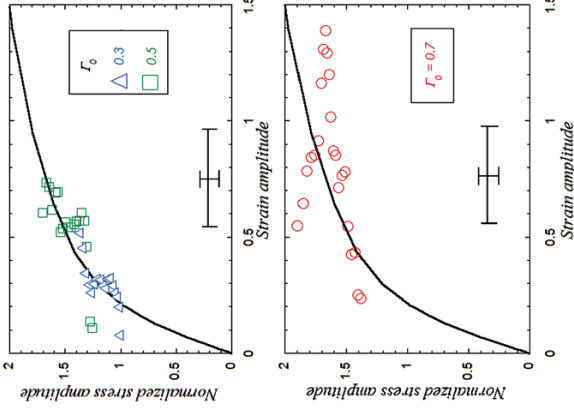

Fig. 4. a) Normalized amplitude of the curvilinear displacement *versus* radial distance for increasing strain amplitudes Γ_0 applied to the same sample (Gillette foam, bubble diameter = 28 μm) at 1 Hz. The dashed line corresponds to the displacement expected for linear elastic deformation or Newtonian flow (Eq. (10) with $A = -0.11 \text{ mm}^{-1}$ and $B = 71$ mm). Typical error bars are indicated. b) Local strain amplitudes derived from (a) using equation (8) plotted *versus* the radial coordinate. The dotted lines correspond to the local amplitude expected in the middle of the gap for linear elastic deformation or Newtonian flow ($\gamma_0((r_1 + r_o)/2) = \Gamma_0$).

Section 5. As a reference, we calculate the displacement $s_0(r)$ for a Newtonian fluid or a linearly elastic solid. In both cases the displacement amplitude $s_0(r)$, normalized by the displacement amplitude of the rotor, $s_0(r_1)$ is predicted by

$$\frac{s_0(r)}{s_0(r_1)} = Ar + \frac{B}{r}, \qquad (10)$$

where the constants A and B are chosen to fit the boundary conditions at r_1 and r_o. Figure 4a compares equation (10) to the normalized displacement amplitudes measured for Gillette foam during a strain amplitude sweep. In view of the experimental uncertainty, the data for $\Gamma_0 = 0.3$ and 0.5 are in good agreement with equation (10). How-

Fig. 8. Normalised elastic and loss shear moduli *versus* normalised strain amplitude. The symbols correspond to Gillette and AOK foams at two frequencies, as 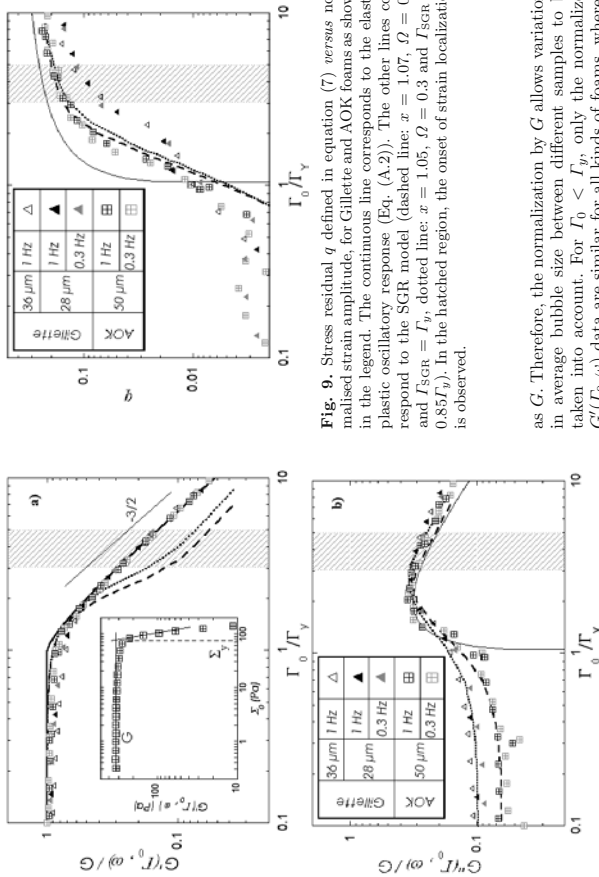shown in the legend of panel (b). The full line corresponds to the elastoplastic response (Eq. (A.2)). The other lines show the prediction of the SGR model (see text) (dashed line: $x = 1.07$, $\Omega = 0.3$ and $\Gamma_{SGR} = \Gamma_y$, dotted line: $x = 1.05$, $\Omega = 0.3$ and $\Gamma_{SGR} = 0.85\Gamma_y$). In the hatched region, the onset of strain localization is observed. The insert in a) shows the evolution of the elastic modulus with stress amplitude for AOK foam.

with other methods for detecting the yield stress in 3D foams [12]. From this estimation, we derive the yield strain amplitude using the relation $\Sigma_y = G^*(\Gamma_y,\omega)]\Gamma_y$. Within the studied range of frequency and bubble size, we obtain $\Gamma_y = 0.15 \pm 0.01$ for Gillette foam, and $\Gamma_y = 0.22 \pm 0.02$ for the AOK foam. Figure 8a and b show the evolution of the elastic and loss moduli normalized by G as a function of the normalized strain amplitude Γ_0/Γ_y. We notice the evolution of G^* with strain amplitude usually observed for foams: At small Γ_0 a solid-like regime where $G''(\Gamma_0,\omega) \ll G$, at large Γ_0 a liquid-like behaviour with $G'(\Gamma_0,\omega) \ll G''(\Gamma_0,\omega)$ and a crossover between $G'(\Gamma_0,\omega)$ $G''(\Gamma_0,\omega) \ll G''(\Gamma_0,\omega)$ close to the maximum of $G''(\Gamma_0,\omega)$. Our results are in qualitative agreement with previously reported data for moderately dry foams [8,12] and concentrated emulsions [33]. Let us recall that G scales as surface tension divided by the mean bubble radius and that the complex shear modulus at low frequency scales

Fig. 9. Stress residual q defined in equation (7) *versus* normalised strain amplitude, for Gillette and AOK foams as shown in the legend. The continuous line corresponds to the elastoplastic oscillatory response (Eq. (A.2)). The other lines correspond to the SGR model (dashed line: $x = 1.07$, $\Omega = 0.3$ and $\Gamma_{SGR} = \Gamma_y$, dotted line: $x = 1.05$, $\Omega = 0.3$ and $\Gamma_{SGR} = 0.85\Gamma_y$). In the hatched region, the onset of strain localization is observed.

as G. Therefore, the normalization by G allows variations in average bubble size between different samples to be taken into account. For $\Gamma_0 < \Gamma_y$, only the normalized $G'(\Gamma_0,\omega)$ data are similar for all kinds of foams, whereas the normalized $G''(\Gamma_0,\omega)$ is smaller for AOK foam than for Gillette foam. This can be explained by the differences in gas volume fraction [8] and rate of coarsening induced bubble rearrangements [34,35]. For $\Gamma_0 > \Gamma_y$ the G^* data obtained at 1Hz and 0.3Hz with AOK foam and with Gillette foam for both investigated bubble sizes superimpose to a good approximation. Remarkably, at the strain amplitude where the onset of localized flow is observed, there are no distinctive features on the curves representing the G^* data. Moreover, we notice that yielding and strain localization induced by oscillatory deformation are clearly distinct phenomena, since they set in at well-separated strain amplitudes. This result is qualitatively consistent with previous observations of yielding and localization in steady shear start-up experiments with dry foam [14].

Finally, we plot in Figure 9 the anharmonic residual stress q defined in equation (7). For strain amplitude $\Gamma_0 \ll \Gamma_y$, the observed small level of anharmonicity is too close to the limit of detection to be interpreted quantitatively. However, for $\Gamma_0 \gtrsim \Gamma_y$, q increases by more than one order of magnitude as the strain increases by a factor of 3. At amplitudes where strain localization sets in, the residual stress saturates. In contrast to the modulus $G^*(\Gamma_0,\omega)$ which is very similar for Gillette and AOK foam for $\Gamma_0 > \Gamma_y$, the respective stress residuals are clearly distinct: q rises much faster with strain amplitude for AOK foam compared to Gillette foam. We finally note that the stress residuals measured for an applied strain oscillation frequency of 1Hz and 0.3Hz are very similar. These lat-

ter findings strongly argue against artifacts related to the limited frequency bandwidth of the rheometer.

6.4 Comparison of our data with models

To introduce the discussion of specific models, we first recall recent measurements showing that complex shear modulus of foams scales with strain amplitude and frequency as expected if a single structural relaxation time dependent on strain rate amplitude governed the stress relaxation and the rearrangement processes on the bubble scale. This relaxation time characterizes the dynamics globally, but it does not indicate how bubble rearrangement events are distributed in time within a strain cycle. This is a new feature that our harmonics (or Lissajous) data allow us to probe. An analogy with the Green Tobolsky model [36], well known in polymer rheology, suggests that rearrangements that relax stress and that occur *randomly* in time would lead to Maxwell liquid behaviour. (Here, we make the simplifying assumption that foam elasticity in the absence of any rearrangements is linear.) For a Maxwell liquid the Lissajous plot has an elliptical shape. This is approximately true for strain amplitudes up to the yield strain, but at higher amplitudes the plots clearly have a different shape, resembling a parallelogram. We find this behaviour up to the highest investigated strain amplitudes where we observe flow localization. The parallelogram-shaped plot arises because rearrangements typically occur only if enough elastic energy has been built up locally. Our data contain the signature of this process, and therefore allow us to refine the physical description of the process of yielding. On this basis, we discuss in the following paragraphs the elastoplastic and SGR models. It would also be of great interest to combine our data to fluidity models, but this would require complex calculations which are beyond the scope of the present paper. A similar remark applies to models based on a minimal strain rate [23] which successfully describe steady foam flow. In their present form, they do not yet capture transient viscoelastic effects. Further theoretical work allowing additional models to be compared to our data would be of great interest.

Note that the full analytic solution presented in Appendix A shows that equation (11) is already reached at strain amplitudes close to Γ_y, whereas the asymptotic power law for $G''(\Gamma_0,\omega)$ is reached only at strain amplitudes more than a decade larger than Γ_y. Figure 8a shows good agreement between equation (11) and the experimental data in the whole range of Γ_0/Γ_y. The prediction for $G''(\Gamma_0,\omega)$ given by equation (A.2) is in good agreement with the loss moduli data only for $\Gamma_0/\Gamma_y > 1$ (cf. Fig. 8b). This is consistent with the fact that, for $\Gamma_0/\Gamma_y \ll 1$, the dissipation is mainly due to coarsening induced bubble rearrangements which are not taken into account by this elastoplastic model. Moreover, it is remarkable that the predictions of the elastoplastic model still hold in the regime where we observe a cross-over to localized flow. Here, one might identify the slider of the model with the region where the shear is localized and the spring with the part of the foam that may remain elastic.

The merit of the elastoplastic model is to predict the nonlinearity of $G^*(\Gamma_0,\omega)$ with strain amplitude using only two free parameters G and Γ_y, whose physical origin on the scale of the microstructure is known [1]. The scaling of G with surface tension T and bubble radius R arises from the change of interfacial energy induced when the foam is sheared. Yielding in foams and emulsions is due to bubble or droplet rearrangements that arise when, under the effect of an applied strain, unstable configurations are created. Dimensionally, the yield stress also scales as T/R. The quantitative evolution of yield strain and elastic shear modulus with gas volume fraction has been described by phenomenological expressions [8].

Despite its success in describing the behaviour at large strain amplitudes, basic elastoplasticity remains an incomplete phenomenological model. It predicts a sharp transition from linear elastic behavior to plastic flow as a function of Γ_0. As a consequence, the predicted anharmonicity for strain amplitudes just above Γ_y is much larger than the measured data, as shown in Figure 9. A related weak discrepancy appears in the decay of G' with Γ_0 close to Γ_y. All these features suggest that a distribution of yield strains is necessary to describe the data more accurately. Marmottant *et al.* have recently introduced a phenomenological yield function that describes such a distribution and which allows experimental complex shear modulus data to be fitted accurately [27]. Explicit predictions for the anharmonicity derived in this framework have not yet been published. Only if the same distribution of yield strains can be used to predict strain amplitude dependencies of both the stress Fourier spectrum and G^* close to Γ_y is elastoplasticity a good concept for modelling foams accurately. A second shortcoming of the basic elastoplastic model is that it does not account for the dissipation experimentally observed for $\Gamma_0 \ll \Gamma_y$. To describe this feature, a viscous element connected in parallel to the plastic and elastic elements of the model has been proposed [27]. It allows the foam data to be fitted at a given frequency, but this model is not able to predict the experimentally observed $G^*(\Gamma_0)$ over an extended range of frequencies. Indeed, it reduces to a Voigt model in the linear viscoelastic regime, which is incompatible with the Maxwell liquid

Comparison with viscoelastoplastic models

For elementary elastoplastic behaviour, an analytical calculation first presented in [28] and recalled in Appendix A predicts the stress response to oscillatory shear, given by equation (A.2). At strain amplitudes $\Gamma_0 \gg \Gamma_y$, this result reduces to the asymptotic power law decays

$$G'(\Gamma_0,\omega) = \frac{16G}{3\pi}\left(\frac{\Gamma_0}{\Gamma_y}\right)^{-3/2} \quad (11)$$

and

$$G''(\Gamma_0,\omega) = \frac{4G}{\pi}\left(\frac{\Gamma_0}{\Gamma_y}\right)^{-1} . \quad (12)$$

behaviour experimentally observed [13,34,37,38] at low frequencies and the power law increase $G^* \sim \omega^{1/2}$ found at high frequency [13,37,39].

Comparison with the SGR model

For noise temperatures x close to 1, the SGR model predicts a strain amplitude dependence of the shear modulus similar to the experimental results shown in Figure 8. The ratio $G''(\Gamma_0,\omega)/G'(\Gamma_0,\omega)$ at low strain amplitude and low frequency is predicted to depend on x as follows:

$$\frac{G''(\Gamma_0,\omega)}{G'(\Gamma_0,\omega)} = \tan\left(\frac{\pi}{2}(x-1)\right). \quad (13)$$

We have $G''(\Gamma_0,\omega)/G'(\Gamma_0,\omega) \cong 0.10$ for the Gillette foam for both bubble sizes and frequencies, and $G''(\Gamma_0,\omega)/G'(\Gamma_0,\omega) \cong 0.055$ for AOK foam. Therefore, relation (13) suggests $x \cong 1.07$ and $x \cong 1.05$ for the Gillette and AOK foams, respectively. These values then have to be tuned slightly to allow for the fact that the fitted (dimensionless) frequency Ω will not necessarily be small enough for equation (13) to apply exactly. In practice, we fit x and Ω to the data for G''/G', as this has the most structure in its dependence on strain amplitude Γ_0. This is done by minimizing the error in the predicted values for the maximum of G''/G' and the height of the plateau in G''/G' in the linear response regime of small Γ_0. The strain is then fitted afterwards to reproduce the experimental value of the strain where the maximum of G''/G' occurs.

The best fits obtained in this way are for $x = 1.07$ (Gillette) and $x = 1.05$ (AOK), close to the values expected from relation (13). Fits of similar quality can be obtained by varying x within the range ± 0.01. The optimal associated values of the fitted frequency vary over a rather broad range, $\Omega = 0.3 \pm 0.2$ for both Gillette and AOK. Translating to the attempt frequency via $\Omega = 2\pi\nu\tau_0$ with $\nu = 0.3$Hz or 1Hz, one gets values of τ_0 in the range from 0.01s to 0.3s. As regards the strain scale, finally, $\Gamma_{SGR} = \Gamma_y$ is satisfactory for the Gillette foam, while for AOK the best fit value is slightly smaller at $\Gamma_{SGR} \approx 0.85\Gamma_y$. The fitted strain scale is therefore close to Γ_y as expected.

The SGR predictions using the parameter values given above are shown in Figures 7 and 8. For all foams and frequencies investigated, the predicted elastic modulus G'/G agrees with the experimental data for strain amplitudes up to Γ_0/Γ_y around 2, with deviations setting in at larger strain amplitudes. The predictions for the loss modulus G''/G agree quite well across the whole range of Γ_0 calculated. For the AOK foam, also the anharmonic residual q is predicted rather well by the model, while for the Gillette foam the onset of anharmonicity is predicted to be much steeper than observed experimentally. The lower quality of the predictions for G''/G and q may in part be due to the fact that the SGR model cannot capture the observed onset of strain localization at large values of Γ_0/Γ_y given that it treats elements from all areas of the sample as statistically indistinguishable. In addition, it is likely that the exponential form of the yield rate assumed in the model, cf. equation (1), becomes unrealistic for large strain amplitudes: Physically one expects that even elements which are strained beyond their yield barrier cannot yield arbitrarily quickly, so that the exponential increase of the yield rate with Γ^2 must be cut off eventually. One might expect that this would restore a somewhat more gradual decrease of G''/G, in line with experimental data, than predicted by the SGR model. Independently of these two shortcomings, why the model prediction for the anharmonicity q is so much more accurate for the AOK than for the Gillette foam remains unclear.

To explore the above suggestion further, we have investigated a modified SGR model where the exponential in equation (1) is replaced with unity when the exponent becomes positive, i.e. once an element has been strained past its notional yield point. Because the l dependence then no longer appears as a simple factor, this model is not easy to study analytically, but can be simulated efficiently using waiting time Monte Carlo techniques [40]. At large strain amplitudes most SGR elements are pushed quickly into the regime where the cutoff on the yield rate kicks in, and one can show analytically that the predictions for $G''(\omega)$ then become amplitude independent and reduce to those of a Maxwell model with relaxation time τ_0.

To rectify this clearly unphysical behaviour, one can in addition postulate that the basic yield rate $1/\tau_0$ in equation (1) should increase with strain rate and be replaced with $1/\tau_0 + b\dot\gamma$ for some constant b, see, e.g. [9,41]. The predictions of this version of the SGR model can still be worked out analytically in the limit of large strain amplitudes. Intriguingly, we find —and have confirmed by comparing with simulation results— that G' and G'' decay with strain amplitude according to the same power laws as in the elastoplastic model, see equations (11, 12). This supports the view expressed above that such a modified SGR model should be capable of producing a good overall fit to the experimental data. Because results at intermediate strain amplitudes currently have to be obtained by simulation, we have not, however, attempted detailed fits of the relevant model parameters.

6.5 Connection with the foam microstructure and its dynamics

From a physicist's point of view, a complete model of foam rheology should explain how the macroscopic response arises due to processes on the scale of the bubbles and the liquid films. At this level of understanding it should be possible to predict all the free parameters of phenomenological models. In this pioneering work, Princen has provided insight about the dependence of the shear modulus and the yield stress on bubble size [1,2]. This is enough to predict the free parameters from a basic elastoplastic model from foam liquid fraction, surface tension of the foaming liquid and bubble size, or to fix the elastic constant of the mesoscopic regions and the scale of the distribution of trap depths in the SGR model. Providing a microscopic interpretation of the effective noise temper-

ature x in the SGR model is more challenging. To discuss this point, we recall that quiescent coarsening foams have intrinsic, non-thermal dynamics due to the Laplace pressure driven diffusive gas exchange between neighbouring bubbles [1]. It induces intermittent structural rearrangements in small bubble clusters. One might therefore correlate the rate of coarsening to the effective noise temperature. Indeed, the Gillette foam that coarsens faster also has the higher noise temperature, according to the fits reported above. However, the rate of bubble rearrangements is known to be enhanced by steady flow [41], so that the noise temperature would have to depend on shear rate, a possibility which is not considered in the standard SGR model. Moreover, previous experiments and simulations have shown how coarsening induced rearrangements relax stress and lead on a macroscopic scale to Maxwell liquid behaviour in the low frequency limit [34,35,38]. A Maxwell liquid, mimicked by a spring in series with a viscous element, is characterized by a single characteristic time τ. As a consequence, G' progressively goes to zero for frequencies such that $\omega\tau < 1$, in agreement with experimental data reported in [13]. The results of creep experiments are consistent with these findings [34]. In the SGR model a large spectrum of relaxation times is predicted and the experimentally observed very low frequency behaviour of the complex shear modulus is not found for $x = 1.07$. An additional feature not captured by the SGR model is the transient slowing down of bubble dynamics observed following a transient flow [17], which is the opposite of the shear rejuvenation effect observed in glasses.

7 Conclusion and outlook

The recent literature on liquid foam rheology raises the question whether the stress in a liquid foam is a well-defined function of strain and strain rate, and, if so, how this constitutive law is related to physico-chemical processes and structures on a mesoscopic, bubble, or film scale. To answer the first question, we probe in situ the bubble displacement profile at the free sample surface of a Couette cell and show that strain localization clearly distinct from wall slip and not directly induced by heterogeneous stress is a robust feature of the investigated types of foams and oscillatory flows. Such behaviour is incompatible with conventional constitutive laws. However, localization only sets in at strain amplitudes far above the yield strain, demonstrating that there is indeed an extended regime of strains where it makes sense to compare the data to models.

This conclusion allows us to investigate the second question raised above, and we focus on a previously unexplored feature of the nonlinear rheological response. A variety of models of complex yield strain fluid rheology predict how the fundamental harmonic component of stress induced by an oscillatory strain depends on strain amplitude at low frequency. This information is generally represented in terms of the amplitude dependent complex shear modulus $G^*(\Gamma_0,\omega)$. To assess to what extent such models actually capture the relevant physics for foams, we measure and report for the first time in addition to $G^*(\Gamma_0,\omega)$ the full harmonic spectrum of the stress response of foam which can equivalently be represented in the form of a Lissajous plot. These data resolve quantitatively how stress relaxation is distributed in time within a cycle of deformation, so that elastoplastic and viscoelastic behaviour with a strain rate dependent relaxation time can be distinguished. We find that this feature depends significantly on the physicochemical constitution of the sample, in contrast to the $G^*(\Gamma_0,\omega)$ data which do not show such a dependency in the vicinity of the yield strain.

For the driest investigated foam and at strain amplitudes well below the onset of flow localization, the SGR model accurately predicts the evolution with strain amplitude of three a priori independent functions, describing the nonlinear rheology: $G'(\Gamma_0,\omega)$, $G''(\Gamma_0,\omega)$ and the measure of the anharmonic response q. The fit is obtained with only two adjustable parameters (x,Ω). Phenomenological elastoplastic models capture the power law decay of the real and imaginary parts of the complex shear modulus in the liquid-like regime. The two respective exponents are predicted correctly, without any free parameters. However, neither of the two mentioned approaches predicts the previously reported frequency dependence of the viscoelastic behaviour over an extended range [13,37,39] and accounts for the flow localization observed at high strain amplitudes. As a perspective for future work, it would be of great interest to construct a model of foam viscoelasticity and plasticity by combining the known facts about foam physics on the bubble scale with features of successful phenomenological models. We expect that the data reported in this paper will be useful in this context.

Appendix A. Oscillatory response of an elastoplastic material

Figure 10 illustrates the basic elastoplastic response that can be mimicked by a combination in series of a spring and a slider (cf. Fig. 1). Plastic strain and elastic strain, respectively, correspond to elongations of the slider and of the spring. The total strain Γ in the material that can be applied experimentally is given by the sum of its elastic and plastic components. Figure 10a illustrates the relation between shear stress Σ and strain Γ predicted for an ideal elastoplastic material subjected to the oscillatory strain shown in Figure 10b.

We now calculate the stationary response of such an elastoplastic element to an applied strain $\Gamma(t) = \Gamma_0\cos(\omega t)$. If Γ_0 is smaller than or equal to Γ_y, the response is purely elastic and $G^*(\Gamma_0,\omega) = G$. In this case, the stress oscillates sinusoidally with the same phase as
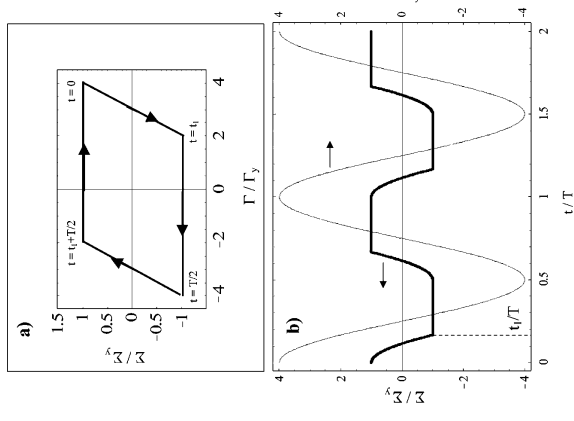
Fig. 10. a) Elastoplastic stress-strain relation, in response to a sinusoidal applied strain of period T and amplitude Γ_0 (cf. Fig. 1a). The instant t_1 is defined by equation (A.1). b) Time evolution of the stress (thick line) if a sinusoidal strain (thin line) is imposed with an amplitude exceeding the yield strain.

the strain. If the strain amplitude is larger than Γ_y, the stress-strain relation becomes hysteretic, as shown in Figure 10b. As long as the slider is stuck, the plastic strain is constant so that any variation of the applied strain $\Delta\Gamma$ induces an equal change of the elastic strain and a stress variation $\Delta\Sigma = G\Delta\Gamma$. If the stress magnitude reaches the yield stress, the slider becomes mobile and any further increase of the applied strain magnitude induces only plastic strain while the elastic strain remains constant in this case.

As the applied strain decreases after having reached its maximum value, as for instance at $t = 0$ in Figure 10b, the slider becomes stuck. From here on, the evolution of the applied strain induces a negative variation of the elastic strain equal to $\Gamma(t) - \Gamma_0$ and therefore a stress $\Sigma(t) = G\Gamma_y + G\Gamma_0(\cos(\omega t) - 1)$. Indeed, this expression satisfies the initial condition at $t = 0$ as well as the relation $\Delta\Sigma = G\Delta\Gamma$ that must be valid as long as the slider is stuck. As time goes on, the stress decreases to $-\Sigma_y$ at a time denoted as t_1 (cf. Fig. 10b). An elementary calculation yields

$$t_1 = \frac{1}{\omega}\arccos(-2\Gamma_y/\Gamma_0 + 1). \qquad (A.1)$$

The stress then remains saturated until the minimum of the applied strain is reached at a time which is half the oscillation period T. As the strain starts increasing again, the elastic strain increases by $\Gamma(t) + \Gamma_0$. Therefore the stress increases as $\Sigma(t) = -G\Gamma_y + G\Gamma_0(\cos(\omega t) + 1)$ until it reaches the value Σ_y, at the time $T/2 + t_1$. The evolution then remains saturated until the time $t = T$, and from then on the whole process continues periodically. To determine $G^*(\Gamma_0, \omega)$, we calculate the Fourier component of the stress oscillation at the frequency ω and divide it by the strain amplitude [28]. These expressions are simplified without any loss of generality by scaling stress and strain so that $G = 1$ and $\Gamma_y = 1$

$$G^*(\Gamma_0, \omega) = \frac{2}{\Gamma_0 T}\left\{\int_0^{t_1}(1 + \Gamma_0(\cos(\omega t) - 1))e^{-i\omega t}dt\right.$$
$$-\int_{t_1}^{T/2}e^{-i\omega t}dt + \int_{T/2}^{T/2+t_1}(-1 + \Gamma_0(\cos(\omega t) + 1))e^{-i\omega t}dt$$
$$\left.+\int_{T/2+t_1}^{T}e^{-i\omega t}dt\right\} = \frac{1}{\pi}\left(\arccos\left(\frac{-2 + \Gamma_0}{\Gamma_0}\right)\right.$$
$$\left.-\frac{2(-2 + \Gamma_0)}{\Gamma_0}\sqrt{\frac{-1 + \Gamma_0}{\Gamma_0^2} + i\frac{4(\Gamma_0 - 1)}{\Gamma_0^2}}\right). \qquad (A.2)$$

References

1. D. Weaire, S. Hutzler, *The Physics of Foams* (Oxford University Press, Oxford, 1999).
2. R. Höhler, S. Cohen-Addad, J. Phys.: Condens. Matter **17**, R1041 (2005).
3. A.M. Kraynik, Annu. Rev. Fluid Mech. **20**, 325 (1988).
4. A.D. Gopal, D.J. Durian, J. Colloid Interface Sci. **213**, 169 (1999).
5. N.D. Denkov, V. Subramanian, D. Gurovich, A. Lips, Colloids Surf. A **263**, 129 (2005).
6. N.D. Denkov, S. Tcholakova, K. Golemanov, K.P. Ananthapadmanabhan, A. Lips, Phys. Rev. Lett. **100**, 138301 (2008).
7. S. Rodts, J.C. Baudez, P. Coussot, Europhys. Lett. **69**, 636 (2005).
8. A. Saint-Jalmes, D.J. Durian, J. Rheol. **43**, 1411 (1999).
9. H.M. Wyss, K. Miyazaki, J. Mattsson, Z. Hu, D.R. Reichman, D.A. Weitz, Phys. Rev. Lett. **98**, (2007).
10. K. Hyun, S.H. Kim, K.H. Ahn, S.J. Lee, J. Non-Newtonian Fluid Mech. **107**, 51 (2002).
11. R.H. Ewoldt, C. Clasen, A.E. Hosoi, G.H. McKinley, Soft Matter **3**, 634 (2007).
12. F. Rouyer, S. Cohen-Addad, R. Höhler, Colloids Surf. A: Physicochem. Engin. Asp. **263**, 111 (2005).
13. A.D. Gopal, D.J. Durian, Phys. Rev. Lett. **91**, 188303 (2003).
14. F. Rouyer, S. Cohen-Addad, M. Vignes-Adler, R. Höhler, Phys. Rev. E **67**, 021405 (2003).
15. S.A. Khan, C.A. Schnepper, R.C. Armstrong, J. Rheol. **32**, 69 (1988).
16. F. DaCruz, F. Chevoir, D. Bonn, P. Coussot, Phys. Rev. E **66**, 051305 (2002).
17. S. Cohen-Addad, R. Höhler, Phys. Rev. Lett. **86**, 4700 (2001).
18. V. Labiausse, R. Hohler, S. Cohen-Addad, J. Rheol. **51**, 479 (2007).
19. T.G. Mason, J. Bibette, D.A. Weitz, J. Colloid Interface Sci. **179**, 439 (1996).
20. L. Becu, S. Manneville, A. Colin, Phys. Rev. Lett. **96**, 138302 (2006); L. Becu, P. Grondin, A. Colin, S. Manneville, Colloids Surf. A: Physicochem. Engin. Asp. **263**, 146 (2005); A. Ragouilliaux, G. Ovarlez, N. Shahidzadeh-Bonn, B. Herzhaft, T. Palermo, P. Coussot, Phys. Rev. E **76**, 051408 (2007).
21. C. Derec, G. Ducouret, A. Ajdari, F. Lequeux, Phys. Rev. E **67**, 061403 (2003).
22. G. Picard, A. Ajdari, L. Bocquet, F. Lequeux, Phys. Rev. E **66**, 051501 (2002).
23. P. Coussot, Q.D. Nguyen, H.T. Huynh, D. Bonn, Phys. Rev. Lett. **88**, 175501 (2002).
24. P. Sollich, Phys. Rev. E **58**, 738 (1998).
25. P. Sollich, F. Lequeux, P. Hebraud, M.E. Cates, Phys. Rev. Lett. **78**, 2020 (1997); M.E. Cates, in *Slow Relaxations and Nonequilibrium Dynamics in Condensed Matter*, edited by M.F.J.L. Barrat, J. Kurchan, J. Dalibard, Vol. LXXVII (Springer, Berlin, 2002), pp. 74; M.E. Cates, P. Sollich, J. Rheol. **48**, 193 (2004).
26. P. Saramito, J. Non-Newtonian Fluid Mech. **145**, 1 (2007).
27. P. Marmottant, F. Graner, Eur. Phys. J. E **23**, 337 (2007).
28. V. Labiausse, PhD Thesis, Université de Marne-la-Vallée, 2004.
29. S. Bénito, C. Bruneau, T. Colin, C. Gay, F. Molino, Eur. Phys. J. E **25**, 225 (2008).
30. C.O. Klein, H.W. Spiess, A. Calin, C. Balan, M. Wilhelm, Macromolecules **40**, 4250 (2007).
31. C. Macosko, *Rheology, Principles, Measurements And Applications* (Wiley-VCH, New York, 1994).
32. P. Coussot, J.S. Raynaud, F. Bertrand, P. Moucheront, J.P. Guilbaud, H.T. Huynh, S. Jarny, D. Lesueur, Phys. Rev. Lett. **88**, 218301 (2002).
33. T.G. Mason, J. Bibette, D.A. Weitz, Phys. Rev. Lett. **75**, 2051 (1995).
34. S. Cohen-Addad, R. Höhler, Y. Khidas, Phys. Rev. Lett. **93**, 028302 (2004).
35. S. Vincent-Bonnieu, R. Höhler, S. Cohen-Addad, Europhys. Lett. **74**, 533 (2006).
36. R. Larson, *Constitutive Equations for Polymer Melts and Solutions* (Butterworth-Heinemann, Boston, 1988).
37. S. Cohen-Addad, H. Hoballah, R. Höhler, Phys. Rev. E **57**, 6897 (1998).
38. S.P.L. Marze, A. Saint-Jalmes, D. Langevin, Colloids Surf. A **263**, 121 (2005).
39. A.J. Liu, S. Ramaswamy, T.G. Mason, H. Gang, D.A. Weitz, Phys. Rev. Lett. **76**, 3017 (1996).
40. A.B. Bortz, M.H. Kalos, J.L. Lebowitz, J. Comput. Phys. **17**, 10 (1975).
41. A.D. Gopal, D.J. Durian, Phys. Rev. Lett. **75**, 2610 (1995).

Chapitre 2

Transport de liquide et stabilité d'une mousse aqueuse ou de verre fondu

Collaborations : Olivier Pitois (MDC), Elise Lorenceau (CR), Nicolas Louvet (Doctorant UPEMLV) pour les mousses aqueuses et Franck Pigeonneau (IR Saint Gobain Recherche) et Helena Kocarkova (Doctorante UPEMLV) pour les mousses de verre

L'existence d'une mousse est conditionnée par la stabilité des films qui entourent les bulles qui la constituent. Ces films sont d'autant plus sujets à la rupture qu'ils s'amincissent [1]. Il est donc important de connaître les propriétes d'écoulement de liquide dans les films et le réseau des bords de Plateau pour mieux appréhender la vie d'une mousse.

La phase liquide de la mousse est continue et la mousse est ainsi perméable au liquide. La particularité de ce milieu poreux est d'avoir des pores délimitées par des interfaces (liquide-air) déformables et fluides dont la géométrie peut être variable (la taille des pores dépend de la fraction liquide ϕ_l) et dont les conditions limites d'écoulement sont propres à des interfaces fluides (vitesse non nulle aux interfaces).

La grande majorité des modèles de drainage de liquide dans une mousse aqueuse considère les dissipations visqueuses dans le réseau liquide que forment les bords de Plateau et nœuds et font totalement abstraction de l'écoulement du liquide dans les films [2, 3, 4, 5]. Notons que les films sont généralement très fins et représentent une infime partie du liquide de la mousse. Cependant il a été observé, aussi bien au sein d'une mousse [6] qu'à l'échelle d'un bord de Plateau unique [7], des mouvements de recirculation de liquide dans les films.

La géométrie habituellement utilisée pour décrire le drainage de liquide dans une mousse consiste en un réseau de bords de Plateau et de noeuds résultant de la jonction des films
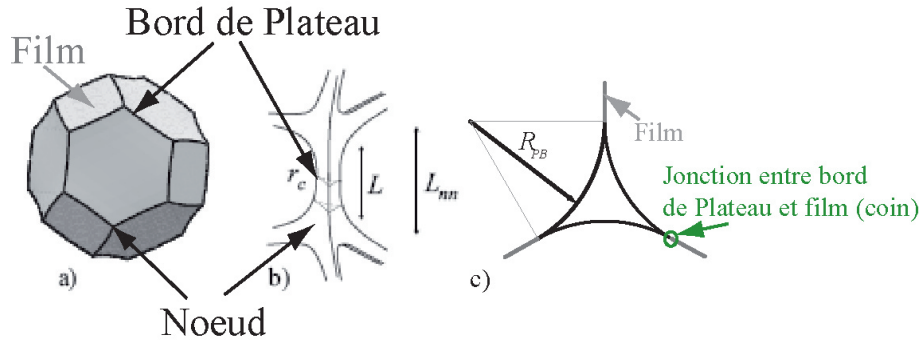
FIGURE 2.1 – Schéma illustrant le géométrie modèle de la phase liquide d'une mousse contenue dans le réseau de bords de Plateau et noeuds. a) cellule de Kelvin ; b) un bord de Plateau joignant deux noeuds ; c) section d'un bord de Plateau.

entre bulles dans un empilement de cellule modèle dite cellule de Kelvin (cf. figure 2.1.a et b). La section "idéale" d'un bord de Plateau est un triangle équilatéral délimité par des arcs de cercle de rayon R_{PB} et de centre extérieur au triangle (cf. figure 2.1.c). Si le volume de liquide contenu dans les films est négligé, la relation entre la géométrie des bords de Plateau (courbure- R_{PB} et longueur- L) et la fraction liquide au sein de la mousse peut alors s'écrire :

$$\phi_l \approx 0.141 (R_{PB}/L)^2 \tag{2.0.1}$$

La mobilité des interfaces fluides est modélisé par la notion de viscosité interfaciale qui traduit la résistance d'une interface fluide à son propre cisaillement. La contrainte de surface $\sigma_{surface}$ générée par le cisaillement de l'interface est proportionnelle au paramètre de viscosité interfaciale de cisaillement noté η_s et à la variation du taux de cisaillement de l'interface qui s'écrit comme le laplacien surfacique de la vitesse : $\sigma_{surface} = \eta_s \Delta_s \overrightarrow{v}$. Pour décrire un écoulement à l'équilibre, une condition de vitesse nulle aux jonctions avec les films (coin du bord de Plateau) est classiquement supposée, ainsi que l'égalité des contraintes à l'interface (la contrainte de cisaillement de l'interface est égale à la contrainte visqueuse sur l'interface de l'écoulement dans le volume du fluide de viscosité η). Cet équilibre impose les conditions limites suivantes :

- $\overrightarrow{v} = 0$ aux jonctions entre bord de Plateau et film (coin)
- $\eta_s \Delta_s \overrightarrow{v} = \eta \overrightarrow{n}.\overrightarrow{\nabla} \overrightarrow{v}$ sur les interfaces, où $\overrightarrow{n}$ est la normale sortante à la surface.

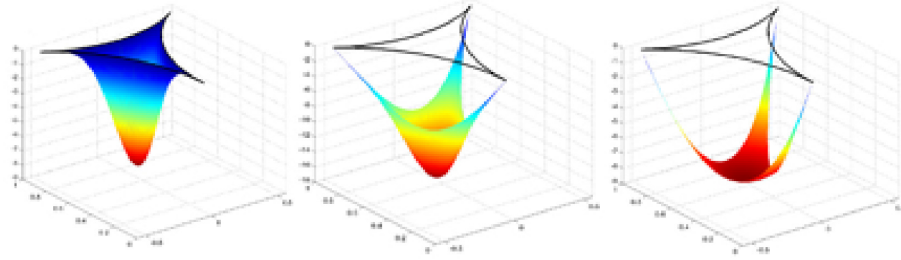L'adimensionnement de cette dernière équation fait apparaître un nombre sans dimension

FIGURE 2.2 – Profils type de vitesse dans une section de bord de Plateau "ideal" pour Bq=1 ; 0.1 et 0.01.

appelé nombre de Boussinesq (Bq) qui est caractéristique du mode d'écoulement dans un canal de largeur caractéristique L : $Bq = \frac{\eta_s}{\eta L}$. Avec ces considérations, il est possible de modéliser l'écoulement de liquide à l'échellement locale dans un canal ayant la forme d'un bord de Plateau "ideal" en faisant varier le nombre de Boussinesq (cf. figure 2.2). Pour $Bq << 1$, l'écoulement tend vers un écoulement de type bouchon pour lequel les dissipations visqueuses seront faibles comparés à des écoulements à plus grand Bq pour lesquels l'écoulement tend vers une écoulement de type "Poiseuille" avec des vitesses nulles aux interfaces. Le nombre de Bq est caractéristique de la mobilité des interfaces.

Dans ce chapitre je presente mes travaux concernant les écoulements de liquide aux différentes échelles : celle d'une mousse dans sa globalité et celle des éléments constitutifs de celle-ci (Bord de Plateau et Nœud) en considérant l'effet d'un couplage entre l'écoulement de liquide dans les canaux et dans les films par effet Marangoni. Enfin je terminerai par l'étude de l'écoulement de liquide dans un film de verre fondu et l'effet sur sa stabilité.

2.1 Perméabilité d'une mousse aqueuse et d'une suspension de bulles

Publications : EPJE 2009, Langmuir 2009, PoF 2010.

Plus l'interface liquide-air est mobile, plus elle est facilement entrainée par l'écoulement de

liquide et moins elle s'oppose à l'écoulement. La perméabilité d'une mousse est donc d'autant plus grande que les interfaces qui entourent les bulles sont mobiles. Quantitativement la perméabilité (k) d'un milieu poreux est décrite par la loi de Darcy : $Q/S = \frac{k}{\eta}\frac{\Delta P}{L}$ et a la dimension d'une longueur au carré. Un raisonnement par analogie avec la loi de Poiseuille dans un canal montre que la perméabilité est de l'ordre de grandeur de la section transverse du canal. Dans le cas d'une mousse, la taille caractéristique des canaux dépend à la fois de la taille des bulles et de la fraction liquide.

Jusque récemment, les propriétés de drainage des mousses étaient généralement présentées en terme de variation de la vitesse de front de drainage en fonction du débit imposé en drainage forcé (cf. figure 2.3 pour l'illustration du principe de l'expérience de drainage forcé) qui ne permet pas de comparer des expériences réalisées avec des paramètres physiques différents (taille de bulles ou viscosité de fluide). Il est possible de comparer sur une même représentation graphique l'ensemble des résultats de la littérature et d'expériences menées au laboratoire en normalisant la perméabilité des mousses par le diamètre moyen de leurs bulles au carré (k/D^2) pour différentes fractions volumiques de liquide et différentes rhéologies interfaciales. L'ensembles des courbes obtenues dans une représentation k/D^2 en fonction de ϕ_l se regroupe en un faisceau de courbes de pente d'autant plus faible que la perméabilité est grande et se rejoignant aux grandes fractions liquide (cf. figure 2.4). Une des mousses produites au laboratoires s'identifie comme l'une des mousses les plus perméables et une autre comme la moins perméable pour une fraction liquide donnée. Nous y ferons référence par la suite et les nommerons mousse à interface "mobile" $(Bq << 1)$ et mousse à interface "immobile" $(Bq \simeq 1)$.

Pour des faibles fractions liquide, il est possible d'extraire une loi de puissance de la perméabilité en fonction de la fraction liquide : $k/D^2 \propto \phi_l^n$. Pour les mousses à interface "immobile", $n = 2$ et cette valeur se justifie à l'aide d'un modèle de dissipation visqueuse dominée par les bords de Plateau (modèle de canaux) [3]. A l'opposé, pour des mousses à interface "mobile", $n = 3/2$ et cette valeur se justifie à l'aide d'un modèle de dissipation visqueuse dominé par les jonctions entre les bords de Plateau (modèle des noeuds) [4]. Cependant ces lois de puissances ne sont plus vérifiées pour des fractions liquides supérieures à 0.1 . Notons que la justification de ces lois de puissance n'est valide que pour des fractions liquides bien plus faibles puisqu'elles supposent une géométrie vérifiant l'équation 2.0.1 obtenue en négligeant le volume des noeuds et des films. Une modélisation plus précise de la géométrie des bords de Plateau à plus forte
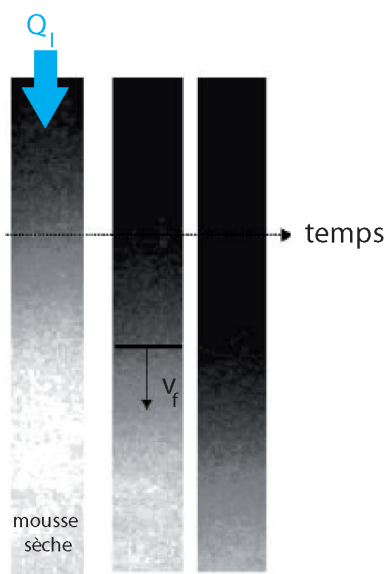
FIGURE 2.3 – Schéma d'illustration du principe de l'expérience de drainage forcé : 3 images successives d'une colonne verticale de mousse initialement sèche et arrosée par le haut par un débit de liquide imposé
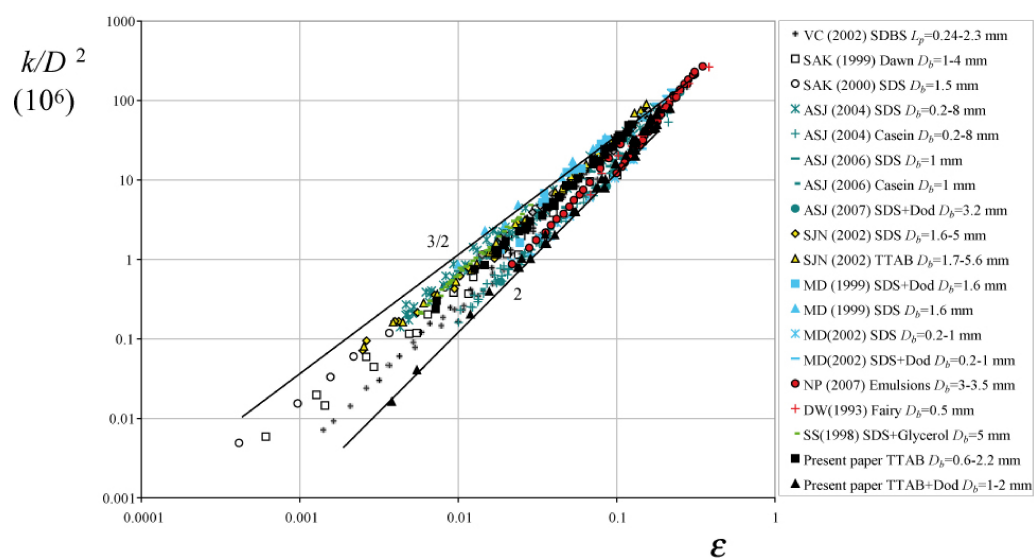

FIGURE 2.4 – Perméabilité normalisée d'une mousse en fonction de la fraction liquide pour différentes solutions moussantes
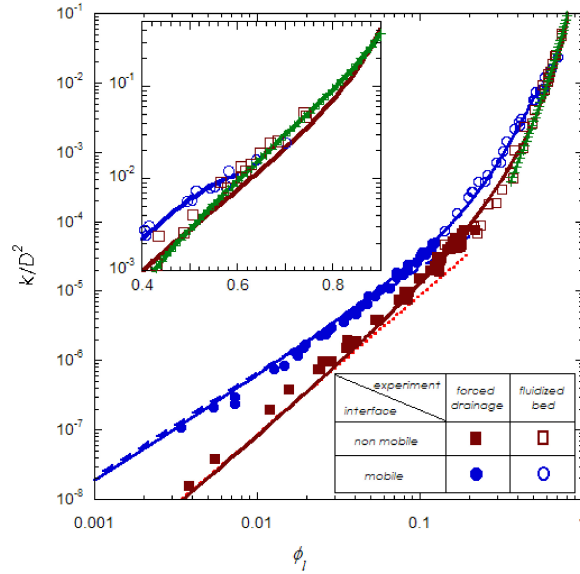
FIGURE 2.5 – Perméabilité normalisée d'une mousse en fonction de la fraction liquide pour les solutions dites "mobiles" et "immobiles" mesurée en drainage forcé et en lit fluidisé

fraction liquide semble indiquer que le paramètre intrinsèque caractérisant la fluidité des interfaces d'une mousse pour décrire son drainage n'est pas la viscosité de surface mais le nombre de Boussinesq.

Afin de sonder la perméabilité d'une assemblée de bulles pour des fractions liquide élevées, nous avons effectué des mesures dans un lit fluidisé de bulles. Nous montrons que jusqu'à des fractions liquides proche de 0.6, la perméabilité d'une assemblée de bulles avec des interfaces "mobiles" est toujours plus élevée que celle avec des interfaces "immobiles" (cf. figure 2.5). La perméabilité d'une assemblée "diluée" de bulles quelque soit la phyisco-chimie des interfaces, tend vers celle attendue pour une assemblée de sphères dures. La rigidification des interfaces des bulles avec l'augmentation de la fraction liquide est effective bien au-delà de la fraction de liquide à laquelle la surface des films séparant les bulles s'annule ($\phi_l > 0.36$, c'est-à-dire lorsque que les bulles ne sont plus au contact - la mousse devient une suspension de bulles disjointes). Cette rigidification s'opère progressivement entre $\phi_l = 0.36$ et $\phi_l = 0.6$. L'ensemble de la courbe de perméabilité mesurée, sur 7 décades, pour des interfaces "immobiles" est parfaitement décrite par le modèle de Carman-Kozeny prenant en compte la surface effective des canaux.

Une conclusion de ces premiers travaux est que la compréhension de l'écoulement de liquide à l'échelle macroscopique est bonne tant que les interfaces des bulles se comportent comme des parois solides. Cependant la modélisation de l'écoulement de liquide pour des interfaces mobiles n'est pas encore satisfaisante. Notons que la mobilité des interfaces est liée à la mobilité des surfactants susceptible d'induire des courants Marangoni. Nous considérons alors l'écoulement de liquide à l'échelle microscopique (quelques bords de Plateau connectés entre eux par un noeud et leurs films adjacents) afin de mieux comprendre l'origine et les effets d'un couplage entre l'écoulement dans les bords de Plateau et des recirculations dans les films [6, 7].

2.2 Ecoulement de liquide à l'échelle locale : considération des écoulements Marangoni dans les films

Publications : Colsua 2008, EPJE 2009.

2.2.1 Modèle de Recirculation de liquide dans les films

Par simple conservation du débit surfacique sur une face d'un noeud joignant 2 faces de bord de Plateau, nous montrons que la concentration de surface en amont et en aval d'un nœud ne peuvent être égales. En effet dans le cas de la géométrie représentée sur la figure 2.6 : $q_s^{amont} = uR\Gamma_{eq} > q_s^{aval} = 2(u/3)R\Gamma_{eq}$, et ainsi la concentration de surface de surfactants (Γ) est plus importante à la sortie qu'à l'entrée d'un bord de Plateau. Aussi, nous proposons qu'il se développe au niveau des jonctions entre canal et film (flèche verte sur le dessin) un courant de Marangoni orienté dans le sens opposé à l'écoulement du fait d'une valeur de tension de surface plus élevée en amont qu'en aval d'un bord de Plateau.

Nous remettons alors en question la première condition aux limites précédemment énoncé pour un écoulement à l'équilibre à savoir $\overrightarrow{v} = 0$ aux jonctions entre bord de Plateau et film (coin). Nous proposons d'introduire une amplitude de vitesse V_{up} et une longueur ζ caractéristiques du contre-écoulement généré par les contraintes Marangoni dans le film, nous définissons ainsi une zone de transition à l'intérieur d'un bord de Plateau se déplaçant en sens contraire à l'écoulement moyen et d'étendue spatiale ζ (cf. figure 2.7).
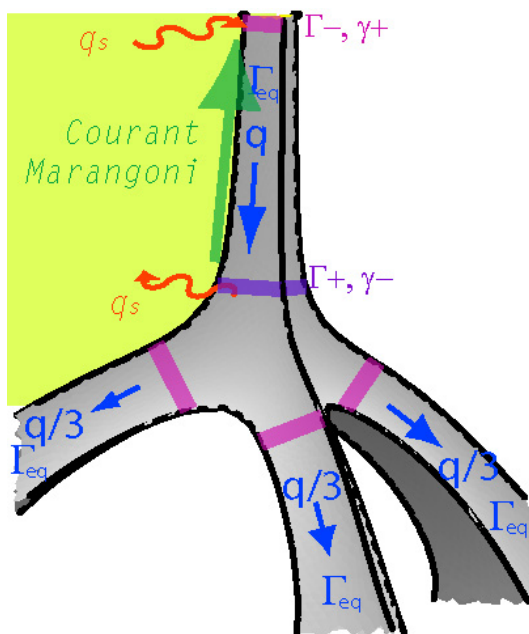
FIGURE 2.6 – Schéma illustrant le modèle de recirculation.

L'équilibre des contraintes visqueuses et de Marangoni dans cette zone de transition ainsi que la conservation des surfactants à la surface d'un bord de plateau (courant Marangoni, diffusion vers le volume et transport en surface), permettent l'estimation de l'amplitude du contre-écoulement en fonction des différents paramètre physico-chimique du liquide. Ce modèle prédit que l'amplitude des contre-écoulements est proportionnelle (avec un préfacteur d'ordre 1) à la vitesse débitante du liquide dans le canal. Ce dernier point est en accord avec l'observations de mouvements dans le film dans une zone très proche du bord de plateau (vraisemblablement le déplacement de lentilles liquide plus épaisses que le film).

Les conséquences de ces courants Marangoni sont :

– diminution de la section hydrodynamique et perméabilité du canal. La variation relative de la perméabilité avec l'amplitude du contre-écoulement est présentée au paragraphe 2.2.2.

– formation d'un pincement à la jonction du bord de Plateau et d'un film (coin), et donc une déformation de la section de bord Plateau comme pour le cas de la régénération marginale dans un film vertical [8]. L'influence de la géométrie de la section sur la perméabilité d'un bord de Plateau est également présentée au paragraphe 2.2.2.
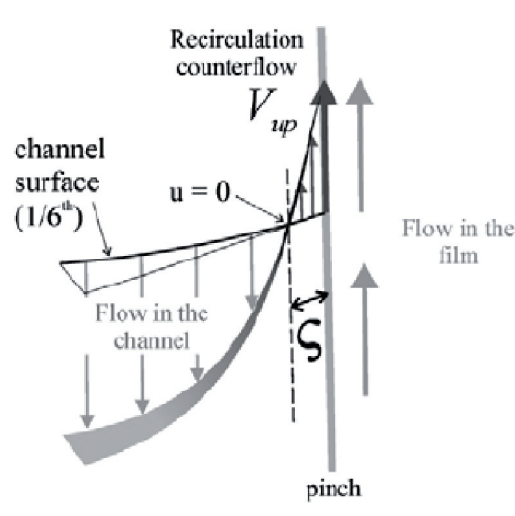
FIGURE 2.7 – Schéma représant la zone de transition entre un bord de Plateau et un film.

– épaississement du film d'autant plus important que l'écoulement dans le bord de Plateau est grand car la recirculation du liquide dans le film est d'autant plus importante que le courant Marangoni est grand. Nous verrons au paragraphe 2.3 que cet effet influence le mûrissement d'une mousse.

2.2.2 Modélisation de la perméabilité d'un bord de Plateau et l'influence des jonctions avec les films

Nous présentons ici des résultats numériques quantifiant l'effet de la zone de transition sur la perméabilité d'un bord de Plateau par rapport au cas classiquement modélisé [9, 10] et présenté à l'introduction de ce chapitre. Nous considérons d'une part l'influence de la géométrie et d'autre part l'influence de la condition limite d'écoulement dans les coins.

La perméabilité est calculée à partir de simulations numériques par éléments finis avec le logiciel Comsol. Nous considérons ici un bord de Plateau infini. La modélisation la plus simple se fait alors à 2D et correspond à l'écoulement $(u(r))$ à travers un sixième de section d'un bord de Plateau comme illustrée par la zone rouge de la figure 2.8.a (symétrie de la géométrie par rapport aux 3 axes portés par le centre et chacun des trois coins). L'équation du mouvement du fluide est l'équation de Stokes adimensionnée qui s'écrit $\Delta u = 1$. La fluidité de l'interface
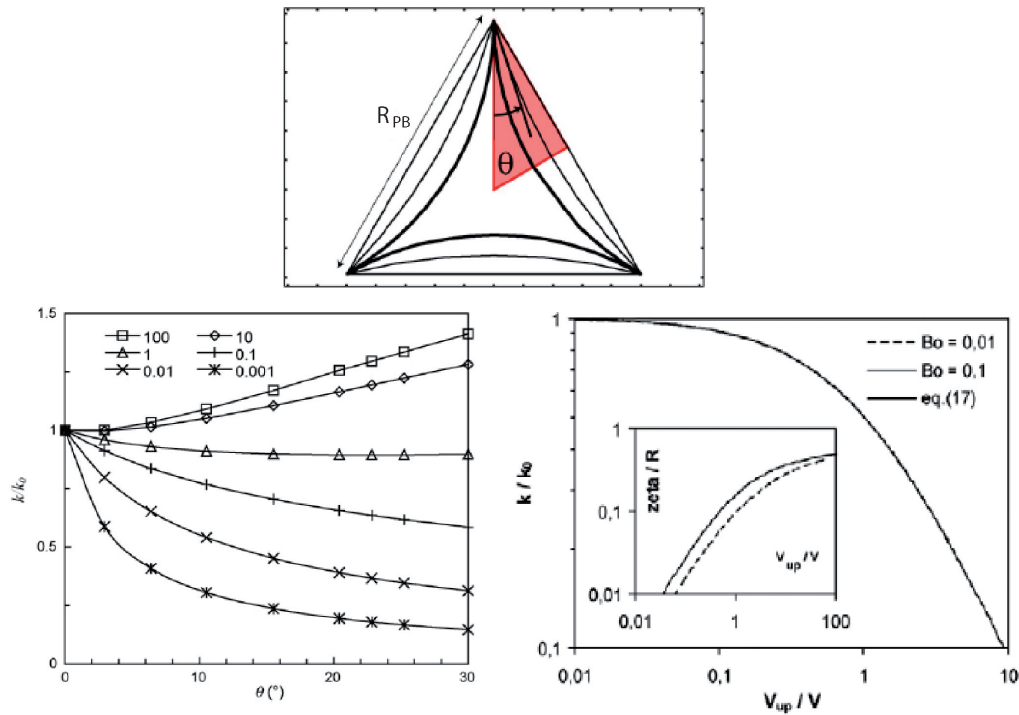
FIGURE 2.8 – a) Schéma de la section d'un bord de Plateau, la zone rouge représente 1/6 ième de la géométrie et correspond à la section effectivement considérée pour les simulations numériques. b) Perméabilité d'un bord de Plateau en fonction de l'angle θ entre les arcs de cercle le délimitant. La perméabilité k_0 correspond à la perméabilité d'un bord de Plateau idéal. c) Perméabilité d'un bord de Plateau en fonction de la vitesse de remontée à la jonction avec le film

liquide-air est également modélisée par l'équation adimensionnée $\overrightarrow{n}.\overrightarrow{grad}\,u = Bo\,\Delta_s u$ qui est introduite sous forme de "weak term" aux coins des bords de Plateau [11].

Influence de la géométrie des jonctions :

Nous considérons ici la géométrie du bord de Plateau limitée par les pincements à la jonction avec les films où la vitesse du fluide est nulle. Nous varions continuement la section d'un bord de Plateau de la forme triangulaire isocèle délimitée par des arcs de cercle de rayon R_{PB} à la forme triangulaire isocèle délimitée par des segments droits de longueur R_{PB} en variant le demi-angle (θ) entre chaque arc de cercle délimitant le canal de 0° à 60° (cf. figure 2.8.a).

Pour $Bq \leq 1$ la perméabilité décroit avec θ et de manière significative aux petits angles.

Notons que pour des interfaces entièrement immobiles (paroi solide), la perméabilité augmente avec θ car la section s'"ouvre" et donc le rayon hydraulique et la surface spécifique des canaux augmentent. Par conséquent, il est évident que la perméabilité d'un canal augmente avec θ lorsque les interfaces tendent vers des parois solides. À l'inverse pour $Bq > 1$ la perméabilité augmente légèrement avec θ. Qualitativement, la diminution de la perméabilité peut s'expliquer à faible Bq par la localisation des gradients de vitesse proche du pincement (point de vitesse nulle) et donc une dissipation plus grande lorsque cette zone s'agrandit quand θ augmente.

Ainsi nous montrons qu'une modification de la géométrie "idéale" habituellement considérée pour la modélisation du drainage dans une mousse aqueuse peut se traduire par une diminution de moitié de la vitesse moyenne d'écoulement pour $Bq = 0.01$ et θ entre $5° - 10°$.

Influence des conditions limites d'écoulement : Nous reprenons le modèle de simulation numérique précédemment exposé en modifiant la condition limite de l'écoulement au point de jonction avec le film, c'est-à-dire en variant la vitesse (V_{up}) dans un sens opposé à l'écoulement moyen. La taille de la zone de contre-écoulement ζ augmente avec V_{up} (cf. insert figure 2.8.c). La section hydrodynamique contribuant au drainage est donc diminuée et la vitesse maximale au centre du canal est plus importante que dans le cas "idéal" par conservation du débit.

La perméabilité du canal varie de manière significative (de moitié) pour V_{up} de l'ordre de la vitesse débitante (cf. figure 2.8) ce qui correspond à ζ de l'ordre d'un dixième du rayon de courbure du bord de Plateau.

Ces simulations numériques ainsi que l'obervation faite lors des expériences nous permettent de conforter le modèle de recirculation présenté au paragraphe 2.2.1 et montrent ainsi les défaillances des modèles jusqu'alors utilisés pour décrire quantitativement le drainage de liquide dans une mousse aqueuse. Il serait intéressant d'entreprendre une modélisation numérique plus complète qui prendrait en compte le couplage entre l'écoulement de liquide en volume et aux interfaces dans les bords de Plateau et les films via le tranfert des surfactants à l'échelle d'une jonction (figure2.6). Mais cela nécessite une maitrise de l'outils numérique bien au-delà de mes moyens et de mes objectifs ...

2.3 Couplage drainage-mûrissement à l'échelle microscopique

Publications : JCIS 2009.

Un dispositif expérimental permet d'isoler une bulle en situation de drainage forcé (cf. figure 2.9). Un gaz (C_6F_{14}) peu soluble dans la solution moussante est utilisé pour créer une bulle sous un bord de Plateau vertical. Une différence de concentration de ce gaz, de part et d'autres des films qui forment cette bulle, entraine un flux diffusif de gaz soluble (N_2) de l'extérieur vers l'intérieur de la bulle. Il est ainsi possible de reproduire à l'échelle locale une expérience de mûrissement. De plus, un drainage imposé de liquide dans le bord de Plateau supérieur permet d'étudier le couplage drainage - mûrissement.

Les expériences montrent que les bulles en situation de drainage mûrissent d'autant moins vite que le débit de liquide imposé dans les canaux est grand. Qualitativement cela s'explique par un épaississement des films qui entourent la bulle sous l'effet de l'écoulement de liquide dans les bords de Plateau (en accord avec le modèle 2.2.1) : plus les films sont épais, plus le temps diffusion du gaz à travers les films est grand. Une description quantitative des données expérimentales nécessite la connaissance de l'épaisseur (e) et la surface (A) des films à traverser. En effet l'accroissement du volume (V) de la bulle est imposé par le flux de gaz N_2 à travers les trois films : $dV/dt = 3AD_m\frac{\Delta C}{e}S\nu_m$ où $\Delta C = C_0V_0/V$ avec D_m le coefficient de diffusion moléculaire, C_0 la concentration initiale de C_6F_{14}, V_0 le volume inital de la bulle, S la solubilité de N_2 et ν_m le volume molaire d'un gaz parfait.

Il est possible expérimentalement de mesurer l'épaisseur des films par interférométrie en lumière blanche. Il est beaucoup plus difficile d'accéder expérimentalement à la surface des films entourants la bulle car non seulement leur limite géométrique avec les bords de Plateau est le lieu de multiple réflexion (faible rayon de courbure des bords Plateau) mais en plus les films sont courbes (d'autant plus que la bulle est petite et se rapproche d'une forme sphérique).

Nous avons donc utilisé le logiciel Surface Evolver pour modéliser numériquement en condition statique la géométrie de la bulle sous un bord de Plateau dans les conditions de l'expérience (cf. figure 2.9). Les paramètres imposés dans la simulation sont : - la hauteur initiale du bord de Plateau ; - les orientations des 3 films verticaux (120° entre chaque) ; - le volume de la bulle ; - la tension de surface et la masse volumique du liquide.
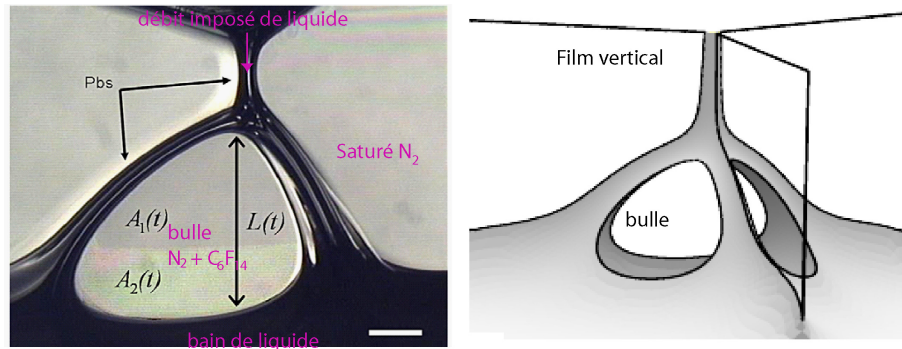
FIGURE 2.9 – a) Montage expérimental d'une bulle en situation de drainage forcé. b) Simulation sous Surface evolver de la géométrie expérimentale.
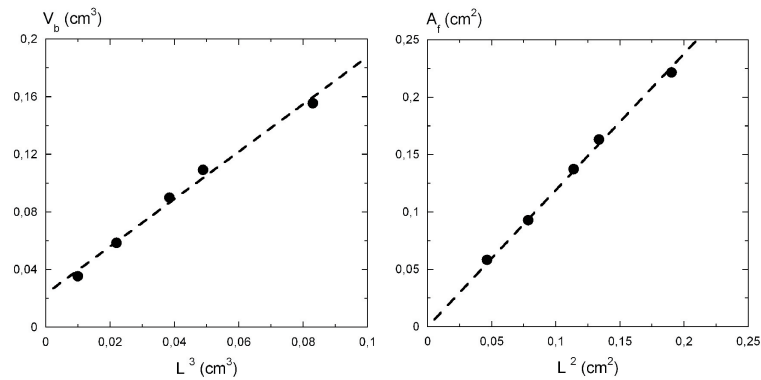
FIGURE 2.10 – a) Dépendance du volume de la bulle en fonction de la hauteur L. b) Dépendance de l'aire des films entourant la bulle en fonction de la hauteur L.

Nous mesurons numériquement la hauteur des films L (qui est aussi mesurable expérimentalement cf. figure 2.9) et leur surface pour des volumes de bulles variant de 0.05 à 0.2 cm^3 correspondant aux tailles bulles de l'expérience (cf .figure 2.10).

Ces conditions géométriques étant prise en compte il est possible de décrire sans paramètre ajustable la variation de la taille de la bulle au cours du temps. A l'exception des petites bulles pour lesquelles des épaississements au coeur du film sont observés.

L'analyse complète et précise de ces expériences montre ainsi que l'épaississement des films dans une mousse en condition de drainage est nécessaire. Ce résultat expliquerai les désaccords entre expériences dans une mousse et théorie concernant la dépendance du mûrissement avec

la fraction liquide [12]. En effet ces théories considérent la diminution de la surface des films lorsque la fraction liquide augmente mais une épaisseur de film indépendante de ϕ_l.

2.4 Drainage d'un film de verre fondu et stabilité d'une bulle unique à la surface d'un liquide

Publications : 1 article en préparation pour soumission à "JCIS" sur le sujet de drainage dans un film au-dessus d'une bulle à la surface d'un bain liquide ; 1 article en préparation pour soumission à "Glass Technology : European Journal of Glass Science and Technology Part A" sur le sujet de stabilité de bulles de verre.

Cette étude est menée en collaboration avec F. Pigeonneau et H. Kocarkova (doctorante - soutenance prévue fin octobre 2011) du laboratoire Surface des Verres et des Interfaces (S.V.I- UMR CNRS- St Gobain Recherche) et a pour objectif initial de mieux comprendre la formation de mousse dans les fours verriers. Néanmoins, nous verrons que cette étude n'est pas exclusivement dédiée à l'industrie verrière et qu'elle présente des résultats nouveaux concernant l'hydrodynamique des écoulements à interfaces libres.

La condition essentielle à la formation d'une mousse est l'existence dans les premiers instants d'une bulle unique. Si cette bulle ne disparaît pas avant d'être rejointe par une autre bulle et ainsi de suite, alors une mousse peut etre créée. Nous avons donc étudié le comportement d'une bulle unique à la surface d'un verre fondu : de l'amincissement du film liquide qui la recouvre jusqu'à sa rupture qui génére dans certains cas de très petites bulles.

2.4.1 Présentation des verres fondus

Un verre est un milieu amorphe constitué d'oxyde de silicium, il est obtenu par fusion de grains de silice (SiO_2) et de carbonate (de calcium $CaCO_3$ et/ou de sodium $NaCO_3$). Dans les premiers instants de ce procédé, de nombreuses bulles sont présentes dans le mélange fondu. Le gaz constituant ces bulles est soit issu d'un simple piégeage d'air entre grains ou alors de réactions chimiques. En effet, bien souvent des produits d'affinage (notamment le sulfate de sodium - Na_2SO_4) sont ajoutés au mélange afin de créer des bulles dont le rôle

est celui d'un agitateur pour obtenir un mélange plus homogène. Les bulles grossissent au sein du bain de verre fondu, et sont poussées sous l'effet de la gravité vers la surface. Pour certains types de verre, une mousse relativement stable se forme. Si la présence de bulles en mouvement est souhaitable dans les premiers instants de l'affinage du verre, la mousse présente un inconvénient majeur par la suite. En effet, la mousse forme un écran thermique entre le bain de verre fondu et l'atmosphère du four qui est la source de chauffage dans de nombreux procédés industriels.

Depuis la deuxième moitié du 20eme siècle de nombreuses études, motivées par l'amélioration du rendement en énergie calorifique, ont vues le jour. Ces études sont bien souvent qualitatives et comparent des expériences pour lesquelles différents paramètres physiques ou physico-chimiques sont variés et fournissent rarement des modèles physiques quantitatifs. Elles ont néanmoins permis de montrer que la température et l'atmosphère dans le four sont des facteurs influençant l'apparition et la stabilité d'une mousse de verre. Ces facteurs dépendent de la composition chimique du verre. Avant de présenter nos résultats, je résume et commente ci-dessous l'essentiels des résultats reportés dans la litterature verrière relatifs à un film de verre fondu (film vertical ou au-dessus d'une bulle à la surface d'un bain) :

– **La tension de surface** d'un verre fondu, mesurée par la méthode de goutte pendante par exemple, est grande par rapport à celle des solutions aqueuses (de l'ordre de 350mN/m) et dépend de sa composition chimique. Certains composants abaissent ou augmentent la tension de surface du verre (cf. table ci-dessous).

composants chimiques	composants chimiques
diminuant la tension de surface	augmentant la tension de surface
V ; B ; Ti ; Na ; K ; Rb ; Cs	Cd ; Zn ; Ce ; Zr ; Ni ; Co ; Fe ; Al ; Mn ; Li ; Alkaline earth metal

Cet effet peut-etre interprété par la polarisabilité des atomes, plus un atome est grand, plus il est polarisable et plus il diminue la tension de surface. C'est en ce sens que certains composants chimiques dans le verre peuvent être appelés surfactants car ils agissent sur la valeur de la tension de surface bien qu'ils soient différents des surfactants amphililes habituellement rencontrés dans le cas des mousses aqueuses et responsables de la stabilisation des films séparant les bulles dans une mousse. L'action de ces composants chimiques dans un verre fondu se comparerait plutot à celui de l'alcool qui diminue la tension de surface de l'eau. Ainsi une évaporation d'un composant diminuant la tension

de surface (V ; B ; Ti ; Na ; K ; Rb ; Cs dans le verre ou alcool dans l'eau) augmente la tension de surface de la solution. Une conséquence bien connue de cet effet est l'apparition des larmes de vin sur les bords d'un verre à la surface d'un liquide alcoolisé par courant Marangoni.

– L'**amincissement d'un film de verre fondu** ralentit au cours du temps [13, 14] : 1- au début, l'épaisseur h du film décroît exponentiellement jusqu'à des épaisseurs de l'ordre de la centaine de nanomètres. Cette décroissance exponentielle de h s'explique par le fait que les interfaces sont mobiles (pas de viscosité de surface). Le taux d'amincissement décroît comme l'inverse de la viscosité du verre fondu $\frac{1}{h}\frac{dh}{dt} \propto 1/\eta$. 2- Pour des épaisseurs plus faibles, un fort ralentissement voir un arrêt du drainage du film est évoqué et les films sont qualifiés de "metastable" [13]. Ce ralentissement suggère une rigidification des interfaces lorsque le film devient très mince. P. Laimbock [14] propose une origine physique à cette rigidification des interfaces par effet Marangoni. Il suppose qu'un composant tel que l'oxide de sodium (Na_2O) joue le role d'un surfactant en dessous de la cmc (interface non saturé) et qu'ainsi la tension de surface est plus grande là où le film est le plus mince par conservation des espèces lors de l'étirement du film (cf. figure 2.11a).

– La relation entre **le temps de vie** d'un film et la dynamique de drainage de celui-ci est sujet à controverse. D'après Berkeens et Schaaf [15, 16], le temps de vie d'un film se déduit simplement du temps nécessaire pour qu'un film draine d'une épaisseur h_0 initiale jusqu'à une épaisseur critique h_c (critère de Schedulko écrit en considérant des interactions de Van der Waals uniquement) en dessous de laquelle toute perturbation d'épaisseur du film est instable et mène à la rupture du film. Considérant que les interfaces des films ne sont jamais exclusivement mobiles ou immobiles, ils proposent une écriture du temps de vie d'une bulle comme la somme des temps de vie estimés pour des interfaces mobiles et pour des interfaces immobiles pondérée par un facteur d'immobilité de surface. Cette approche suppose donc qu'il existe un temps de vie bien defini pour une bulle de taille donnée et une composition de verre fondu connues ! Selon Hrma [17], le temps de vie d'une bulle à la surface d'un bain de verre fondu n'est pas uniquement dépendant du drainage du film en surface. Il distingue deux étapes dans la vie d'un film : le drainage du film jusqu'à une épaisseur critique suivi de la survie du film fin à cette épaisseur critique. Cette dernière approche suppose donc qu'il est possible que le drainage d'un film de verre fondu soit stoppé à partir d'une certaine épaisseur comme
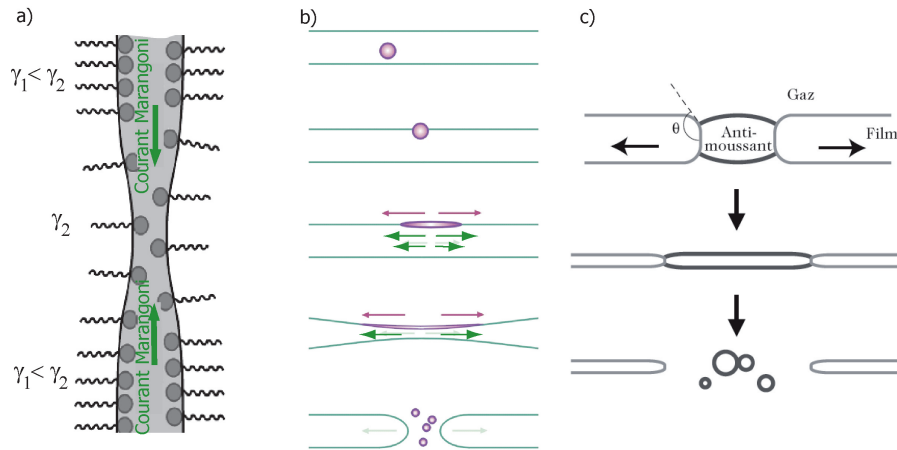
FIGURE 2.11 – a) Schéma illustrant le courant Marangoni suite à un étirement local d'un film fin. b) et c) Schémas illustrants la rupture d'un film par étalement (b) ou étirement (c) d'une gouttelette de tension de surface plus faible que le liquide contenu dans le film. Schéma extraits du livre "Les mousses - Structure et Dynamique", édition Belin, collection Echelles

cela est le cas pour des films de savons stabilisés par des surfactants dont l'encombrement stérique ou les répulsions électrostatiques suffisent à contre-balancer la succion capillaire. Cette dernière hypothèse est évoquée dans le travail de Cable et al. [18] mais, à notre connaissance, n'a jamais été démontrée.

– La **présence de sulfate** dans le gaz ou dans le verre fondu sous forme composé avec un agent d'affinage (bien souvent avec le sodium) agit sur le temps de vie d'un film de verre fondu. Cette action dépend de la température. A basse température (inférieure a 1100^oC), le sulfate associé au sodium (Na_2SO_4- sulfate de sodium) est un liquide appelé "*Sulfate gall*" immiscible dans le verre fondu et ayant une tension de surface avec l'air ($200mN/m$) beaucoup plus faible que le verre ($350mN/m$). Cette "*gall*" migre en surface du verre fondu dans une configuration plus favorable énergétiquement. Ainsi à basse température le présence de sulfate diminue le temps de vie d'un film de verre fondu [13, 14], par des mécanismes de rupture analogues à ceux bien connue de la rupture d'un film de savon (rôle du verre fondu) par une gouttelette d'huile (rôle de la "*gall*") (cf. figure 2.11b-c). La distinction entre les deux scénarios se fait à partir du paramètre d'étalement faisant intervenir la tension de surface entre la "*gall*" et le verre fondu, qui à ma connaissance n'est pas connue. A plus forte température cette "*gall*" se mélange dans le verre fondu (mélange complet au-delà de 1300^oC) et le sulfate et l'agent d'affinage (sodium, potassium etc ...) s'évapore vers l'atmosphère. Dans des conditons d'oxidation,

les gaz dégagés sont sous forme Na_2O et SO_3 alors que dans des conditons de reduction, les gaz dégagés sont sous forme Na_2S et CO_2.

– L'**évaporation de sodium et de potassium** est d'autant plus active que la température du four est élévée (fort accroissement au-delà de 1300^oC) et que l'atmosphère environnante est en mouvement (vitesse de convection favorise l'évaporation par un renouvellement de l'air à la surface du verre fondu). La présence de vapeur d'eau dans l'atmosphère favorise également l'évaporation du sodium. La présence de Bore (B) est également un facteur favorable à l'évaporation de sodium et potassium. Les travaux de Kucuk et al. [19] montrent que l'évaporation de sodium engendre une augmentation de la tension de surface dans un verre avec du calcium alors que l'évaporation de potassium n'influence pas la tension de surface dans un verre sans calcium. Ces différences s'expliqueraient par une diffusion plus rapide pour le potassium que pour le sodium qui serait "bloqué" par la présence de calcium dans un verre sodo-sili-calcite. Ainsi une diminution de la concentration de sodium dans une fine couche sous la surface du verre fondu est attendue.

2.4.2 Drainage d'un film liquide aux interfaces mobiles au-dessus d'une bulle unique à la surface d'un liquide visqueux

Afin de caractériser le drainage du film au-dessus d'une bulle à la surface d'un bain de verre fondu, un montage interférométrique est disposé au-dessus d'un four (cf. figure 2.12) dans lequel une bulle de taille contrôlée peut être créée au fond d'un récipient en platine.

Pour l'ensemble des expériences réalisées (tous types de verre confondu), il est obervé un décroissance exponentielle de l'épaisseur du film au cours du temps :

$$h(t) = h_0 \exp(-t/\tau_{drainage}) \qquad (2.4.1)$$

Ce résultat est en accord avec les études précédemment citées (cf. paragraphe 2.4.1). Qualitativement nous observons que le drainage est d'autant plus rapide que la température est élevée (viscosité faible) et que la bulle est grosse. Par un argument dimensionnel à l'échelle
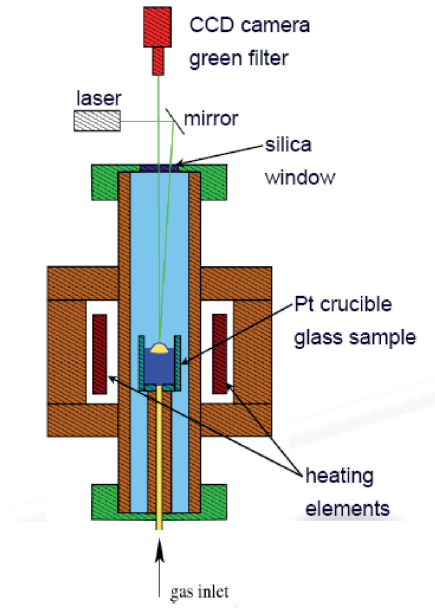
FIGURE 2.12 – Schéma illustrant le montage expérimental

de la bulle considérant uniquement les effets de la pesanteur (moteur du drainage) et la viscosité dynamique du liquide (frein au drainage), un temps caractéristique peut être déduit : $\tau_{dim} = \eta/(\rho g D)$, ce temps caractéristique est d'autant plus petit que la viscosité du fluide est faible et que la bulle est grosse, et semble en accord avec l'expérience. Cependant les courbes de drainage mesurées pour différentes tailles de bulles et adimensionné par τ_{dim} ne se superposent pas (cf. figure 2.13a).

En temps relatif le film au dessus d'une petite bulle s'amincit plus vite que le film au-dessus d'une grosse bulle. Qualitativement, ce résultat peut être compris par le fait que plus la bulle est petite moins elle déforme l'interface et la surface du film fin (S_{cap}) représente une moins grande proportion de la surface de la bulle (cf. schéma figure 2.13b). Ainsi la dissipation visqueuse de l'écoulement de liquide dans un film fin est en proportion moins importante pour une petite bulle que pour une grosse bulle (la force motrice étant toujours fixée par la taille de la bulle).

Plus précisement, la forme quasistatique du film au dessus-d'une bulle à la surface d'un bain liquide est régie par la gravité qui pousse la bulle hors du liquide et par la tension de surface du liquide qui résiste à la déformation et dépend ainsi du nombre de Bond : $Bo = \rho g D^2/\gamma$. Sur
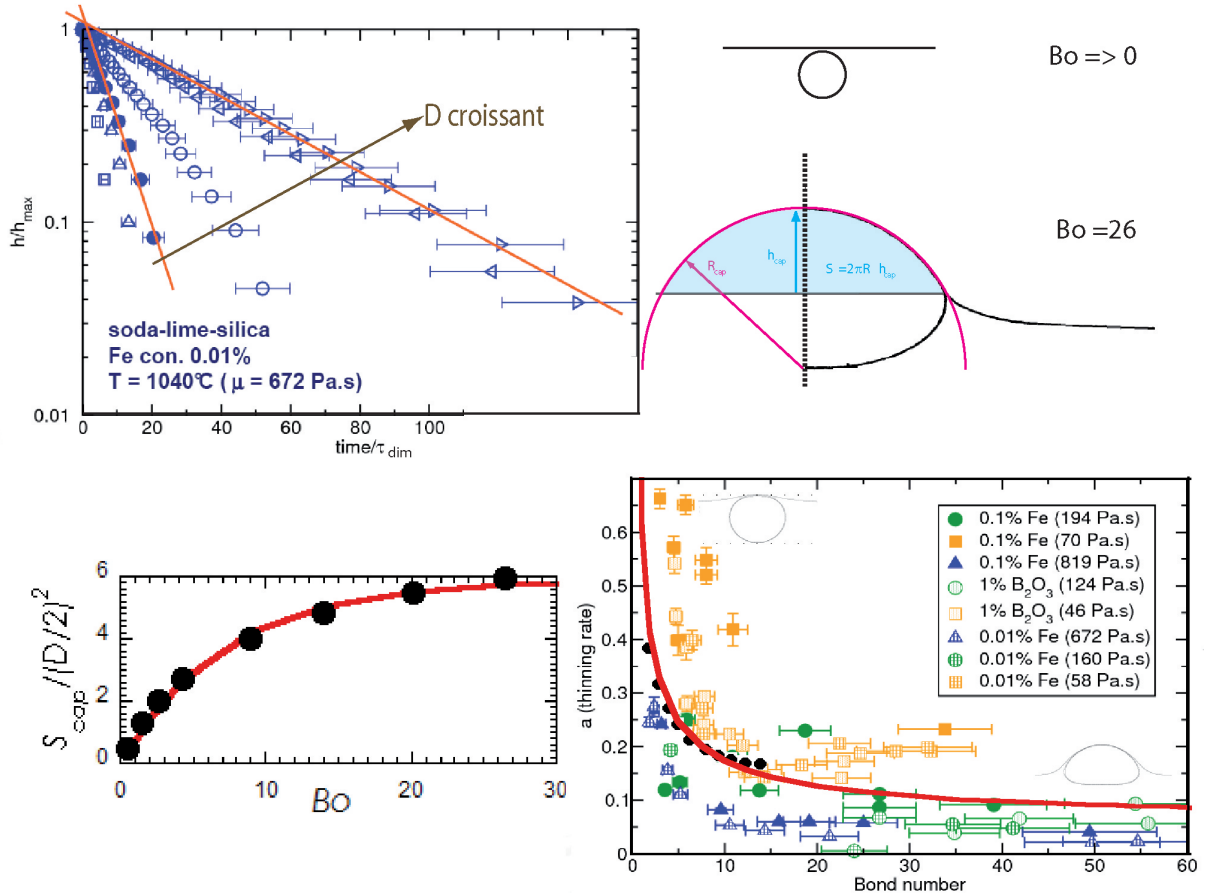
FIGURE 2.13 – a) Courbe de variation relative de l'épaisseur du film $h(t)/h_0$ en fonction du temps adimensionné t/τ_{dim} en coordonnées log-lin. b)Schéma illustrant la forme d'une bulle à la surface d'un bain pour Bo tendant vers 0 et Bo=26, et les paramètres physiques R_{cap}, h_{cap}, S_{cap}. c) Coube de variation adimensionnée de la surface du film fin $S_{cap}/(D/2)^2$ en fonction de Bo. d) Coube de variation adimensionnée du taux d'amincissement de film (a) en fonction du nombre de Bond (Bo).

la figure 2.13c des résultats extraits des travaux de Princen datant de 1963 [20] représentent la variation de la surface de la bulle adimensionnée par $(D/2)^2$ en fonction du nombre de Bond. Nous choisissons une régression de type : $S_{cap}/(D/2)^2 = 2\pi(2)^{2/3}(A \times Bo + Bo^2)/(B + C \times Bo + Bo^2)$ où $A = 94.7$, $B = 901.96$ et $C = 142.46$ qui satisfait, $S_{cap} \propto Bo$ dans la limite $Bo = 0$ et $S_{cap}/(D/2)^2 = 2\pi(\frac{R_{cap}}{(D/2)})^2 = 2\pi(2)^{2/3}$ dans la limite $Bo \to \infty$.

Finalement, nous représentons sur un même graphique (figure 2.13d) l'ensemble des taux d'amincissement adimensionnées en fonction de Bo obtenus pour différents verres fondus à différentes températures et dans différentes atmosphères. Le taux adimensionné d'amincissement de film se définit : $a = \frac{\tau_{dim}}{h}\frac{dh}{dt} = \tau_{dim}/\tau_{drainage}$.

Les points sont dispersés mais montrent un décroissance systématique de a en fonction de Bo aux petits nombres de Bo pour rejoindre une valeur proche de 0.1 aux grands nombres de Bo. Des simulations numériques par une méthode d'éléments intégrals aux frontières (point noir) ainsi qu'un modèle théorique (courbe rouge) décrivent bien les résultats expérimentaux. Nous avons écrit le modèle théorique en supposant que le moteur de l'écoulement de liquide dans le film fin au-dessus de la bulle est la pression appliquée par le poids de la bulle sur la surface de ce film fin $(4\pi/3(D/2)^3\rho g/S_{cap})$ et que le frein à cet écoulement est un contrainte visqueuse d'origine élongationnelle $(3\eta\frac{1}{h}\frac{dh}{dt})$. Nous en déduisons une expression analytique du taux adimensionné d'amincissement du film liquide au dessus d'une bulle :

$$a = \frac{\tau_{dim}}{\tau_{drainage}} = \frac{2\pi}{9}\frac{(D/2)^2}{S_{cap}} = \frac{1}{9(2)^{2/3}}\frac{901.96 + 142.46Bo + Bo^2}{94.7Bo + Bo^2} \qquad (2.4.2)$$

Les travaux expérimentaux de Debregeas et al. obtenus pour de grosses bulles d'air à la surface du PDMS sont en très bon accord avec nos résultats dans la limite des grands nombres de Bond [21]. En effet, nous déduisons de leur figure 1.a $1/\tau_{drainage} = 1.63(s^{-1}m^{-1})R_{cap}$ soit $a = \tau_{dim}/\tau_{drainage} = 0.104$. Notons que leur modèle d'écoulement gravitaire bouchon dans une fine calotte sphérique prédit $a = 0.63$ et surestime ainsi d'un facteur 6 environ les résultats expérimentaux ! Ce facteur peut être corrigé en considérant que les dissipations visqueuses sont élongationnelles et ainsi être divisé par 3. Mais cela n'est pas suffisant ... De mon point de vue la grande différence entre notre modèle et le leur est le moteur de l'écoulement : le poids du liquide (leur modèle) et le poids apparent de la bulle (notre modèle).

Ces résultats confirment que l'épaisseur d'un film décroit exponentiellement dans le temps et que par conséquent les interfaces d'un film de verre fondu sont mobiles. Cependant, nous

montrons qu'un simple argument dimensionnel n'est pas suffisant pour déterminer le temps caractéristique de drainage d'un film au dessus d'une bulle quelque soit sa taille. En effet, les petites bulles drainent relativement plus vite que les grosses bulles. Grâce au modèle théorique nous établissons un forme analytique du taux d'amincissement du film liquide au-dessus d'une bulle en fonction du nombre de Bond qui permet ainsi de prédire le temps caractéristique de drainage en fonction des paramètres physiques suivants : taille de bulle, tension de surface et viscosité du verre fondu.

2.4.3 Temps de vie d'une bulle unique à la surface d'un liquide : effet Marangoni par évaporation de Sodium

Nous définisson le temps de vie d'une bulle par l'intervalle de temps pendant lequel la forme de la bulle vue de dessus reste figée à la surface du bain liquide c'est-à-dire le temps que la bulle reste à la surface après avoir déformé celle-ci et avant la rupture du film supérieur. Notons que la bulle est figée mais que le liquide s'écoule dans le film (les franges d'interférence évoluent dans le temps). Si aucun effet stabilisant n'est attendu pour un film de verre fondu, le temps de vie d'une bulle à la surface liquide serait unique et proportionel au temps caractéristique de drainage (cf. "Présentation des verres fondus").

Pour des températures de chauffage du four inférieures à 1300^oC, les temps de vie de bulle pour l'ensemble des verres testés sont très peu dispersés et sont environ 10 fois plus grand que le temps caractéristique de drainage calculé à partir de l'équation 2.4.2 (cf. figure 2.14 pour le verre avec du Fe à 0.1% et le verre avec de Bore à 1%)).

Pour des températures de chauffage du four supérieures à 1300^oC, cette proportionnalité n'est plus vérifiée pour l'ensemble des verres testés. Les temps de vie sont très dispersés et peuvent être de 10 fois à 100 fois plus grand que le temps de drainage ! Le film ne peut pas drainer sur un temps si long, il existe donc un mécanisme stabilisant pour les films de verre à température supérieure à 1300^oC.

Dans les premiers instants, l'observation des franges d'interférence dans le film montrent un drainage "régulier" du film pendant lequel les franges sont à peu près circulaires, elles apparaissent proche du sommet de la bulle et s'ouvrent du centre vers la périphérie de la bulle où elles disparaissent. La durée du drainage régulier est d'environ $10\tau_{drainage}$ et réprésente la

majeure partie du temps de vie des bulles à faible température. Cela correspond au temps nécessaire pour qu'un film s'amincisse d'un facteur 10^4 environ, ce qui est réalisé lorsqu'un film épais de quelques centaines de μm s'amincit jusqu'à des épaisseurs de quelques dizaines de nm.

Aux plus fortes températures, nous observons à la suite du drainage "régulier" que les franges se déforment (boucles pas circulaires), que certaines parties se figent et que d'autres parties se déplacent vers le sommet de la bulle. Ces motifs et mouvements semblent chaotiques et sont comparables à ceux décrits dans le cas d'un bulle hémisphérique chauffée à l'équateur [22].

Des analyses chimiques par SIMS sur un film de verre refroidi (verre avec du Fe à 0.1%) initialement étiré dans un état fondu à un température $T_{etirement}$ égale à 1200^oC et 1400^oC montrent un apauvrissement en sodium à la surface du film bien plus important pour $T_{etirement}$ égale à 1400^oC qu'à 1200^oC. Ces mesures sont en accord avec l'explication de Kucuk et al concernant la diminution de la tension de surface dans le temps à une température de 1400^oC, du fait de l'évaporation de Sodium en surface et d'une diffusion trop lente du sodium du volume vers la surface. De plus, il est à noté qu'un verre fondu voit sa masse volumique diminué avec sa concentration en sodium [23].

Ainsi, l'évaporation de sodium engendre une augmentation de la tension de surface à la surface du film et de la densité du liquide dans le film par rapport au bain liquide. Quantitativement nous estimons pour un film de $100nm$ la variation de concentration en Na_2O entre le film et le bain liquide, serait d'environ 4% ; ce qui implique une variation de tension de surface d'environ $4mN/m$ à (1400^oC), soit une variation de tension de surface d'environ 1% et une variation de densité d'environ 0.1%. C'est donc l'effet de l'évaporation sur la tension de surface qui apparait le plus important. Un modélisation numérique du drainage d'un film vertical montre qu'une telle variation de tension de surface permettrai de stabiliser le film à des épaisseurs d'environ $100nm$. (travail en cours).

Pour conclure, nous proposons qu'un courant Marangoni généré par l'évaporation de sodium est capable de s'opposer au drainage du film et donc d'augmenter de manière significative le temps de vie d'une bulle à la surface d'un bain de verre fondu. Ce scénario pour expliquer la stabilité des bulles est analogue aux larmes de vins observé sur les bords d'un verre rempli d'une boisson alcoolisée et est différent de celui proposé par Laimbock qui comparait le sodium à un surfactant en dessous de la cmc.
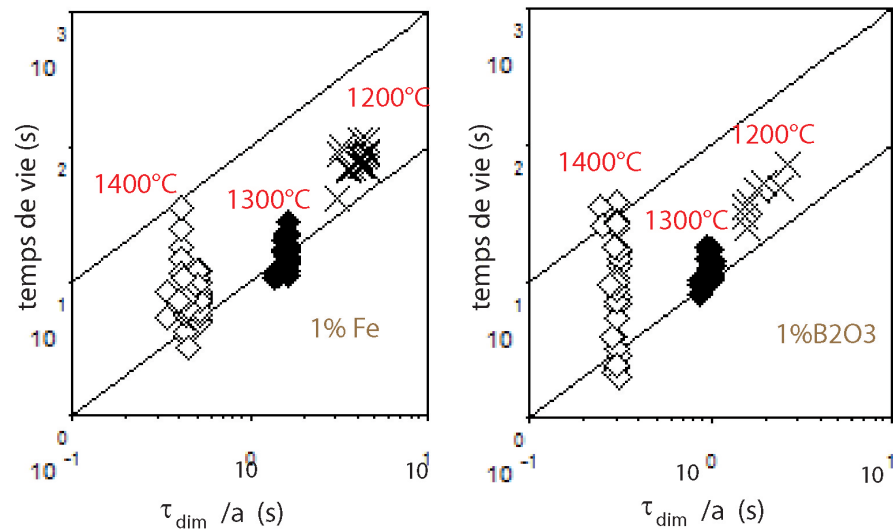
FIGURE 2.14 – temps de vie en fonction du temps caractéristique de drainage

2.4.4 Apparition de bulles "filles" lors de la rupture d'une bulle unique à la surface d'un liquide

Pour des températures élévées et des verres au Bore (faible viscosité), nous observons de très petites bulles dites "filles" disposées en corolle à la périphérie de la bulle initiale dite "mère" (cf. figure 2.15). Il est important de noté qu'une petite bulle à tous les atouts pour vivre plus longtemps qu'une grosse bulle (temps de drainage absolue plus grand et épaisseur critique du film plus petite). Il est donc possible que la rupture d'une grosse bulle soit à l'origine d'un amas de petites bulles (les petites bulles s'attirent entre elle du fait des forces capillaires) qui peut être très stable et généré une mousse.

Bird et al. ont observé de telles bulles filles et présentent un critère d'apparition de ces bulles filles [24] dépendant des nombres de Reynolds ($Re = \rho D U / 2\mu$) et des nombres Capillaire ($Ca = U\mu/\gamma$) où la vitesse U est celle d'ouverture du film : - pour $Re < 2$, il n'y a pas formation de corolle de petites bulles ; pour $Re > 2$, il y a formation d'une corolle de petites bulles si Ca est plus petit que l'unité et de deux corolles de petites bulles si Ca est plus grand que l'unité.

Le dispositif d'acquisition vidéo initialement utilisé pour la mesure de l'amincissement du film ne permettait pas la mesure de la vitesse de l'ouverture du film pendant sa rupture. Néanmoins, nous estimons la vitesse d'ouverture à partir de la vitesse de Taylor-Culick (limite
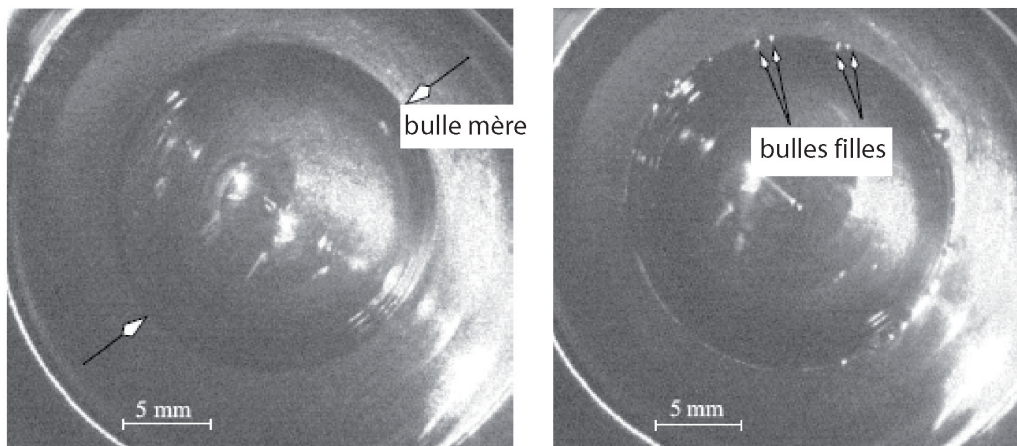
FIGURE 2.15 – Image vue de dessous d'une bulle à la surface d'un bain liquide avant (vue de gauche) et après (vue de droite) la rupture du film supérieur.

inertielle) et établissons que le critère d'apparition de bulle fille correspondrait à des nombres de Reynolds d'au moins un ordre de grandeur plus grand que l'unité. Afin de mieux quantifier ce seuil d'apparition de petites bulles filles dans le verre, des expériences sont envisagées mais avec une caméra rapide cette fois-ci !

Bibliographie

[1] A. Vrij, *Discuss. Faraday Soc.* **42**, 23 (1966)
   A. Vrij et J.Th Overbeek, *J. Am. Chem. Soc.*, **90**, 3074 (1968) .

[2] R.A. Leonard et R. Lemlich, *A.I.Ch. E. Journal*, **11**, 18 (1965).

[3] D. Weaire, S. Hutzler, G. Verbist et E. Peters, *Adv. Chem. Phys.*, **102**, 315 (1997).

[4] S. A. Koehler and S. Hilgenfeldt and H. A. Stone, *Langmuir*, **16**, 6327 (2000).

[5] A. Saint-Jalmes, *Soft Matter*, **2**, 836 (2006).

[6] V. Carrier, S. Destouesse, A. Colin, *Phys. Rev. E* **65**, 061404, (2002).

[7] O. Pitois, C. Fritz et M. Vignes-Adler, *J. Coll. Int. Sci.*, **282**, 458 (2005).

[8] M. Aradian, E. Raphael, P.-G. de Gennes, *Europhys. Lett.* **55**, 834 (2001.)

[9] A. V. Nguyen, *Journal of Colloid and Interface Science* **249**, 194Ű199 (2002)

[10] S.A. Koehler and S. Hilgenfeldt et H.A Stone, *J. Colloid Int. Sci.*, **276**, 420 (2004).

[11] W. Drenckhan, H. Ritacco, A. Saint-Jalmes, A. Saugey, P. McGuinness, A. van der Net, D. Langevin, D. Weaire, *Phys. Fluids* **19**, 102101 (2007).

[12] K. Feitosa, D.J. Durian, *Eur. Phys. J.E* **26** 309 (2008).

[13] J. Kappel, R. Conradt, H.Scholze, *Glass Science and Technology* **60**, No.6, pp.189-201 (1987).

[14] P. Laimbock, Ph.D study "Foaming of Glass Melts", University of Technology, Eindhoven (1998).

[15] J. Van Der Schaaf, R.G.C. Beerkens, *Journal of Colloid and Interface Science*, **295** 1, 218-229 (2006).

[16] R.G.C. Beerkens, J. Van Der Schaaf, *Journal of the american ceramic society*, **89** 1, 24-35 (2006).

[17] P. Hrma, *Journal of Colloid and Interface Science* **134** 1, 161-168 (1990).

[18] M. Cable, C. G. Rasul and J. Savage. *Glass Technol.*, **9**, pp. 25Ű31 (1968).

[19] A. Kucuk,A.G. Glare, L.E. Jones, *Glass Science and Technology*, **73** 5, 123-129 (2000).

[20] H.M. Princen, *Journal of Colloid Science*, **18** 2, 178 (1963).

[21] G. Debregeas, P.G. de Gennes, F. Brochard-Wyart, *Science*, **279** 5357, 1704-1707 (1998).

[22] F. Seychelles, Y. Amarouchene, M. Bessafi, H. Kellay, *Physical review letters*, **100** 14, 144501 (2008).

[23] A. Fluegel, D.A. Earl, A.K. Varshneya, T.P. Seward, *Phys. Chem. Glasses : Eur. J. Glass Sci. Technol. B*, **49** (5), 245Ű257 (2008). http ://glassproperties.com/density/GlassMeltDensityCTECalc.xls.

[24] J.C. Bird, R. de Ruiter, L. Courbin, H.A. Stone, *Nature*, **465** 7299, 759-762(2010).

Regular Article

**THE EUROPEAN
PHYSICAL JOURNAL E**

Permeability of aqueous foams

E. Lorenceau[a], N. Louvet, F. Rouyer, and O. Pitois

Université Paris-Est, Laboratoire de Physique des Matériaux Divisés et des Interfaces, UMR 8108 du CNRS, 5 Boulevard Descartes, 77 454 Marne-la-Vallée cedex 2, France

Abstract. We perform forced-drainage experiments in aqueous foams and compare the results with data available in the literature. We show that all the data can be accurately compared together if the dimensionless permeability of the foam is plotted as a function of liquid fraction. Using this set of coordinates we highlights the fact that a large part of the published experimental results corresponds to relatively wet foams ($\varepsilon \sim 0.1$). Yet, most of the foam drainage models are based on geometrical considerations only valid for dry foams. We therefore discuss the range of validity of the different models in the literature and their comparison to experimental data. We propose extensions of these models considering the geometry of foam in the relatively wet-foam limit. We eventually show that if the foam geometry is correctly described, forced drainage experiments can be understood using a unique parameter —the Boussinesq number.

PACS. 47.56.+r Flows through porous media – 47.57.Bc Foams and emulsions – 68.03.Cd Surface tension and related phenomena

1 Introduction

The complex rheology of foams and the few quantity of liquid that they contain make them interesting materials for various industrial applications. For example, they appear as alternative ecological materials to classical liquids for decontamination of radioactive tank [1]. In this context of sustainable development, it is important to know how the liquid phase flows within the porous skeleton made of bubbles to transport the required active agents. Yet, liquid foams are different from classical porous materials: the dispersed matrix is not rigid and can deform. As a consequence, the local liquid content is not constant and can adjust under external conditions. For example, due to the large density contrast between the gas and the liquid phase, the continuous phase irreversibly flows under gravity. This process is called drainage. Drainage has been extensively studied in the situation of forced-drainage experiment where a constant flux of liquid is added at the top of uniform dry foam. As a result, a uniform liquid front invades the foam and its velocity of impregnation is measured as a function of the liquid flow rate. This geometry is of peculiar interest in the framework of porous media: forced-drainage experiments indeed mimic the experimental measurement of the permeability of classical porous media [2].

Within the last twenty years, a large number of experimental [3–14], numerical [15,16] and theoretical works [17–21] have been devoted to forced drainage. The velocity of foam drainage is a balance between gravity and the viscous bulk shear dissipation in the fluid network (the Plateau borders or the nodes) as in classical porous material. Note that, while some experimental results are often associated with one of the limiting cases corresponding to dissipation in Plateau border or in nodes, most of the real measurements are in between. Yet, for aqueous foams, the precise knowledge of the viscous shear dissipation is not easy to determine. Indeed, the boundaries between the dispersed and liquid phases are liquid/air interfaces edged with surfactants. These can flow with the liquid phase, thus the velocity at the interface does not necessarily vanish. Therefore, to understand foam drainage, the rheology of the monolayer of surfactants at the liquid air/interface due to the liquid flow must be taken into account. So far, two main behaviours have been exhibited. While non-mobile surfactants are static and impose a vanishing velocity at the rigid interface, mobile surfactants flow with the liquid phase. The velocity profile within the Plateau borders cross-section of foam made with non-mobile surfactants is Poiseuille-like and the one of mobile surfactants is close to a plug flow [22,23]. The viscous bulk dissipation associated with these two velocity profiles are different, the first one being much more dissipative than the second one, thus leading to different kinetics of drainage. It has

also been shown that mobile surfactants associated with cosurfactants can exhibit rigid-like behaviour [12,24–27]. Despite the large number of experiments and the impressive theoretical framework devoted to drainage [3–27], several questions remain open.

First, foams of small bubbles made out of mobile surfactants exhibit unexpected behaviour. The surface mobility of foams has been observed to continuously decrease with the bubble diameter until a critical diameter of 500 μm is reached. Below this critical diameter, the surface mobility increases again. This is quite unexpected since the drainage of foam of bubbles larger than 500 μm with the same surfactants is in agreement with theory [7].

Then, experiments often report a front velocity significantly larger than what is predicted by theory: the velocity front has been observed to scale with the flow rate power 0.55 which is significantly larger than the value 0.5 predicted by theory [7,10,12] and present paper.

Last, so far no consensus has been reached for the value of the hydrodynamic resistance of a node: when compared altogether, the available values for the hydrodynamic resistance of a node span over more than one order of magnitude as discussed in [28].

To address these points, we present new data of forced foam drainage experiments and compare them with experimental results from the literature. For each set of data, we extract the permeability of the foam normalized by the square of bubble diameter and report it as a function of the liquid fraction. Indeed, it is a classical feature of porous materials to characterize a media studying the permeability as a function of the liquid fraction [2], and this has been successfully applied to aqueous foams [5,7–30]. We show that the discrepancy observed between experiments and theory can be explained considering the evolution in foam geometry with increasing liquid fraction.

2 Experimental set-up

We perform forced-drainage experiments using two different foaming solutions. To obtain the foam, we release into the aqueous solutions a slow flow of C_6F_{14} gas either through a blunt-end syringe needle or through a porous glass frit. The foam shows no sign of coarsening over the course of a day.

To measure the diameter of the bubbles we sample tens of bubbles, squeeze them between two glass plates separated from 100 μm and measure the surface exposed with a microscope. Using volume conservation, we calculate the volume of gas inside the bubble and the diameter D_b of the bubble. This method ensures a very good precision over the measurement of the bubbles diameter.

Typically, the standard deviation of the bubbles distribution is less than 4% when the foam is produced with a needle. The foam obtained from the porous glass frit is less regular with a typical standard deviation of 18%.

To perform the forced drainage experiment, the foam is put inside a Perspex tube. We use two different cylindrical tubes, respectively, 50 and 60 cm long with a section S of 22.90 and 8.81 cm² cross-section areas. We make sure that the section of the tubes contains at least 20 bubbles. The bottom of the tube is in contact with the foaming solution via the glass frit or the needle and the top of the tube is open. The foaming solution is composed of distilled water and surfactants. We used TTAB (TetradecylTrimethylAmmonium Bromide) at 3 g/L which is well above the CMC of 1 g/L. It is used pure or mixed with dodecanol at concentration 0.2 g/L. All the surfactants were purchased from Aldrich and used as received. The foaming solution has a surface tension $\gamma = 38 \pm 1$ mN/m, a viscosity $\eta = 1$ mPa s and a density $\rho = 1000$ kg/m³.

Prior to any measurement, we wait for twenty minutes for the foam inside the solution to reach static equilibrium. This ensures a very dry, well-drained foam with no sign of evolution. This equilibrium being reached, a constant flux of the soap solution Q is added at the top of the foaming tube. Typically, Q ranges from 0.1 to 50 mL/min. The foam is uniformly illuminated from one side and a digital camera with a field of view of 20 cm by 10 cm records the transmitted light at a frame rate of 10 images/second. Wet foams transmit less light than dry foams, so the camera easily detects the liquid velocity v_l in the laboratory frame. The bottom of the foam column —in contact with the rigid glass frit or with the needle— is static, thus, as liquid is introduced in the top of the column, the foam expands and the bubbles move up. We measure the ascending velocity of the bubble U and eventually deduce the front velocity v_f —that is the liquid velocity in the frame of the bubbles— from v_l and U using $v_f = v_l + U$. We also make sure that the upward motion of the foam is indeed due to expansion as liquid is introduced at the top of the column checking that $U = Q/S$.

3 Results and comparison with the literature

3.1 Experimental results

To analyze our data and compare them with existing results from the literature, we calculate the liquid fraction ε and the macroscopic permeability k of the foam. The use of the macroscopic permeability k and the liquid fraction ε is a classical feature of porous media [2] and has been recently proved to be also accurate for aqueous foam in [5,7–30]. ε, defined as the volume of liquid in a macroscopic foam region divided by the total volume of the same region, is given by

$$\varepsilon = \frac{Q}{S v_f}. \quad (1)$$

Then, we extract the permeability k of the foam using the following relation defined by Darcy for gravity driven flow through porous media [2]:

$$\rho g = \eta \frac{Q}{kS}. \quad (2)$$

Note that the above definition of the permeability differs from the microscopic permeability reported in [5,6].

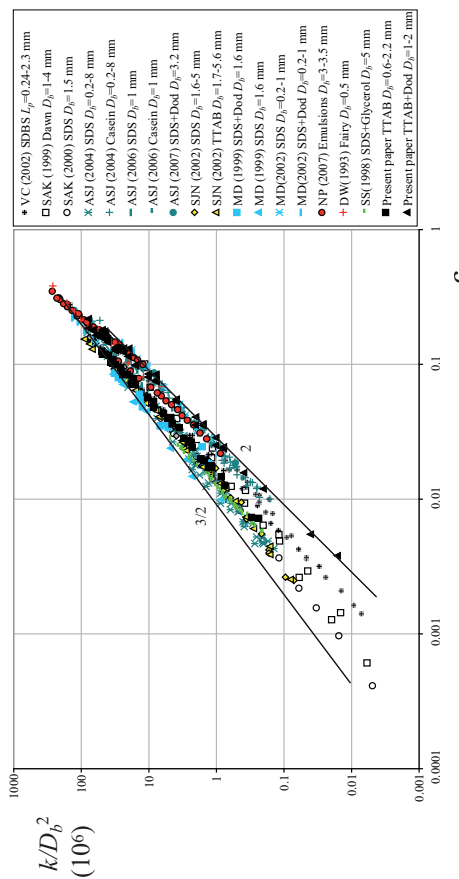a e-mail: elise.lorenceau@univ-mlv.fr

---

Fig. 1. Foam permeability scaled with the square of the bubble diameter as a function of the liquid fraction. Closed symbols: TTAB+dodecanol foam ($C_{TTAB} = 3$ g/L), open symbols: TTAB+dodecanol foam ($C_{TTAB} = 3$ g/L, $C_{dodecanol} = 0.2$ g/L). The two dashed lines of exponents 2.2 and 1.5 illustrate that there is not a unique power law between k/D_b^2 and ε.

Legend:
- ◆ D_b = 2.2 mm (TTAB)
- ■ D_b = 2.0 mm (TTAB)
- ■ D_b = 1.9 mm (TTAB)
- ◇ D_b = 1.3 mm (TTAB)
- ● D_b = 1.2 mm (TTAB)
- ✕ D_b = 1.1 mm (TTAB)
- ▲ D_b = 0.68 mm (TTAB)
- ○ D_b = 2.0 mm (TTAB+Dod.)
- △ D_b = 1.0 mm (TTAB+Dod.)

We scale the permeability with the square of the bubble only characteristic length of the system $-D_b$ the bubble diameter—and reported k/D_b^2 in a logarithmic scale in Figure 1 as a function of the liquid fraction ε.

We observe in Figure 1 that the permeability of the foam is, as expected, an increasing function of ε: as the liquid fraction increases, the foam dampens and the typical dimensions of the foam network change. We also see that all our data collapse on two different curves —corresponding to the two different solutions— whatever the diameter of the bubbles. While the two curves are well separated at low liquid fraction (the permeability of the TTAB foam is four times larger than the permeability of the TTAB+dodecanol foam at $\varepsilon = 0.01$), they get closer when $\varepsilon \sim 0.1$.

This experimentally shows that, within the range of D_b and ε investigated, the dependency of the permeability with the bubble diameter is only D_b^2. Additionally, we notify that, for a given soap solution, different ranges of liquid fraction are investigated when D_b is changed; a careful look at the data shows that the curves corresponding to different bubbles diameter do not cover the same range of ε. Indeed, due to experimental constraints (limited range of flow rate investigated), the smaller the bubbles, the wetter the foam.

The good collapse of the data confirms that k and ε are useful to characterize aqueous foam. Yet, it has been recently proposed by Stevenson [29,30] that the dimen-

sionless permeability should scale with a unique power of the liquid fraction ($k/D_b^2 \sim \varepsilon^a$) for any value of ε. We observe in Figure 1 that this proposition is not verified; the two dashed lines do not fit the data on the whole range of liquid fraction investigated. Obviously, as already mentioned in the introduction and proved by previous authors [3–12], the permeability of the foam is strongly dependent on the mobility of the surfactants that stabilized the interface. Even for a given soap solution, the foam permeability cannot be described using a unique power law.

3.2 Comparison with results from the literature

Using the same set of coordinates (ε, k/D_b^2) we compare our results with other data points extracted from the literature on forced drainage experiments in Figure 2. All the reported data concern foam drainage except for the set of data labelled {NP (2007) Emulsions $D_b = 3-3.5$ mm} that concern the drainage of oil in water emulsion. Note also that the data labelled {ASJ (2007) SDS+Dod $D_b = 3.2$ mm} correspond to microgravity experiments. We only report forced-drainage data from works where the bubble diameter, radius or the parietal Plateau border length L_p was explicitly mentioned. To obtain the bubble diameter from the Plateau border length, we divide L_p by 1.2 as suggested in [31]. We experimentally validate this value within 5%.

Legend:
- ∗ VC (2002) SDBS L_p=0.24-2.3 mm
- □ SAK (1999) Dawn D_b=1-4 mm
- ○ SAK (2000) SDS D_b=1.5 mm
- ✕ ASJ (2004) SDS D_b=0.2-8 mm
- + ASJ (2004) Casein D_b=0.2-8 mm
- – ASJ (2006) SDS D_b=1 mm
- – ASJ (2006) Casein D_b=1 mm
- ● ASJ (2006) Casein D_b=1 mm
- ◆ ASJ (2007) SDS+Dod D_b=3.2 mm
- ◇ SJN (2002) SDS D_b=1.6-5 mm
- ■ SJN (2002) TTAB D_b=1.7-5.6 mm
- ■ MD (1999) SDS+Dod D_b=1.6 mm
- ▲ MD (1999) SDS D_b=1.6 mm
- ✕ MD(2002) SDS D_b=0.2-1 mm
- — MD(2002) SDS+Dod D_b=0.2-1 mm
- ● NP (2007) Emulsions D_b=3-3.5 mm
- + DW (1993) Fairy D_b=0.5 mm
- ■ SS(1998) SDS+Glycerol D_b=5 mm
- ■ Present paper TTAB D_b=0.6-2.2 mm
- ▲ Present paper TTAB+Dod D_b=1-2 mm

Fig. 2. (Colour online) Permeability of the foam scaled with the square of bubbles diameter k/D_b^2 as a function of the liquid fraction ε. The different symbols correspond to different experiments with different bubbles sizes and foaming solutions. The legend should be understood as follows: the letters are the initial of the first author followed by the year of publication of the work. Then, the surfactant used (SDS stands for Sodium DodecylSulfate, Dod for Dodecanol, TTAB for TetradecylTrimethyl-AmmoniumBromide) is indicated and finally the diameter range of the bubbles is given. The data of Figure 1 appear in full black square and full black triangles. The two lines show the slope of the two-power laws expected by the node-dominated and the channel-dominated models presented in Section 4.
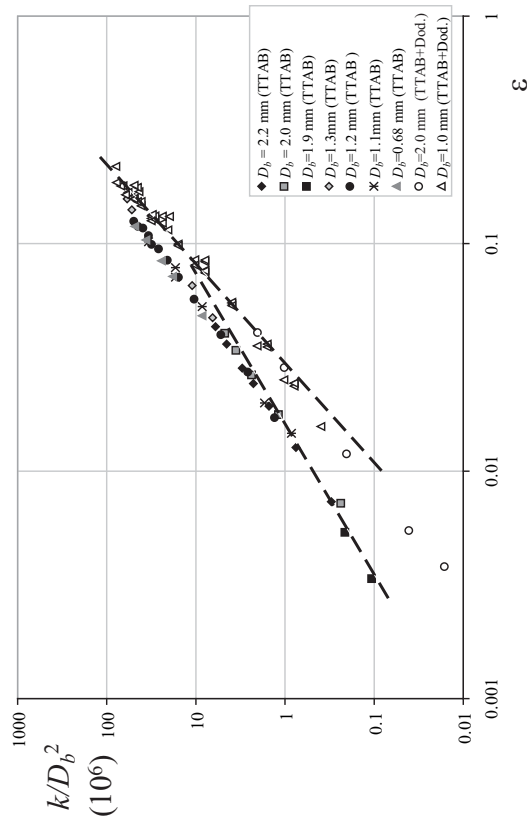
We observe in Figure 2 that forced-drainage experiments have been carried out on a wide range of liquid fraction: from $\varepsilon = 0.0004$ up to $\varepsilon = 0.25$. The same trends as in Figure 1 can be seen: for $\varepsilon < 0.01$, the scaled permeability strongly varies with the foaming solution and spans over one order of magnitude. However, for $\varepsilon > 0.1$, the data concerning different surfactants tend to get closer and overlap onto a single curve. We also stress that the set of data presented in Figure 1 is perfectly representative of the two extreme behaviours of rigid and mobile surfactants.

We also show two limiting curves that appear in black in Figure 2. The slope of the upper line is 3/2 while it is 2 for the lower line. These two exponents correspond, respectively, to the exponents predicted by the node-dominated and the channel-dominated models discussed in the following section. We observe that the exponent 2 of the channel-dominated model describes quite well the data of references [6,8,14] up to $\varepsilon = 0.1$. At higher liquid fraction, the exponent is 2.2 before decreasing again to 1.7.

4 Existing models for foam permeability

In this section, we give an overview of the different models of drainage that can be found in the literature. Most of the studies concerning forced drainage experiments aim to explain the non-linear power law between the front velocity v_f and the flow rate $Q(v_f \sim Q^\alpha)$, or the front velocity v_f and the liquid fraction $\varepsilon(v_f \sim \varepsilon^\beta)$.

The liquid phase in foam can be distributed within different elements. Indeed, aqueous foams are constituted of i) soap films ii) liquid channels, known as Plateau borders, where three films meet, iii) vertex or nodes where four Plateau borders meet. We denote as r the radius of the Plateau Border and r_c its minimum value. L is the length of the Plateau border and L_{nn} the minimum node to node distance. D_b refers to the bubble diameter. For

A careful look at the data from [3,4,10,12] demonstrate that—within experimental uncertainties on the diameter of the bubbles varied within a factor of 10— the permeability varies with the bubble diameter as D_b^2. This is in agreement with the data of Figure 1 but differs from what is published in [7], where a variation of the front velocity with the diameter of the bubbles more complex than D_b^2 is observed. However, as the correspondence between the front velocity and the bubble diameter is not explicitly reported in the experimental data of [7], we are not able to check the proposed dependence in Figure 2 (unfortunately, the authors were not able to give us the corresponding information). We still add these experimental data in Figure 2, adjusting the diameters of the bubbles as best as we can within the experimental errors on the bubble diameter reported in [7] in the order of 30%.

Fig. 3. a) Kelvin cell in the dry limit. b) Two nodes and a Plateau border in the wet limit.

the sake of clarity, the Plateau borders will be referred to as PB in the following.

We recall that all the models for forced foam drainage considered the simplest idealized monodisperse foam structure, the Kelvin foam, constituted of regular tetrakaidecahedral bubbles (called Kelvin cells) organised in a bcc lattice. We display in Figure 3 a Kelvin cell obtained in the dry limit using Surface evolver software [32] and a Plateau border in the wet limit.

4.1 Dry-foam models

We first describe drainage models where dry foams are constituted of long and slender PB. Before describing the different models, we recall several features of dry foams ($\varepsilon < 0.01$) which are commonly used in the different models described in this section.

In this limit of dry foam, several quantities match: $r = r_c$, and $L = L_{mn}$. Then, neglecting the volume of the nodes, there is a simple relation between ε, r and L:

$$\varepsilon = \frac{12(\sqrt{3} - \pi/2)r_c^2 L_{mn}}{27^{1/2}L_{mn}^3} = 0.171\frac{r_c^2}{L^2}. \quad (3)$$

The accuracy of this expression can be evaluated. Indeed, the complete relation that includes the nodes volume —given in Section 4.2— has been computed up to $\varepsilon = 0.1$ (see Eq. (8)). The error committed using equation (3) rather than equation (8) is less than 25% if $\varepsilon < 0.02$. Thus, any model using equation (3) rather than (8) is reasonably accurate up to $\varepsilon = 0.02$.

The last point worth noting in the dry-foam limit is that L_{mn} and D_b are proportional. For Kelvin foam, it yields

$$D_b = 2.78 L_{mn} = 2.78 L. \quad (4)$$

In a pioneer work [3], Weaire et al. proposed a model for dry foams to explain their experimental observations where $\alpha = 0.5$. They considered the viscous dissipation in a network of long and slender PB. Assuming a quasi-Poiseuille flow and rigid interfaces in the section of the PB, yields $v_f \sim \rho g r^2/\eta$. Using equations (2) and (3), it comes

$$k = 8.5 \, 10^{-4} \varepsilon^2 D_b^2. \quad (5)$$

The permeability in equation (5) varies with ε^2, which is in very good agreement with the TTAB+dodecanol data in Figure 1 and the data labelled {ASJ (2004) Casein $D_b = 0.2\text{-}8$ mm, ASJ (2007) SDS+Dod $D_b = 3.2$ mm, NL(2008) TTAB+Dod $D_b = 1\text{-}2$ mm} in Figure 2. The numerical coefficient of equation (5) is related to the peculiar shape of the PB cross-section. We observe that the corresponding equation, which is plotted in Figure 4 from $\varepsilon = 0.001$ up to $\varepsilon = 0.02$ systematically underestimates the permeability of all the experimental data. Indeed, as proved later by Koehler et al., the flow profile is never a real Poiseuille [22]. Yet, it correctly describes the variation of the permeability with the liquid fraction for rigid surfactants. This model is usually referred to as *channel dominated*.

Then, considering that dissipation occurs in the different constitutive elements of the foam, the nodes and the channels, Koehler et al. proposed a different interpretation of new forced-drainage experiments [5,6]. Indeed, they observe an exponent $\alpha = 0.4$ quantitatively different from $\alpha = 0.5$ reported by Weaire. In the case of mobile surfaces, the flow in the long and slender channels is nearly plug-like and exhibits no viscous dissipation. In that case, the flow is *node-dominated* and the permeability given by

$$k = 6.7 \, 10^{-4} \varepsilon^{3/2} D_b^2. \quad (6)$$

The numerical coefficient in equation (6) is deduced from Koehler's results after a correction to convert the Plateau border length into bubble diameter. Equation (6) —plotted in Figure 4— describes quite well the experimental data corresponding to a mobile surfactant for ε between 0.001 and 0.02. However, it gives no insight on the permeability above $\varepsilon = 0.02$ for mobile surfactant.

To quantify the transition between the *node-dominated* regime and the *channel-dominated* limit, one can use the analytical or numerical results of [15,20,21] where the flow in a single PB with interfaces that are neither perfectly rigid nor perfectly mobile is considered. To quantify the coupling between bulk and surface shear flows, the surface shear viscosity and Bo are introduced and the variation of the average velocity of liquid with Bo is calculated. For high value of Bo (low surface mobility), the flow is Poiseuille like, the interfaces do not flow and the average velocity does not depend on Bo. Yet, as Bo decreases, the average velocity increases and eventually reaches a regime where it scales with $(Bo)^{-1/2}$ [15]. Following previous approaches [10,6], Saint-Jalmes et al. [7] quantify the transition between the *node-dominated* regime and the *channel-dominated* regime. To describe the experimental data, they consider the association in series of a 1/2 node and a Plateau border. The front velocity therefore depends on both the permeability of the channel and the node. The key point is that the permeability of the channels and the nodes are not constant and both depend *a priori* on Bo. While Leonard and Lemlich calculation [20] predicts the variation of the channel permeability with Bo, there is yet no model describing how the node permeability evolves with Bo. The node permeability K_n is thus set constant.
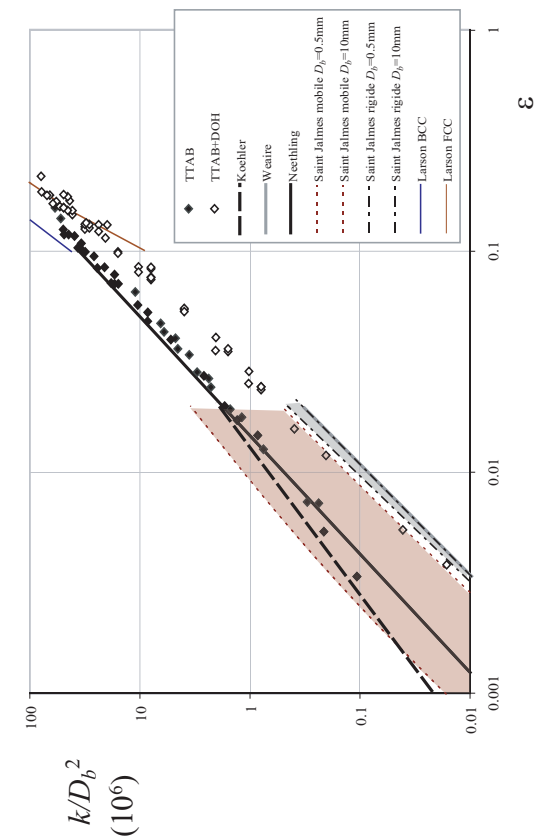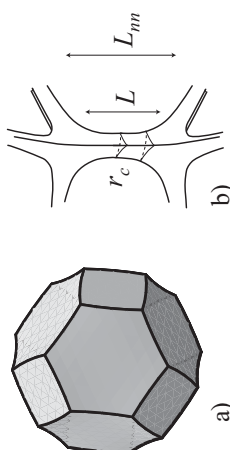
Fig. 4. (Colour online) Experimental data of Figure 1 and the different models discussed in Section 4. The two shaded regions correspond to the range of validity of the model described in [7] for bubbles with diameters between 0.5mm and 10mm.

In this framework, the permeability is given by the following relation:

$$k = \frac{1}{2.78^2} \frac{\varepsilon^2 D_b^2}{\dfrac{1}{K_c^0(1+2.48\frac{1}{Bo})} + \dfrac{\sqrt{\varepsilon}}{K_n}}, \quad (7)$$

where $K_c^0 = 6.6 \cdot 10^{-3}$ is determined from numerical calculation in [15], a single value of $K_n \sim 3 \cdot 10^{-3}$ is deduced from the experiment and $Bo = 1.1\eta_s/\eta D_b\sqrt{\varepsilon}$ for all ε investigated.

At high value of Bo ($Bo > 10$) and low liquid content (*i.e.* when the first term of the denominator of Eq. (7) dominates over the second) the flow is Poiseuille-like and the permeability is given by the channel permeability (first term of the denominator). k is given by equation (5) again, except for a small variation due to Bo.

At low value of Bo ($Bo < 0.25$) and high liquid content, the permeability is only given by the node and within experimental errors an expression similar to equation (6) is found.

For intermediate values of Bo, the two elements should be taken into consideration for the calculation of the permeability. The permeability scales with the liquid fraction like $k \sim \varepsilon^\delta$, with $1.5 < \delta < 2$, but in this model, its variation with the bubble diameter D_b is more complicated than just D_b^2, as can be seen in equation (7). The largest deviation from D_b^2 scaling is expected for low Bo (rigid interface).

To determine whether the drainage is channel-dominated, node-dominated or both, the authors measure the exponent α. The relative dissipation between the PB and the nodes is obtained from comparison between α and the theoretical value: if $\alpha < 0.36$, the dissipation is node-dominated, $\alpha > 0.42$ it is channel-dominated and when $0.36 < \alpha < 0.42$ both the node and the channels are taken into account. In this model, a unique mean value of surface viscosity η_s and of the node permeability K_n —characteristic of a given foaming solution— are extracted for a range of ε that typically varies within one order of magnitude. Equation (7) is plotted in Figure 4 for casein and SDS foams, the two different foaming solutions used and for the range of bubble diameter D_b investigated in [7]. For the sake of clarity, we delimit these two zones in shaded. We note that the region corresponding to casein foam is quite narrow, but the region corresponding to SDS foams is very broad, thus illustrating the complex variation of the permeability with the bubble diameter in this framework.

While this model has been compared to an impressive set of data, the following points are worth noting: i) The model is unable to describe the drainage of foams made of bubbles smaller than 0.5 mm [7] (we stress that the drainage of these sizes corresponds to large value of ε typically $0.01 < \varepsilon < 0.2$ for casein foams and $0.005 < \varepsilon < 0.2$ for SDS foams). ii) The model attributes all the deviations from the theoretical exponent to variations in the Plateau border permeability only.

This induces that values extracted for surface viscosities η_s of identical foaming solutions vary with the range of ε studied. Thus, for a given solution, values of η_s that change by a factor 10 are reported (for the same SDS/dodecanol solution with a concentration of SDS of 10 g/L and DOH of 0.1 g/L, values of $1.8 \cdot 10^{-6}$ kg s^{-1} and $2 \cdot 10^{-7}$ kg s^{-1} are reported [7,33]). iii) Exponent $\delta = 2.18$, larger than 2, has been reported without any theoretical explanation. iv) Values extracted for the node permeability are ten times larger than what is predicted from numerical simulations and measurements at the microscale [28].

As will be discussed in Section 5, the discrepancies of points i), ii) and iii) can be clarified by considering appropriate foam geometry. Indeed, the liquid fraction of most of the experimental data presented in [7] is far larger than 0.02, yet, the connection between D_b and ε is made using equation (3), only valid in the limit of dry foams.

4.2 Wet foams

Several authors proposed a detailed model for foam drainage valid up to $\varepsilon = 0.1$ [4,10]. Prior to any modelling, foam geometry should be described with great care.

First, a relation between ε, L_{nn} and r must be given. Note that r is defined as the characteristic radius of curvature of the interface by $\gamma C = \gamma/r$, where C is the curvature of the interface. Such a relation has been computed for Kelvin foams from $\varepsilon = 0.001$ up to $\varepsilon = 0.1$ with Surface Evolver [32,6].

$$\varepsilon = 0.171 \left(\frac{r}{L_{nn}}\right)^2 + 0.20 \left(\frac{r}{L_{nn}}\right)^3. \quad (8)$$

Using the same software, Phelan et al. provide an identical equation for any kind of crystallized foam up to $\varepsilon = 0.08$ [34]. In the limit of dry foams —where $r = r_c$ and $L = L_{nn}$— the second term is negligible and equations (3) and (8) are identical. Unlike other authors, Neethling et al. [10] or Carrier et al. [4] keep the two terms of the equation (8) in their models.

Neethling et al. [10] also take into account foam expansion during the drainage. As a consequence of this expansion, the relation between L_{nn} and D_b for wet foams also depends on ε:

$$f(\varepsilon) = \frac{D_b}{L_{nn}} = \left(\frac{6}{\pi}\right)^{1/3} \frac{1}{2^{7/6}(1-\varepsilon)^{1/3}}. \quad (9)$$

Equations (9) and (4) are identical for $\varepsilon = 0$. For $\varepsilon = 0.1$, the difference between equations (9) and (4) is of 4%. The combination of equations (8) and (9) leads to (10) linking the bubble and the liquid fraction:

$$\varepsilon = 1.327 \left(\frac{r}{D_b}(1-\varepsilon)^{1/3}\right)^2 + 4.321 \left(\frac{r}{D_b}(1-\varepsilon)^{1/3}\right)^3. \quad (10)$$

Eventually, one should also consider the evolution of the relative extension of the PB and the node. Indeed, the wetter the foam, the wider the node and the shorter the PB. Several authors [4,10,34] therefore state the following relation between L the PB length, L_{nn} and r:

$$L = L_{nn} - \xi r, \quad (11)$$

where ξ is a numerical constant. ξ is evaluated either considering that at close-packed limit (i.e. for $\varepsilon = \varepsilon_{fcc}$) the lengths of the PB vanish —yielding $\xi = 1.588$— [10] or computing the foam geometry with Surface Evolver —yielding $\xi = 1.50$ [34]— or from geometrical considerations —yielding $\xi = 2.31$ [4].

The geometry of the foam being clearly identified, Neethling et al. or Carrier et al. consider the association in series of a PB and a node as proposed in [10,4]. In particular, the model proposed by Neethling et al. was experimentally verified for two types of mobile surfactants and various bubbles sizes. The typical permeability of a node extracted from their experiments is in good agreement with numerical predictions and measurement at the node scale [28]. This model, plotted in Figure 4, describes well the experimental data obtained with TTAB for ε between 0.001 and 0.1. Nevertheless, despite this useful work, the model of foam drainage as described by Neethling et al. still lacks several issues: i) the surface rheology of surfactants is not considered; ii) it is useless for foam with liquid fraction larger than $\varepsilon = 0.1$ due to the limited range of validity of equation (8). Yet, as can be seen in Figure 2, an important part of the experimental data corresponds to $\varepsilon > 0.1$.

Forced foam drainage experiments of wet foam can also be described using numerical calculations of permeability for a periodic grain model of porous media proposed by Larson et al. [35] in the limit of rigid interfaces. In this work, the radius of the solid spheres is allowed to increase past the point of touching, thus mimicking the facets of bubbles. The overlapping spheres then form a medium with liquid fraction that can vary between 0 and the closed-packing value. This geometry specification describes quite well wet foam near the close-packing limit, however, in the dry limit it ensures that PB cross-sections are enclosed by three circular arcs that are not always tangent but instead exhibit a non-zero contact angle θ. A typical value of θ extracted from Larson model in the dry limit is 25° for $\varepsilon = 0.05$. Variations of contact angle, which have been observed experimentally (so far, values up to $\theta \sim 10°$ have been reported [36]) are known to influence drainage velocity [37]. Yet, the 25° value due to the geometrical assumption of Larson is far too large to be compatible with the experimental observations. We therefore only use Larson's results for ε between 0.1 and the close-packing liquid fraction. Three different lattices, simple cubic (sc), face centred cubic (fcc) and body centred cubic (bcc) are investigated. We extract the permeability as defined in equation (1) and the liquid fraction using the calculation provided in [13] for fcc and bcc lattices. The corresponding results are plotted in Figure 4. Both, the fcc and bcc curves are in reasonable agreement with the TTAB+DOH data and TTAB data for $0.12 < \varepsilon < 0.26$. We stress that this good accuracy is obtained without any adjustable parameter.

Fig. 5. Typical radius of curvature of the foam scaled with the bubble diameter as a function of the liquid fraction.

5 Discussion

Since the range of liquid fraction investigated in foam drainage experiments is quite large (from 0.0005 up to 0.25), and that current foam drainage models are relatively efficient for low ε, we propose to extend these models to wet foams by precisely describing wet-foam geometry. We show that these modifications allow us to fit experimental data over the whole range of ε.

5.1 Foam geometry

5.1.1 Curvature of the interfaces

Another approach to simulations performed with Surface Evolver presented in equation (8) consists in considering the osmotic pressure Π, which is the pressure difference between the atmosphere P_0 and the pressure in the liquid phase P_l. It can be expressed using the pressure difference between the liquid phase P_l and the bubble P_b:

$$\Pi = P_0 - P_l = (P_0 - P_b) + (P_b - P_l) = (P_0 - P_b) + \frac{\gamma}{r}. \quad (12)$$

We recall that in equation (12) r is defined as the characteristic radius of curvature of the interface by $\gamma C = \gamma/r$, where C is the curvature of the interface.

In wet foams ($\varepsilon > 0.1$), the bubbles are nearly spherical, hence $P_b - P_0 \cong 4\gamma/D_b$. In drier foams, $P_b - P_0$ is unknown. Yet, the appearance of flat films between different bubbles —that corresponds to a surface energy decrease— leads to an increase of the radius of curvature of the bubbles. Hence, $P_b - P_0 \leq 4\gamma/D_b$. This yields

$$\frac{r}{D_b} \geq \frac{1}{4 + \Pi D_b/\gamma}. \quad (13)$$

The two terms of equation (13) are strictly equal for foams at a liquid fraction near the random close-packing liquid fraction. The second term of equation (13) therefore gives a good approximation of r/D_b in the limit of wet foams. It is obviously less accurate for dry foams. Yet, when the PB are long and slender it has rigorously been shown that $P_b - P_0$ is negligible and that $r/D_b = \gamma/\Pi D_b$ [38].

Much work has been devoted to osmotic pressure; expressions for osmotic pressure in the wet and dry limits have been deduced from theoretical considerations. Experimental or numerical data on polydisperse, monodisperse emulsions and monodisperse foams can also be found [38-43]. For intermediate values of ε (in the range [0.005; 0.26]), a recent paper provides a useful empirical relation for the reduced osmotic pressure $\tilde{\Pi} = D_b \Pi/(2\gamma)$ based on experiments on monodisperse foams and numerical simulations [43]

$$\tilde{\Pi} = 7.3 \frac{(\varepsilon - \varepsilon_{fcc})^2}{\sqrt{\varepsilon}}. \quad (14)$$

In equation (14), the osmotic pressure vanishes for $\varepsilon = \varepsilon_{fcc} = 0.26$. Indeed at this liquid fraction, the monodisperse bu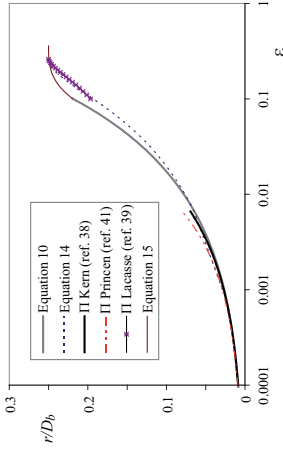bbles that are arranged in a fcc structure cease to touch each other, and the pressure in the liquid reaches the atmospheric pressure (provided that gravity can be neglected). This collapse at $\varepsilon = \varepsilon_{fcc} = 0.26$ is inadequate in the context of foam drainage where the bubbles are polydisperse, yet, as can be seen in [43], the expression given in (14) also describes osmotic pressure data concerning polydisperse emulsions up to $\varepsilon = 0.2$. A more accurate expression would provide that Π vanishes at the random close-packing liquid fraction, i.e. for $\varepsilon = \varepsilon_{rep} = 0.36$.

In Figure 5, we plot the characteristic radius of curvature scaled with the diameter of the bubbles (obtained from different expressions of osmotic pressure) as a function of the liquid fraction in their range of validity. For comparison, we also add relation (10) in Figure 5.

There is a good agreement between the different expressions for $\varepsilon < 0.05$. Above this value, relation (10) and the relation obtained from relations (12) to (14) significantly differ. To obtain an expression valid in the full range of investigated liquid fraction, we propose to use relation (10) on its whole domain of validity, i.e. for $\varepsilon < 0.1$ and to extend it with an empirical function of the same type as equation (14). This empirical function should ensure i) continuity with relation (10) in $\varepsilon = 0.1$; ii) continuous differentiation with relation (10) in $\varepsilon = 0.1$; iii) that $r = D_b/4$ in $\varepsilon = 0.36$; iv) a horizontal tangent in $\varepsilon = 0.36$. These different conditions yield

$$\varepsilon = 1.327 \left(\frac{r}{D_b}(1-\varepsilon)^{1/3}\right)^2$$
$$+ 4.321 \left(\frac{r}{D_b}(1-\varepsilon)^{1/3}\right)^3, \quad \varepsilon \leq 0.1,$$
$$\frac{r}{D_b} = \frac{1}{4 + \tilde{\Pi}}, \quad \text{with } \tilde{\Pi} = 1.196 \frac{(\varepsilon_{rep} - \varepsilon)^3}{\varepsilon^{1.43}},$$
$$0.1 \leq \varepsilon \leq 0.36. \quad (15)$$

Equation (15) is plotted in Figure 4. It is quite difficult to find analytical solutions for the first part of equation (15), but the problem can be solved numerically. We call g the implicit function $r/D_b = g(\varepsilon)$ for $\varepsilon < 0.36$.
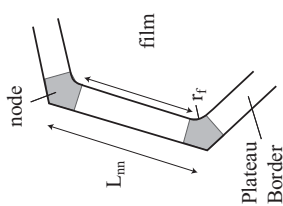
Fig. 6. Sketch of a film edged by nodes and Plateau borders.

5.1.2 Plateau border and node lengths

As liquid fraction is increased, the typical extension of the different constitutive elements of the foam varies. In particular, during the foam impregnation, the length of the PB, L, decreases while the size of the vertices increases.

To link these different lengths, we use equation (11) and propose to evaluate the parameter ξ from geometrical considerations. From the dry limit, the foam films area is known to shrink as the liquid fraction increases. A convenient way to describe this evolution is to expand the straight PBs overlapping the films over a distance equal to $2r/3$. This results in a homothetic reduction of the films except the rounded PBs joining areas defining the nodes, with a radius $r_f = xr$ (see Fig. 6). Following this description, it can be verified that the PB lengths become $L_h = L_{mn} - \frac{2r}{\sqrt{3}}(x+\frac{2}{3})$ and $L_s = L_{mn} - 2r(x+\frac{2}{3})$ for hexagonal and square faces, respectively. The evaluation of the PB shortening then requires the parameter x to be determined. A logical way is to adjust x in order to cancel L_s at the known stability limit of the bcc structure, that is $\varepsilon \approx 0.065$ [23]. This is obtained for $x = 0.34$ (using Eq. (7)), and the resulting PB lengths are $L_h = L_{mn} - 1.15r$ and $L_s = L_{mn} - 2r$. Considering the 8 hexagonal and 6 square faces of the Kelvin cell, an average PB length can be defined as $L = L_{mn} - 1.5r$ and $\xi = 1.5$. As already mentioned in Section 4.2, this value is in close agreement with values reported in the literature [4,10,34].

5.2 Drainage model

To describe foam drainage, we consider —as previously done in most of the works concerning foam drainage [4, 6,7,10]— the pressure losses at the microscale in a foam network unit composed of 1 PB and $2 \times 1/4$ node. The length of this network unit is L_{mn}, the minimum node-to-node distance. The pressure loss over this unit writes as a function of the local flow rate q

$$\frac{\Delta P}{L_{mn}} = \frac{(R_c + R_n/2)}{L_{mn}}q,$$

where R_c and R_n are the resistances of the PB and of the node. Using equation (2), the macroscopic permeability is given by

$$k = \frac{\eta \varepsilon L_{mn}}{3(R_c + R_n/2)\delta_a r^2}. \tag{16}$$

To obtain equation (16), we average over all angles of the foam network unit in the foam which yields the factor 3. We also assume that the local flow rate is $q = \delta_a r^2 v_f$, where δ_a is a numerical constant equal to $\sqrt{3}-\pi/2$. We introduce the dimensionless resistances $\tilde{R}_c = r^4 R_c/\eta(L_{mn} - \xi r)$ and $\tilde{R}_n = r^3 R_n/\eta$. Analytical or numerical expressions of $\tilde{R}_c$ as a function of Bo have been proposed in different works [15,23]. We propose to use the analytical expression provided in [23]

$$\tilde{R}_c = \frac{1}{\delta_a^2}H(Bo)^{-1} = \frac{6}{\delta_a^2}\left(\sqrt{\frac{2}{Bo}}\arctan\left(\sqrt{\frac{1}{8Bo}}\right)\right.$$
$$\left. - \arctan\left(\frac{1}{2\pi Bo}\right) + \frac{3}{25}\right)^{-1}.$$

Using the functions f and g defined in equations (9) and (15), finally yields

$$\frac{k}{D_b^2} = \frac{\eta \varepsilon f(\varepsilon)g(\varepsilon)}{3\delta_a[\tilde{R}_n/2 + \delta_a^2 H(Bo)\left(\frac{f(\varepsilon)}{g(\varepsilon)} - \xi\right)]}. \tag{17}$$

Figure 7 shows the dimensionless permeability as a function of the liquid fraction, calculated with equation (17) for $Bo = $ constant, $\eta_s = $ constant and the experimental data of Figure 1. We set the value of ξ equal to 1.5 (see Eq. (11)) and $\tilde{R}_n$ equal to 750—whatever the value of Bo or η_s—in agreement with measurements at the microscale and numerical simulations [28]. We also plot two lines of slope 3/2 and 2 corresponding, respectively, to the slope of the node-dominated and channel-dominated regimes.

We first note that either the $Bo = $ constant or $\eta_s = $ constant fits exhibit an exponent far larger than 2 around $\varepsilon = 0.1$. This can be explained by geometry; when the length of the PBs decreases, the resistance due to PB vanishes and the global permeability jumps. As stressed in Section 4.1, these large values of the slope of the curves k/D_b^2 as a function of ε are in very good agreement with experimental data. We stress that a value larger than 2 in the exponent of the curve k/D_b^2 as a function of ε corresponds to a value larger than 0.5 in the curve front velocity as a function of flow rate. This feature does not contradict the channel-dominated model, which is only valid for dry foams.

Quite surprisingly, the fit of the data with $Bo = $ constant (Fig. 7a) is better than the one with $\eta_s = $ constant (Fig. 7b). It is especially true for data concerning the rigid surfactant which are perfectly fitted by equation (17) with $Bo = 5$ on the whole range of ε, while the accuracy between the mobile surfactant data and equation (17) is good provided that we choose $Bo = 0.3$. On the contrary, it seems impossible to fit the data on the whole range of ε with a unique η_s.
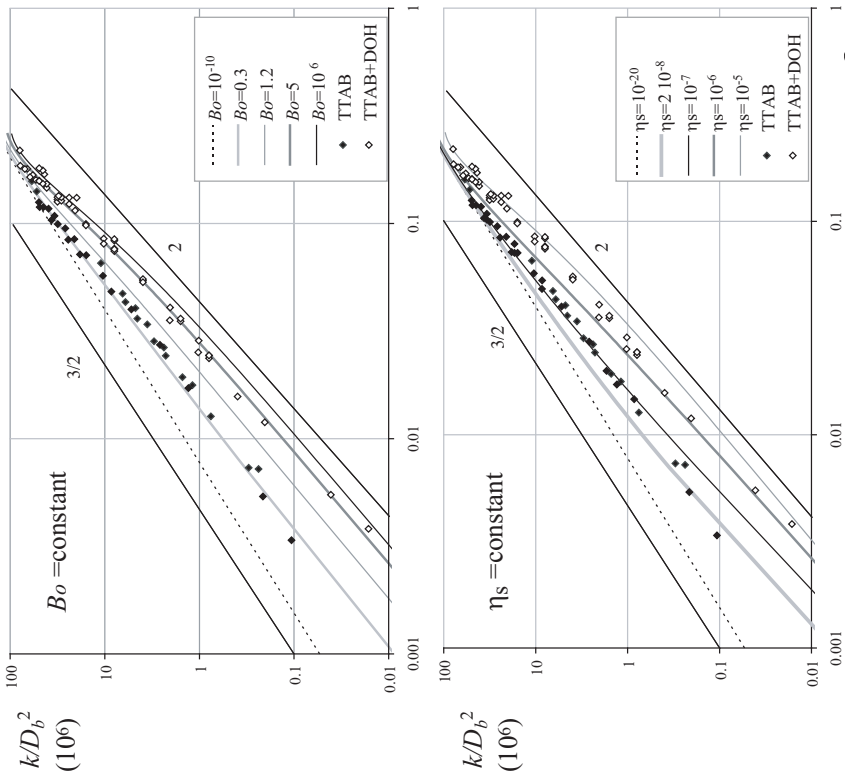
Fig. 7. Scaled permeability as a function of the liquid fraction calculated with equation (17) for $Bo = $ constant and $\eta_s = $ constant and the experimental data of Figure 1.

We also stress that the discrepancy between Figure 7a) and b) cannot be attributed to our geometrical extension of the expression of r/D_b for $0.1 < \varepsilon < 0.36$. Indeed, the results given by the $Bo = $ constant fit are already better than those given by the $\eta_s = $ constant fit for $0.01 < \varepsilon < 0.1$ where equation (9) is still valid. We do not state that the $Bo = $ constant fit is the best fit for the experimental data, but we just stress that the accuracy of the $Bo = $ constant fit is better than the one with $\eta_s = $ constant.

So far, we do not have any physical interpretation for the relative good accuracy between Figure 7a) and the experimental data. Indeed, as the foam is impregnated, r increases, thus Bo —that depends on r, η and η_s— should also vary and we would expect the fit with $\eta_s = $ constant to be more accurate. We believe that this trend is a signature of the complexity of foam hydrodynamics in the dry regime, either due to a non-Newtonian behaviour of the layer of surfactant mentioned in [26,27] —which would imply a non-constant value of η_s— or to variations of $\tilde{R}_n$ with ε described in [28], or to Marangoni flows in the vicinity of the PBs that modify the boundary condition in the corners of the PB section. The importance of this last effect is evaluated in details in [37].

The relatively good accuracy between the experimental data and the $Bo = $ constant fit is also reported in other

42. H.M. Princen, A.D. Kiss, Langmuir **3**, 36 (1987).
43. R. Höhler, Y. Yip Cheung Sang, E. Lorenceau, S. Cohen-Addad, Langmuir **24**, 418 (2008).
44. F. Carn, Ph.D. Thesis, University of Bordeaux I (2006).
45. M. Safouane, Ph.D. Thesis, University of Paris XI (2003).
46. S. Berg, E.A. Adelizzi, S.M. Troian, Langmuir **21**, 3867 (2005).
47. B. Martin, X.-L. Wu, Rev. Sci. Instrum. **66**, 5603 (1995).

systems. When the bulk viscosity η of a TTAB solution is increased by addition of glycerol or solid nanoparticles, the surface viscosity has been reported to increase as well, even without addition of any cosurfactants such as dodecanol [44,45]. This feature has also been reported in the drainage of soap films where the addition of glycerol to the SDS solution seems to slow the drainage [46] or in two-dimensional Couette cell [47]. This trend may therefore be quite general: it would be impossible to extract a single value of surface viscosity from any measurement since the value of surface viscosity would be specific of the particular experimental set-up and conditions used.

6 Conclusion

We perform forced-drainage experiments in aqueous foams and compare our results with experimental data from the literature. We plot the macroscopic permeability as a function of liquid fraction of the foam. Using this set of coordinates shows that a large number of experimental data published on foam drainage corresponds to relatively wet foams ($\varepsilon \sim 0.1$). Yet, these data are usually analyzed using a framework only valid for dry foams ($\varepsilon < 0.02$). We discuss the different models available in the literature and propose to extend these in the limit of wet foams. Then, comparing the models with the experimental data of permeability for foam made of a given foaming solution in a large range of liquid fraction, we demonstrate that it does not seem possible to extract a single value of the surface viscosity for a given foaming solution from drainage experiments. Indeed, we observe that a model based on a constant *Bo* number fits better the data than a model based on a constant η_s fit. We do not have any physical understanding of this effect, yet, we wonder whether it is linked to an inappropriate description of the coupling between the bulk and surface flows or not. The understanding of this behaviour, probably due to fine coupling between the physico-chemistry and hydrodynamics, is beyond the scope of this paper.

References

1. C. Dame, C. Fritz, O. Pitois, S. Faure, Colloids Surf. A **263**, 210 (2005).
2. H. Darcy, *Les fontaines publiques de la ville de Dijon* (V. Dalmont, Paris, 1856).
3. D. Weaire, N. Pittet, S. Hutzler, D. Pardal, Phys. Rev. Lett. **71**, 2670 (1993).
4. V. Carrier, S. Destouesse, A. Colin, Phys. Rev. E **65**, 061404 (2002).
5. S.A. Koehler, S. Hilgenfeldt, H.A. Stone, Phys. Rev. Lett. **82**, 4232 (1999).
6. S.A. Koehler, S. Hilgenfeldt, H.A. Stone, Langmuir **16**, 6327 (2000).
7. A. Saint-Jalmes, Y. Zhang, D. Langevin, Eur. Phys. J. E **15**, 53 (2004).
8. A. Saint-Jalmes, Soft Matter **2**, 836 (2006).
9. A. Saint-Jalmes, S. Marze, H. Ritacco, D. Langevin, S. Bail, J. Dubail, L. Guingot, G. Roux, P. Sung, L. Tosini, Phys. Rev. Lett. **98**, 058303 (2007).
10. S.J. Neethling, H.T. Lee, J.J. Cilliers, J. Phys.: Condens. Matter **14**, 331 (2002).
11. M. Durand, G. Martinoty, D. Langevin, Phys. Rev. E **60**, R6307 (1999).
12. M. Durand, Ph.D. Thesis, University of Paris XI (2002).
13. N. Peron, S.J. Cox, S. Hutzler, D. Weaire, Eur. Phys. J. E **22**, 341 (2007).
14. S. Stoyanov, C. Dushkin, D. Langevin, D. Weaire, G. Verbist, Langmuir **14**, 4663 (1998).
15. A. Nguyen, J. Colloid Interface Sci. **249**, 194 (2002).
16. S.J. Cox, G. Bradley, S. Hutzler, D. Weaire, J. Phys.: Condens. Matter **13**, 4863 (2001).
17. I.I. Goldfarb, I.R. Sheiber, Fluid Dyn. Trans. USSR Acad. Sci. Mech. Liquid Gas Ser. **23**, 244 (1988).
18. M. Durand, D. Langevin, Eur. Phys. J. E **7**, 35 (2002).
19. S.A. Koehler, H.A. Stone, M.P. Brenner, J. Eggers, Phys. Rev. E **58**, 2097 (1998).
20. R.A. Leonard, R. Lemlich, AIChE J. **11**, 18 (1965).
21. D. Desai, R. Kumar, Chem. Eng. Sci. **37**, 1361 (1982).
22. S.A. Koehler, S. Hilgenfeldt, E.R. Weeks, H.A. Stone, Phys. Rev. E **66**, 040601R (2002).
23. S.A. Koehler, S. Hilgenfeldt, H.A. Stone, J. Colloid Interface Sci. **276**, 420 (2004).
24. A.M. Poskanzer, F. Goodrich, J. Phys. Chem. **79**, 2122 (1975).
25. N.F. Djabbarah, D.T. Wasan, Chem. Eng. Sci. **37**, 175 (1982).
26. O. Pitois, C. Fritz, M. Vignes-Adler, Colloid Surf. A **261**, 109 (2005).
27. O. Pitois, C. Fritz, M. Vignes-Adler, J. Colloid Interface Sci. **282**, 458 (2005).
28. O. Pitois, N. Louvet, E. Lorenceau, F. Rouyer, J. Colloid Interface Sci. **322**, 675 (2008).
29. P. Stevenson, Chem. Eng. Sci. **61**, 4503 (2006).
30. P. Stevenson, Colloid Surf. A **305**, 1 (2007).
31. V. Carrier, Ph.D. Thesis, University of Bordeaux I (2001).
32. K. Brakke, Exp. Math. **1**, 141 (1992).
33. W. Drenckhan, H. Ritacco, A. Saint-Jalmes, A. Saugey, P. McGuinness, A. van der Net, D. Langevin, D. Weaire, Phys. Fluids **19**, 102101 (2007).
34. R. Phelan, D. Weaire, E.A.J.F. Peters, G. Verbist, J. Phys.: Condens. Matter **8**, L475 (1996).
35. R.E. Larson, J.J.L. Higdon, Phys. Fluid A **1**, 38 (1989).
36. P.M. Kruglyakov, D.R. Exerowa, *Foam and Foam Films* (Khimia, Moscow, 1990).
37. F. Rouyer, E. Lorenceau, O. Pitois, Colloid Surf. A **324**, 234 (2008).
38. N. Kern, D. Weaire, Philos. Mag. **83**, 2973 (2003).
39. M.-D. Lacasse, G.S. Grest, D. Levine, Phys. Rev. E **54**, 5436 (1996).
40. T.G. Mason, M.-D. Lacasse, G.S. Grest, D. Levine, J. Bibette, D.A. Weitz, Phys. Rev. E **56**, 3150 (1997).
41. H.M. Princen, Langmuir **2**, 519 (1986).

Permeability of a bubble assembly: From the very dry to the wet limit

Florence Rouyer, Olivier Pitois, Elise Lorenceau, and Nicolas Louvet
*Laboratoire de Physique des Matériaux Divisés et des Interfaces, Université Paris-Est,
UMR CNRS 8108, 5 bvd Descartes, 77454 Marne la Vallée Cedex 2, France*

Bubble assemblies offer the remarkable property of adjusting their packing fraction over three orders of magnitude, thus providing an interesting system for the study of liquid flows through granular matter. Although significant work has been done in several fields of research, e.g., foams, porous media, and suspensions, a complete set of data over such a wide range of porosity ε is still lacking. In this paper, we measure the permeability of a bubbly system in the range $0.1 < \varepsilon < 0.8$ and we connect these new data with a recently published set obtained for foams corresponding to $\varepsilon < 0.2$ [E. Lorenceau et al., Eur. Phys. J. E **28**, 293 (2009)]. Moreover, measurements performed with two different surfactants, the so-called "mobile" and "nonmobile" interfaces, allow us to determine the influence of the bubbles' surface mobility, which is proved to be a significant parameter up to $\varepsilon \approx 0.6$, thus well above the bubbles packing fraction. Above $\varepsilon \approx 0.6$, surface elasticity is fully mobilized over the bubbles' surface and the behavior of rigid spheres is observed for both solutions. We show that all the permeability values obtained for the bubble assembly with "nonmobile" interfaces are properly described with the Carman–Kozeny model. © *2010 American Institute of Physics.* [doi:10.1063/1.3364038]

I. INTRODUCTION

Dispersions of gas bubbles in liquid exhibit a large variety of dynamical behavior. It is a rich field of fundamental research, as bubbles assemblies are often used as model systems for soft matter. Moreover, bubbly systems are used in a lot of industrial applications: gas is mixed in many materials to improve their mechanical or acoustic properties or to make them lighter. In these bubbly systems, the homogeneity of the sample can be drastically affected by the drainage of the interstitial liquid (and the simultaneous rising of the bubbles); thus justifying the large amount of work devoted to the understanding of drainage in foams, for example. Note however that in spite of the significant progress realized in this field, most of the results only concern aqueous dry foams,[1,2] whereas mostly loose bubbly systems are encountered in industry.

From a more general point of view, flows through bubbles assemblies are similar to flows in porous media made of packed beads and in settling suspensions of hard spheres. In these systems, the Reynolds number is generally low meaning that viscous effects are dominant compared to inertia. However, the interfacial mobility behavior induced by the surfactant of the foaming solution has to be taken into account in addition to the ability of bubbles to form thin films when packed. For foams, it has been shown that high interfacial mobility, the so-called "mobile" behavior, could increase significantly the velocity of the liquid flow at a given porosity,[3] which definitely distinguishes this "soft" system from its "solid" counterpart. Very recently however, the permeability of foams characterized by less mobile interfaces, the so-called "nonmobile" behavior, was found to be properly described by the model of Carman–Kozeny,[4] originally validated for packed beds of solid spheres, i.e., liquid volume fractions (porosity) $\varepsilon \approx 0.4$. Note, however that the

influence of the mobility parameter is nontrivial: while for dry foams ($\varepsilon \approx 0.01$) this effect was found to govern the drainage dynamics, for wet foams ($\varepsilon \approx 0.1$) this influence seems to be reduced.[3] This complex behavior might be due to the loss of confinement as the porosity increases or to the behavior of the foam films, which are believed to have a significant effect on the flow through foam channels,[5] despite the small quantity of liquid they comprise. Yet, one has to stress that published data for foam permeability do not allow concluding for the influence of the mobility parameter above $\varepsilon \approx 0.1-0.2$. This raises the following major question of the influence of the surfactant used to stabilize the bubbly system close to the packing fraction, i.e., when foam films disappear. The complexity of such system might also remain above the packing fraction: as the liquid content increases, the typical size of the interstices varies and the boundary conditions for the flow at the surface of the bubbles are expected to evolve as well. The present paper aims to bring an experimental answer to this tricky and open issue. In contrast to previous works performed on aqueous foams, the foam permeability is measured over a very large range for the porosity, $0.1 < \varepsilon < 0.8$, thanks to a dedicated fluidized bed method. The main interest of this new set of data is that, for the first time, the bubble packing transition range is covered, for both "mobile" and "nonmobile" systems. Moreover, we connect these new data with a recently published set obtained for foams, i.e., $\varepsilon < 0.2$,[3] allowing for complete curves to be plotted over three orders of magnitude for the porosity. In the discussion of the paper, it is shown that the data can be described in the range $0.6 < \varepsilon < 0.8$ by models dedicated to non-Brownian hard spheres suspensions for both "mobile" and "nonmobile" systems. All the permeability values obtained for the bubble assembly with "nonmobile" interfaces are properly described with the Carman–Kozeny model.

II. FLUIDIZED BED EXPERIMENT

We build up a fluidized bed of monodisperse bubbles and measure its permeability over a large range of porosity. Soap solution is used to stabilize the contacts between bubbles and thus to avoid coalescence. To investigate the influence of the boundary conditions for the liquid flow at the surface of the bubbles, we use two different soap solutions known for providing opposite interfacial behaviors.[3]

A. Materials

As explained above, we use two soap solutions. In order to connect the results obtained in this work with available data for foams permeability, we chose the same solutions than those used in Ref. 3. A solution of tetradecyltrimethylammoniumbromide (TTAB) at a concentration of 3 g/l was found to give the highest permeability values in the range of $\varepsilon < 0.1-0.2$.[3] Interfaces obtained with this solution will be referred to as "mobile" interfaces. In opposition, a solution of TTAB 3 g/l mixed with 0.2 g/l dodecanol was found to give the smallest permeability values within the same range for the porosity.[3] The corresponding interfaces will be referred to as "nonmobile" interfaces. For both solutions, surfactant concentration is well above the critical micelle concentration (CMC=1 g/l), the density is ρ=1000 kg/m^3, the bulk shear viscosity is η=1 mPa s. For "mobile" and "nonmobile" interfaces, respectively, surface tensions are γ=38 and 25 mN/m, and surface shear viscosities $\eta_s \sim 10^{-8}$ and 10^{-6} kg s^{-1}.[6]

The gas used to create the bubbles is saturated with perfluorohexane (C$_6$F$_{14}$) to avoid size evolution of the bubbles during the experiment.

B. Experimental setup

The fluidized bed is constructed in a Plexiglas column (radius R=4.75 mm and height=200 mm), set vertically and partially immersed in a bath of the soap solution. A needle is placed at the open bottom of the column and allows monodisperse bubbles to be produced at constant gas flow rate Q_g (cf. Fig. 1). The top of the column ends with a grid (gray in Fig. 1) and is connected to a syringe pump that delivers soap solution at fixed liquid flow rate Q_l in the range of 0.01–10 ml/min. The mesh size of the grid is smaller than the bubble diameter. This latter has been chosen such that the Reynolds number Re for the liquid flow through the bubbles assembly is small. For "mobile" and "nonmobile" interfaces, respectively, the bubble size is D=260 and 190 μm. The maximum value of Re is obtained at high porosity, for which Re=$\rho V_{\text{Stokes}} D / \eta$=4 for bubbles of 200 μm in diameter (V_{Stokes} is the Stokes velocity equal to the terminal velocity of an isolated buoyant sphere in an infinite medium with no slip conditions on its surface at low Re). We checked that the bubble bed was stable during measurements for every liquid fraction. Note also that the ratio R/D is larger than 20, which prevent from pertubative wall effects and that the Bond number is of the order of 10^{-3}, meaning that bubbles are expected to remain spherical for porosity above packing.[7]

Initially, a small liquid flow rate ($Q_l < 1$ ml/min) is

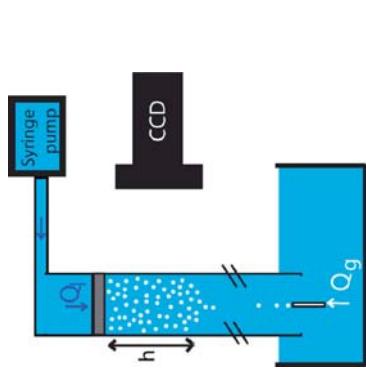imposed from top to bottom of the column while the gas bubbles are produced with at a rate Q_g at the bottom of the column. The resulting growth of the bubble assembly is characterized by the rate dh/dt, where h is the bubble assembly height (see Fig. 1). The evolution $h(t)$ is followed with a charge coupled device camera, allowing for dh/dt to be measured. Note that we checked that dh/dt is constant during the bed production. Then, the gas flow rate is stopped for $h>3R$, and the corresponding initial height is noted h_i. Next, the bubble bed is fully fluidized by a large liquid flow rate (Q_l>5 ml/min). Finally, several liquid flow rates are successively imposed and the corresponding height h is measured. The initial porosity ε_i and the porosity ε of the bubble bed for each liquid flow rate are, respectively, calculated with the following equations:

$$\varepsilon_i = 1 - \frac{Q_g}{(\pi R^2)\dfrac{dh}{dt}} \quad \text{and} \quad \varepsilon = 1 - (1-\varepsilon_i)\frac{h_i}{h}.$$

FIG. 1. (Color online) Sketch of the experimental setup of the fluidized bed.

C. Permeability measurements

The permeability of the bubble assembly is deduced from the Darcy law[8] with a pressure gradient induced by buoyancy[9,10]

$$k = \frac{\mu Q_l}{\Delta \rho g \pi R^2 (1-\varepsilon)} = \frac{1}{18} \frac{Q_l}{V_{\text{Stokes}} \pi R^2 (1-\varepsilon)} D^2. \tag{1}$$

III. RESULTS AND DISCUSSION

Normalized permeability curves k/D^2 are shown in Fig. 2 as a function of porosity for both soap solutions. Data already published for foams[3] ($\varepsilon < 0.1-0.2$) are also presented to be compared to the present work. First of all, it is shown that this new set of data connects well with the previous one, although both the measurement method and the setup are different. To this respect, permeability values ob-

energy dissipation during the homogeneous sedimentation or the particulate fluidization of non-Brownian hard spheres in a concentrated suspension, Mills and Snabre retrieved the RZ fit in the limit of low Reynolds number[17] and proposed to account for inertial effects in it. In their model, the average settling velocity of suspensions is $V_{settling} = V_{Stokes}\varepsilon^n$, where n is a decreasing function of the particulate Reynolds number (Re_p).[18] In particular, $n = 4.9$ for $Re_p = 4$. We see in Fig. 2 that the theoretical prediction $k/D^2 = 1/18[\varepsilon^{4.9}/(1-\varepsilon)]$ describes very well the experimental data at large porosity ($\varepsilon > 0.6$). The maximum relative deviation is less than 10% for both solutions. We conclude that indeed, for moderate Re_p and small Bo, bubble assemblies stabilized with surfactants behave like hard sphere suspensions for $\varepsilon > 0.6$.

We now discuss the data at intermediate porosities $0.2 < \varepsilon < 0.6$, around the packing fraction $\varepsilon \approx 0.4$. The permeability behavior is expected to be complex because the permanent foam films existing in the bubble assembly for $\varepsilon < 0.4$ disappear for $\varepsilon > 0.4$. Note also that transient foam films may survive due to bubbles collisions.

First we consider the case of the "nonmobile" interfaces. In this system, we have shown that the boundary conditions resemble the ones for rigid interfaces for $\varepsilon > 0.6$. Besides, a recent work indicated that "nonmobile" interfaces really mimic rigid walls at the scale of the bubbles for $\varepsilon < 0.2$.[4] In order to investigate the interfaces behavior in the intermediate range of porosity, we use the Carman–Kozeny model, that has been proved to be relevant for the description of permeability with this system for $\varepsilon < 0.2$.[4] We recall that the model relates the specific surface area S to the permeability of a porous medium characterized by a porosity ε (Ref. 19)

$$k = \frac{\varepsilon^3}{5S^2}. \quad (2)$$

Physically, the specific surface area represents the inverse of the characteristic length of channel that constitutes the porous medium, and thus it is the inverse of the relevant length for estimating viscous dissipation, i.e., the mean hydraulic radius: $m = \varepsilon/S$. Originally, this model has been developed for granular beds.[20] Very recently, the model was adapted to foams, considering the effective porosity instead by capillary effects;[4] the bubbles are not spherical and each bubble shares a film (two very close interfaces) with its neighbors. The specific surface area has been estimated from the geometrical Kelvin cells models, for foam porosities $0.001 < \varepsilon < 0.32$ [packing fraction of the Kelvin (bcc) arrangement of spheres]. Note that remarkably, the constant "5," which was proposed by Carman for beds of rigid grains around $\varepsilon \approx 0.36$ was found to be in full agreement with permeability measurements for foams within the full investigated range of liquid fraction. For $\varepsilon > 0.32$, bubbles are mainly spherical and the specific surface area is equal to $S = 6(1-\varepsilon)/D$, similarly to bed and suspension of rigid spheres. The inset of Fig. 3 represents the variation of the normalized specific surface area SD as a function of ε for foams, i.e., $0 < \varepsilon < 0.32$ (from Ref. 4), and hard spheres suspensions, i.e., $0.36 < \varepsilon < 1$. Note that at small porosity ($\varepsilon < 0.05$), S varies as the square root of ε: $S(\varepsilon)D \approx 15.8\sqrt{\varepsilon}$.

tained in this work are in agreement with the data deduced from previous experiments with the forced drainage method in the range of $0.1 < \varepsilon < 0.2$. We recall that this latter method is known to be problematic for liquid fractions above 0.1 due to the appearance of convective instabilities.[11] Second, the present measurement method allowed for the permeability to be plotted over three decades for a unique porous system. Note that the corresponding range of porosity has been increased by a factor of 4 with respect to published data.

Now, we focus on data obtained at high porosity, i.e., $\varepsilon > 0.6$. As observed in Fig. 2, the two sets of data overlap in this range of porosity, suggesting that the boundary conditions are similar for both systems. In other words, the mobility parameter introduced for the study of foam drainage has no influence as the liquid fraction reaches 0.6. This can be understood considering the work performed on isolated bubbles rising in soap solutions. Indeed, the rising velocity is close to the velocity of buoyant spheres with no slip conditions due to a kinetic rigidification induced by Marangoni flows at the surface.[12,13] It is thus deduced that (i) this mechanism affects both systems of "mobile" and "nonmobile" interfaces, and (ii) the rigidification effect predicted for isolated bubbles covered with surfactants appears as soon as the liquid fraction raises close to 0.6 in the bubble assembly. Consequently, the corresponding permeability is expected to be described by models derived for non-Brownian hard sphere suspensions. Up to now, the Richardson–Zaki (RZ) empirical law is the reference for average settling velocity of suspensions,[14] and it is also valid to describe the upward fluid velocity in case of fluidized suspensions;[15] this law writes $V_{settling} = V_{Stokes}\varepsilon^{5.5,16}$, thus $k/D^2 = 1/18[\varepsilon^{5.5}/(1-\varepsilon)]$. More recently, using a mean field approach to estimate the

FIG. 2. (Color online) Permeability of particulate systems made of monodisperse bubbles as a function of porosity. Experimental data of the fluidized bed are compared with previous experimental data of foam (see legend for details). The dotted line corresponds to permeability calculated by $k/D^2 = 1/18[\varepsilon^{4.9}/(1-\varepsilon)]$, which is derived for hard spheres suspensions (Ref. 18).

mum relative deviation is less than 20%). Eventually, we stress that in the fluidized bed the particles are in permanent agitation due to hydrodynamic interactions,[22,23] but the present result suggests that the effects induced by agitation of the fluidized bed are not crucial for permeability. This experimental observation is consistent with previous numerical simulations,[9] but differs from Davies et al. conclusions, who stated that the Carman–Kozeny constant c can be much larger than 5 and depend on porosity as well as on particle suspension properties.[10] Here, we demonstrate that a unique constant allows to describe fairly well the permeability of suspensions made of monodisperse spherical entities (solid particles or bubbles with "nonmobile" interface).

Finally, we discuss the results for the system with "mobile" interfaces in the intermediate porosity range. For convenience, we also provide an analytical expression for this system (see Fig. 3)

$$k(\varepsilon) = \frac{\varepsilon^{3/2}}{1700(1 - 2.7\varepsilon + 2.2\varepsilon^2)^2}D^2 \quad \text{for } \varepsilon < 0.4, \quad (4a)$$

$$k(\varepsilon) = \frac{\varepsilon^3}{180(1-\varepsilon)^2}D^2 \quad \text{for } \varepsilon > 0.6. \quad (4b)$$

SD reaches a maximal value (approximately 4) for porosity around 0.2. To conveniently describe the variation in S for $0 < \varepsilon < 0.4$, we propose to introduce an empirical function $g(\varepsilon)$ such as $S(\varepsilon)D = 15.8\sqrt{\varepsilon g(\varepsilon)}$. This function should be chosen in such a way that it satisfies the limit conditions $g(0) = 1$ and insures the continuity of the function $S(\varepsilon)$ for $\varepsilon = 0.4$, i.e., $S(0.4)D = 3.6$ and $dS/d\varepsilon(0.4)D = -6$. Assuming that g is a function of second order, we find $g(\varepsilon) = 1 - 2.15\varepsilon + 1.37\varepsilon^2$. The specific surface is thus describes as $S(\varepsilon)D \approx 15.8\sqrt{\varepsilon g(\varepsilon)}$ for $\varepsilon < 0.4$ and $S(\varepsilon)D = 6(1-\varepsilon)$ for $\varepsilon > 0.4$. We note that the function $g(\varepsilon)$ is not a fit but rather a basic function that permits us to connect the description at low and high porosity. From the above, the theoretical permeability is

$$k(\varepsilon) = \frac{\varepsilon^2}{1248(1 - 2.15\varepsilon + 1.37\varepsilon^2)^2}D^2 \quad \text{for } \varepsilon < 0.4, \quad (3a)$$

$$k(\varepsilon) = \frac{\varepsilon^3}{180(1-\varepsilon)^2}D^2 \quad \text{for } \varepsilon > 0.4. \quad (3b)$$

It is shown in Fig. 3 that Eq. (3) describes very well previous and present results corresponding to the system with nonmobile interfaces over the whole range explored for the porosity. This law permits us to describe experimental results from low to high porosity which is not trivial has recently shown for emulsion by Peron et al.[21] At this point, we conclude that the bubble assembly made of the called "nonmobile" interface really mimics porous media made of no-slip solid walls over the whole range of porosity. Note also that over the large range $0.4 < \varepsilon < 0.85$, Carman–Kozeny model provides permeability values in fair agreement with the model for hard spheres suspensions (the maxi-
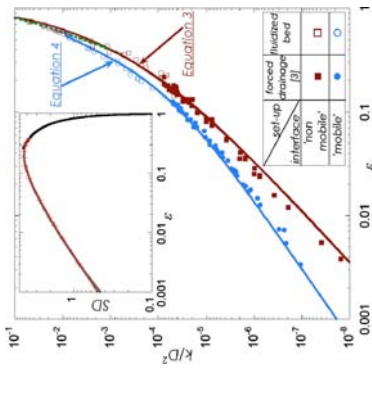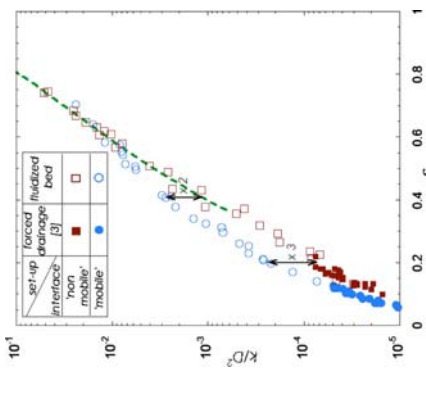

FIG. 3. (Color online) Permeability of particulate systems made of monodisperse bubbles as a function of porosity. Experimental data (see legend for details) are compared with the permeability calculated from Carman–Kozeny law [Eq. (3)] and to fit proposed in Eq. (4). Inset: Variation of the normalized specific surface area of particulate systems made of monodisperse entities as a function of porosity. For $\varepsilon < 0.32$ (lighter line) the specific surface of foam as explained in the text (Ref. 4). For $\varepsilon > 0.32$ (black) $SD = \pi D^2 n_\varepsilon = 6(1-\varepsilon)$. The plus symbol line corresponds to the function $S(\varepsilon)D \approx 15.8\sqrt{\varepsilon}(1-2.15\varepsilon+1.37\varepsilon^2)$.

There is not yet a model to predict permeability for the "mobile" interfaces. However, we can guess that the length scale over which viscous dissipation would occur is smaller than the length scale associated to specific surface area in the Kozeny–Carman model. In particular, it would decrease as the mobility increases.

The data for the system of "mobile" interfaces are found to be larger than for "nonmobile" interfaces. Yet, previous results[3] suggested an overlapping expected for liquid fractions close to 0.2. It is shown here that around the packing porosity ($\varepsilon \approx 0.4$), the permeability of the system with mobile interfaces is approximately twice the permeability of the system with nonmobile interfaces. This deviation, remaining between 0.4 and 0.6, is rather surprising as Marangoni stresses are expected to rigidify the surface of rising bubbles in both soap solutions. On the other hand, it has been shown that for dry foams, the bubbles' surface is not rigidified by Marangoni stresses. This behavior is not fully understood but seems to be related to the presence of the foam films. The mobilization of surface elasticity (and the resulting surface rigidification) is therefore expected to be correlated with the proportion of those films in the bubble assembly. However, the present result indicates that the full rigidification of the bubbles' surface do not coincide with the vanishing of films at the packing fraction, as highlighted by the two arrows in Fig. 2. Instead, the surface rigidification develops progressively in the intermediate porosity range, i.e., $0.2 < \varepsilon < 0.6$. This unexpected behavior could be attributed to the complex coupling of surfactant surface flows and liquid flow between the bubbles. Although such mechanism has been considered

Recirculation model for liquid flow in foam channels

O. Pitois[a], N. Louvet, and F. Rouyer

Université Paris-Est, Laboratoire de Physique des Matériaux Divisés et des Interfaces, UMR CNRS 8108, 5 bvd Descartes, 77454 Marne la Vallée Cedex 2, France

Abstract. Although extensively studied in the past, drainage of aqueous foams still offers major unaddressed issues. Among them, the behaviour of foam films during drainage has great significance as the thickness of the films is known to control the Ostwald ripening in foams, which in turn impacts liquid drainage. We propose a model relating the films' behavior to the liquid flow in foam channels. It is assumed that Marangoni-driven recirculation counterflows take place in the transitional region between the foam channel and the adjoining films, and the Gibbs elasticity is therefore introduced as a relevant parameter. The velocity of these counterflows is found to be proportional to the liquid velocity in the channel. The resulting channel permeability is determined and it is shown that Marangoni stresses do not contribute to rigidify the channel's surfaces, in strong contrast with the drainage of horizontal thin liquid films. New experimental data are provided and support the proposed model.

PACS. 47.57.Bc Foams and emulsions – 68.03.Cd Surface tension and related phenomena

1 Introduction

The drainage properties of liquid foams have been extensively studied in the past [1–4], but a generalized foam drainage theory has been only recently proposed [5]. As a predictive tool, the foam drainage equation accounts for the evolution of the liquid volume fraction under various drainage conditions, such as free gravity drainage or forced stationary drainage. In order to quantitatively describe these effects, the foam permeability has to be precisely known, resulting in many experimental and theoretical efforts devoted to its determination [6–9]. As a major result, the permeability of aqueous foams was proven to be strongly dependent on the viscosity of the liquid/gas interfaces that confine the liquid flow. Moreover, it was recognized that the magnitude of the interfacial shear induced by the bulk liquid flow is the parameter relevant for the problem of drainage in foam channels. This was modeled using the surface shear viscosity μ_S and introducing the associated Boussinesq number $Bo = \mu_S/\mu R$, where μ is the shear viscosity of the bulk and R the characteristic size of the foam channels. Futher investigations attempted to achieve the validation of this simple idea, on both the foam scale and the microscopic scale, i.e. a single foam channel. Acceptable agreement was obtained [8,10–12], thus proving the relevance of this simple description for the coupling of interfacial/bulk flows in the problem of foam drainage. Note, moreover, that for large Boussinesq num-

bers, foam permeability is very close to that obtained for a solid porous material with the same pore geometry [13].

On the other hand, whereas interfacial elasticity is known to have a major effect for the drainage of horizontal thin liquid films [14–16], its contribution to foam drainage remains to be evaluated. Experimental support for such an effect has not yet been reported. Models including the Gibbs elasticity as a parameter controling the drainage velocity have been recently proposed by Durand et al. [17]. Depending on the diffusion properties of the surfactant, Marangoni stress develops at the channel surface and rigidifies it. However, the model does not account for the high liquid permeability of foam channels reported for mobile surfactants.

Following a different approach, Carrier et al. [6] focussed on the measurement of the thickness of the films during foam drainage experiments. It has been shown that a coupling mechanism exists between liquid flow through the Plateau border network and the thickness of the films. As a result, the film thickness is found to increase as the draining liquid flow rate increases. This relation between the thickness of the films and the liquid flow rate has been confirmed by measurements performed on a single Plateau border [11]. The magnitude of the observed film swelling phenomena has been proven to be dependent on the foaming solution [6,11], and non-uniform thickness profiles have also been reported, suggesting convection cells developing in bubble films [6,19].

Moreover, recent results for foam coarsening [20] suggest that a constant film thickness approach does not

^a e-mail: olivier.pitois@univ-mlv.fr

---

for isolated rising bubbles, more complex situations involving several bubbles has never been investigated. To this respect, the present work provides an interesting experimental result to be elucidated.

IV. CONCLUSION

We present experimental data for the permeability of a bubble assembly over a wide porosity range (0.15–0.75) with two different surfactants, characterized by their opposite interfacial rheological behavior, the so-called "mobile" and "nonmobile" interfaces. These new data connect well with previous one obtained for foams, i.e., the dry limit, and for non-Brownian hard spheres suspensions, i.e., the wet limit. We prove that the bubbles' surface mobility is a significant parameter up to $\varepsilon \approx 0.6$. Indeed, the surface rigidification develops progressively in the intermediate porosity range, i.e., $0.2 < \varepsilon < 0.6$, instead of being a sharp event around packing when soap films shrink to zero. This unexpected behavior, which could be attributed to the complex coupling of surfactant surface flows and liquid flow between the bubbles, remains to be elucidated.

For the particular case of "nonmobile" interfaces, we show that the Carman–Kozeny law properly accounts for the evolution of permeability as a function of liquid fraction. More precisely, we demonstrate that a unique constant ($c = 5$), proposed initially by Carman for beds of rigid grains around $\varepsilon = 0.36$ allows to describe fairly well the permeability of bubbly assemblies over almost three orders of magnitude.

We give fits to estimate the variation in permeability as function of porosity from 0 to 0.85 for both "mobile" and "nonmobile" interfaces. We assume that these functions envelop the permeability curves as a function of porosity for any assembly of monodisperse spherical entities for porosity varied from 0 up to 0.85.

We expect that this work is of great interest for other systems, in addition to foam and suspensions, where the continuous liquid phase varies over a wide range and the rheological properties of the interfaces between phases might be complex, for example, emulsions or complex biological systems.

1. D. Weaire, N. Pittet, S. Hutzler, and D. Pardal, "Steady-state drainage of an aqueous foam," Phys. Rev. Lett. **71**, 2670 (1993); G. Verbist, D. Weaire, and A. M. Kraynik, "The foam drainage equation," J. Phys.: Condens. Matter **8**, 3715 (1996).
2. S. A. Koehler, S. Hilgenfeldt, and H. A. Stone, "A generalized view of foam drainage: Experiment and theory," Langmuir **16**, 6327 (2000).
3. E. Lorenceau, N. Louvet, F. Rouyer, and O. Pitois, "Permeability of aqueous foams," Eur. Phys. J. E **28**, 293 (2009).
4. O. Pitois, N. Louvet, E. Lorenceau, and F. Rouyer, "Specific surface area model for foam permeability," Langmuir **25**, 97 (2009).
5. O. Pitois, N. Louvet, and F. Rouyer, "Recirculation model for liquid flow in foam channels," Eur. Phys. J. E **30**, 27 (2009).
6. O. Pitois, C. Fritz, and M. Vignes-Adler, "Liquid drainage through aqueous foam: Study of the flow on the bubble scale," J. Colloid Interface Sci. **282**, 458 (2005).
7. S. G. Yiantsios and R. H. Davis, "Close approach and deformation of two viscous drops due to gravity and van der Waals forces," J. Colloid Interface Sci. **144**, 412 (1991); M. H. Manga and H. A. Stone, "Buoyancy-driven interactions between two deformable viscous drops," J. Fluid Mech. **256**, 647 (1993).
8. H. Darcy, Les Fontaines Publiques de la Ville de Dijon (V. Dalmont, Paris, 1856).
9. A. J. C. Ladd, "Hydrodynamic transport coefficients of random dispersions," J. Chem. Phys. **93**, 3484 (1990); R. J. Hill, D. L. Koch, and A. J. C. Ladd, "The first effects of fluid inertia on flows in ordered and random arrays of spheres," J. Fluid Mech. **448**, 213 (2001).
10. L. Davies and D. Dollimore, "Theoretical and experimental values for the parameter k of the Kozeny-Carman equation, as applied to sedimenting suspensions," J. Phys. D **13**, 2013 (1980).
11. S. Hutzler, D. Weaire, and R. Crawford, "Convective instability in foam drainage," Europhys. Lett. **41**, 461 (1998).
12. V. G. Levich, Physicochemical Hydrodynamics (Prentice-Hall, Englewood Cliffs, NJ, 1962).
13. F. Takemura, "Adsorption of surfactants onto the surface of a spherical rising bubble and its effect on the terminal velocity of the bubble," Phys. Fluids **17**, 048104 (2005); B. Cuenot, J. Magnaudet, and B. Spennato, "The effects of slightly soluble surfactants on the flow around a spherical bubble," J. Fluid Mech. **339**, 25 (1997).
14. X. Yin and D. L. Koch, "Hindered settling velocity and microstructure in suspensions of solid spheres with moderate Reynolds numbers," Phys. Fluids **19**, 093302 (2007).
15. S. Y. Tee, P. J. Mucha, M. P. Brenner, and D. A. Weitz, "Velocity fluctuations in a low-Reynolds-number fluidized bed," J. Fluid Mech. **596**, 467 (2008).
16. J. F. Richardson and W. N. Zaki, "Sedimentation and fluidization: Part I," Trans. Inst. Chem. Eng. **32**, 35 (1954).
17. P. Mills and P. Snabre, "Settling of a suspension of hard spheres," Europhys. Lett. **25**, 651 (1994).
18. P. Snabre and P. Mills, "Settling and fluidization of non Brownian hard spheres in a viscous liquid," Eur. Phys. J. E **1**, 105 (2000).
19. J. Kozeny, "Ueber kapillare leitung des wassers im boden," Ber Wien Akad **136a**, 271 (1927).
20. P. C. Carman, "Fluid flow through granular bed," Trans. Inst. Chem. Eng. **15**, 150 (1937); "Some physical aspects of water flow in porous media," Discuss. Faraday Soc. **3**, 72 (1948).
21. N. Peron, S. J. Cox, S. Hutzler, and D. Weaire, "Steady drainage in emulsions: Corrections for surface Plateau borders and a model for high aqueous volume fraction," Eur. Phys. J. E **22**, 341 (2007).
22. G. K. Batchelor, "Sedimentation in a dilute dispersion of spheres," J. Fluid Mech. **52**, 245 (1972).
23. R. E. Caflisch and J. H. C. Luke, "Variance in the sedimentation speed of a suspension," Phys. Fluids **28**, 759 (1985); M. P. Brenner, "Screening mechanisms in sedimentation," ibid. **11**, 754 (1999); X. Yin and D. L. Koch, "Velocity fluctuations and hydrodynamic diffusion in finite-Reynolds-number sedimenting suspensions," ibid. **20**, 043305 (2008).

account for the coarsening rate over the whole range of investigated liquid fractions. In other words, the coupling between coarsening and drainage is stronger than initially expected [21], involving the film thickness variation with the liquid velocity in the Plateau borders, as recently demonstrated at the bubble scale [19]. Note that the influence of the films on the permeability of the channel has been theoretically investigated: both the film thickness [22] and the apparent contact angle in the transitional region [23] were found to have a significant effect. But none of the existing models for foam drainage accounts for the swelling phenomenon and this constitutes a limiting stage in the complete understanding of the coarsening of draining foams [24].

On the other hand, draining properties of isolated vertical thin films have received considerable attention [25-28]. Despite significant progress in our understanding of thin-film behaviour, a full hydrodynamic analysis describing the flow behaviour including micellar kinetics, surfactant adsorption and desorption effects, and Marangoni stresses, is not yet available in the literature. One can notice similarities with the work performed within the context of foam drainage [6,11,19]: some studies [25,29] have reported that film drainage is influenced by lateral flow into the Plateau borders (near the vertical wires of the frame), attributed to capillary suction and marginal regeneration.

In this paper, we propose a new mechanism accounting for all experimental aspects of foam drainage, including low channel permeability and film swelling. The associated model contrasts with existing ones as it is based on the existence of recirculation cells in the films, ensuring the conservation of surfactant molecules at the surface of the channels. Rather than a complete and rigorous treatment for the surfactant conservation, we focus on the minimal ingredients allowing for the film swelling phenomenon to be related to the liquid flow in foam channels. New experimental data are provided and support the proposed model.

2 Model for liquid flow through foam channels

Existing models are based on an infinite channel [2,10,30], assuming translational symmetry for both bulk and surface velocity profiles. It is thus assumed that the quantity of surfactant molecules convected along the channel's surface by unit of time is exactly the same as that entering the channel's surface upstream as well as that leaving the channel's surface downstream. However, these boundary conditions are not appropriate for the liquid flow through the channels network, because the surfactant concentration is continually changing. This can be understood considering the situation depicted in fig. 1. The bulk liquid flow rate is Q in the channel upstream of the node and $Q/3$ in the three channels downstream of the node. As the assumed velocity profile for bulk liquid flow is not crucial for the following, we simplify the present discussion in considering a plug-like profile, so that the surface
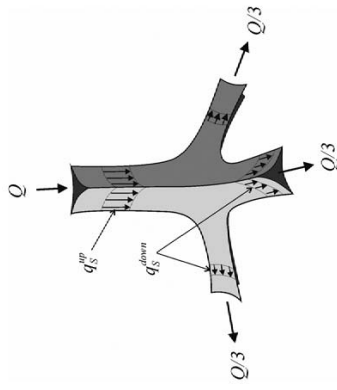
channels in foam. Note that each surface of the upper channel branches into two lower channels. The surface flow rate of the surfactant upstream of the node (q_S^{up}) is larger than the surface flow rate downstream of the node (q_S^{down}), involving a continual readjustment of the surfactant concentration at the node surface.

flow is directly proportional to the bulk flow. Far from the node, the velocity at the surface of the channel is constant and equal to u, and the surface concentration of the surfactant is $\Gamma = \Gamma_{eq}$. The radius of curvature of the channel R corresponds also to the channel's width. The surface flow rate of surfactant upstream of the node is thus $q_S^{up} \approx Ru\Gamma_{eq}$, whereas the surface flow rate downstream of the node is $q_S^{down} \approx 2R(u/3)\Gamma_{eq}$, because the surface of the upper channel splits up into two new surfaces, so that $q_S^{down} < q_S^{up}$. This means that the surfactant concentration at the channel's surface is greater close to the node (upstream). This result can be generalized to other flow configurations for the junction and shows that the assumption of constant surface concentration for the surfactant cannot apply to the channel network.

In the following, we assume that this excess (or lack) of surfactant molecules is partly counteracted by diffusion into/from the bulk and by surface flows. More precisely, we assume that convection of surfactant molecules takes place in the films and is driven by surface tension gradients on the surfaces of the top and bottom of the channels (see the white arrows in fig. 2). Note that the existence of such a mechanism is suggested by the recently reported patterns of foam films under draining conditions [6,19].

2.1 Recirculation model

Let us consider now the simpler situation of a single channel surface element and its adjoining film's surface, as depicted in fig. 2. The length of the system is L and represents the typical length of a convection cell, i.e. film size. In other words, L does not necessarily equal the length of a single Plateau border but may represent several Plateau borders along a bubble film, as suggested in [6,19].

Fig. 1. Flows for the surfactant at the surface of the foam channels in foam. Note that each surface of the upper channel branches into two lower channels. The surface flow rate of the surfactant upstream of the node (q_S^{up}) is larger than the surface flow rate downstream of the node (q_S^{down}), involving a continual readjustment of the surfactant concentration at the node surface.

Surface diffusion of surfactant is driven by concentration deviations $\Delta\Gamma$ over a distance of the order of R

$$q^S \approx D_S \frac{\Delta\Gamma}{R} \cdot R = D_S\Delta\Gamma, \quad (2)$$

where D_S is the surface diffusion coefficient. Note that the concentration deviation is related to the difference in concentration at the channel's surface $\Delta\Gamma = (\Gamma^+ - \Gamma^-)/2$, so that

$$q^S \approx D_S \frac{(\Gamma^+ - \Gamma^-)}{2}. \quad (3)$$

The concentration gradient $(\Gamma^+ - \Gamma^-)/L$ induces a Marangoni stress

$$\tau_M = \frac{d\gamma}{dz} \approx \frac{E}{\Gamma_{eq}}\left(\frac{\Gamma^+ - \Gamma^-}{L}\right), \quad (4)$$

where the Gibbs elasticity $E = -\Gamma(d\gamma/d\Gamma) \simeq -\Gamma_{eq}(d\gamma/d\Gamma)_{eq}$ has been introduced [31]. As a result, a Marangoni-driven flow takes place in the film/channel transitional region, in the opposite direction to the flow in the channel. We assume the characteristic length and velocity for this flow to be, respectively, ς and V_{up}. Note that ς and V_{up} also set the surface flow rate of surfactant convected by the counterflow in the transitional region: $q^M \approx \varsigma V_{up}\Gamma_{eq}$. Neglecting the bulk viscous stress in the transitional region [10], the Marangoni stress is related to ς from the interfacial stress balance (except at both channel's ends)

$$\tau_M \approx \mu_S \frac{V_{up}}{\varsigma^2}, \quad (5)$$

allowing for the characteristic velocity to be expressed as a function of the concentration deviation

$$V_{up} \approx \frac{\varsigma^2 E}{\mu_S L}\left(\frac{\Gamma^+ - \Gamma^-}{\Gamma_{eq}}\right) \quad (6)$$

and the corresponding surface flow rate is

$$q^M = V_{up}\Gamma_{eq}\varsigma \approx \frac{E\varsigma^3}{\mu_S L}(\Gamma^+ - \Gamma^-). \quad (7)$$

The order of magnitude of ς corresponds to the characteristic size over which surface velocity gradients take place. For small Boussinesq numbers, velocity variations are known to be essentially confined within the corner of the cross-section, so that ς/R is expected to be small (see fig. 3b). More precisely, ς/R can be estimated from the force balance for the channel. Neglecting bulk viscous stress in the thin transitional region, the driving pressure ΔP induces a force $f_m = A\Delta P$, which is opposed by the force arising from shearing the Newtonian surface $f_S = 6L\mu_S du/dy$ (the coefficient 6 accounts for the three transitional regions, each of them counting as two interfaces). This gives the variation of the surface velocity

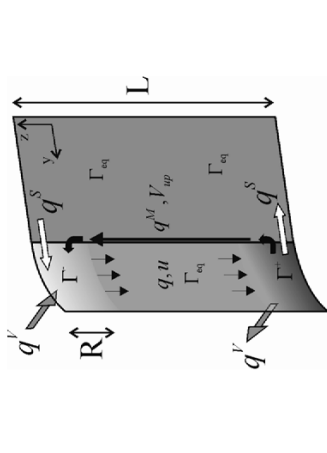$$\frac{du}{dy} \approx \frac{A}{6\mu_S}\frac{\Delta P}{L}. \quad (8)$$

Fig. 2. Single-channel surface element and its adjoining film surface. Deviations of surface concentration with respect to equilibrium induce molecular exchanges with the bulk of the channel (with flow rates q^V) and with the surface of the films, assuming a diffusive flow (q^S) and a Marangoni-driven flow (q^M). Due to the presence of the film that acts as a reservoir of surfactants, it is assumed that the Marangoni flow takes place in the transitional region (black arrows) rather than at the channel surface.

Let z be the coordinate along the axis of the channel and coordinates (y,z) are used along the film's surface. The channel's cross-section is A. Under stationary conditions, the velocity at the surface of the channel is constant and equal to u as shown in fig. 2. Far from channel's ends, the surface concentration of surfactant is $\Gamma = \Gamma_{eq}$, so that the surface flow rate of surfactant convected along the channel can be approximated by

$$q \simeq uR\Gamma_{eq}. \quad (1)$$

At both channel's ends, the surface flow rate of surfactant q_e exchanged with the node surface differs from q (inducing an excess or a lack of surfactant as explained above), so that surface concentration gradients take place over the characteristic length of the node, i.e. R. As the precise value of q_e has no particular importance, we set $q_e = 0$ in the following. At the surface of both channel's ends, the surfactant concentration is assumed to be Γ^+ and Γ^-, upstream and downstream, respectively. Deviations of surface concentration with respect to equilibrium are supposed to be small: $(\Gamma_{eq} - \Gamma^-) \ll \Gamma_{eq}$ and $(\Gamma^+ - \Gamma_{eq}) \ll \Gamma_{eq}$. In the following, we consider that $(\Gamma_{eq} - \Gamma^-) = (\Gamma^+ - \Gamma_{eq}) = \Delta\Gamma$. These deviations induce molecular exchanges with the bulk of the channel, at a flow rate q^V, and with the surface of the films that act as reservoirs with a surface concentration Γ_{eq}. The surface exchanges involve a diffusive flow, at a flow rate q^S, and a Marangoni-driven flow, at a flow rate q^M, resulting from the deviations in surface tension associated to the deviations in surfactant surface concentration. In the following, we derive expressions for q^V, q^S and q^M.
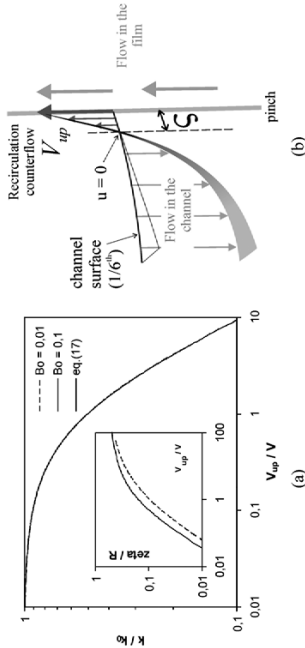
Fig. 3. (a) Channel permeability ratio as a function of the ratio of the counterflow velocity with bulk channel velocity, for $Bo = 0.01$ and $Bo = 0.1$. Equation (17) is plotted for comparison. In the inset: characteristic size for the counterflow as a function of the velocity ratio, for $Bo = 0.01$ and $Bo = 0.1$. (b) Sketch of the transitional region showing the upward counterflow velocity and the bulk channel velocity.

Replacing du/dy with $\bar{v}/\varsigma$ [10] and introducing the permeability factor for the channel, i.e. $\tilde{k} = k\,\mu\bar{v}/A(\Delta P/L)$, ς is obtained

$$\varsigma \approx 6\tilde{k}\,\frac{\mu_S}{\mu} \tag{9}$$

For low Boussinesq numbers, i.e. $Bo \approx 0.01$, $\tilde{k} \approx 1$ [10,30], so that $\varsigma \approx 10^{-5}$ m with $\mu_S \approx 10^{-8}$ kg/s, $\mu \approx 10^{-3}$ Pa s. Note that for larger Boussinesq numbers, i.e. $Bo \approx 1$, bulk viscous stress has to be taken into account in the force balance and $du/dy \neq \bar{v}/\varsigma$ in the transitional region [10].

It is interesting to estimate the ratio of flow rates q^M and q^S

$$\frac{q^S}{q^M} \approx \frac{D_S \mu_S L}{2E\varsigma^3}. \tag{10}$$

Typical values are $D_S \sim 10^{-11}$ m^2/s, $\mu_S \sim 10^{-8}$ kg/s, $L \sim 10^{-3}$ m, $E \sim 10^{-2}$ N/m, $R \sim 10^{-4}$ m and $\varsigma \sim 10^{-5}$ m and we find that $q^S/q^M \ll 1$. From this point, q^S is thus neglected.

Exchange of surfactants with the bulk liquid at the surface of both channel's ends can be modeled as a transport of molecules limited by diffusion (fast adsorption/desorption) with a diffusion coefficient D. The bulk concentration gradient is $\sim \Delta C/R$ and can be related to the surface concentration using the ratio of bulk and surface concentrations $\beta = (d\Gamma/dC)_{eq}$; $\Delta C \approx \Delta\Gamma/\beta$. β is derived from the Langmuir equation: $1/\beta = (2a/\Gamma_{eq})(C/a+1)^2 \simeq C^2/a\Gamma_{eq}$, where a is the Szyszkowski concentration. With typical values $C \approx 1$ kg/m^3, $\Gamma_{eq} \approx 10^{-6}$ kg/m^2 and $a \approx 0.1$ kg/m^3, the order of magnitude of β is 10^{-7} m. Thus, the corresponding flow rate can be approximated by

$$q^V \approx D\left(\frac{\Delta C}{R}\right)R^2 \approx R^2\frac{D}{2\beta}\left(\Gamma^+ - \Gamma^-\right). \tag{11}$$

The conservation of surfactant molecules at the surface of both channel's ends can be written as

$$q \simeq q^V + q^M. \tag{12}$$

We recall that in the above equation, q^S has been neglected and q_e has been set to zero. Using eqs. (1), (7) and (11), eq. (12) becomes

$$uR\Gamma_{eq} = \frac{RD}{2\beta}\frac{\mu_S V_{up}\Gamma_{eq}L}{E\varsigma^2} + \varsigma V_{up}\Gamma_{eq}, \tag{13}$$

As mentioned above, the surface velocity approximately equals the bulk velocity for small Boussinesq numbers, i.e. $u \simeq \bar{v}$, so that the ratio $V_{up}/\bar{v}$ can be approximated by

$$\frac{V_{up}}{\bar{v}} = \left(\frac{D\,\mu_S L}{2\beta E\varsigma^2} + \frac{\varsigma}{R}\right)^{-1}. \tag{14}$$

Typical values are $D \sim 10^{-9}$ m^2/s, $\mu_S \sim 10^{-8}$ kg/s, $L \sim 10^{-3}$ m, $E \sim 10^{-2}$ N/m, $R \sim 10^{-4}$ m, $\varsigma \sim 10^{-5}$ m and $\beta \sim 10^{-7}$ m. Numerically, we find that $\varsigma/R \sim 0.1$ and $\frac{D\mu_S L}{2\beta E\varsigma^2} \sim 0.1$.

Thus, the counterflow velocity is expected to be proportional to the bulk liquid velocity with the same order of magnitude. Moreover, independently of the bulk liquid velocity, the counterflow velocity is influenced by the Gibbs elasticity. Finally, from (6), the surface concentration deviation $\Delta\Gamma/\Gamma_{eq}$ is of the order $V_{up}\mu_S L/E\varsigma^2$ and $\Delta\gamma/\gamma_{eq} \approx (E/\gamma_{eq})\Delta\Gamma/\Gamma_{eq} \sim 0.1$, with $V_{up} \approx 0.1$, i.e. $V_{up} \approx \bar{v} \approx 10^{-2}$ m/s.

2.2 Channel permeability

The foregoing analysis suggests that the channel permeability can be determined following the approach proposed by Lemlich, except that the liquid velocity at the corners of the channel's cross-section is not set to zero, but instead is set to V_{up}. This implies that the hydrodynamic resistance of the channel is now dependent not only on the Boussinesq number but also on V_{up}. We now present numerical calculations for the channel permeability assuming these modified boundary conditions.

We consider a channel cross-section of area A in a plane (x, y). In the plane, the channel boundaries are three circular arcs of radius R whose centers are outside the domain and form an equilateral triangle. This geometry has three axes of symmetry, thus only one-sixth of the area is considered in the simulation (see fig. 3b). The liquid flow through the channel is assumed to be uniaxial and stationary, i.e. $\bar{v} = v(x, y)\bar{e}_z$. Typical values for the Reynolds number for the liquid flow are smaller than unity, so that the Stokes equation is used

$$\Delta v = -\frac{1}{\mu}\frac{dp}{dz}, \tag{15}$$

where p is the liquid pressure (the pressure gradient includes gravity forces). Partial mobility of channel interfaces is obtained balancing the bulk viscous stress with the surface viscous stress [2] on the circular boundary

$$\mu(\bar{n} \cdot \bar{\nabla}v) = \mu_S \Delta_S v, \tag{16}$$

where $\bar{n}$ is the vector normal to the channel's surface and Δ_S is the surface Laplacian. Finally, we consider that the velocity is V_{up} at the corner (upwards). These equations are made dimensionless and solved numerically using R and $V = (dp/dz)R^2/\mu$ as length and velocity scales, and the Boussinesq number $Bo = \mu_S/\mu R$. Numerical resolution is performed for two values for Bo and several ratio $V_{up}/\bar{v}$, providing values for the channel permeability factor $\tilde{k} = \mu\bar{v}/A(dp/dz)$. Note that due to the counterflows, the effective cross-sectional area A_{eff} available to the liquid flow (not including the recirculation flow) is slightly smaller than the geometric cross-section A. The velocity $\bar{v}$ is thus defined as $\bar{v} = (1/A_{eff})\iint_{A_{eff}} v\,ds$. Results are expressed as the ratio $\tilde{k}/\tilde{k}_0$, where $\tilde{k}_0$ is the Lemlich permeability factor (thus corresponding to $V_{up}/\bar{v} = 0$), and are plotted as a function of $V_{up}/\bar{v}$ in fig. 3a. Whatever is the value for Bo, the channel permeability is noticeably reduced as $V_{up}/\bar{v}$ reaches unity. More precisely, the channel permeability is reduced by a factor 2 for $V_{up}/\bar{v} = 1$. The evolution for $\tilde{k}/\tilde{k}_0$ can be described by the functional form $\tilde{k}/\tilde{k}_0 \simeq f(V_{up}/\bar{v})$ with

$$f(V_{up}/\bar{v}) = \frac{1}{1 + V_{up}/\bar{v}}. \tag{17}$$

The characteristic size ς over which the counterflow takes place in the transitional region can be determined from the numerical results, as the distance separating the corner of the cross-section with the point corresponding to $v = 0$ (see fig. 3b). Taking $R \approx 10^{-4}$ m, $\mu_S \approx 10^{-8}$ kg/s, $\mu \approx 10^{-3}$ Pa s, and $V_{up}/\bar{v} \approx 1$, the Boussinesq number is set to 0.1 and gives the numerical result $\varsigma \approx 10^{-5}$ m, wich is in good agreement with the value deduced from eq. (6).

2.3 Film swelling

It is now assumed that the Marangoni flow drives some amount of bulk liquid in the film of thickness e (through the well-known Marangoni effect) at a flow rate

$$q_{in} \approx \varsigma e V_{up}. \tag{18}$$

Note that such a liquid exchange lateral flow has been already envisaged by others in the past [25,29]. Moreover, the behaviour of foam films under drainage conditions has been found to resemble the drainage of thin horizontal films, exhibiting characteristic dimple and pinching near the film edge. The Marangoni effect has to be strong enough to open the border pinch. It can be further assumed that the entering liquid is convected along the transitional region, forming a dimpled interface area (bulge), close to the border pinch. This local interface deformation induces a relaxation flow towards the film (rather than through the pinch towards the Plateau border) [32], and as a result, the liquid is partly absorbed by the film whose thickness increases at the same time. This increase is expected to stop as q_{out}, the liquid flow rate towards Plateau borders (due to capillary suction), balances the Marangoni driven flow rate, i.e. $q_{in} \approx q_{out}$. The flow rate of liquid exchange between the Plateau border and the film is obviously strongly dependent on the thickness of the pinch. This information is not available for foam films, which renders difficult the estimation of the corresponding liquid flow rate, q_{out}. However, an estimation will be made in sect. 4 for the configuration corresponding to the experimental system presented in the following.

3 Experiments

The experimental setup used in this study has been previously described and more details can be found elsewhere [11]. We just recall that a vertical Plateau border and the three adjoining films are formed on withdrawing a tripod from a reservoir containing the foaming solution, and that liquid can be injected through the channel at a controlled flow rate Q. The resulting liquid velocity is of the order 10 mm/s, which corresponds to measured velocities during foam drainage experiments.

The soap solution is composed of TTAB (TetradecylTrimethylAmmoniumBromide) at a concentration 3 g/L in pure water. This concentration is above the CMC (1 g/L). The surface tension is $\gamma \approx 38$ mN/m, the density $\rho = 1000$ kg/m^3 and the bulk shear viscosity $\eta = 1$ mPa s.

3.1 Marangoni-driven counterflow

Investigation of counterflow velocities has been performed. The typical length over which V_{up} has to be measured is expected to be of the order of 10^{-5} m. We were not able to measure liquid velocities over such small lengths. Instead, we followed the upward motions of surface irregularities (thin spots) in the films, near the channel/film transitional region. The spots appear at the bottom of the film and then, they are dragged by the counterflow. Note that, although close to the corner of the channel, these spots seem to move apart from the channel, with
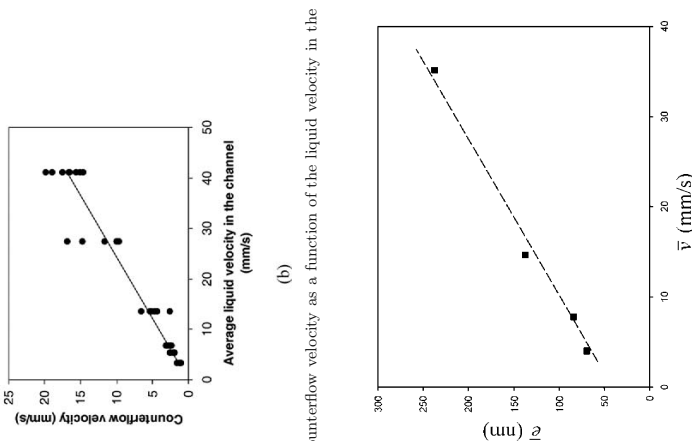
Fig. 4. (a) Picture of the channel/film transitional region. (b) Counterflow velocity as a function of the liquid velocity in the channel.

a separating distance which can be reasonably estimated to be two orders of magnitude smaller than R. This distance presumably corresponds to the typical width of the pinch between the channel and the film.

During their upward motion, the spots are stretched by the shear flow (middle of the film in fig. 4a) so that their lateral spread rapidly reaches a small value. This value is not measurable, but the spots remain distinguishable, allowing for their velocity to be measured. Ascending velocities were deduced from spatio-temporal images obtained along a vertical line close to the pinch. Because of the small lateral spread of these patterns, it is assumed that the velocity of the dragged spots is of the same order of magnitude as V_{up}, although probably smaller due to their finite size. The measurement for the evolution of the spots velocity provides useful information about the evolution of V_{up} with the liquid velocity in the channel. In fig. 4b, resulting values are plotted as a function of $\bar{v}$, determined as the ratio of the injected liquid flow rate to the channel's cross-section area. First of all, the order of magnitude of the counterflow velocity is the same as $\bar{v}$, suggesting that $V_{up}/\bar{v} \sim 1$. Moreover, this velocity is found to be proportional to the liquid velocity in the channel, so that $V_{up} \propto \bar{v}$, in agreement with the evolution predicted by eq. (14).

The present model relies on the presence of small surface tension deviations along the channel. This assumption can be tested through the present experiment. The Laplace law relates the liquid pressure to R: $p_l \simeq p_0 - \gamma/R$. In the present experiment, the liquid pressure at the channel's entrance is [11] $p_l \simeq p_0 - \rho g L + \Delta P$, so that the effective value for the surface tension (dynamical) can be expressed as: $\gamma \simeq (A/\delta_a)^{1/2}(\rho g L - \Delta P)$, where $\delta_a = 0.161$ is a constant relating the channel's cross-section area to R. From experimental results, we find that $\Delta\gamma/\gamma_{eq} \approx 3/38 \sim 0.1$ which validates the assumption made in the model. Moreover, γ is found to increase as a function of ΔP or $\bar{v}$, which is also in agreement with the present model. Unfortunately, due to uncertainties in the measurement of A, the data do not allow for a clear functional form to be determined.

3.2 Films thickness

The films' thickness e is measured by illuminating one film with white light. Each resulting color fringe corresponds to a wavelength λ related to e by [25]: $I/I_m = \sin^2(2\pi n e/\lambda \cos\Phi)$, where n is the refractive index of the soap solution ($n \approx 1.41$), Φ is the angle between the reflected ray and the normal to the film, I/I_m the intensity ratio where the subscript m refers to the maximum measured intensity. The smallest measurable film thickness corresponds to the first intensity maximum, i.e., $e = \lambda/4n$. Black films are thus observed as soon as $e \leq 70$ nm. Note that this value is larger than the known value for the common black film with these solutions [11,33]. At high flow rate, films exhibit an approximately flat thickness profile [11]. In contrast, at low flow rates, the film thickness was found to evolve as a function of z and an average film thickness was therefore defined as: $\bar{e} = \frac{1}{L}\int_0^L e(z)dz$. Corresponding values of $\bar{e}$ are plotted in fig. 5 as a function of the average liquid velocity in the channel. The films' thickness is found to increase linearly as a function of $\bar{v}$. The intercept of the dashed line at $\bar{v} = 0$ is in reasonable agreement with the thickness of common black films for such a solution [33].

4 Discussion

First, we discuss the results for the counterflow velocity and the film thickness. Both of them were found to increase linearly as a function of the average liquid velocity in the channel. The experimental system corresponds to the situation depicted in fig. 2, i.e. a vertical film facing a straight Plateau border. The film area is L^2 and the thickness is e. Due to the presence of pinches near the vertical Plateau border, one can reasonably assume that liquid leaves the film towards the bottom. This situation corresponds to the drainage of a vertical film continuously fed on liquid (wetted) by the counterflow. Although the drainage of vertical films has been extensively studied in the past, our understanding of drainage velocities remains incomplete, especially regarding interfacial boundary conditions and their relation to Marangoni stresses and the associated surfactant adsorption and desorption effects. It was recently shown that effective interfacial mobility can be accounted for by replacing the conventional no-slip boundary condition by an effective slip boundary condition. The introduction of this effective slip parameter enables for measured film thinning rates to be described [34] with a power law function. We assume that the drainage behaviour of the present wetted film is similar to the one corresponding to fresh suspended films. At very short times, the decrease in film thickness can be described with an exponential function: $e \simeq e_0 e^{-\alpha t}$, where α is the thinning coefficient [34]. The thinning rate is thus $de/dt = -\alpha e$ and the flow rate of the liquid leaving the film is $q_{out} = -L^2 de/dt = \alpha e L^2$. Note that the film is continuously wetted and that the film's thickness is constant, i.e. $e = e_0$. For SDS solutions above the CMC, Berg et al. [34] have established the expression for the thinning coefficient: $\alpha = B e_0$, with the constant $B \simeq 10^4$ m^{-1} s^{-1}. q_{out} thus is:

$$q_{out} = BL^2 e^2. \qquad (19)$$

The stationary value for the film's thickness can be obtained from the balance of q_{out} with q_{in} given by eq. (18)

$$e \approx \frac{\varsigma V_{up}}{BL^2}. \qquad (20)$$

The linear relation measured for the evolution of V_{up} as a function of $\bar{v}$ enables the film thickness to be finally expressed as

$$e \approx \frac{\varsigma}{BL^2}\left(\frac{V_{up}}{\bar{v}}\right)\bar{v}. \qquad (21)$$

The film's thickness is thus expected to increase linearly with the liquid velocity in the channel. This is in agreement with experimental results obtained in this study. The order of magnitude of the slope is 10^{-5} s (for the present Plateau border $L \approx 10^{-2}$ m), which compares well with the experimental value, $6 \cdot 10^{-6}$ s. Note that in fig. 5, the

Fig. 5. Stationary thickness of adjoining films as a function of the liquid velocity in the channel. The intercept of the dashed line at $\bar{v} = 0$ is in reasonable agreement with the thickness of common black films with this solution.

Finally, eqs. (17) and (21) account for the coupling between the liquid flow in the channel and the one in the adjoining films. Note, however, that we do not argue that adjoining films have an active contribution to foam drainage. The increase of the films' thickness reflects both the magnitude of surface flows in the transitional region, via the ratio $V_{up}/\bar{v}$, and the intrinsic film permeability, via the thinning coefficient B. The corresponding channel permeability has been previously measured and the model of Lemlich was used to fit values for the surface shear viscosity, as already described in a previous paper [11]. Note that the value for this surface parameter corresponds to an apparent surface shear viscosity and accounts for all viscous dissipation mechanisms associated to the liquid flow in the system but not included in the model. We found [11]: $\mu_S \approx 2.2 \cdot 10^{-8} \pm 0.3\,10^{-8}$ kg s^{-1}, which indeed corresponds to high interfacial mobility. The associated Boussinesq number is $Bo \approx 0.04$ and the permeability coefficient is close to unity, $k_0 \approx 1$. Note that models including Marangoni stresses [17] predict surface rigidification even for low values of E. In contrast, eq. (17) provides a way to relate the Gibbs elasticity with the channel's permeability via the velocity ratio $V_{up}/\bar{v}$. From experimental results, $V_{up}/\bar{v} \approx 1$ and the channel's permeability is given by $k \approx k_0 f(V_{up}/\bar{v}) \approx 0.5$, which is one order of magnitude larger than the permeability of the corresponding rigid channel, i.e. $k_0 = 0.02$. The decrease in channel permeability as a function of surface elasticity is therefore limited. Note, however, that attributing this effect to the surface viscosity, i.e. using the model of Lemlich, results in an overestimate of the fitted value for the surface parameter. For the present case, the ratio $k/k_0 \approx 0.5$ corresponds to a Boussinesq number and a surface parameter slightly overestimated by a factor 2.5. This effect is therefore small compared to error bars generally associated to the measurement of the surface parameter.

5 Conclusion

The present work is the first attempt to relate the flow in foam channels to the behaviour of the adjoining films. As a minimal ingredient accounting for film swelling, Marangoni stress and Gibbs elasticity have been introduced in a model based on a recirculation mechanism for the surfactant in the transitional region between the channel and the adjoining films. An expression for the velocity of the corresponding surface flows has been obtained and predicts a proportionality relation as a function of the liquid velocity in the channel. New experimental data have been provided and prove this relation to be linear. The effect of these surface flows on the channel's permeability has been determined. The permeability was found to depend explicitly on Gibbs elasticity, but in contrast to previous work, this effect does not contribute to rigidify the channel surface. This behaviour definitely distinguishes

the drainage in foam channels from the drainage of thin horizontal films.

Many improvements can be brought to the present model. Among them, the flow rate for liquid exchange between the channel and the film should be carefully investigated. Finally, a dedicated study of the influence of the surface elasticity should be undertaken. This latter should combine measurements of channel permeability, counter-flow velocity and film thickness measurements, as well as a complete rheological characterisation of the investigated interfaces.

Appendix A. List of symbols

Bo	Boussinesq number, $Bo = \mu_S/\mu R$
μ_S	surface shear viscosity
μ	shear viscosity of the bulk
R	channel width
L	channel length
Γ	surface concentration of surfactant
Γ_{eq}	equilibrium surface concentration of surfactant
Γ^-, Γ^+	surface concentration of surfactant at both channel ends, upstream and downstream, respectively
$\Delta\Gamma$	deviations of surface concentration with respect to equilibrium
q	flow rate of surfactant convected along the channel surface
q_e	flow rate of surfactant exchanged at both channel ends
q^V	flow rate of surfactant due to diffusion from/into the bulk
q^S	flow rate of surfactant due to diffusion from/into the films surface
q^M	Marangoni-driven flow rate of surfactant
q_{in}	flow rate of liquid driven by Marangoni effect in the film
q_{out}	flow rate of liquid leaving the film
Q	liquid flow rate through the channel
A	channel cross-sectional area
u	velocity at the channel surface
$\bar{v}$	average liquid velocity in the channel
E	Gibbs elasticity
D	bulk diffusion coefficient
D_S	surface diffusion coefficient
τ_M	Marangoni stress
ς	characteristic length of the Marangoni flow in the transitional region
V_{up}	characteristic velocity of the Marangoni flow in the transitional region
$\bar{k}$	permeability factor $\bar{k} = \mu\bar{v}/A(dp/dz)$
$\bar{k}_0$	Lemlich permeability factor
β	ratio of surface and bulk concentrations of surfactant, $\beta = (d\Gamma/dC)_{eq}$
e	film thickness
γ_{eq}	equilibrium surface tension
$\Delta\gamma$	deviation of the surface tension with respect to equilibrium

References

1. G.D. Miles, L. Shedlovsky, J. Ross, J. Phys. Chem. **49**, 93 (1945).
2. R.A. Leonard, R. Lemlich, AIChE J. **11**, 18 (1965).
3. D. Weaire, N. Pitter, S. Hutzler, D. Pardal, Phys. Rev. Lett. **71**, 2670 (1993).
4. Bhakta, E. Ruckenstein, Adv. Colloid Interface Sci. **70**, 1 (1997).
5. S.A. Koehler, S. Hilgenfeldt, H.A. Stone, Langmuir **16**, 6327 (2000).
6. V. Carrier, S. Destouesse, A. Colin, Phys. Rev. E **65**, 061404 (2002).
7. S.J. Neething, H.T. Lee, J.J. Cilliers, J. Phys.: Condens. Matter **14**, 331 (2002).
8. A. Saint-Jalmes, Y. Zhang, D. Langevin, Eur. Phys. J. E **15**, 53 (2004).
9. E. Lorenceau, N. Louvet, F. Rouyer, O. Pitois, Eur. Phys. J. E **28**, 293 (2009).
10. S.A. Koehler, S. Hilgenfeldt, E.R. Weeks, H.A. Stone, Phys. Rev. E **66**, 040601 (2002).
11. O. Pitois, C. Fritz, M. Vignes-Adler, J. Colloid Interface Sci. **282**, 458 (2005).
12. O. Pitois, C. Fritz, M. Vignes-Adler, Coll. Surf. A **261**, 109 (2005).
13. O. Pitois, E. Lorenceau, N. Louvet, F. Rouyer, Langmuir **25**, 97 (2009).
14. I.B. Ivanov, D.S. Dimitrov, in *Thin Liquid Films* (Dekker, New York, 1988).
15. D.E. Tambe, M.M. Sharma, J. Colloid Interface Sci. **147**, 137 (1991).
16. A.A. Sonin, A. Bonfillon, D. Langevin, J. Colloid Interface Sci. **162**, 323 (1994).
17. M. Durand, D. Langevin, Eur. Phys. J. E 7, 35 (2002).
18. M. Durand, G. Martinoty, D. Langevin, Phys. Rev. E **60**, R6307 (1999).
19. N. Louvet, F. Rouyer, O. Pitois, J. Colloid Interface Sci. *In press* (2009) doi:10.1016/j.jcis.2009.02.042.
20. K. Feitosa, D.J. Durian, Eur. Phys. J. E **26**, 309 (2008).
21. S. Hilgenfeldt, S. A. Koehler, H.A. Stone, Phys. Rev. Lett. **86**, 4704 (2001).
22. S.A. Koehler, S. Hilgenfeldt, H.A. Stone, J. Colloid Interface Sci. **276**, 420 (2004).
23. F. Rouyer, E. Lorenceau, O. Pitois, Coll. Surf. A **324**, 234 (2008).
24. A. Britan, M. Liverts, G. Ben-Dor, S.A. Koehler, N. Bennani, Coll. Surf. A **344**, 15 (2009).
25. K.J. Mysels, K. Shinoda, S. Frankel, *Soap Films, Studies of Their Thinning* (Pergamon Press, New York, 1959).
26. K.J. Mysels, M.C. Cox, J.D. Skewis, J. Phys. Chem. **65**, 1107 (1961).
27. K.J. Mysels and M.C. Cox, J. Colloid Sci. **17**, 136 (1962).
28. J. Lyklema, P.C. Scholten, K.J. Mysels, J. Phys. Chem. **69**, 116 (1965).
29. J.B.M. Hudales, H.N. Stein, J. Colloid Interface Sci. **138**, 354 (1990).
30. A. Nguyen, J. Colloid Interface Sci. **249**, 194 (2002).
31. J.W. Gibbs, *The Collected Works* (Longmans Green, New York, 1931).
32. A. Aradian, E. Raphael, P.-G. de Gennes, Europhys. Lett. **55**, 834 (2001).
33. E. Terriac, F. Artzner, C. Meriadec, P. Chasle, J. Ohana, J. Emile, Langmuir **23** 12055 (2007).
34. S. Berg, E.A. Adelizzi, S.M. Troian, Langmuir **21**, 3867 (2005).

ELSEVIER

Letter

Film junction effect on foam drainage

F. Rouyer*, E. Lorenceau, O. Pitois

Université Paris-est, Laboratoire de Physique des Matériaux Divisés et des Interfaces, UMR CNRS 8108, 5 bvd Descartes, 77454 Marne la Vallée Cedex 2, France

ABSTRACT

Foam drainage is modelled by the flow of liquid through Plateau borders (PBs) that are the liquid channels resulting from the merging of three liquid films separating the gas bubbles. Available models generally neglect the influence of these films. Yet, within drainage conditions, experimental observations indicate a strong coupling of these films with the channels. We consider the influence of films on foam drainage through their effect on the cross-section geometry of the channels. More precisely, we assume that the Plateau border cross-section is enclosed by three circular arcs that are not always tangent but instead exhibit a non-zero contact angle θ as it has been observed experimentally. The liquid flow through the channels is studied using numerical simulations whose parameters are θ and the Boussinesq number, Bo, that reflects the surface shear viscosity of the interface. We show that, for values of Bo relevant for foam drainage conditions, a slight increase of θ results in a strong decrease of the average liquid velocity.

© 2008 Elsevier B.V. All rights reserved.

1. Introduction

Aqueous foam can be viewed as a porous medium in which the foaming liquid is the continuous phase confined between the gas bubbles. For relatively dry foams, the liquid flow does not concern essentially in the narrow channels resulting from the merging of the liquid lamella separating the bubbles, but instead takes place through their effect on the cross-section geometry of the channels. More precisely, we assume that the lamella 3×2 [1], called the Plateau borders (PBs). Due to capillary forces, the cross-section of these channels is almost an equilateral triangle except that the three segments joining the vertices are tangent circular arcs of radius R (cf. Fig. 1).

Liquid foam drainage theories [1,2] consider essentially the unidirectional flow transverse to the planar area that sketches the PB cross-section. Recently some advance has been done in the understanding of drainage velocities in relation with the rheological properties of the surfactants monolayers confining the liquid phase. Indeed, in addition to the fact that area and shape of the channels can vary during drainage, the velocity at the boundaries is not zero and its value depends on the properties of surfactants: different molecules are more or less likely to be set in motion with the liquid flow. The Boussinesq number Bo, that compare viscous dissipations in the bulk and in the interfaces [3], has been found to reasonably describe reported drainage velocities, although the drainage behaviour of foams with bubble sizes lower than a few hundred micrometers seems still to defy this theoretical frame-

work [4]. However, we stress that the comparison of the theoretical predictions with experimental results consider the surface shear viscosity as the only adjustable parameter over the whole range of investigated liquid fractions, assuming the PB cross-section to be the ideal cross-section described above. Is this assumption reasonable? Response elements have to be found from the study of the PB/films joining areas under drainage conditions. Previous studies on liquid drainage did not focus on this aspect so that it is still difficult to describe, even qualitatively, the hydrodynamic coupling of flows through the PB and the films. Some authors reported counter-current flows within the PB adjoining films [3], as well as dimples and pinchings associated to films swelling occurring as liquid drainage proceeds [5]. The study of drainage through a single isolated PB reveals the same films swelling phenomena [6]. A previous theoretical work has demonstrated that the influence of the film thickness, h, is non-negligible for h/R larger than 10^{-2} [7]. Such films thicknesses are consistent with films thickness measurements, but the authors assumed planar films joining the PB, in contradiction with observed interface distortions [5]. Obviously, the complete understanding of the films behaviour in response to the liquid flow through the PB is far from being achieved, but, a deviation of the geometry with reference to the ideal case is conceivable. In particular, the evaluation of the impact of this deviation on the PB permeability would be of interest for the analysis of experimental data. In this work, we propose to take into account the deviation of the PB cross-section geometry by introducing an *apparent contact angle* (θ) of the PB interfaces with the adjoining films. If the film is subjected to complex internal flows resulting in the formation of pinchings and dimples associated to swelling process, then

The liquid flow through PB channel is assumed to be uniaxial and stationary. It is modeled by the liquid velocity $v(x, y)$ along the axis z in the Cartesian space (x, y, z). In foam drainage where the typical velocity and length (radius of PB) are, respectively, of the order of 1 mm/s and 100 μm, the typical Reynolds number of the flow is smaller than 1, and the Stokes equation is used:

$$\Delta v = -\frac{1}{\mu}\frac{dp}{dz} \tag{1}$$

where μ is the liquid viscosity and p is the liquid pressure (the pressure gradient in 1 includes gravity forces). Partial mobility of the PB interfaces is obtained balancing the bulk viscous stress with the surface viscous stress [3] on the circular boundary:

$$\mathbf{n}.\nabla v = \frac{\mu_s}{\mu}\Delta_s v \tag{2}$$

where μ_s is the shear surface viscosity and Δ_s is the surface Laplacian. Finally, we consider that the velocity is 0 at the corner [3].

All these equations are made dimensionless and implemented in Comsol using l and $U = (dp/dz) l^2/\mu$ as length and velocity scales, and introducing the Boussinesq number $Bo = \mu_s/l\mu$. Numerical resolution is performed for all cross-sections and for parameter Bo varied from 0.001 to 1000. Fine mesh size is chosen in the PB domain, and on the circular boundary, mesh size is imposed to be less than 10^{-4} with a growth rate equal to 1.05.

3. Results and discussion

The results are expressed as the channel dimensionless permeability factor defined as the $k = \bar{v}/\mu/A)/(dp/dz)$ where $\bar{v}$ is the mean velocity. This factor is equal to the scaled average velocity and represents the ability of the liquid to flow for given values of the variation of k as a function Bo for several geometries. First of all, let us emphasize that the simulations presented in this paper are in complete agreement with previous computational and analytical results [9,10] for $\theta = 0°$ and $30°$. We denoted k_0 the values of k for $\theta = 0°$. The effect for intermediate values of θ can be considered as a function of the Bo number: for large values ($Bo \gg 1$) it is observed that $k/k_0 > 1$, whereas for small values ($Bo \ll 1$), $k/k_0 < 1$. For intermediate values ($Bo \sim 1$), the dependence of the permeability as a function of θ is very limited, whatever is θ. Considering Bo values corresponding to drainage conditions with usual surfactants,

θ only reflect the dynamical configuration of the interfaces within the joining area (see Fig. 2). Note also that some authors [4] refer to coarsening experiments to argue that these swelling phenomena are restricted to bubbles larger than the millimetre range, and that for smaller bubbles, the liquid films thickness may be independent of liquid flow through the channel, as a result of PB capillary suction. Thus, if the dynamical situation is assumed to be close to the static equilibrium of films with the PB, it is justified to consider that the film thickness remains close to that of the black film (no swelling). Precisely, a nonzero contact angle between a thin film and a bulk liquid is observed in a number of experiments and in particular with foam films [8], these angles can reach values up to 10°. In that case, the angle θ introduced in the present study corresponds to this thermodynamical contact angle. To resume, introducing a contact angle in the film joining area appears to be a convenient way to describe the effect of films on the PB cross-section geometry, whatever is the nature of the films equilibrium: dynamical for thick and swelled films or static for Newton black films. The influence of this angle on the liquid flow through the channel is reported in this letter.

2. Governing equations and simulations

We consider a PB cross-section of area A in a plane (x, y). PB boundaries are three circular arcs of radius R whose centers are outside the domain and form an equilateral triangle. Junctions 2×2 of these boundaries are vertices of an equilateral triangle of length l (cf. Fig. 2). The ideal PB geometry is composed of tangent circular arcs of radius $R = l$, θ is varied in the range [0°, 30°] corresponding to values of R, respectively, from l to infinity. This geometry has three axes of symmetry, thus only one-sixth of the area is considered in the simulation.
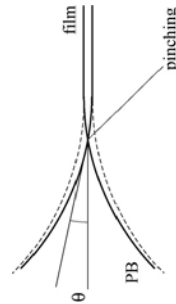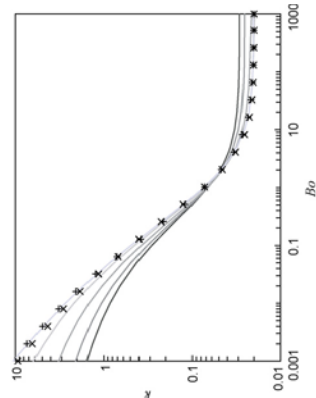
F. Rouyer et al. / Colloids and Surfaces A: Physicochem. Eng. Aspects 324 (2008) 234–236

235

Contents lists available at ScienceDirect

Journal of Colloid and Interface Science

Ripening of a draining foam bubble

N. Louvet *, F. Rouyer, O. Pitois

Université Paris-Est, Laboratoire de Physique des Matériaux Divisés et des Interfaces, UMR CNRS 8108, 5 bvd. Descartes, 77454 Marne la Vallée Cedex 2, France

A B S T R A C T

A forced Ostwald ripening experiment is performed on a single foam bubble. The bubble size is followed as the system is wetted with a constant liquid flow rate delivered from one of the bubble Plateau borders. Obtained ripening velocities cannot be described with a model based on a constant film thickness assumption. Within these well-controlled experimental conditions, the film thickness is measured and found to depend on the imposed liquid flow rate. It is shown that the bubble growth rate is well predicted as the films thickness evolution is explicitly introduced in the ripening model. Finally, it is suggested that existing results for the coarsening of draining foams could be understood following the approach validated on the bubble scale.

© 2009 Elsevier Inc. All rights reserved.

1. Introduction

Liquid foam is a soft material constituted of gas and liquid containing surfactants. The main part of the liquid phase is confined within Plateau borders (Pbs), that are the liquid channels resulting from films merging (three by three) and within the nodes (connecting four Pbs). Foam evolves by three interdependent mechanisms: liquid drainage driven by gravity and capillary pressure differences, coarsening due to the bubble capillary pressure differences, and coalescence, i.e. the bursting of liquid films separating neighboring bubbles. Previous works have focussed on experiments enabling these mechanisms to be decoupled. For example, forced drainage has been preferred to free drainage in order to performed permeability measurements on a time scale much smaller than the characteristic time scale for coarsening [1–3]. Equivalently, gas diffusion process was strongly reduced using fluorated gas [4]. Other studies have referred to more general situations, i.e. the coupling between drainage and coarsening [4–8]. Quantitative agreement was found for the evolution of the bubbles radius R using the following relation:

$$R\,dR/dt = D \cdot g(\varepsilon) \qquad (1)$$

where D is a constant with units of a diffusion coefficient, $g(\varepsilon)$ is a function of the liquid fraction [4] determined as follows: gas transfer is assumed to occur only through the thin films facing the foam bubbles, and the corresponding surface area is estimated using numerical tools. Then, coarsening rates are deduced assuming a constant film thickness e_0 as a fitting parameter. Several proposi-

tions exist for $g(\varepsilon)$ [4–6] but in any case, the film thickness is assumed to be constant. Moreover, e_0 has been shown to be a major parameter in the description of coarsening data [9]. Obtained values have been found to fall within the broad range of expected thicknesses for common black films, thus justifying the constant thickness approach. However, through extensive work on draining foams, Feitosa et al. [7] have recently weakened this simple picture for coarsening: available models failed in describing the whole range of investigated liquid fractions, so that an empirical relation was preferred for $g(\varepsilon)$. The origin of this disagreement is not yet explained.

On the other hand, a recent work focussed on the measurement of films thicknesses during foam drainage experiments [10]. It has been shown that a coupling mechanism exists between liquid flow through the Plateau borders network and film thicknesses. As a result, the film thickness is found to increase as the draining liquid flow rate increases. Moreover, this relation between the film thickness and the liquid flow rate has been confirmed by measurements performed on a single Plateau border [11]. The magnitude of the observed film swelling phenomena has been proved to be dependent on the foaming solution [10,11], and non-uniform thickness profiles have also been reported [10], suggesting complex involved phenomena. It is sometimes argued that such a swelling effect is restricted to large bubbles, i.e. millimeter range [12].

Obviously, the understanding of this coupling is very poor [10,11], and this constitutes a limiting stage in the complete description for the coarsening of draining foams. To progress further this way, it seems to us that a study of foam coarsening in relation with the films thicknesses within draining conditions should be undertaken. We realized that an experiment on the bubble scale offers a simple way to control the draining liquid flow rate

* Corresponding author. Fax: +33 1 60 95 72 97.
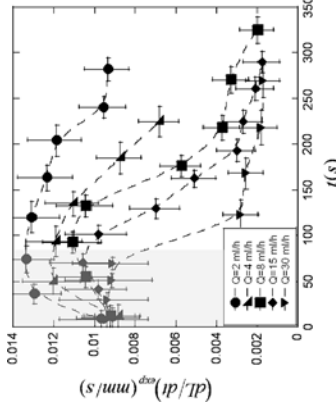 E-mail address: nicolas.louvet@univ-mlv.fr (N. Louvet).

Fig. 4. Rescaled dimensionless permeability factor k as a function θ for Bo varied from 0.001 to 100. k is rescaled by k_0 measured for $\theta = 0°$.

i.e. $Bo \sim 0.01$–0.1, it can be observed that the decrease in channel permeability is effective as soon as θ reaches a few degrees. The permeability decreases from 10% up to 25% of its value for small angle of contact equal to 5°, and decreases from 20% up to 45% of its value for angle of contact equal to 10°. Qualitatively, the behaviour can be explained by the strong localization of velocity gradients in areas close to the corners that are precisely the most affected areas as θ slightly increases. It is difficult to compare these values of θ with experimental one in the case of pinchings, but for static black films values close to 5° have been often reported.

From a practical point of view, an analytical approximate expression is provided to describe the effect of θ on the channel permeability. The channel permeability is expressed as $k = k_0 f(\theta, Bo)$ where

$f(\theta, Bo)$

$= \left(1 + \sin\left(\theta\frac{Bo}{1+Bo}\right)\right) \exp\left(-0.59\,Bo^{-0.24}\sin(\theta)^{0.78+0.022\ln(Bo)}\right)$ (3)

This expression provides values that are close to the one obtained from simulations within error bars less than 10% over the whole ranges of values for θ and Bo.

Finally, we would like to emphasize that the contact angle has also a strong effect on PBs cross-section areas. Although the variation of A as a function of θ is taken into account in the determination of the PB permeability via Eq. (3), it should be recalled that in the foam, the radius of curvature R is fixed by the pressure jump across the fluid interface and by surface tension σ. For relatively dry foams, this relation can be expressed as: $\Delta p = p - p_{gaz} \cong \sigma/R$ [1]. Thus, for a given pressure gradient through the channels (this corresponds to the experimental situation), R is fixed whatever is the contact

angle. As a result, the PB cross-section area is given by the relation:

$A = \delta_a^\theta R^2$ with

$$\delta_a^\theta = 2\sin^2\left(\frac{\pi}{6} - \theta\right)\cos\left(\frac{\pi}{6}\right) - 3\left(\left(\frac{\pi}{6} - \theta\right)\cos\left(\frac{\pi}{6} - \theta\right)\right)$$

Because of this influence of the contact angle on A (note that Bo is also slightly modified), it is more appropriate to compare the mean velocities of the liquid through the channel for a given pressure gradient. It can be verified for example that for $Bo = 0.01$, the decrease observed in the mean velocity reaches 35% and even 60% for contact angles equal to 5° and 10°, respectively.

This result shows that the contact angle may have a large effect on drainage velocities. In fact, this effect on the channel permeability is found to be of the same order of magnitude than the one calculated in a previous numerical work that considered planar thick films tangentially connected to the Plateau border [7].

4. Conclusions

Numerical results have been presented for the flow of liquid through a fluid foam channel exhibiting a contact angle with the adjoining films. In addition to reflect the thermodynamical equilibrium of the channel connected to Newton Black Films, the introduction of this angle is a convenient way to describe the interface distortion in the joining area as drainage proceeds through the channel. It is shown that for low values of Bo, the channel permeability is strongly affected by the presence of this angle, even for the smallest values. As the PB permeability and average drainage velocity are found to be extremely dependent on the cross-section geometry as soon as the corners are concerned (present paper and 7), further improvement of the drainage theory certainly requires to complete the understanding of these joining areas with the films.

Acknowledgements

We acknowledge the ANR (ANR-05-JCJC-0234-01) for financing the investment of the software and hardware necessary to the modeling.

References

[1] D. Weaire, S. Hurzler, Physics of Foam, Oxford University Press, 1999.
[2] S.A. Koehler, S. Hilgenfeld, H.A. Stone, Liquid flow through aqueous foams: the node-dominated foam drainage equation, Physical Review Letters 82 (1999) 4232.
[3] R.A. Leonard, R. Lemlich, A study of interstitial liquid flow in foam. Part I. Theoretical model and application to foam, AIChE Journal 11 (1965) 18.
[4] A. Saint-Jalmes, Physical chemistry in foam drainage and coarsening, Soft Matter 2 (2006) 836.
[5] V. Carrier, S. Destouesse, A. Colin, Foam drainage: a film contribution? Physical Review E 65 (2002) 061404.
[6] O. Pitois, C. Fritz, M. Vignes-Adler, Liquid drainage through aqueous foam: study of the flow on the bubble scale, Journal of Colloid and Interface Science 282 (2002) 458.
[7] S.A. Koehler, S. Hilgenfeld, H.A. Stone, Foam drainage on the microscale. I. Modeling flow through single Plateau borders, Journal of Colloid and Interface Science 276 (2004) 420.
[8] P.M. Kruglyakov, D.R. Exerowa, Foam and Foam Films, Khimia, Moscow, 1990.
[9] D. Desai, R. Kumar, Flow through a plateau border of cellular foam, Chemical Engineering Science 37 (1982) 1361.
[10] A.V. Nguyen, Liquid drainage in single plateau borders of foam, Journal of Colloid and Interface Science 249 (2002) 194.

As we are interested with diffusion processes, the film surface A can be divided into N areas A_i with a corresponding thickness e_i, so that the effective film thickness e^* can be introduced:

$$1/e^* = (1/A)\sum_{i=1}^{N} A_i/e_i \quad (5)$$

As explained above, investigated bubble films can be reasonably described with N = 2. In the following we will use the approximation: $1/e^* \approx (1/A)(A_1/e_1 + A_2/e_2)$, where A_1, e_1 and A_2, e_2 are respectively the area and the thickness for the thin and thick parts of the film area. Note that e_1 is chosen equal to 60 nm and e_2 equal to the thickness corresponding to the dominant color fringe.

3. Modelling the bubble growth rate

Exchange of N_2 through the bubble surface is driven by the difference in N_2 concentration between surrounding gas (C_{out}) and the internal bubble volume (C_b). Neglecting the bubble mean curvature, the gas bubble pressure is $P_b \approx P_0$ and the total (all species: soluble –s– and insoluble –ins–) gas concentration is:

$$\frac{n_T}{V_b} = \frac{n_s + n_{ins}}{V_b} \approx \frac{P_0}{RT} \quad (6)$$

The concentration of soluble species (N_2) is thus $C_b = n_s/V_b \approx P_0/RT - n_{ins}/V_b$ so that the nitrogen concentration difference $\Delta C_s = C_{out} - C_b \approx n_{ins}/V_b$. Introducing the initial concentration of insoluble species,$C_0 = n_{ins}/V_0$, the nitrogen concentration difference can be written, using Eq. (2):

$$\Delta C_s \approx C_0 \cdot f(L) \quad (7)$$

where $f(L) = (L_0^3 + c/h)/(L^3 + c/h)$. Note that $f(L)$ is a decreasing function of time.

Considering a diffusion process for the transport of soluble gas species through the bubble surface, the change in bubble volume dV_b/dt can be expressed as:

$$\frac{dV_b}{dt} = 3k_f^s A\Delta C_s S v_m \quad (8)$$

where v_m is respectively the ideal gas molar volume and $k_f^s = D_m/e^*$ is the effective permeability of a bubble covering film. From Eqs. (2), (3), (7) and (8), the theoretical bubble size growth rate is thus given by:

$$\left(\frac{dL}{dt}\right)_{th}^* = f(L)\frac{b}{h}C_0\frac{D_m}{e^*}Sv_m \quad (9)$$

Note that assuming a constant film thickness, the growth rate becomes:

$$\left(\frac{dL}{dt}\right)_{th}^0 = f(L)\frac{b}{h}C_0\frac{D_m}{e_0}Sv_m \quad (10)$$

this latter unambiguously decreases as a function of time.

4. Results and discussion

In Fig. 2, the bubble growth rate is plotted as a function of time for several injected liquid flow rates. As clearly distinct curves are obtained, it can be concluded that the liquid flow rate affects the bubble ripening. Note however that just after the bubble formation, the system drains freely so that the flow rate of liquid that really flows through the system is larger than Q. This effect is all the more dominant that the flow rate is small. In fact, the flow rate appears to be controlled only after a short period represented in gray in Fig. 2. Consequently, data plotted in the gray area will not be discussed in the following. After this short period, the bub-

ble growth rate is found to be a decreasing function of time, the decrease being all the more pronounced than the liquid flow rate is high. However, as dL/dt depends on the bubble size, it is more relevant to compare the growth rates for several fixed values of the bubble size. In Fig. 3, the ratio $(dL/dt)_{exp}/(dL/dt)_{exp}^0$ is plotted as a function of Q for several fixed values of L, assuming $e_0 = 60$ nm. The data confirm that the growth rate is a decreasing function of the injected liquid flow rate, whatever is the bubble size. Moreover, the decrease is dependant on the bubble size. For the largest bubble size, the growth rate is getting closer to the theoretical value as the liquid flow rate is decreased to lowest investigated value. Thus, the constant thickness approach fails in describing the results obtained for the bubble ripening under steady drainage conditions. Note that for experiments performed on macroscopic foam samples, the film surface area contributing to gas exchange is a model dependent parameter, so that several relations coexist to estimate this parameter. In the present situation, no geometrical assumption is required to estimate the films surface area: it is precisely known from the bubble size measurements. The observed discrepancy therefore results from the films thickness variations.

The effective thickness e^* is now plotted as a function of the liquid flow rate for several bubble sizes (Fig. 4). For the smallest

Fig. 2. Bubble growth rate as a function of time for several flow rates.

Fig. 3. Bubbles growth rates as a function of the liquid flow rate for several bubble sizes.

---

and to measure the bubble size as well as the film thicknesses. Moreover, and as a major advantage with respect to the macroscopic scale, interpretation of data is not related to any assumption for the foam geometry. The presentation of this experiment and the resulting experimental data is precisely the purpose of this paper.

2. Experiment

The coupling between coarsening and drainage is studied on the bubble scale using the Plateau border apparatus previously described in Refs. [11,13]. A single Pb is generated by pulling a dedicated frame out of a bath of soap solution. A gas bubble is then formed below the Pb with a syringe, so that one node, four Pbs and associated films are obtained (Fig. 1a). The gas diffusion is forced by producing the bubble partly with a gas that is insoluble in water and that is not present outside of the bubble. The growth of the bubble is expected to depend on the gas concentration gradient (difference of concentration over film thickness), properties of the gas (solubility, diffusion coefficient) and area of exchange (film surface area).

Beforehand, the chamber is saturated with N_2 gas. The bubble is then formed with a mixture of N_2 and C_6F_{14} obtained by bubbling N_2 in a bottle of C_6F_{14}. The resulting concentration C_0 in C_6F_{14} has been determined from the mass variation m of C_6F_{14} in the bottle for a flowed volume V of N_2: $C_0 = m/(MV)$, where M = 338 g mol^{-1}. An average value $C_0 \approx 10$ mol/m^3 was obtained. This is in good accordance with the concentration deduced from the saturated vapor pressure for C_6F_{14} in air at a temperature T = 298 K: $C_0 = P_{sat}/(RT)$. With $P_{sat} \approx 2.9 \times 10^4$ Pa and R = 8.314 J K^{-1} mol^{-1}, this gives $C_0 \approx 12$ mol/m^3.

Molecular diffusion coefficient and Ostwald coefficient of solubility for N_2 in water are respectively $D_m = 2 \times 10^{-5}$ cm^2/s, and $S = 1.65 \times 10^{-2}$ [14]. Solubility of C_6F_{14} is known to be almost 1000 times lower than N_2, so that in the following, C_6F_{14} is considered as an insoluble species.

The soap solution is obtained from TTAB (Tetradecyl Trimethyl Ammonium Bromide) at a concentration 3 g/L in pure water. This concentration is well above the CMC (1 g/L). The surface tension is $\gamma = 38$ mN/m, the density $\rho = 1000$ kg/m^3, the bulk shear viscosity $\eta = 1$ mPa s and the surface shear viscosity $\eta_s \approx 10^{-5}$ g/s [11]. This low value for η_s corresponds to a high mobility for the interfaces.

A motor driven syringe is used to deliver soap solution through the upper Pb at a controlled flow rate Q. Note that due to the geometrical configuration of the Pbs, the flow rate in each of the three lower Pbs is equal to Q/3. In the following, Q = 2, 4, 8, 15 and
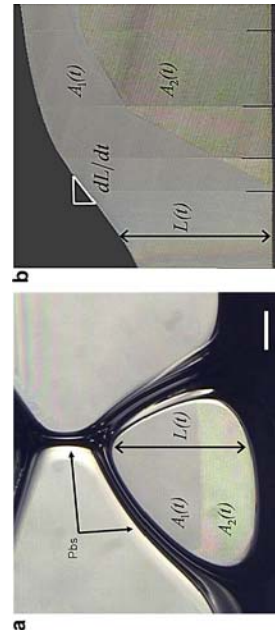
30 ml/h. The resulting liquid velocity is of the order 1 mm/s, which corresponds to measured velocities during foam drainage experiments.

The evolution of the bubble was followed with a colored CCD camera operating at frame rate of 1 Hz. The bubble growth can be determined from the measurement of the vertical distance L separating the liquid bath from the node (Fig. 1a). The numerical counterpart of the experimental bubble configuration was simulated using Surface Evolver software [15] to relate L to the volume V_b and film surface area A of the bubble (one bubble trapped under a Plateau border created at the junction of three vertical films considering density, and surface tension values of the experiment). Simulations are performed for bubble sizes which fall in the range of experimental values. The bubble volume and the surface area for one film were found to be accurately described by the following relations:

$$V_b = hL^3 + c \quad (cm^3) \quad (2)$$
$$A = bL^2 \quad (3)$$

where h, c and b are constant and equal respectively to 1.646, 0.0023 and 1.189.

In our system and within the range of investigated liquid flow rates, A was not found to depend on Q for a given bubble volume. In practice, L is determined as a function of time from spatio-temporal diagrams for the bubble height, such as the one presented in Fig. 1b. In this diagram, the slope of the upper dark boundary is the bubble size growth rate: $(dL/dt)_{exp}$.

The bubble films thickness e is measured by illuminating one film with white light. Each resulting color fringe corresponds to a wave length λ related to e by [16]:

$$I/I_m = \sin^2(2\pi ne/\lambda \cos \Phi) \quad (4)$$

where n is the refractive index of the soap solution ($n \approx 1.41$), Φ is the angle between the reflected ray and the normal to the film (note that due to the meridian curvature of the films, Φ varies within the range 20–30°), I/I_m the intensity ratio where the subscript m refer to the maximum measured intensity. The smallest measurable film thickness corresponds to the first intensity maximum, i.e. $e \approx \lambda/4n$. Black films are thus observed as soon as $e \leqslant 70$ nm. Note that this value is larger than the known value for the common black film with this solution [17,11].

Fig. 1a shows that the bubble film exhibits a non-uniform thickness profile. For the most part of investigated films, the top is thin and is black/silver color, whereas the bottom is much thicker with corresponding color fringes. This "step" profile can be observed in the diagram of Fig. 1b. As time increases, the bubble height increases and the thicker part covers a higher fraction of the total film area.

Fig. 1. (a) Bubble with it four Pbs. Q = 15 ml/h and t = 140 s. The white scale bar is 1 mm. (b) Spatio-temporal evolution of the bubble size. The horizontal axis is time and the z-axis is the vertical position (bubble size). The white line illustrates the measurement of the bubble size growth rate.
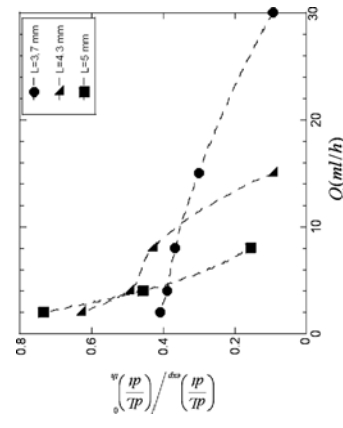
Fig. 4. Equivalent film thickness as a function of the liquid flow rate for several bubble sizes.

bubbles and smallest liquid flow rates, the soap solution seems to flow down through a central dimple (Fig. 5), and to flow up near the Plateau borders (not distinguishable in Fig. 5). The observed flow pattern has a strong likeness with the one previously reported for foams under steady drainage conditions [10]. For such conditions, the equivalent film thickness was difficult to determine. A value was however obtained assuming the "step" profile, but in these cases, the equivalent film thickness is generally underestimated (concerned data are plotted in white circles in Figs. 4 and 6).

In Fig. 4, e^* is found to increase as a function of the injected liquid flow rate, whatever is the bubble size. Considering several bubbles with the same size, it is shown that the velocity of the liquid flowing through the system strongly affects the films thickness. From Fig. 4 it can be also concluded that e^* increases as a function of the bubble size. We interpret this dependence by the following argument. The geometry of the system is dictated only by capillary forces due to the low pressures involved in the liquid flow, thus, the Pbs cross-section at the junction with the node is given by: $a \approx (\gamma/\rho gL)^{1/2}$ [11], so that the value of Q, increases with L for a fixed value of Q and obviously increases with Q for a fixed value of L. Again, this shows the strong influence of the liquid velocity in this problem. Also not well understood for the moment, films swelling phenomena appear to be related to
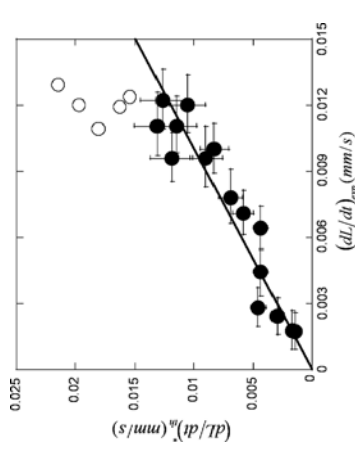
the strong Marangoni counter-flows developing at the Pb/film junction. As an additional qualitative information, we observed that the intensity of these counter-flows (velocity and size) increases as the Pb liquid velocity increases. It can be therefore understood that the film opens as the liquid velocity reaches a critical value. Moreover, the film swelling probably begins with a transitional stage associated to a central dimple. As pointed out by Carrier et al. [10], the appearance of this dynamical structure is related to the soap solution. The present work reveals that for a given soap solution, the observation of the central dimple is limited to a given range of liquid flow rates. Obviously, the presence of these dynamical structures suggest that the swelling mechanism cannot be understood only from considerations about the static equilibrium for the thin film. Whatever is the physical origin of the swelling mechanism, this later strengthen the coupling between the ripening and liquid drainage, involving the films thickness variation with the liquid velocity in the Plateau borders.

Using the values for the effective films thickness, the theoretical bubble growth rate is compared to experimental data. This comparison is presented in Fig. 6, showing a good agreement. Disregarding for data corresponding to the dimple flow pattern as already explained (white spots in the figure), the bubble growth rate is well predicted as soon as the effective films thickness is taken into account.

At this point, an attempt is done to find some link between the present result and results obtained on the macroscopic scale. In a recent paper, Feitosa et al. [7] compared together a consequent set of results for the coarsening of draining foams, over a wide range of values for the liquid volume fraction ε. It is shown that the dependence of the coarsening rate with ε is better described with an empirical functional form for $g(\varepsilon)$ in Eq. (1):

$$RdR/dt = D_1 \cdot g_1(\varepsilon) = \frac{D_1}{\sqrt{\varepsilon}} \qquad (11)$$

In contrast, a functional form that measures the ratio of gas bubbles covered by thin films [4]:

$$RdR/dt = D_2 \cdot g_2(\varepsilon) = D_2 \cdot \left(1 - \sqrt{\varepsilon/0.44}\right)^2 \qquad (12)$$

appears to fail in describing the data over the whole range of investigated liquid fractions [7]. (note that another function: $g_1(\varepsilon) = 1 - \sqrt{\varepsilon/0.36}$, has been proposed by Hutzler et al. [5] and provides similar values). In Eqs. (11) and (12), D_1 and D_2 are the

Fig. 5. For the smallest bubbles and smallest liquid flow rates, the soap solution seems to flow down through a central dimple, and to flow up near the Plateau borders (not distinguishable this figure).

two associated constants obtained by fitting. From the Fig. 7 of [7], it is shown that these two ripening rates are close together for liquid fractions $\varepsilon \approx 0.001$. Then $D_2 \cdot g_2(\varepsilon)$ remains almost constant over the range $0.001 \leqslant \varepsilon \leqslant 0.01$ whereas a significant decrease is observed in the experimental data. Although not based on physical fundamentals, the distinct advantage of $g_1(\varepsilon)$ is to better describe the strong dependence of the coarsening rate at small liquid fractions ($0.001 \leqslant \varepsilon \leqslant 0.01$). Obviously, the ripening characteristics highlighted in the present work for a single foam bubble can be used to imagine a similar effect for draining foams. A stronger dependence can be introduced in $D_2 \cdot g_2(\varepsilon)$ with an additional coupling arising from the film swelling effect as liquid flows throughout the foam. In other words, it is suggested that, through this coupling, the geometry of draining foams can markedly differ from the geometry of static foams. At the bubble scale, a major parameter in this coupling has been found to be the liquid velocity. For macroscopic foams samples, this parameter can be related to the liquid fraction introducing the foam permeability $k(\varepsilon)$: $v = k(\varepsilon)\varepsilon^{-1} \rho g/\eta$. To progress further this way, the film thickness has to be known as a function of v and R for the investigated soap solution. Although partial elements have been recently provided [10], such a relation is still lacking. In the meantime, one can allow the film thickness to vary in Eq. (12), so that the constant D_2 is now a function of ε, i.e. $D_2(\varepsilon)$ proportional to $1/e$. From the Fig. 7 of [7] and assuming a common black film with thickness $e_b = 35$ nm, it can be estimated that an increase of e by a factor 2.5 over the range $0.001 \leqslant \varepsilon \leqslant 0.01$ is sufficient to obtain the equality $D_1 \cdot g_1(\varepsilon) = D_2(\varepsilon) \cdot g_2(\varepsilon)$. Even if no experimental data support this estimation, such a variation is highly conceivable. This approach means that the functional form $g_2(\varepsilon)$, describing the evolution of the geometry of static foams as they become wetter, is still appropriate. Obviously, a study of foam coarsening in relation with the films thicknesses within draining conditions would be useful to resolve this point.

5. Conclusion

Ripening characteristics have been measured for a single foam bubble under forced drainage conditions. Models based on a constant films thickness failed to predict the reported experimental values. In the present study, the knowledge of the film surface area available for ga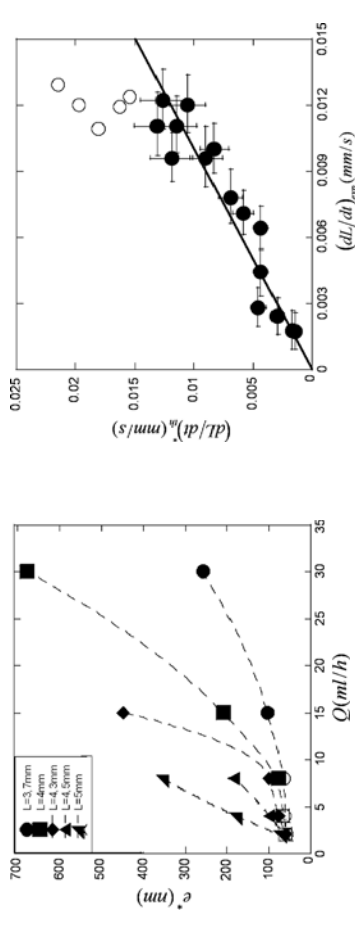s exchange allowed for the origin of the observed discrepancy to be precisely understood, namely the films swelling phenomenon associated to the liquid flow in the Pbs. In contrast to previous works, it is thus suggested that during coarsening of draining foams, the films thickness is related to the liquid velocity in the Pbs network. In other words, the knowledge of the static foam geometry as a function of the liquid fraction turns out to be insufficient to describe the data for the coarsening of draining foams over the whole range of liquid fractions. Up to now, the explicit variation of the films thickness had not been considered in the interpretation of experimental data. We hope that this work will legitimate this approach and justify further investigation about to understanding of the films swelling phenomenon.

References

[1] D. Weaire, N. Pittet, S. Hutzler, Phys. Rev. Lett. 71 (1993) 2670.
[2] A. Saint-Jalmes, Y. Zhang, D. Langevin, Eur. Phys. J. E 15 (2004) 53.
[3] E. Lorenceau, N. Louvet, F. Rouyer, O. Pitois, Eur. Phys. J. E (2009) doi:10.1140/epje/i2008-10411-7.
[4] S. Hilgenfeldt, S.A. Koehler, H.A. Stone, Phys. Rev. Lett. 86 (2001) 4704.
[5] S. Hutzler, D. Weaire, Philos. Mag. Lett. 80 (2000) 419.
[6] M.U. Vera, D.J. Durian, Phys. Rev. Lett. 88 (2002) 088304.
[7] K. Feitosa, D.J. Durian, Eur. Phys. J. E 26 (2008) 309.
[8] S.A. Magrabi, B.Z. Dlugogorski, G.J. Jameson, Chem. Eng. Sci. 54 (1999) 4007.
[9] A. Saint-Jalmes, M.-L. Peugeot, H. Ferraz, D. Langevin, Coll. Surf. A 274 (2005) 110.
[10] V. Carrier, S. Destouesse, A. Colin, Phys. Rev. E 65 (2002) 061404.
[11] O. Pitois, C. Fritz, M. Vignes-Adler, J. Colloid Interface Sci. 282 (2005) 458.
[12] A. Saint-Jalmes, Soft Matter 2 (2006) 836–849.
[13] O. Pitois, N. Louvet, E. Lorenceau, F. Rouyer, J. Colloid Interface Sci. 322 (2008) 675.
[14] H.M. Princen, S.G. Mason, J. Colloid Interface Sci. 20 (1965) 353.
[15] K. Brakke, Exp. Math. 1 (1992) 141.
[16] K.J. Mysels, K. Shinoda, S. Frankel, Soap Films: Studies of their Thinning and a Bibliography, Pergamon, Elmsford, NY, 1959.
[17] E. Terriac, F. Artzner, C. Meriadec, P. Chasle, J. Ohana, J. Emile, Langmuir 23 (2007) 12055–12060.
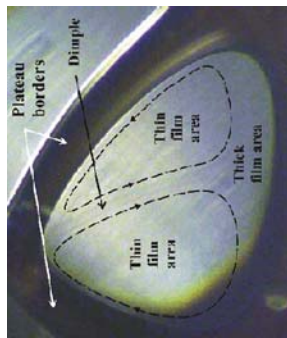

Fig. 6. Theoretical bubble growth rate as a function of the experimental one. The black line is a linear regression with a slope equal to unity.

Chapitre 3

Transport de particules dans une mousse aqueuse

Des particules solides sont bien souvent présentes dans la phase liquide d'une mousse comme par exemple lors de processus de flotattion utilisés notamment pour la séparation du minerai (figure 3.1a). Un autre exemple est celui de mousses très stables visibles en bord de mer qui sont chargées en Phaeocystis (figure 3.1b). Ce dernier est un plancton végétal marin qui peut se trouver sous forme de cellule isolée, ou d'agrégat de cellules regroupées en colonies et pouvant formé un gel.

Ces particules sont alors amenées à être transportées et dispersées dans la mousse comme dans un milieu poreux. Cependant comme nous l'avons vu dans le chapitre précédent les pores de ce milieu poreux sont déformables et ont des parois fluides ne vérifiant pas les conditions de non-glissement du fait de la mobilité des surfactants sur l'interface liquide-air. Le transport de particules dans un tel système est donc loin d'être trivial et présente un intérêt fondamental.

Dans le cas de la sédimentation ce qui pourra être le cas dans une mousse à l'équilibre (fluide au repos), il est bien connu qu'une particule le long d'une paroi solide sédimente moins vite [1] qu'en milieu infini, inversement une particule le long d'une interface mobile sédimente plus vite qu'en milieu infini [2]. Dans un bord de Plateau une petite particule peut être dans une position centrale loin des interfaces, ou proche d'une interface voire de deux interfaces, celles-ci pouvant être mobiles ou immobiles (comparable à des parois solides). La synergie entre les différents paramètres de positionnement, de confinement et de mobilité des interfaces sur la simple vitesse de sédimentation d'une particule unique dans un bord de Plateau apparaît ainsi complexe et propice à une grande variété de comportement.

FIGURE 3.1 – a) Image en surface d'un cuve flotta-tion de minérai, extraite d'une page internet de J. Cilliers : *http ://www3.imperial.ac.uk/engineering/research/impact/casestudies/jancilliers* ; b) Image illustrant une mousse contenant des particules de plancton. *Source Ifremer - Efflorescence de Phaeocystis observée en avril 2002 à l'embouchure de la rivière Le Wimereux à marée montante - Photo N. Cuvelier*

Dans le cas de particules transportées par l'écoulement du fluide intersticiel, ce qui corres-pondra à une situation de drainage d'une mousse, les paramètres précédemment cités appa-raissent également très influants sur le transport d'une particule. Deux cas extrêmes peuvent être distingués : 1- une petite particule située dans une zone de contre-écoulement (cf 2.2.1) est susceptible d'être transportée dans un sens opposé à l'écoulement moyen ; 2- une particule moyenne au centre du canal est susceptible d'être transportée plus rapidement que l'écoule-ment moyen (profil de vitesse de type Poiseuille) [3].

Dans le cadre de l'ANR " Microfluidique particulaire appliquée aux mousses " (ANR-05-JCJC-0234-01) et des thèses de N. Louvet et de C. Fritz, nous nous sommes intéressés à cette problématique. Je me suis particulièrement investie dans l'étude de la sédimentation et le transport de particules dans les canaux fluides d'une mousse aqueuse. En complément des expériences menées au laboratoire, j'ai développé des simulations numériques sous COMSOL Multiphysics qui modélise la " fluidité " des interfaces (cf. chapitre précédent paragraphe 2.2.2). Comme cela sera mis en évidence par la suite, ces simulations permettent une compré-hension plus précise de l'influence de chacun des paramètres physiques : confinement - mobilité des interfaces - poids de particules - vitesse d'écoulement.

3.1   Sédimentation

Publications : Softmatter 2010.

Une unique particule solide plus petite que le cercle inscrit à l'intérieur de la section du bord de Plateau (cf. figure 3.2.a) et plus dense que le liquide sédimente sous l'effet de son propre poids. Nous notons sa vitesse V_{sed}. Récemment, Olivier Pitois et ses collaborateurs ont mis en évidence une large variation des vitesses de sédimentation en fonction de la taille et du positionnement de la particule dans un bord de Plateau aux interfaces mobiles [4]. Dans la continuité de leur travail, j'ai étudié l'effet de la mobilité des interfaces.

Les expériences sont menées à l'échelle d'une mousse ou d'un bord de Plateau vertical unique avec deux solutions moussantes modèles, engendrant pour l'une des interfaces mobiles, et pour l'autre des interfaces immobiles (cf. 2.1).

Pour les simulations numériques, nous supposons que la particule est sphérique de rayon d et qu'elle a atteint un mouvement stationnaire suivant l'axe du bord de Plateau. Le mouvement du liquide est modélisé par l'équation de Stokes adimensionnée et la mobilité des interfaces est modélisée par le nombre de Boussinesq défini à l'échelle du rayon de bord de Plateau sur une gamme de valeur allant de 0.001 à 1, comme cela a été présentée au chapitre précédent au paragraphe 2.2.2. Les simulations sont réalisées dans le référentiel de la particule en mouvement. Ainsi une vitesse nulle est imposée à la surface de la particule et nous varions le paramètre de vitesse v_p imposée à l'entrée, à la sortie et aux coins du bord de Plateau (cf. figure 3.2.b). Lorsque la force de l'écoulement autour de la sphère s'oppose exactement au poids de la particule F_g (norme égale et sens opposé), la vitesse v_p est alors égale à vitesse de sédimentation ; en choisissant un adimensionnement des vitesses par la vitesse de Stokes, un adimensionnement des longueurs par R_{PB} et un adimensionnement de la viscosité par celle du fluide, alors F_g s'écrit $3\pi(d/R_{PB})$.

Les expériences dans un bord de Plateau vertical montrent que la vitesse de sédimentation d'une telle particule dépend de la mobilité des interfaces, de sa positon dans le canal, et du confinement ($\lambda = d/d_{lim}$) : une particule sédimente d'autant plus vite qu'elle est proche des interfaces et que celles-ci sont fluides (cf. figure 3.3a). La gamme de vitesse accessible s'étale sur près d'une décade : entre deux fois et un tiers de la vitesses de Stokes. Dans le cas d'interfaces mobiles, une petite particule située proche du coin d'un bord de Plateau sédimente plus vite qu'en milieu infini car le fluide et les interfaces à proximité de la particule
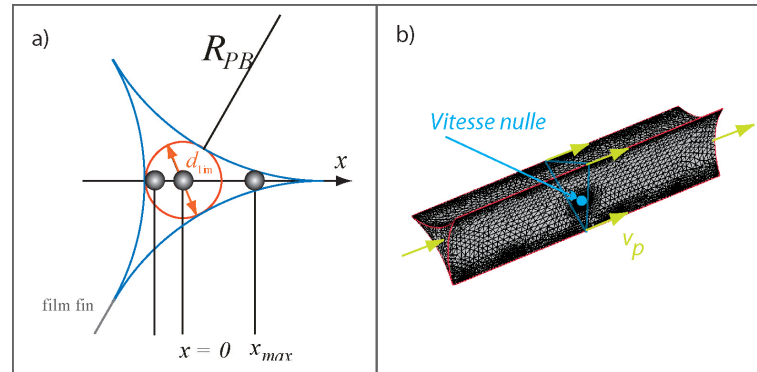
FIGURE 3.2 – a) Schéma illustrant le positionnement d'une "petite" particle dans une section de bord de Plateau b) Schéma illustrant les conditions aux limites des vitesses imposées dans le référentiel de la particule

sont entrainés vers le bas et le contre-écoulement de fluide s'effectue dans une zone "large" opposée au coin. Dans ce cas, la vitesse de la particule diminue avec la distance aux interfaces : la vitesse est maximale au coin et minimale au centre du bord de Plateau. Inversement, dans le cas d'interfaces immobiles, une petite particule située proche du coin d'un bord de Plateau sédimente moins vite qu'en milieu infini car le contre-écoulement de fluide s'effectue dans une zone "étroite". Dans ce dernier cas, la vitesse de la particule augmente avec la distance aux interfaces : la vitesse est minimale au coin et maximale au centre du bord de Plateau. Enfin, notons que, d'après ces expériences, la vitesse au centre du bord de Plateau apparaît indépendante de la mobilité des interfaces.

L'étude numérique de la sédimentation de particules solides dans les bords de Plateau permet de reproduire les résultats expérimentaux obtenus dans un bord de Plateau unique vertical pour des paramètres de confinement variant entre 0.1 et 0.8 et avec un nombre de Boussinesq de l'ordre 0.001 pour des interfaces mobiles et de l'ordre de 1 pour des interfaces immobiles (cf. figure 3.3a).

Les résultats expérimentaux obtenus dans une mousse sont très peu dispersés pour un confinement donné. Cette faible dispersion des vitesses s'explique par le fait que les particules sédimentent à l'intérieur d'un canal incliné vers la position la plus basse d'une section, ce positionnement est confirmé par l'observation des particules dans l'expérience. De plus, ces expériences mettent en évidence une forte influence du confinement lorsque les interfaces sont
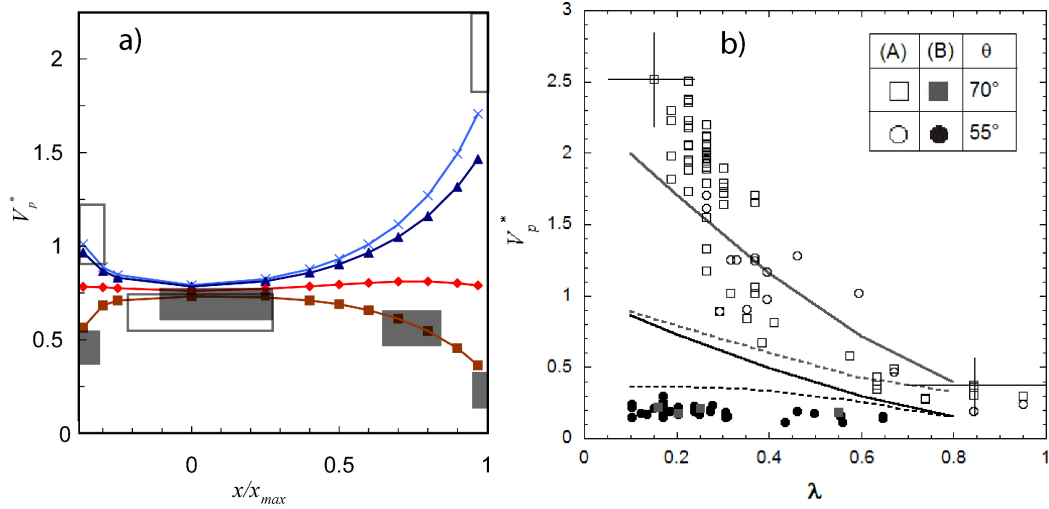
FIGURE 3.3 – Vitesse de sédimentation normalisée : a) influence de la position de la particule pour un paramètre de confinement $\lambda = 0.2$ et différente mobilité des interfaces, les rectangles blancs et gris correspondent respectivement aux expériences avec des interfaces mobiles et immobiles, les courbes numériques sont obtenues pour des $Bq = 0.001(\times); 0.01(\triangle); 0.1(\diamond); 1(\square)$; b) Vitesses expérimentales mesurées dans un canal incliné d'un angle θ dans une mousse et normalisées $(V_p/(V_{Stokes}sin(\theta))$ en fonction du paramètre de confinement λ pour des interfaces dites mobiles (symbol vide) et des interfaces dites immobiles (symbol plein) et comparées aux valeurs maximales et minimales obtenues pour des simulations avec un nombre de $Bq = 0.001$ (gris) et $Bq = 1$ (noire).

mobiles et quasiment pas d'effet du confinement sur la vitesse des particules lorsque les inter-faces sont immobiles (cf. figure 3.3b). Ces expériences sont bien décrites par les simulations de particules proches des coins. Enfin, nous notons que pour des interfaces mobiles les particules sédimentent plus vite dans le canal d'une mousse qu'en milieu infini tant que son paramètre de confinement (λ) est plus petit qu'un-demi.

Les résultats numériques nous permettent d'étudier de manière systématique l'effet du paramètre de confinement λ et de mobilité Bq. Pour la position extrême où l'influence de ces paramètres est la plus importante sur la vitesse de sédimentation de la particule, c'est-à-dire quand celle-ci est située dans un coin de bord de Plateau, nous mettons en evidence que les effets de confinement et de mobilité de surface peuvent être découplés. En effet, la vitesse d'une particule dans un coin de bord de Plateau peut être décrite comme le produit de la vitesse de Stokes, d'une fonction du paramètre λ et d'une fonction du nombre de Boussinesq particulaire Bq' défini à l'échelle du diamètre de la particule ($Bq' = Bq\frac{R_{PB}}{d}$), soit :

$$V_{coin} = V_{Stokes}h(\lambda)g(Bq') \tag{3.1.1}$$

où les fonctions h et g sont approximées par $h(\lambda) = 1 - 1.488\lambda + 0.535\lambda^2$ et $g(Bq') = (4.3 + Bq')/(1.8 + 2.2Bq')$.

La fonction h est relative au confinement et correspond à la vitesse au centre du canal qui est quasi-independante de la mobilité de l'interface (cf. figure 3.3a), arbitrairement nous choisisions $h = V_{sed}/V_{Stokes}$ pour une particule centrée et pour $Bq = 1$. La fonction g est relative à la mobilité des interfaces. Rappelons que la position la plus probable d'une particule dans un bord de Plateau d'une mousse est celle dans un coin car les canaux sont pour la plupart inclinés par rapport à la gravité, nous disposons ainsi d'une fonction pour estimer la vitesse de sédimentation d'une particule dans une mousse (cf. figure 3.3b). Enfin nous montrons que pour un paramètre de confinement fixé, il existe une mobilité de surface pour laquelle la vitesse de la particule devient indépendante de la position dans le canal correspondant à des nombres de Boussinesq particulaires (Bq') de l'ordre de 2.

3.2 Transport de particules par écoulement de la phase liquide

En plus de la sédimentation, l'écoulement de liquide au sein du réseau de bord de Plateau peut être le moteur du transport de particules dans une mousse.

Les expériences sont menées à l'échelle d'une mousse ou d'un bord de Plateau vertical unique avec une solution moussante engendrant des interfaces mobiles (cf. 2.1) et avec des particules de même densité que le fluide ou plus dense que celui-ci.

Les simulations numériques pour modéliser le transport d'une particule isodense sont similaires à celles de l'étude de la sédimentation à l'exception des conditions limites et de l'adimensionnement des vitesses (cf. figure 3.4). Une vitesse d'écoulement est imposée à l'entrée et à la sortie du canal. Une vitesse de remontée est imposée au coin des sections du bord de Plateau pour la modélisation du contre-écoulement (cf. paragraphe 2.2.1). L'adimensionnement des vitesses se fait par la vitesse moyenne débitante effective, c'est-à-dire, tel que $\frac{1}{A} \int_A H(v)v(r)dr = 1$, où H est la fonction Heavyside. Nous déduisons ainsi la vitesse de transport de la particule isodensité par l'écoulement de liquide pour laquelle la force de l'écoulement autour de la sphère s'annule. Il est à noter que nos résultats numériques pour les particules situées au centre du canal sont en très bon accord (moins de 0.2% d'erreur) avec la loi de Faxen qui prédit la vitesse d'une particule à partir de la connaissance du champ de vitesse de l'écoulement "rampant" non perturbé (sans particule) : $v_{particule}(r) = v_{ecoulement}(r) + \frac{d^2}{24}\Delta v$. Cependant, de même que pour des particules proches des bords d'un canal aux parois solides pour lesquelles il existe des interactions hydrodynamiques entre paroi et particule [3], la loi de Faxen surestime la vitesse des particules proches des coins (là où la condition limite de vitesse est imposée) et d'autant plus que les particules sont petites pour lesquelles l'erreur peut atteindre 8%.

Afin de s'affranchir dans un premier temps des effets de sédimentation et de dispersion liés au réseau de la mousse, des expériences et des simulations sont menées pour des particules isodenses à l'échelle d'un canal unique. La comparaison de ces résultats expérimentaux et numériques permettent d'identifier les paramètres pertinents pour modéliser le transport de particules provoqué par l'écoulement de la phase liquide.
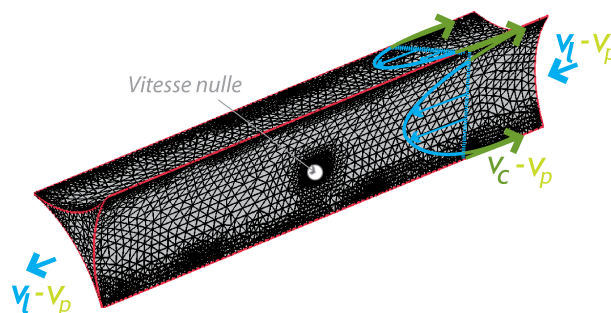
FIGURE 3.4 – Schéma illustrant les conditions aux limites des vitesses imposées dans le référentiel de la particule pour une modélisation de transport d'une particule isodensité par l'écoulement de fluide

Les expériences montrent une très grande dispersion des vitesses pour des particules faiblement confinées (cf. figure 3.5). Les vitesses les plus faibles sont presque nulles et correspondent à des particules proches d'un coin, à l'opposé, les vitesses les plus élevées peuvent atteindre 1.3 fois la vitesse moyenne du liquide et correspondent à des particules localisées au centre du canal.

La modélisation considérant des vitesses nulles au coin du bord de Plateau (pas de contre-écoulement à l'intérieur du canal- theorie de Lemlich) ne permet pas de reproduire les résultats expérimentaux. Cependant, les modélisations considérant une vitesse de contre-écoulement trois fois supérieure à l'écoulement moyen permet de reproduire les résultats expérimentaux. Nous avons ici une nouvelle preuve que les contre-écoulements de liquide induit par effet Marangoni empiètent sur la géométrie du canal et que la vitesse ne s'annule pas à la jonction géométrique entre bord de Plateau et film.

Toujours à l'échelle d'un canal unique, les résultats expimentaux obtenus pour des particules denses se comparent très bien aux résultats numériques des particules isodenses dans un coin du canal dès l'instant où la vitesse de sédimentation (cf. équation 3.1.1) est rétranchée à la vitesse de la particule. Notons que, du fait de l'injection en forme d'"entonnoir" du dispositif expérimental, les particules denses se localisent en périphérie du bord de Plateau et donc dans les coins de celui-ci. La vitesse d'une particule dense dans un bord de Plateau est donc égale à la somme de la vitesse de sédimentation de celle-ci et de la vitesse d'une particule isodensité de même taille transportée par l'écoulement du fluide. Ce résultat est conforme au théorème de superposition pour des écoulements à faible Reynolds.
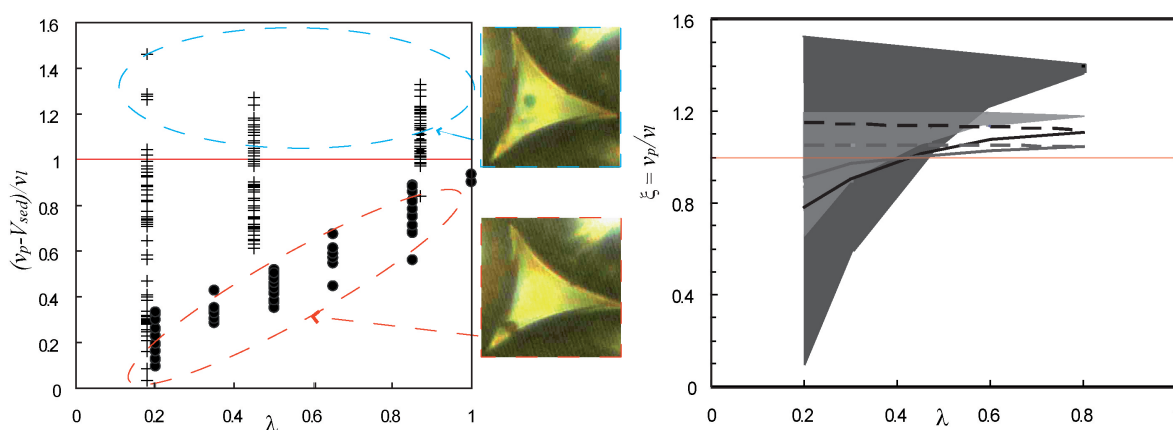
FIGURE 3.5 – Vitesse des particules isolées dans un bord de Plateau vertical normalisée par la vitesse moyenne de l'écoulement en fonction du paramètre de confinement : a) résultats expérimentaux pour des particules isodensités (+) et particules plus denses que le liquide (o). b) résultats numériques obtenus pour une mobilité interfaciale, les courbes continues et pointillées correspondent respectivement aux vitesses minimales et maximales des particules dans un canal de mobilité interfaciale $Bq = 0.1$ (noir) et $Bq = 0.01$ (gris) avec des conditions limites de vitesse nulle au coin ; les zones grises représentes les gammes de vitesses accessibles aux particules dans un canal de mobilité interfaciale $Bq = 0.1$ (gris foncé) et $Bq = 0.01$ (gris clair) avec des conditions limites de vitesse de remontée égale à trois fois la vitesse moyenne du liquide.

Nous pouvons à présent nous intéresser au transport de particules denses dans le réseau de bord de Plateau. Expérimentalement, nous mesurons le temps nécessaire à ces particules pour parcourir une hauteur H au sein d'une mousse en situation de drainage forcée. Nous corrigeons l'effet de la sédimentation en corrigeant le temps de transport : $t_c = H/(H/t_{transport} - V_{sed}/3)$, où le facteur $1/3$ moyenne les orientations des différents canaux dans le réseau de la mousse et V_{sed} est déduit de l'équation 3.1.1. Les vitesses des particules dans la mousse corrigées de la sédimentation et normalisées par la vitesse débitante augmente en moyenne avec le paramètre de confinement (cf. figure 3.6.a), de manière analogue au transport de particules dans un canal unique. Cependant, cette comparaison entre le transport à l'échelle d'un canal et à l'échelle d'une mousse ne peut être que qualitative. En effet, au très grand rapport d'aspect, la vitesse corrigée d'une particule peut atteindre 1.6 fois la vitesse moyenne du liquide alors que dans un canal unique la vitesse corrigée ne dépasse pas 1.3 fois la vitesse du liquide. Nous suspectons alors un effet lié au réseau des canaux. De plus, nous remarquons que les valeurs obtenues pour des confinements identiques mais pour des particules différentes se comparent très mal (par exemple pour $\lambda \sim 0.6$ et des particules de diamètre 42.5 et $85\mu m$) : les particules les plus grosses sont transportées plus vite que les plus petites. Nous expliquons ces différences par le fait que les particules les plus denses sédimentent à l'échelle des jonctions entre les canaux et sont donc dirigés vers les canaux les plus verticaux et donc plus "rapides". Cette hypothèse peut être testée en comparant les temps de transport convectif et de sédimentation dans une jonction pour l'ensemble des mesures. Ce rapport des temps peut s'écrire : $0.16v_l/V_{Stokes}$. Lorsque le temps de sédimentation est petit devant le temps de convection ($0.16v_l/V_{Stokes} < 1$), les particules sont en moyennes plus rapides que le liquide et leur vitesse sont relativement peu dispersées, inversement si la sédimentation dans les jonctions entre les canaux est lente ($0.16v_l/V_{Stokes} > 1$), les particules vont en moyenne moins vite que le liquide et leur vitesse sont très dispersées (cf. figure 3.6.b et .c). Nous pouvons alors conclure que plus les particules sont denses plus leur trajet parcouru dans la mousse s'approche de la verticale (plus court et moins dispersé). Ce trajet s'apparente à celui de petites particules dans un empilement sec de sphères [6]. A l'opposé, des particules légères se comportent comme des "traceurs" de l'écoulement liquide à travers le réseau de bord de Plateau dont les trajectoires sont beaucoup plus aléatoires et dispersées [7].
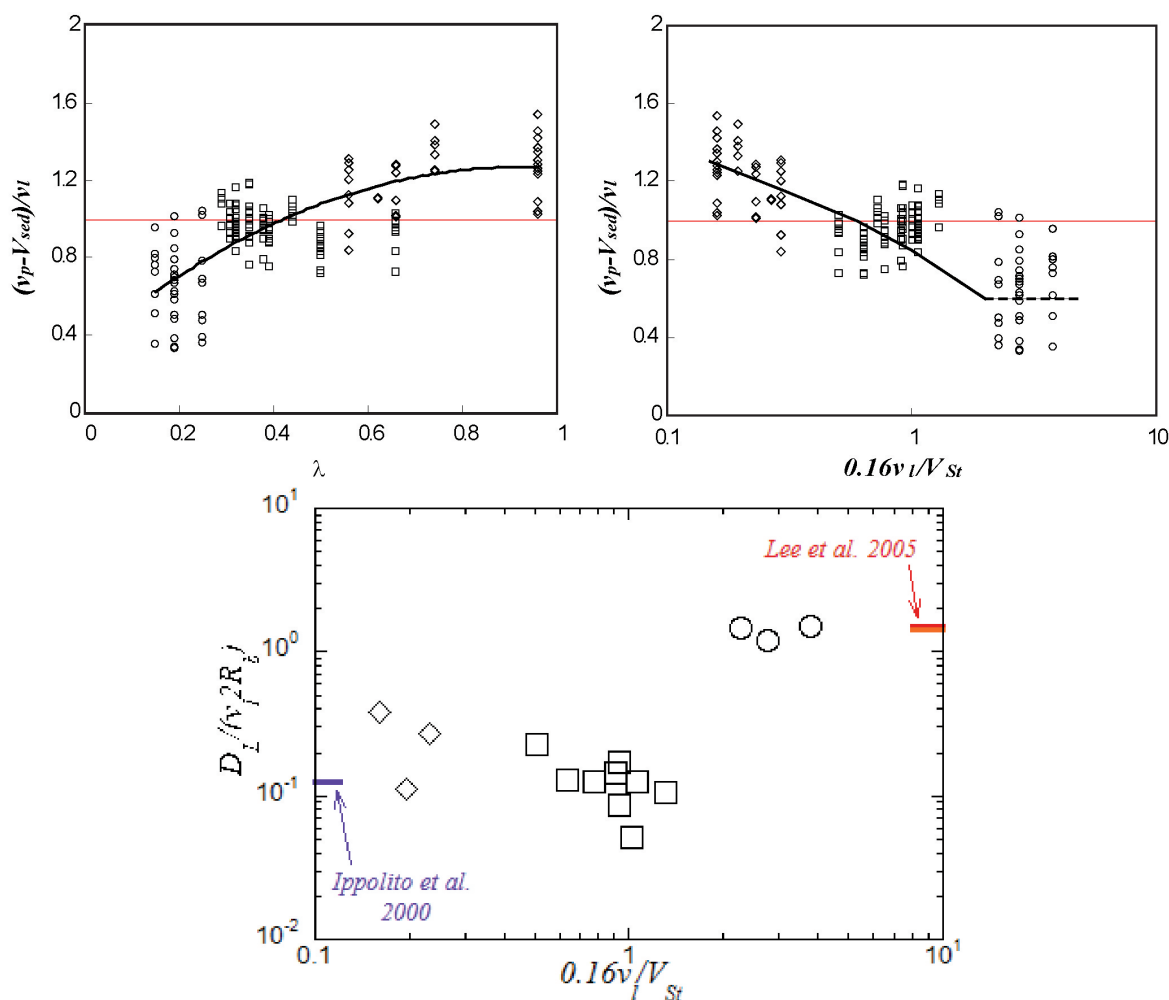
FIGURE 3.6 – a) Vitesses de particules isolées dans une mousses corrigés de l'effet de sédimentation et normalisées par la vitesse moyenne de l'écoulement en fonction du parmètre de confinement. b)Mêmes vitesses que précédemment mais en fonction du rapport d'un temps de sédimentation et de convection. c)Coefficient de dispersion normalisé en fonction du rapport d'un temps de sédimentation et de convection. Les symboles o, □ et ◇ correspondent respectivement à des particules de diamètre égale à 22.5, 42.5 et 85μm

Bibliographie

[1] J. Happel and H. Brenner, Low Reynolds Number Hydrodynamics, 2nd ed. Noordhoof, Leiden, (1973).

[2] K. D. Danov, R. Aust, F. Durst, U. Lange, *Int. J. Multiphase Flow* **21**, 1169 (1995).

[3] M.E. Staben, A.Z. Zinchenko, R.H. Davis, Phys. Fluids 15, 1711-1733, (2003).

[4] O. Pitois, C. Fritz, L. Pasol, M. Adler, *Phys. Fluids*, **21**, 103304 (2009).

[5] M.E. Staben, A.Z. Zinchenko, R.H. Davis, *Phys. Fluids*, **15**, 1711-1733 (2003).

[6] I. Ippolito, L. Samson, S. Bourlès, J.P. Hulin, *Eur. Phys. J. E*, 3, 227-236 (2000).

[7] H.T. Lee, S.J. Neethling, J.J. Cilliers, *Colloids and Surfaces A : Physicochem. Eng. Aspects*, 263, 320-32 (2005).

The sedimentation of fine particles in liquid foams

Florence Rouyer, * Christelle Fritz and Olivier Pitois

We investigate the sedimentation of fine particles in liquid channels of foams. The study combines numerical simulations with experiments performed in foams and in isolated vertical foam channels. Results show that particulate motion is controlled by the confinement parameter (λ) and the mobility of the channel surfaces modelled by interfacial shear viscosity. Interestingly, whereas the position of the particle within the channel cross-section is expected to be a relevant parameter, it is shown that in foam there is no effect of this parameter on the sedimentation velocity. For low surface mobities, particles' velocities are small and almost independent on the size ratio; in opposition, for high surface mobilities, the particle velocity is always larger than the Stokes velocity, whereas it is always smaller for λ > 0.5. This behaviour has been understood from the generally observed position of moving particles along corners of the channels' cross-section.

1. Introduction

The transport of fine particles in aqueous foams is at the heart of the process of froth flotation for separating mineral ore from gangue.[1] In broad outline, hydrophobic particles are attached to bubble interface whereas hydrophilic particles remain in the liquid phase column, whereas hydrophilic particles remain in the liquid phase of the froth and are thus not expected to be collected. However, depending on their transport properties through liquid channels formed between the bubbles, hydrophilic particles are likely to be "captured" within the liquid phase of the rising froth. This is expected to occur as soon as the sedimentation velocity of those particles is smaller than the rising velocity of the froth, and this contributes to reduce the efficiency of the separation process. Through lack of a precise description for this transport, existing flotation models often consider that the sedimentation velocity of these particles is that of spheres in an unbounded liquid.[1,2] Recently, the behaviour of particles within a quasi two-dimensional rising foam has been investigated.[3] It was shown that for fine particles the foams channels (so-called Plateau borders-PB-) help to establish a general law for particulate transport in Plateau borders. Based on a single foam channel experiment, Pitois et al. provided results for the settling behaviour of particles in settling motion along a vertical fluid channel with very mobile interfaces.[4] It has been shown that for sufficiently small particles, slow and fast motions can be observed (the velocity corresponding to fast motions can be as high as twice the Stokes velocity in an unbounded fluid), depending on the particle position within the channel cross-section and the sphere/channel size ratio. Moreover, the fast motions are not observed anymore when the size ratio exceeds a critical value which has been found to be approximately equal to 0.5. These experimental results were

modelled by numerical simulation with Stokes flows and slip condition (free boundary condition) at the walls of the channel. Note that, in such confined geometry, the particle can settle faster than in an unbounded liquid due to the presence of mobile interface, even so the inertia is negligible. Obviously, such results are of great interest for the modeling of particulate motions through the liquid channels of froth. However, a complete insight into this difficult problem should include the effect of mobility of the channel walls, which is known to depend on the surfactant used to stabilize the froth[5,6,7] and currently modelled by the interfacial shear viscosity. In this paper, we focus on this aspect and we investigate the motions of fine particles along the Plateau borders of liquid foams. Both experimental and numerical results show that the mobility of the interface is precisely a central parameter in this problem.

2. Experiments

2.1. Materials

Solid particles are silica spheres (Duke Scientific Corporation, density ρ$_S$ = 2450–2500 kg m⁻³). Diameters d are in the range 15–140 μm (Δd/d ≈ 5%). The maximal particulate Reynolds number (Re$_p$) is equal to 3.4 for the largest particles and less than or equal to 0.1 for particle diameter smaller than 45 μm. A dedicated delivery system was developed to introduce the particles into the PB channels without additional liquid flow. The particles are first mixed with the foaming solution and placed in a modified 3-path valve, ensuring their transfer to the feed tube where they are allowed to settle.

2.2. Foam experiment

The experimental cell consists of two cylindrical glass containers separated by a sintered glass disk (Fig. 1). The cell is first filled with the foaming solution and bubbles with 2.5 mm diameter are generated in the upper container (diameter: 50 mm, height: 100 mm) by blowing filtered nitrogen through a capillary. A lid is used to ensure water vapour saturation inside the foam cell. The lower container is connected to a liquid reservoir. Decreasing—respectively increasing—the vertical position (L) of the liquid reservoir with reference to the cell enables us to decrease—respectively increase—the liquid pressure inside the cell. As a result, liquid solution is forced out of—respectively into—the foam from the bottom and the Plateau border cross-sections increase—respectively decrease—as long as the foam remains in contact with the base of the container;[8] this was achieved by controlling the hydrophobicity of the inner cell wall as well as of the porous plate (a solution of perfluorodecyltrichlorosilane was used for coating). Under these conditions, the radius of curvature of PBs located in the plane at height z inside the foam is given by

$$R_{PB}(z) = \sqrt{\frac{\sigma}{\rho g(z-L)}}$$ and is typically in the range 100–200 μm.

A 3D micropositioner is used to drive the delivery tube to the desired position inside the PB network. Images of PBs inside the foam (a few bubbles far from the cell wall) can be grabbed using a CCD camera set on a 3D translation stage and connected to a computer. Magnification levels allowed images of one or several PBs (including nodes) to be obtained. The camera and the cell were oriented in such a way that the studied PBs were located in a plane perpendicular to the optical axis of the camera. As an illustration of the particle tracking procedure, Fig. 2 presents an
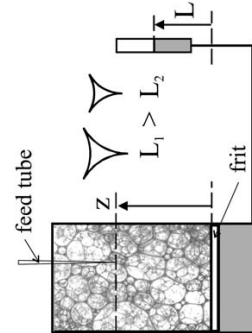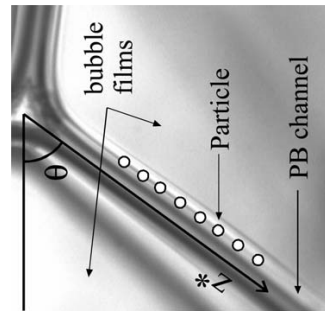

Fig. 2 Successive positions occupied by a glass sphere (35 μm) in settling motion through a Plateau border in a foam of solution B, the acquisition time is Δt = 200 ms.

example of the successive positions occupied by a sphere in sedimentation through investigated foams.

2.3. Single vertical channel experiment

This experiment has been shown to be useful for the study of particulate motions in Plateau borders, especially for the study of the position of the sphere within the channel cross-section. It is described in details in ref. 4 and we briefly recall that the vertical channel is obtained by withdrawing a dedicated frame from a reservoir containing the foaming solution. The frame consists of a vertical metallic tube on which three rods (diameter 1 mm) are fixed. Due to capillary forces, the cross-section of the resulting vertical liquid channel (Plateau border) is almost an equilateral triangle except that the three segments joining the corners are tangent circular arcs of radius R$_{PB}$. Each corner joins to a thin vertical liquid film—of negligible thickness—attached to the holder and stabilized with surfactants contained in the solution. The frame is accurately positioned with reference to the reservoir to easily adjust the length of the channel (typical lengths are in the range 5–10 mm).

The inner diameter of the holder is 10 mm and a circular outlet of diameter 1 mm is opened at its lower part: it is used to deliver the particles through the channel. Images of the channel during the experiments were grabbed through windows in the cell cover. The successive positions occupied by a sphere along the channel axis are then determined using simple image processing procedures. Another window was also placed at the bottom of the channel (through the holder) and using a high speed camera equipped with an appropriate lens, pictures of the channel cross-section could be obtained during particles motion. The pictures are then used to determine the position of the particle within the channel cross-section during the sedimentation and to estimate de radius of curvature of the Plateau border: R$_{PB}$ ≈ 400 μm. As this experiment is dedicated to the study of the position of the sphere within the channel cross-section, we focussed on the smallest

Fig. 1 Sketch of the foam cell connected at the bottom to a liquid reservoir which controlled altitude permits to vary the size of the channel cross section.

Université Paris-Est, Laboratoire de Physique des Matériaux Divisés et des Interfaces, CNRS FRE 3300, 5 bvd Descartes, 77454 Marne la Vallée Cedex, France. E-mail: florence.rouyer@univ-mlv.fr; Fax: +33 1 60 95 72 97; Tel: +33 1 60 95 72 63

particles reach a constant velocity (V) with the two foaming solutions. As a qualitative information, it is deduce from Fig. 4 that V(A) > V(B), as expected from the lower "mobility" of solution (B).

Velocities measured for particles motions in the foam are presented in Fig. 5. We have grouped results obtained for Plateau borders inclined of angle θ = 55 ± 2° and θ = 70 ± 2°, for which data were significant; the effect of this angle is taken into account in the reported values: $V_p^* = V/(V_{Stokes} \sin\theta) = 1/f$. This set of data confirms the information given by Fig. 4: sedimentation velocities are strongly dependent on the surfactant used to stabilize the interfaces. Indeed, two distinct curves appear in spite of some scatter in the data, each curve corresponding to a given solution. This "mobility" effect is very large for low values of λ, but is strongly reduced as λ increases, although always noticeable. More quantitatively, at low λ the measured velocity for solution (A) is twice the Stokes velocity, which is tenfold the one measured for solution (B). For this latter, all measured velocities are smaller than the Stokes velocity. This shows that the interfacial mobility is a central parameter in this problem. The confinement parameter λ has a great influence on the motions of spheres in foam (A), but there is no evidence for such an effect for solution (B).

Experimental velocity values obtained for solution (B) are reported as a function of the position of the particle along the median axis in Fig. 6, and compared with results already published for solution (A).[4] As already explained, we focussed on the smallest confinement parameter, i.e. λ = 0.2, for which the number of positions that can be distinguished experimentally is the largest. The velocity appears to be: minimum as the sphere locates at the corner of the channel cross-section, maximum as it locates in the central area of the cross-section. It can be said that the velocity decreases as the sphere settles closer to the walls. A normalized velocity $V_p^* = V_2 ≈ 0.2$ is measured as the sphere is

close to two walls (corner), $V_p^* = V_0 ≈ 0.7$ as there is no wall close to the sphere. The normalized velocity V_0 for spheres in the central zone measured for solution A and solution B are identical.

Dependence of the numerical velocity with the sphere position is presented in Fig. 6 for Bo = 0.001, 0.01, 0.1 and 1. For small Bo values, the velocity is maximum as the sphere is at the centre of the cross-section, minimum as it is at the centre of the cross-section, and intermediate as it is at the opposite interface. For the larger Bo value, this order reverses: the velocity is minimum as the sphere is at the corner of the cross-section and maximum as it is at the centre of the cross-section. For the intermediate value of Bo, the dependence of the velocity with the sphere position is very weak and the profile is essentially flat. For position of sphere in the central zone, the influence of Bo is weak.

In Fig. 5, numerical values for maximum and minimum sphere velocities are plotted as a function of λ for Bo = 0.001 and Bo = 1. It can be noted that: (i) velocities corresponding to Bo = 0.001 are larger than those for Bo = 1; (ii) velocities are decreasing functions of λ; (iii) for both Bo values, the λ-dependence is stronger for the maximum velocity than for the minimum velocity.

5. Discussion

Results for the sedimentation of fine particles in foams (A) and (B) have revealed a very strong effect of the interfacial mobility, especially at low λ (Fig. 5). Comparisons with data obtained from both the vertical Plateau border experiment and numerical simulations of Fig. 5 suggest that the measured velocity in foam is always close to the velocity expected at a corner of the channels cross-section, i.e. (i) maximum for high interfacial mobility (solution A, small Bo), (ii) minimum for low interfacial mobility

Fig. 6 Normalized settling velocity as a function of x for λ = 0.2. Experimental data obtained in the Plateau border apparatus for solution (A) and (B) are represented by open and grey boxes. Numerical results are represented by squares, diamonds, triangles and times lines for respectively for Bo =1, 0.1, 0.01, 0.001.

Fig. 5 Normalized settling velocity as a function of confinement parameter: Experimental data measured within foam made from solutions (A) and (B) are respectively represented by open and full symbols. Minimal (dash line) and maximal (continuous line) values obtained from numerical simulations for Bo = 0.001 and 1 are respectively presented by grey and black lines.

---

sphere/channel size ratio, for which the number of different positions that can be distinguished experimentally is the largest.

3. Numerical simulation

To model the settling velocity V of a particle along a Plateau border made of a fluid interface we solve the fluid flow by use of COMSOL Multiphysics software. The Plateau border geometry is delimited by 3 tangential cylinders of radius R_{PB} and length $4R_{PB}$; this latter has been chosen large enough such that it does not influence results (see Fig. 3a). The position of the particle is set at the middle height of the channel and is varied along the median x axis (see Fig. 3b). The origin of x is chosen in the middle of the section and the x axis is oriented positively in direction of a corner. We note that the three corners of the Plateau border cross-section are equidistant (equilateral triangle with length R_{PB}) and the distance between one corner to the center is equal to $R_{PB}/\sqrt{3}$. The parameter λ = d/d_{lim} is the confinement parameter; it compares the size of the particle with the maximum diameter of the circle inscribed in the PB cross-section: $d_{lim} = 2(2/3R_{PB}\sqrt{3} - R_{PB}) = 2R_{PB}(2/\sqrt{3} - 1)$. Four values of λ have been studied systematically: 0.2, 0.4, 0.6 and 0.8. For each λ, the position of the particle is within two extremes values $0.97x_{min}$ and $0.97x_{max}$

that verifies: $x_{min} = d/2 - d_{lim} = -\frac{2R_{PB}}{\sqrt{3}} + R_{PB} + d/2$ and

$$x_{max} = \frac{R_{PB}}{\sqrt{3}} - \sqrt{\left(R_{PB} + \frac{d}{2}\right)^2 - R_{PB}^2} = \frac{R_{PB}}{\sqrt{3}} - \sqrt{R_{PB}d + \frac{d^2}{4}}$$

We use an "auto" extra-fine mesh refined near the particle (maximum element size = 0.02 and growth rate = 1.1) and the

corner of the PB (maximum element size = 0.05 and growth rate =1.05) as illustrated in Fig. 3. For the smaller confinement parameter (λ = 0.1), we refined even more the mesh size close to the particle.

We consider dimensionless Stokes equations (fluid density and viscosity are respectively set to zero and one in "the Fluid Dynamic, Incompressible Navier–Stokes" user interface). The simulations are run in the frame of the particle and zero velocity is imposed at the surface of the particle (no-slip conditions). Fluid velocities at the entrance and the outlet of the channel, as well as the one of the edges of the Plateau border, are constrained to the parameter $-V_p^*$. The dimensionless viscous force F_V^* exerted on the sphere is calculated from the integral of the Lagrange multiplier along the axis of the channel. The fluidity of the interface is modelled using weak terms[9] for balancing the bulk viscous stress with the surface viscous stress on the circular boundary $μ_s \nabla v = μ_s Δ_s v$ where v is the velocity of the fluid. The two relevant parameters are the Boussinesq number Bo and Bo' which compare shear stress of the interface to the shear stress of the bulk at the scale of the channel: $Bo = μ_s/μ_l R_{PB}$[10] and at the scale of the particle: $Bo' = \frac{μ_s}{μ_l d} = \frac{Bo}{2λ(2/\sqrt{3} - 1)}$[11] The parameter Bo is varied from 0.001 to 1. For given λ, x and Bo, a parametric simulation that varied V_p^* is run for at least three values of V_p^* that permit to check for the proportionality relation: $F_V^* = αV_p^*$. Indeed, we are concerned with low particulate Reynolds number, so that the only hydrodynamic force is the viscous drag $F_V = βπfd V_p$ where f is a correction factor due to the presence of the channel walls. Balancing F_V^* with the dimensionless buoyancy force of the sphere ($F_g^* = 3πd$), we thus deduce the normalized terminal settling velocity of the particle for: $V_p^* = V/V_{Stokes} = 1/f = 3πd/α$.

4. Results

A typical example of the measurements performed with the foam experiment is presented in Fig. 4. In this figure, $Δz^* = z^* - zo^*$, where zo^* is the position z^* for which the particle reach a stable position in the cross-section of the channel. It is important to note that as the particles enter a PB channel (from a node), it needs some distance for them to find a stable position in the channel cross-section, over which the velocity evolves toward a constant value. From the present results, it appears that the

Fig. 4 Typical example of the position measurements as a function of time performed with the foam experiment for solution A (squares) and solution B (circles).

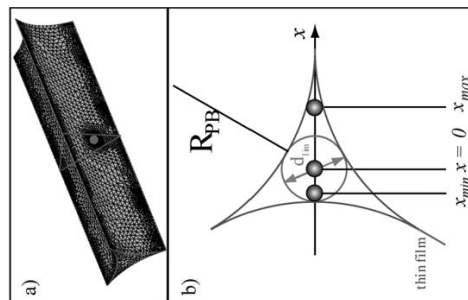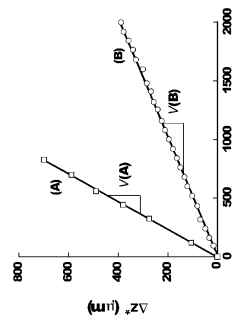**Fig. 3** (a) Example of mesh used to compute the settling velocity of a sphere inside a Plateau border. The sphere (for λ = 0.4) drawn in red colour. (b) Sketch of a Plateau border cross-section.

Fig. 8 Numerical results of the amplitude of the deviation ΔV as a function of Bo for confinement parameter varied from 0.1 to 0.8.

As V_2 is the relevant velocity for sedimentation of fine particles in foams, it is of interest to precise the complete dependence of this velocity with both confinement and mobility parameters. To this respect, Fig. 7a presents a complete set of numerical data for V_2 (we recall that due to numerical limitations this values are obtained for $x = 0.97x_{max}$). Qualitatively, the main features of this behaviour are: (i) at low λ, V_2 is strongly decreased as Bo increases, (ii) at low Bo, V_2 is strongly decreased as λ increases, (iii) at high λ or high Bo, V_2 remains close to ≈ 0.3. Note that for Bo larger than approximately 0.01, numerical results indicate that V_2 is smaller for particles with $\lambda = 0.1$ than for particles with $\lambda = 0.2$. This result can be understood in considering that for such small values of λ, the effect of the backflow is negligable (as the sphere is at the corner). In other words, the precise shape of the channel far from the sphere has not a significant influence on the sphere velocity; this latter is essentially controlled by the geometry and the mobility of the closest walls. As a consequence, the relevant length scale accounting for interfacial shear is the size of the sphere (instead of the size of the channel) and the relevant mobility parameter is Bo'. This is similar to the settling motion of a particle between two vertical viscous interfaces, for which the effect of the backflow is negligible and $1/f$ decreases with Bo'.[11] Consequently, for a given Bo, i.e. a given R_{PB} and a given μ_s in our case, Bo' decreases with the particle size, and $1/f$ increases with λ, for small λ and negligible backflow effects. Indeed, the increase of λ induced a slow down effect due to the backflow which superimposes to the effect of mobility. It is tempting to model the global behaviour in considering independently the two basic effects. This suggests to write V_2 as: $V_2(\lambda, Bo) = g(Bo')h(\lambda)$, where $g(Bo')$ accounts for the mobility effect and $h(\lambda)$ accounts for the backflow effect. We argue that this latter can be reasonably assessed by the evolution for the velocity of spheres axially centred in the channel, i.e. V_0. This is supported by the fact that V_0 is only weakly dependent on Bo over the range of three decades investigated in this study (see Fig. 5 for example). For the estimation of the confinement effect, we choose $h(\lambda)$ such that $h(\lambda) = V_0(\lambda, Bo = 1)$. The confinement factor is classically described using polynomial functions,[15] so that we approximate $h(\lambda)$ by $h(\lambda) = 1 - 1.488\lambda + 0.535\lambda^2$ (the deviation with numerical data is less than 1% for $\lambda < 0.6$). In Fig. 7b we plot $V_2/h(\lambda)$ as a function of Bo', showing that numerical data approximately collapse on the same curve. This supports our simple approach and allows for the function $g(Bo')$ to be determined: $g(Bo') = (4.3 + Bo')/(1.8 + 2.2Bo')$, thus providing a useful expression to estimate the velocity of particles within the channel of foams.

Finally, we discuss the deviation between the maximum and the minimum velocities. As the interfacial shear viscosity increases from low to high values, V_2 evolves from $V_2 > 1$ (the maximum velocity) to $V_2 < 1$ (the minimum velocity), whereas in the same time, V_0 remains almost unchanged. As a consequence, there exists a particular value of Bo for which the deviation between the maximum and the minimum velocities becomes very small or even vanish. In Fig. 8, we plot $\Delta V = (\max(V_0, V_1, V_2) - \min(V_0, V_1, V_2))$ as a function of Bo. For every λ value, this value correspond to $Bo' \approx 2$. Note that $Bo' \approx 2$, $V_2 \approx V_0(\lambda, Bo = 1)$. In that particular case, the velocities of spheres in settling motions along a 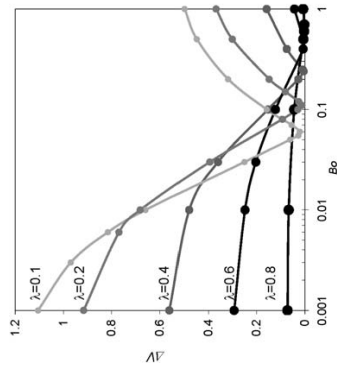corner or along the central axis of a channel are almost the same. This is illustrated in Fig. 6 for $Bo = 0.1$ and $\lambda = 0.2$, where the velocity profile is almost flat over the channel cross-section.

6. Conclusion

We investigated the gravity motion of fine particles in liquid channels of foams. The study combined numerical simulations with experiments performed both in foams and in isolated vertical foam channels. For vertical channels, results show that the motion is controlled by the particle/channel size ratio (λ), the mobility of the channel surfaces (Bo), as well as the position of the particle within the channel cross-section. For small Bo values, the velocity is maximum as the sphere is at the corner of the cross-section, minimum as it is at the centre of the cross-section, and intermediate as it is at the opposite interface. For the larger Bo value, this order reverses: the velocity is minimum as the sphere is at the corner of the cross-section and maximum as it is at the centre of the cross-section. We showed that for every λ, there exists a value of Bo for which the deviation between the maximum and the minimum velocities reduces to a vanishing small value: in that particular case, the dependence of the velocity with the sphere position is very weak. Interestingly, in foam, there is no effect of the position parameter on the sedimentation velocity. For low surface mobility, particles velocities are small and almost independent on the size ratio; for high surface mobility, we found that at low λ the particle velocity is always larger than the Stokes velocity, whereas it is always smaller for $\lambda > 0.5$. This behaviour has been understood from the generally observed position of settling particles along corners of the channels cross-section.

Notation

$Bo = \mu_s/\mu R_{PB}$	Boussinesq number defined at the scale of the Plateau border
$Bo' = \dfrac{\mu_s}{\mu d}$	Boussinesq number defined at the scale of the particle
d	particle diameter
d_{lim}	maximum diameter of the circle inscribed in the PB cross-section

---

(solution B, large Bo). During the foam experiment, the position of the sphere is not measurable with precision. However, we generally observed that the axis of the sedimentation motion in foam channels is often close to a corner. This is because in foams, the channels are inclined with respect to the vertical axis, so that the gravity force always acts to position the particle at the lowest stable position in the channel cross-section, i.e. a corner. Even if the particle were positioned along the central axis of a perfectly vertical channel (a situation that we never observed during foam experiments), it would approach the wall in the following channel. Note that other situations, where the sphere moves along the opposite interface for example, are nevertheless possible but much less probable.

Now we discuss quantitatively the velocity values obtained for channels with low interfacial mobility (solution B). Fig. 5 clearly shows that V_p' is only weakly dependence on the parameter λ. More precisely, no evident dependence is observed for values of λ smaller than ≈ 0.3. As already explained, these velocities are representative of the velocity of spheres in settling motion along a corner of Plateau border channels, referred to as V_2, and correspond for each value of λ. In that case, the particle slow down is mainly due to the shearing of the liquid layer between the sphere and the closest wall,[12] rather than due to the back flow of the fluid through the gap between the sphere and the confining walls.[13] This is in contrast with the settling of spheres axially centred in vertical tubes,[14,15] which is often used as a reference to model the motion of particles confined by solid walls, and for which a significant dependence of the drag coefficient with λ is observed. For $\lambda = 0.2$, both experiments provide a value for V_2 close to 0.2. This suggests that the normalized velocity is not influenced by the inclination angle in the range of investigated values (50°–90°). The numerical value obtained for $Bo = 1$ and $x = 0.97x_{max}$ ($V_2 = 0.3$) is also in good agreement (considering that a better agreement would be obtained if the minimum gap imposed in the simulation was reduced to zero). Extrapolating the data for $Bo = 1$ in Fig. 6 to $x = x_{max}$, one can estimate $V_2 \approx 0.2$, suggesting that mobility parameter of solution (B) has been set to an appropriate value in the simulation. The corresponding value for the surface shear viscosity is approximately equal to 4.10^{-4} g s⁻¹. It is in agreement with generally reported value for this solution.[7] Note that the numerical model does not consider the rolling of the sphere. However, rolling was reported for spheres in settling motions along the bottom wall of inclined solid channels.[16,17] Although the wall of the Plateau border channels is fluid, both slipping and rolling motions were distinguished during experiments with solution B (but we were not able to measure accurately the rotation with the present tracking method). For inclined solid circular tubes (infinite Bo), the drag coefficient has been reported to be almost independent on λ if $\lambda < 0.4$ and if the Reynolds number is smaller than unity[16] (note within our experimental conditions, the Reynolds number of the particle satisfies the condition: $Re_p < 0.1$ for $\lambda < 0.4$). In that case, the drag coefficient can be expressed by the simple relationship: $C_D \approx 225/Re$, so that $V_p' \approx 0.1$. This value is smaller than the one reported in this study (0.2) and this deviation reflects the difference in the geometrical configuration of the "contact" as well as the finite value of the surface shear viscosity.

The case of highly mobile interfaces (solution A) is discussed now. In stark contrast with solution B, the experimental curve (Fig. 5) now exhibits a strong dependence of V_p' on the parameter λ. As might be expected, due to the high mobility of the interface, the values of the drag coefficient are smaller than those obtained for solution B. Similarly to the maximal sphere velocity in a vertical PB; two distinct regimes are observed: for high values of λ ($\lambda > 0.3$–0.5) the sphere moves slower with respect to the unbounded case (slow motion regime), whereas for low values of λ ($\lambda < 0.3$–0.5) the sphere moves faster with respect to the unbounded case (fast motion regime). In the latter regime, the sphere velocity can be as high as twice the value of the velocity in the corresponding unbounded case, in spite of the confining effect of the channel walls. It is to noted that no rolling of the sphere was observed with solution A. This large value for V_2 is obtained from both experiments and from the numerical simulation with $Bo = 0.001$. The corresponding surface viscosity is 4.10^{-7} g s⁻¹, which is quite lower than values reported for this solution. Note also that numerical results compare quiet well with experimental data for every λ, and that the critical value corresponding to the transition between slow motion and fast motion regimes is found to be equal to ≈ 0.5. This behaviour is very similar to results for infinitely mobile interface (free boundary condition), meaning that below a certain value, decreasing the surface viscosity of the interface has insignificant effect.
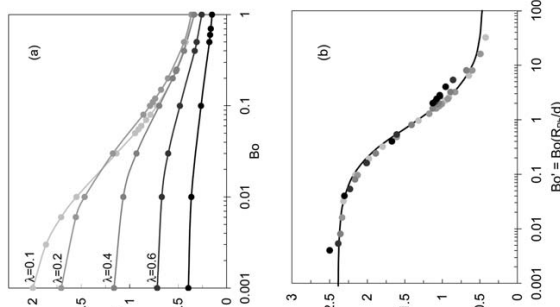

Fig. 7 Numerical results of the normalized settling velocity of sphere in a corner of a Plateau border V_2 for different surface mobility and for confinement parameter varied from 0.1 to 0.8. (a) V_2 vs. Bo; (b) V_2 is normalized by V_0 for $Bo = 1$ vs. $Bo' = BoR_{PB}/d$.

Soft Matter

Transport of coarse particles in liquid foams: coupling of confinement and buoyancy effects

F. Rouyer,[*a] N. Louvet,[b] C. Fritz[a] and O. Pitois[a]

We investigate the behavior of coarse particles confined in foam channels during drainage. Results are reported for particle velocities measured at both microscopic (single foam channel) and macroscopic (foam) scales, as a function of the average velocity of the liquid flow and of the confinement parameter that is the ratio of particle diameter to the maximal particle diameter within channel cross-section. Thanks to numerical simulations, we show that velocities measured for small values of the confinement parameter cannot be understood with the commonly assumed theory for liquid flow in foam channels. Instead, better agreement is obtained by taking into account the characteristics of the flow in the films/channel transitional areas. Finally, values for longitudinal dispersion coefficients are reported, emphasizing effects of buoyancy on particles motions.

1. Introduction

Liquid foams are widely used in various basic applications as well as in elaborated industrial processes. In a large number of cases, particles are incorporated in the foam, and are either attached to liquid–gas interfaces or free to move between gas bubbles. Efficient attachment of hydrophobic particles allows for long-term stable foams to be produced.[1] Incorporation of hydrophilic particles can also have suitable effects, such as the improvement of the mechanical properties.[2] Note also that foams made with complex fluids, such as suspensions, intrinsically contain particles. In the latter case, optimization of a given process requires to predict the average particle velocity (relative to bubbles) and their dispersion within the foam. In froth flotation of mineral ores for example, the efficiency of the separation process is strongly affected by the amount of undesirable hydrophilic particles (unattached particles that compose the gangue) entrained with the liquid of the foam and ultimately recovered with attached valuable particles. The prediction of the behaviour of unattached particles within the foam is therefore of great interest.[3–6] This problem can be compared to particle transport through solid porous media, except that the pore surface is soft and generally 'mobile'. In this regard, a considerable amount of experimental and theoretical work on foam drainage has evidenced the effects of interfacial mobility and has shown that foam permeability varies over one order of magnitude depending on the surfactant used to stabilize the bubbles.[7–10] In contrast,

our knowledge on unattached particle motions in foams is restricted to a limited amount of experimental work.

Confocal microscopy was used by Koehler *et al.*[11] to determine velocities of fluorescent particles in one Plateau border (microscopic scale). In that case, the particles were so small that their velocity was expected to be that of the liquid, allowing for velocity profiles to be measured. Note that this technique does not allow the measurement of velocity in channel's corners, whereas these areas are known to be subjected to specific flow conditions.[12–14] At the scale of the foam (macroscopic scale), Lee *et al.*[15] have shown that the dispersion coefficient characterizing the transport of such small particles is very close to that of the liquid.

For larger particles transported in a two-dimensional rising foam, Bennani *et al.*[16] have reported significant confinement effects. It has been shown that a particle can be strongly slowed down with respect to the liquid due to their interactions with bubble surfaces. For these particles, the gravity force can become significant and particulate motion therefore results from viscous drag due to interstitial liquid flow combined with the sedimentation motion. In this regard, the sedimentation motion of particles confined in foam channels has been investigated in detail,[17,18] providing expressions for the particle velocity as a function of the particle/channel size ratio, the surface shear viscosity characterizing bubble surfaces and the particle position within the channel's cross-section.

Note also that particles with a diameter larger than the size of constrictions in the foam channel network can be permanently trapped, so that the particle velocity (relative to the bubbles) vanishes. The capture criterion proposed recently by Louvet *et al.*[19] enables to predict the critical size below which a particle is free to move in interstices between foam bubbles.

Other works have focussed on drainage of foams made with colloidal suspensions.[21–23] It has been emphasized that drainage

a Université Paris-Est, Laboratoire de Physique des Matériaux Divisés et des Interfaces, CNRS FRE 3300, 5 bd Descartes, 77454 Marne la Vallée Cedex 2, France. E-mail: florence.rouyer@univ-mlv.fr; Fax: +33 1 60 95 72 97; Tel: +33 1 60 95 72 63
b Laboratoire du Futur UMR 5258, 178 avenue du docteur Schweitzer, 33600 Pessac, France

---

Nomenclature

Symbol	Description
f	correction factor for the viscous drag due to the presence of the channel walls
$\lambda = d/d_{lim}$	confinement parameter
Re_p	particulate Reynolds number
R_{PB}	Plateau border radius of curvature
V	settling velocity of the particle
v_p^*	settling velocity normalized by Stokes velocity = dimensionless velocity of the particle in the simulation
V_0	normalized settling velocity for particle in the middle of the cross-section
V_1	normalized settling velocity for particle close to 1 wall
V_2	normalized settling velocity for particle close to 2 walls
$\Delta V = (\max(V_0, V_1, V_2) - \min(V_0, V_1, V_2))$	deviation between the maximum and the minimum velocities
σ	surface tension
μ	shear viscosity of the solutions
μ_s	shear viscosity of the interfaces liquid–air.

References

1 Hans-Joachim Schulze and Anh V. Nguyen, in *Colloidal Science of Flotation, Surfactant Science Series* 118, New York, 2004, ch. 1.
2 S. J. Neethling and J. J. Cilliers, *Int. J. Miner. Process.*, 2003, **72**, 267.
3 N. A. Bennani, A. Fujiwara, S. Takagi and Y. Matsumoto, *Colloids Surf. A*, 2007, **309**, 7.
4 O. Pitois, C. Fritz, L. Pasol and M. Adler, *Phys. Fluids*, 2009, **21**, 103304.
5 A. Saint-Jalmes, Y. Zhang and D. Langevin, *Eur. Phys. J. E*, 2004, **15**, 53.
6 P. Stevenson, *J. Colloid Interface Sci.*, 2005, **290**, 603.
7 E. Lorenceau, N. Louvet, F. Rouyer and O. Pitois, *Eur. Phys. J. E*, 2009, **28**, 293–304.
8 C. Monnereau and M. Vignes-Adler, *J. Colloid Interface Sci.*, 1998, **202**, 45.
9 W. Drenckhan, H. Ritacco, A. Saint-Jalmes and et al., *Phys. Fluids*, 2007, **19**, 102101.
10 R. A. Leonard and R. Lemlich, *AIChE J.*, 1965, **11**, 18.
11 K. D. Danov, T. D. Gurkov, H. Raszillier and et al., *Chem. Eng. Sci.*, 1998, **53**, 3413.
12 A. J. Goldman, R. G. Cox and H. Brenner, *Chem. Eng. Sci.*, 1967, **22**, 637.
13 P. Ganatos, S. Weinbaum and R. Pfeffer, *J. Fluid Mech.*, 1982, **124**, 27.
14 A. Miyamura, S. Iwasaki and T. Ishii, *Int. J. Multiphase Flow*, 1981, **7**, 41.
15 R. P. Chhabra, S. Agarwal and K. Chaudhary, *Powder Technol.*, 2003, **129**, 53.
16 R. P. Chhabra, M. Kumar and R. Prasad, *Powder Technol.*, 2000, **113**, 114.
17 M. E. Staben, K. P. Galvin and R. H. Davis, *Chem. Eng. Sci.*, 2006, **61**, 1932.

laws do not predict the measured drainage velocity. The authors often refer to confinement and collective effects, expressed in terms of trapping of particle aggregates in foam channels. Note that this effect could also be expressed in terms of appearance of a yield stress for the interstitial suspension. In this regard, the interstitial flow of suspensions in foams has been shown to be prevented thanks to the yield stress properties.[24,25] Obviously, the prediction of particle aggregation in the channel network requires better insight into the motions of individual particles. This understanding is still lacking, even for the simplest situation of a single non-Brownian sphere convected in the foam channel network.

In the present work, we investigate the behavior of coarse particles confined in foam channels during drainage. We report results obtained for particle velocities at both microscopic (single foam channel) and macroscopic (foam) scales. In these experiments, particular attention is paid to the control of the ratio of particle size to the radius of passage of the channels, providing thereby a significant insight into the effect of particle confinement on this problem. These experiments coupled with numerical simulations question the theory for liquid flow in foam channels and indicate that the characteristics of the flow in the films/channel transitional area have to be taken into account. The results also emphasize the marked effect of buoyancy on the dispersion process through the foam.

2. Modeling

2.1. Liquid flow in a foam channel

Foam channels, the so-called Plateau borders, are formed by the merging of foam films when they intersect symmetrically three by three. The channel's cross-section is then bounded by three tangentially connected circular arcs of radius R_{PB} and angle $\pi/3$, as depicted in Fig. 1. Channel's interfaces connect to a thin foam film within a transitional area located at each corner of the channel's cross-section.

In a pioneer work, Leonard and Lemlich[12] have proposed a simple model for the liquid flow in such channels. The liquid flow through an infinite Plateau border, with axis along z-axis in the Cartesian space (x,y,z), is assumed to be uniaxial and stationary, characterized by a velocity profile $v(x,y)$ along the z-axis. Typical Reynolds number for the liquid is assumed to be small and the Stokes equation is used:

$$\Delta v = \frac{1}{\mu}\frac{dp}{dz} \quad (1)$$

where μ is the liquid viscosity and p is the liquid pressure (in case of uniform foam channel, the pressure gradient is equal to gravity forces). Partial mobility of channel's interfaces is obtained by balancing the bulk viscous stress with the surface viscous stress on the circular boundary:

$$\mathbf{n}.\nabla v = \frac{\mu_s}{\mu}\Delta_s v \quad (2)$$

where μ_s is the shear surface viscosity and Δ_s is the surface Laplacian and $\mathbf{n}$ is the unit vector normal to the surface pointing out of the channel. The Boussinesq number compares the surface viscous stress to the bulk viscous stress: $Bo = \mu_s/\mu R_{PB}$.[12] Finally, it is assumed that the liquid velocity vanishes at each corner of the channel's cross-section (to distinguish better from the $V_C \neq 0$ case considered subsequently).

Lemlich's model ignores the contribution of surface elasticity in the behavior of channel's interfaces as liquid flows. Very recently, the Marangoni effect has been introduced in the modeling of the flow.[14] The simple picture of the model is the following: surfactant is convected on the central part of the circular interfaces due to the viscous stress from the bulk, inducing surface tension gradients between channel's ends (inlet–outlet) so that Marangoni flows take place in the transitional area at proximity to the channel corners that join channels to films. This mechanism can be expressed in terms of a counterflow velocity V_C in the transitional area, which has been shown to be proportional to the average velocity of the liquid flowing in the bulk of the channel, with a typical coefficient of a few units.[14]

2.2. Particle transport in a foam channel

The motion of a buoyant particle in a foam channel results from the combination of the sedimentation motion and the convection motion due to liquid flow. In opposition to the case of particles

Fig. 1 (a) Sketch of the cross-section of a foam channel with the geometrical limit diameter (d_{lim}) for a transported particle. The position of a particle is measured along the x-axis: $x = 0$ at the center of the channel and $x = x_{max}$ at the corner. (b) Example of mesh used to compute the velocity of a sphere (v_p) in a Plateau border with an average liquid velocity v_l. The velocity profile for the fluid interface is also presented as an illustration: V_c is the liquid velocity at the corner of the channel and one of the parameters of the simulations.

close to solid wall for which rolling motion is observed, no rolling motion is observed in the present case of mobile interface. Indeed, rolling motion is induced by large shear stresses on the side facing the wall in opposition to a low shear stress on the opposite side. In the presence of mobile interface, the difference in shear stresses on different parts of the particle is considerably diminished. For this reason, we neglect rotation of the particle.

For vanishing liquid flow rates in the channel, the particle motion is the pure sedimentation motion already studied in detail.[17,18] For a vertical Plateau border, the sedimentation velocity can be expressed as a function of the confinement parameter λ, which compares the particle diameter d with the diameter of the circle inscribed the channel's cross-section, d_{lim} (see Fig. 1a), the Boussinesq number and the position of the particle within the channel's cross-section. For foam (inclined) Plateau borders, it has been numerically shown that particles settle along the lowest corner in the Plateau border's cross-section, so that the sedimentation velocity can be expressed with λ and Bo only:

$$V_{sed} = h(\lambda)g(Bo)V_{St}\sin(\theta) \quad (3)$$

where θ is the angle of inclination of the Plateau border with respect to the horizontal plane, $h(\lambda) = (1 - 1.488\lambda + 0.535\lambda^2)$, $g(Bo) = (4.3 + Bo')/(1.8 + 2.2Bo')$ and $V_{St} = \Delta\rho gd^2/18\mu$, with the particulate Boussinesq number, $Bo' = \mu_s/\mu d = Bo/2\lambda(2/\sqrt{3} - 1)$ and the confinement parameter $\lambda = d/d_{lim} = d/2R_{PB}(2/\sqrt{3} - 1)$, within the ranges $0.002–20$ and $0.1–0.8$ for Bo' and λ respectively.

For negligible buoyancy effects, the particle velocity can be determined from numerical simulations for the particle suspended in the liquid flowing through the Plateau border. We use COMSOL Multiphysics software to solve the fluid flow through a Plateau channel of radius R_{PB} and length $4R_{PB}$. A sphere is set at midway in the channel ($2R_{PB}$) and its position within the channel's cross-section is referred to the coordinate x along one axis of symmetry of the cross-section (see Fig. 1). We use an "auto" extra-fine mesh refined near the particle-wall area at proximity to the channel corners that join channels to films (inlet-outlet) so that Marangoni flows take place in the transitional area (maximum element size = 0.02 and growth rate = 1.1) and the corner of the PB (maximum element size = 0.05 and growth rate = 1.05) as illustrated in Fig. 1b. We consider dimensionless Stokes equations (fluid density and viscosity are respectively set to zero and one in "the Fluid Dynamic, Incompressible Navier-Stokes" user interface and $R_{PB} = 1$). The simulations are run in the frame of the particle and zero velocity is imposed at the surface of the particle (no-slip conditions). Fluid velocities at the entrance and at the outlet of the channel are constrained to the constant parameter $-V_P + V_l$. Fluid velocities at the edges of the channel are constrained to the parameter $-V_P - V_C$ where V_C is the counterflow velocity imposed at the three corners of the channel. The fluidity of the interface is modeled using weak terms for balancing the bulk viscous stress with the surface viscous stress on the circular boundary. Moreover V_l is chosen such that the effective average liquid velocity, is set to one ($\frac{1}{A_{PB}}\int_{A_{PB}} vH(v)dA = 1$, where H is the Heaviside step function) for every value of Bo and V_C. Thus, the numerical simulations are non-dimensionalised on the scale v_l. Note that the counterflow does not contribute to the mean flow rate through the foam because it is balanced by an inverse flow in the film (that induces thickening of the films) and that counterflow (where $v < 0$ below the red line cf. Fig. 2a) is limited to a region in the corner that increases with Bo. The dimensionless force F_V exerted on the sphere by the viscous flow is calculated from the integral of the Lagrange multiplier along the axis of the channel. For given x, λ, V_c and Bo, a parametric simulation that varied V_P is run to determine the value $V_P = \xi(x,\lambda,Bo,V_C)$ for which $F_V = 0$. The relation between the velocity of a non-buoyant particle and the average liquid velocity is then deduced: $v_p = v\xi(x,\lambda,Bo,V_C)$ where ξ is a dimensionless function. An illustration of calculations made to determine ξ is presented in Fig. 2a for parameter values of V_c and Bo that are consistent with the values reported in the literature and later in this paper. As it can be observed in Fig. 2a, the particle velocity is approximately equal to the velocity of the undisturbed fluid at its centre. For creeping flow, Faxen's law predicts the velocity of a non-buoyant spherical particle from the velocity of the fluid in the channel (undisturbed by the presence of the particle): $v_p(x) = v(x) + \frac{a^2}{6}\Delta v$. The present simulations agree very well with Faxen's law ($\pm 0.002\,\eta$ absolute error) for the centred particle. Note, for the particle at a corner, Faxen's law overestimates our numerical results and all the more that the particle is small (up to 0.07 η absolute error for the smallest particle). Smaller the particle size, smaller is the distance to the corner where we impose the velocity, thus, we attribute the discrepancy to particle-corner hydrodynamic interactions that are not considered in the Faxen theory similarly to particle-wall hydrodynamic interactions evidenced in the Poiseuille flow.[20]

For buoyant particle, the settling velocity of the particle V_{sed} superimposes to convection due to liquid entrainment. Due to the linearity of Stokes equation, the velocity of a non-rotating buoyant particle in a creeping flow is expected to be equal to the sum of its settling velocity and of the velocity of the equivalent non-buoyant particle convected by the flow. Few simulations with dimensional parameters, that correspond to the physically realistic parameter values (density and viscosity, surface shear viscosity, size of Plateau border), have been run to determine the particle velocity in a stationary state for which gravitational force is balanced by the flow, we thus verify the additivity of sedimentation and convective velocities for various particle densities and liquid velocities for the range of parameters considered in this work. Fig. 2b shows how the gravity force affects the particle motion at low liquid velocity. The particle velocity is thus given by the following expression:

$$v_p = V_{sed} + v_l\xi(\lambda,Bo,V_C) \quad (4)$$

2.3. Liquid and particle transport in the foam

In the foam, Plateau borders are connected four by four and form the liquid network in which liquid and particles are transported. Although the interstitial liquid flow rate through the foam, one can relate the microscopic parameters, i.e. the average liquid velocity and the confinement parameter, to the liquid volume fraction and bubble size.

Let us consider a liquid foam of uniform liquid fraction ε during gravity drainage. The interstitial liquid velocity in the macroscopic direction of transport can be written as:[26]

Fig. 2 Numerical simulation for a particle transported through a vertical Plateau border channel, along the closest axis from a channel corner. The confinement parameter $\lambda = 0.2$. (a) Effect of counterflow velocity: liquid velocity profiles (x-axis refers to Fig. 1a) for $Bo = 0.01$ (grey) and $Bo = 0.1$ (black) without (dotted lines) or with (continuous lines) a non-buoyant particle, with $V_c' = 0$ and $V_c' = 3\eta$. The vertical lines illustrate the center of the cross-section ($x = 0$) and the area occupied by the particle (flat velocity profile in this section). (b) Effect of particle buoyancy: particle velocity versus liquid velocity with $R_{PB} = 400$ μm, $\mu = 0.001$ Pa s, $\mu_S = 10^{-5}$ kg s^{-1}, $\rho_f = 1000$ kg m^{-3}, for several values of the reduced particle density. The dotted lines correspond to eqn (3) ($\eta_l = 0$, red times symbol). Dotted lines correspond to a linear fit obtained with a slope = 0.477 ± 0.1% and a coefficient of regression $R = 1$. Continuous line corresponds to the liquid velocity—slope = 1.

$$v_l = \frac{\tilde{K}(\varepsilon)}{\varepsilon} \frac{\rho g R_b^2}{\mu} \qquad (5)$$

where R_b is the bubble radius and the dimensionless foam permeability $\tilde{K}(\varepsilon) = K(\varepsilon)/R_b^2$ depends on the foaming solution i.e. depends on the mobility of the surface and so on the Bo number.[27] For example, for TTAB solution (used in the experiments) $\tilde{K}(\varepsilon) = 4\varepsilon^{3/2}/[1700(1 - 2.7\varepsilon + 2.2\varepsilon^2)]$.[28]

The confinement parameter expresses as a function of the diameter of passage d_{lim} of constrictions in the channel network. According to the expression for d_{lim} published recently,[19] λ can be written as:

$$\lambda(R_b, \varepsilon) = \left(\frac{d}{2R_b}\right)\left(\frac{2R_b}{d_{lim}}\right) = \left(\frac{d}{2R_b}\right)\frac{1 + 0.57\varepsilon^{0.27}}{0.27\sqrt{\varepsilon} + 3.17\varepsilon^{2.75}} \qquad (6)$$

Note that for low liquid fractions, i.e. $\varepsilon \le 0.02$, a simpler expression can be used to relate liquid fraction and the diameter of passage that assumed Kelvin cell geometry for a bubble,[27] so that λ becomes:

$$\lambda(R_b, \varepsilon) = \frac{d\varepsilon^{-1/2}}{2\sqrt{3}(2/\sqrt{3} - 1)R_b} \qquad (7)$$

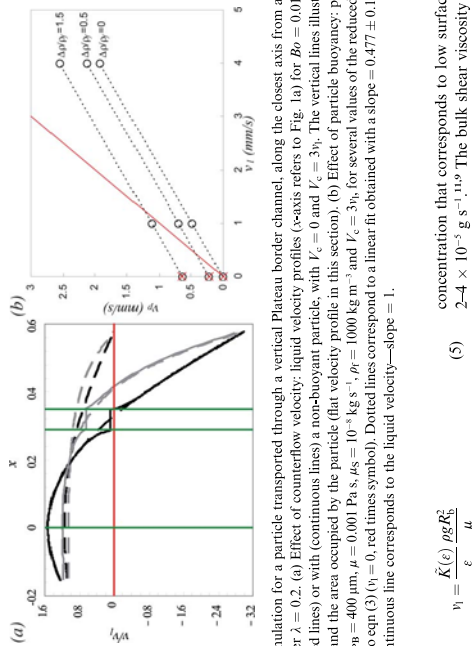Another parameter of interest for particle transport is the coefficient of dispersion D_L of the particles in the longitudinal direction (direction of macroscopic transport). This coefficient accounts for particle velocity fluctuations in the longitudinal direction with respect to the average particle velocity. For particles smaller than 5 μm, it has been shown by Lee et al. that particle dispersion is similar to that of the liquid.[15] As presented in the Introduction, we recall that there are no experimental data for dispersion coefficients of larger particles.

3. Experimental

3.1. Materials

An aqueous foaming solution is prepared with TTAB concentrated at 3 g L^{-1} i.e. three times greater than the critical micelle

concentration that corresponds to low surface shear viscosities: 2–4×10^{-5} g s^{-1}.[19] The bulk shear viscosity μ and density ρ of solutions are equal to those of pure water. Surface tension $\sigma = 37$ mN m^{-1}.

Two types of solid particles are used: polystyrene beads later referred to as non-buoyant particles (Duke Scientific Corporation, density $\rho_{PS} = 1050$ kg m^{-3}, diameter $d = 40$ μm, 80 μm and 140 μm) and silica beads later referred to as buoyant particles (Duke Scientific Corporation, density $\rho_S = 2450$–2500 kg m^{-3}). Diameters, d, are in the range 15–140 μm and hand checked such that size dispersion is small: $\Delta d/d < 5\%$.

3.2. Single vertical channel experiment

The setup has been described in detail in ref. 17. We briefly recall that the vertical channel is obtained by withdrawing a dedicated frame from a reservoir containing the foaming solution. The frame consists of a vertical metallic tube on which three vertical rods (diameter 1 mm) are fixed at the bottom (like a tripod). Due to capillary forces, a Plateau border is formed at the merging line of the three verticals soap films supported by the frame and stabilized with surfactants contained in the solution. The frame is accurately positioned with reference to the reservoir to easily adjust the length of the channel (typical lengths are in the range 5–10 mm).

The inner diameter of the tube is 10 mm and a circular outlet of diameter 1 mm is opened at its lower part: it is used to deliver the particles one by one through the channel and the liquid at a constant flow rate q varied within the range 1–100 mm^3 min^{-1}. A dedicated delivery system was developed to introduce the particles into the foam channels without additional liquid flow. The particles are first mixed with the foaming solution and placed in a modified 3-path valve, ensuring their transfer to the feed tube where they are allowed to settle. Images of the channel were grabbed during the measurements through windows in the cell cover at the rate of 30 frames s^{-1}. The successive positions occupied by a sphere along the channel axis are then determined by image processing procedures. Another window was also placed at the bottom of the liquid reservoir. By illuminating the

---

channel from the top (through the tube) and using a high speed camera equipped with an appropriate lens, pictures of the channel cross-section could be obtained during particle motion. The pictures are then used to correlate the particle position within the channel's cross-section with the velocity of the corresponding particle, and to estimate the radius of curvature of the Plateau border and the cross-sectional area A_{PB}. The average liquid velocity is therefore obtained with the relation: $v_l = q/A_{PB}$. Measured liquid velocities are within the range 0.5–50 mm s^{-1}, and channel width (equal to R_{PB}) is close to 450 μm. With the values obtained for R_{PB} and v_l, the typical values for the Boussinesq number and the Reynolds number are respectively

$$Bo \approx 0.07 \pm 0.05 \text{ and } 0.1 \le Re \le 3.5 \text{ where } Re = \frac{\rho_l v_l d_{lim}}{2\mu}.$$ Note also that for silica particles, the maximal particulate Reynolds number (Re_p) is equal to 3.4 for the largest particle and less than or equal to 0.1 for particles smaller than 45 μm in diameter.

3.3. Foam experiment

Steady drainage experiments are conducted inside vertical Plexiglas cylindrical cells whose height is larger than 500 mm and section S is equal to 29 or 9 cm^2, depending on the bubble size, in such a way that the cell diameter is at least equal to 20 times the bubble diameter (Fig. 3). The cell is first filled with the foaming solution and bubbles are generated by blowing a mixture of nitrogen and C_6F_{14} through a needle in the liquid. C_6F_{14} gas is used with the aim to prevent foam coarsening. For each experiment, the bubbles are monodisperse and their diameter $2R_b$ is equal to 3 mm ($\pm 6\%$). A lid is used to ensure water vapour saturation inside the foam cell. After a long time of drainage (~ 20 min) a very dry foam ($\varepsilon = 0$) is obtained, and a constant liquid flow rate Q is then imposed at the top; Q is varied within the range 5–70 ml min^{-1}. A CCD camera records the evolution of position of the front between the upper wet foam and the dry foam. The front velocity v_f is known to be constant and related to the liquid fraction of the upper wet foam by: $\varepsilon = (Q/S)/v_f$. Measured liquid fractions remain smaller than 0.04 in any case.

The particles are injected one by one, at a height H approximately equal to 10 cm from the liquid bath (Fig. 3). We measure the time t over which the particles flow toward the bottom of the foam. The particle velocity is then calculated as: $v_p = H/t$.

We determine the coefficient of dispersion D_L of the particles in the longitudinal direction (same direction as the transport) as:

$$D_L = \frac{(v_p)^2}{2}\frac{\langle\Delta t^2\rangle}{\langle t\rangle} = \frac{H^2}{2}\frac{\langle\Delta t^2\rangle}{\langle t\rangle^3} \qquad (8)$$

where $\langle\rangle$ denotes average over measurements for which the liquid velocity is fixed and t is the total transport time for one particle through the foam, so $\langle\Delta t^2\rangle$ is the variance of t.

4. Results and discussion

First, we present in Fig. 4 typical results obtained for both polystyrene and silica particle velocities as a function of the average liquid velocity through the vertical Plateau border channel. Presented results correspond to two values of the confinement parameter: $\lambda = 0.2$ and $\lambda = 0.85$ (the particles are respectively 40 μm and 140 μm in diameter). In any case, the
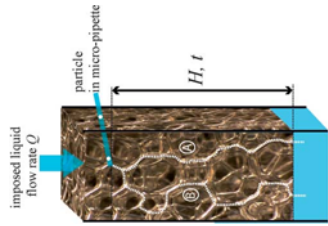

Fig. 3 Sketch of the foam cell that illustrates the foam drainage experiment, the injection of a single particle and two different paths A and B through the foam.

average particle velocity increases with the liquid velocity. For the highest value of λ, both types of particles have velocity values close to the liquid velocity, except for the silica particles at very low liquid velocity. Instead, for $\lambda = 0.2$, silica particle values exhibit drastic differences depending on the particle type: silica particle velocities are only weakly scattered around the average value, whereas polystyrene particle velocity values are extremely scattered. For this latter case, v_p can be either as high as the liquid velocity, or close to zero. For both particle types, however, the average particle velocity increases almost proportionally to the liquid velocity.

The effect of the confinement parameter is presented in Fig. 5. In order to compare this effect for both types of particles, we remove the contribution of sedimentation, which is the major contribution for large silica particles at low liquid velocity. Thus, we report in Fig. 5 ($v_p - V_{sed}$) normalized by the liquid velocity as a function of λ for both types of particles. Fig. 5 supplements the first insight provided by Fig. 4: data for polystyrene beads are highly scattered for small λ values and the scatter reduces as λ increases. This effect does not affect results for silica particles, for which scatter remains limited whatever the value of λ. Another interesting feature can be gathered for the particulate motions: when the contribution of sedimentation is removed for buoyant particles, the resulting velocity is always smaller than the average liquid velocity; in contrast, results for non-buoyant particles exhibit particle velocities that can be significantly larger than the liquid velocity. This effect is all the more likely that λ value is high. Finally, the lowest velocity value for polystyrene particles is close to the average value of velocities measured for silica particles for the same λ value.

Visual inspections at the bottom of the vertical Plateau border during measurements indicate that fastest particles occupy the central position in the cross-sectional area, whereas slowest particles always move along channel's corners, as presented in images inserted in Fig. 5. The visualization also revealed that silica particles are always located at a corner of the channel. Obviously, this specific location of silica particles when moving through the Plateau border channel can be attributed to the
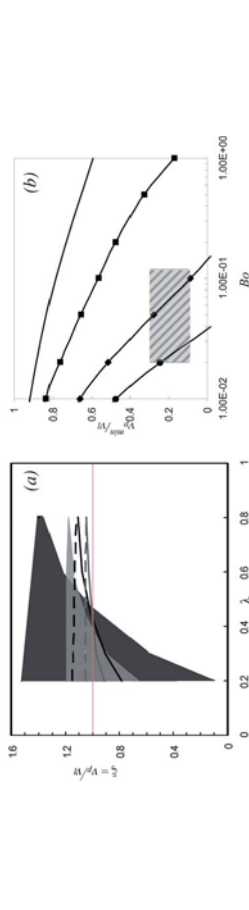
Fig. 4 Typical particle velocity of polystyrene (plus symbols) and silica beads (round symbols) as a function of the average liquid velocity through a vertical Plateau border for two values of the confinement parameter λ: λ = 0.2 (left) and λ = 0.85 (right). The line corresponds to $v_p = v_l$.
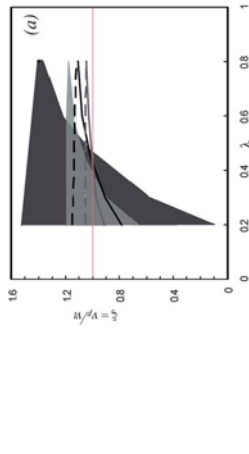

Fig. 5 Convective contribution in measured particle velocity for particles transported through a single vertical Plateau border: polystyrene beads (plus symbols) and silica beads (rounded symbols) as a function of the confinement parameter λ. Dash ovals connected to images underline the data obtained for two typical positions in the cross-section: close to the center (top) and close to the corner (bottom).

effect of the gravity force: buoyant particles have time to settle (vertically) and to migrate towards inclined walls of the injection device before they enter the Plateau border channel. This effect can be also expected for motions of buoyant particles in foams and it will be discussed later.

Now, we compare results presented in Fig. 5 with theoretical predictions obtained through numerical simulations. Both minimal and maximal values for the theoretical velocity are plotted in Fig. 6a for non-buoyant spheres, for two values of the Boussinesq number (0.01 and 0.1) enclosing the expected experimental value, and two values for counterflow velocity: $V_c = 0$ (Lemlich's assumption) and $V_c/V_l = 3$. Numerical results clearly show that theoretical values with $V_c = 0$ are not compatible with experimental data. Indeed, for λ = 0.2, the predicted value for the minimum particle velocity is by far larger than the corresponding measured values for both polystyrene and silica beads. Predicted maximum velocity is lower than the measured one, whatever the value used for Bo in the simulation. As a result, the theoretical velocity deviation, i.e. difference between maximum and minimum, (0.4) is almost four times smaller than the measured deviation for polystyrene beads (1.5). On the other hand, the introduction of counterflow velocity at each corner of the channel cross-section, i.e. $V_c \neq 0$, allows for a better agreement to be obtained for λ = 0.2. Calculated

minimum particle velocities for several values for Bo and V_c are reported in Fig. 6b with the measured minimum velocity. We found that a counterflow velocity equal to $V_c = 3\ v_l$ allows for experimental values to be properly described. This value falls directly within the range of expected values.[14] Note that the counterflow velocity affects the minimum particle velocity because the slowest particles move along channel's corners—thus close to the counterflow area—but it also affects the maximum particle velocity because the counterflow modifies significantly the liquid velocity throughout the channel's cross-section, including the central position corresponding to the fastest particles. This effect is all the more efficient that the counterflow reduces the hydrodynamic channel's cross-section, and all the more that V_c is large. This effect contributes to increase the velocity of particles located in the central part of the cross-section (as illustrated in Fig. 2) and thus contributes to increase the deviation between the fastest and the slowest particles. In this regard, the agreement between measured velocities and calculated ones, for λ = 0.2, is satisfactory.

However, the velocity of larger particles is not properly described, whatever the value for V_c, emphasizing the limits of the modeling for particle transport. Obviously, the presence of a large particle within the channel's cross-section modifies deeply the balance of bulk flow and counterflow in the transitional area. By imposing a constant coefficient for the counterflow velocity at the channel's corner, the drag effect induced by counterflow is underestimated as the size of the transported particle increases. We think that a more complete numerical simulation, including surfactant transport and Marangoni stresses in the transitional area, is required to understand all particle velocities reported in Fig. 5. This disagreement is also evident in Fig. 4b, where eqn (4) overestimates significantly the velocity of large particles: this equation would be presented by a line intercepting the y-axis at $V_{sed} > 0$ with a slope ξ, that depends on the parameter values of Bo and V_c (cf. Fig. 6a).

Now, we present the results for the transport of particles in the foam. Fig. 7 shows typical particle velocities as a function of liquid velocity measured for silica beads with diameters equal to 22.5 µm, 42.5 µm and 85 µm. For every particle size, the particle velocity increases with the liquid velocity. For small particles, we observe that most of the data spread below the line $v_p = v_l$ and that reported velocity can be less than one-third of the average liquid velocity. The average value for the particle velocity is smaller than the average liquid velocity. This effect is in agreement with results obtained at a microscopic scale. In contrast,
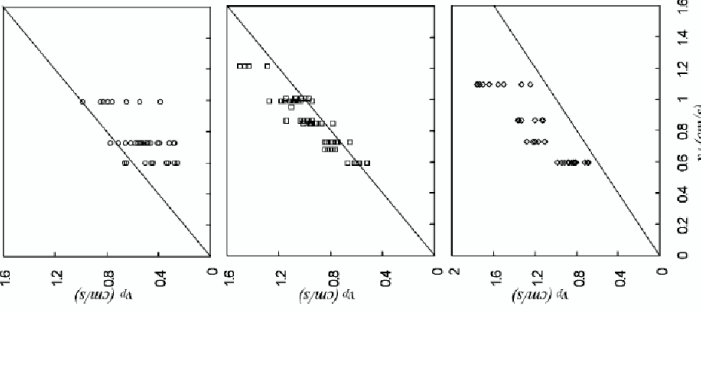
Fig. 6 (a) Numerical values for the normalized particle velocity as a function of confinement parameter λ: minimal (continuous lines) and maximal (dashed lines) particle velocities for Bo = 0.1 (black lines) and 0.01 (grey lines) assuming no counterflow velocity, and range of particle velocities for Bo = 0.1 (dark grey area) and 0.01 (light grey area) assuming a counterflow velocity equals to 3 times the average liquid velocity. (b) Numerical values for the normalized counterflow velocity of particles moving along a channel's corner as a function of the Boussinesq number, for λ = 0.2 and for several values for the normalized counterflow velocity V_c: $V_c = 0$ (no symbols), $V_c = 1$ (square symbols), $V_c = 3$ (diamond symbols), $V_c = 5$ (circle symbols). Dashed area corresponds to the range of experimental data.

velocities of the largest particles are larger than the average liquid velocity. This behavior can be compared to results obtained at a microscopic scale, removing the contribution of sedimentation. The resulting velocity $(v_p - V_{sed})/v_l$ is plotted as a function of the confinement parameter in Fig. 8. This plot shows that the contribution of sedimentation is not responsible for the higher values measured for the largest particles. Qualitatively, this result is in agreement with those obtained at the scale of the single vertical Plateau border (Fig. 5), but quantitatively, velocities measured at foam scale are larger than those measured in the single channel. Therefore, one can deduce that this deviation results from a network effect. Basically, paths of large particles are not equivalent to paths of small particles and liquid, due to the buoyancy force, and independently of the geometrical effect of the confinement parameter. In other words, large particles have time to settle when passing through junctions between two neighbouring channels, resulting in more vertical paths through the channel network. Obviously, a relevant parameter for this effect can be expressed in comparing the particle convection time through a channel junction of typical length αR_{PB} (with α a constant characteristic of a junction size of the order of unity), with the time corresponding to the vertical settling of the particle over a length ℓ allowing particle swapping between streamlines entering different channels. ℓ can be defined as $\ell = \alpha' d_{\mathrm{dim}}/2 = \alpha'(2/\sqrt{3} - 1)R_{PB}$ (with α' of the order of unity). We note that α and α' might depend on the liquid volume fraction and on λ (large particle have access to the smaller cross-section area than small particle) but at first order we estimate $\alpha/\alpha' \approx 1$. The resulting time ratio is thus $(2/\sqrt{3} - 1)v_l/V_{sed} \approx 0.16 v_l/V_{St}$. Particle velocities are now plotted as a function of $0.16 v_l/V_{St}$ in Fig. 8b. Data obtained for all particle sizes sort in a coherent way as a function of this parameter: $v_p - V_{sed} > v_l$ when $0.16 v_l/V_{St} < 1$, $v_p - V_{sed} \approx v_l$ when $0.16 v_l/V_{St} \approx 1$ and $v_p - V_{sed} < v_l$ when $0.16 v_l/V_{St} > 1$. Note also that this parameter is an approximate criteria to distinguish particle that can (<1) or cannot (>1) settle inside channel junctions, and that it can be expressed as $0.16 v_l/V_{St} \approx (9.7 l/3)(K/\ell^2)(\rho/\Delta\rho)$ emphasizing the combined effects of both confinement and buoyancy.

Fig. 7 Typical particle velocity of glass bead as a function of liquid velocity for transport through a foam for various bead diameters: 22.5 µm (circle), 42.5 µm (square), and 85 µm (diamond). The continuous line of slope is a guide for the eyes and represents $v_p = v_l$.
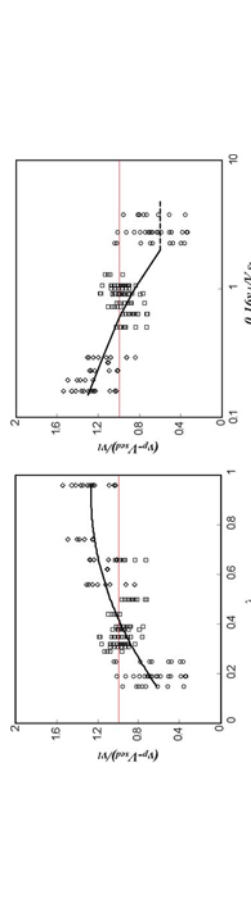
Fig. 8 Normalized particle velocity corrected of sedimentation as a function of confinement parameter λ with glass beads in the foam, for three particle diameters: 22.5 μm (circle), 42.5 μm (square), and 85 μm (diamond). The continuous line is a guide for the eyes.

Values for the longitudinal dispersion coefficient are presented in Fig. 9 as a function of 0.16v_l/V_{St}. The normalized coefficient of dispersion increases dramatically for 0.16v_l/V_{St} > 1. We also report data from the literature in Fig. 9. Lee et al.[15] have shown experimentally that the dispersion of both tracer (colorant) and tiny particles is similar, they find that the ratio $v_l R_{PB}/D_L$ is equal to 0.15 for liquid (tracer colorant) and 0.16 for tiny particles. From their data, we estimate the normalized dispersion coefficient as $\frac{D_L}{v_l 2R_b} = \frac{D_L}{v_l R_{PB}}\frac{R_{PB}}{2R_b}$, respectively, of the order of 1.53 and 1.44 for tracer (colorant) and tiny particles, where $\frac{R_{PB}}{2R_b} \approx 0.23$ (from Fig. 7 in ref. 15). These values are reported in Fig. 9 for 0.16$v_l/V_{St} \gg 1$, showing very good agreement with our experimental results for the smallest particles. This agreement is far to be trivial: first, the liquid drainage of Lee's experiments is said to be dominated by viscous dissipation in PB channels which is not the case in the present experiment; second, their scaling of D_L with R_{PB} is controversial.[28,29] Note that numerical simulations of Meloy et al.[30] are consistent with experimental data of Lee et al.[15] for small particles, but do not predict the strong decrease we observed for the dispersion coefficient of large particles. This disagreement could be attributed to the fact that the authors did not consider the settling of particles in the junctions as a significant effect in this problem.

As transport in the foam can be, to a certain extent, compared to transport in solid porous media, it is interesting to report results obtained by Ippolito et al.[31] when studying experimentally the transport of a single particle through a 3D, dry and random bed of spheres. From their data (Fig. 12 in ref. 31), we estimate a normalized coefficient of dispersion $\frac{D_L}{\langle V \rangle 2R_b} = \frac{L_l}{2R_b} \approx 0.1$ where $\langle V \rangle$ and L_l are respectively the average particle velocity and the dispersion length. We report this value in Fig. 9 for the limit 0.16$v_l/V_{St} \ll 1$. It was shown by Ippolito et al. that the dispersion length (or dispersion coefficient) is independent of the particle size. On the other hand, for foams, a small increase in the dispersion coefficient can be noticed for 0.16v_l/V_{St} < 1 in Fig. 9. Note, however, that if we adopt the normalisation for our data with $\langle v_p \rangle$ instead of v_l, it reduces the values of the normalized coefficient of dispersion for large particles, and thus minimizes the trend observed in Fig. 9 for 0.16v_l/V_{St} < 1. Then similarly to the transport of a single particle through a dry random bed of spheres, the dispersion length of buoyant particles in the foam is found to be independent of the particle size for 0.16v_l/V_{St} < 1.

5. Conclusions

New experimental data have been provided for coarse buoyant and non-buoyant particles transported in foam channels.

As a major result, we show that the velocities of small particles (i.e. 1/5 of the maximum particle size) are smaller than the average liquid velocity, whereas large particles are transported at velocities larger than the liquid velocity, independently of sedimentation effects. We show that the Lemlich theory fails to reproduce these results. Better agreement is obtained for small particles using a recent flow model assuming a recirculation (counterflow) liquid velocity at each corner of the foam channels. However, transport velocities of the largest particles are not properly described, indicating that a more refined model is required.

At the scale of the foam, the relevant parameter has been expressed in comparing the particle convection time through a channel junction with the time corresponding to the vertical settling of particles in channels' junctions: ~0.16v_l/V_{St}, where v_l is the interstitial liquid velocity and V_{St} is the Stokes velocity. A marked evolution for both the average velocity and dispersion of particles is observed around 0.16$v_l/V_{St} \approx 1$, emphasizing both confinement and buoyancy effects.
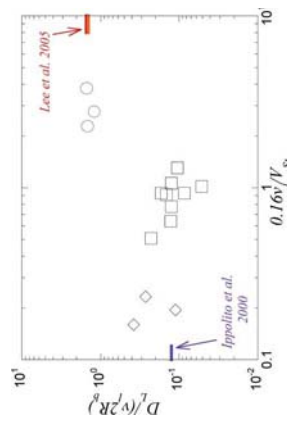
Fig. 9 Normalized dispersion coefficient as a function of the ratio of settling time over convection time in foam junction for three particle diameters: 22.5 μm (circle), 42.5 μm (square), and 85 μm (diamond).

Notations

$Bo = \mu_s/\mu R_{PB}$ — Boussinesq number defined at the scale of the Plateau border

$Bo' = \frac{\mu_s}{\mu d}$ — Boussinesq number defined at the scale of the particle

d — particle diameter

d_{lim} — maximum diameter of the circle inscribed in the PB cross-section

D_L — coefficient of dispersion in the longitudinal direction

$\lambda = d/d_{lim}$ — confinement parameter

ε — liquid volume fraction

$\tilde{K}(\varepsilon)$ — dimensionless foam permeability

R_b — bubble radius

Re_p — particulate Reynolds number

R_{PB} — Plateau border radius of curvature

v_p — velocity of the particle

V_c — dimensionless velocity of the fluid in the corner in the simulation

v_l — average liquid velocity in the direction of transport; at the scale of a single Plateau, experimentally: $v_l = (flow\ rate)/(cross\text{-}sectional\ area)$; numerically:

$$v_l = \frac{1}{A_{PB}}\int_{A_{PB}} |v \times \text{ if}(v < 0)| \, dA = 1;\ \text{at the scale}$$

of a foam, $v_l = \frac{\tilde{K}(\varepsilon)}{\varepsilon}\frac{pgR_b^2}{\mu} = (Q/S)/\varepsilon$

V_l — dimensionless velocity of the fluid at the inlet and outlet of a single Plateau border in the simulation

V_p — dimensionless velocity of the particle in the simulation

V_{St} — Stokes velocity

σ — surface tension

μ — shear viscosity of the solutions

μ_s — surface shear viscosity of the interfaces liquid/air.

References

1. A. C. Martinez, E. Rio, G. Delon, A. Saint-Jalmes, D. Langevin and B. P. Binks, *Soft Matter*, 2008, **4**, 1531–1535.
2. S. Cohen-Addad, M. Krzan, R. Höhler and B. Herzhaft, *Phys. Rev. Lett.*, 2007, **99**, 168001.
3. J. Rubio, M. L. Souza and R. W. Smith, Overview of flotation as a wastewater treatment technique, *Miner. Eng.*, 2002, **15**, 139–155.
4. H.-J. Schulze and A. V. Nguyen, *Colloidal Science of Flotation, Surfactant Science Series 118*, New York, 2004, ch. 1.
5. S. J. Neethling and J. J. Cilliers, *Int. J. Miner. Process.*, 2003, **72**, 267.
6. P. Stevenson, S. Ata and G. M. Evans, *Chem. Eng. Sci.*, 2007, **62**, 5736–5744.
7. G. D. Miles, L. Shedlovsky and J. Ross, *J. Phys. Chem.* 1945, **49**, 93–107.
8. A. Saint-Jalmes, Y. Zhang and D. Langevin, *Eur. Phys. J. E*, 2004, **15**, 53.
9. O. Pitois, C. Fritz and M. Vignes-Adler, *J. Colloid Interface Sci.*, 2005, **282**, 458.
10. E. Lorenceau, N. Louvet, F. Rouyer and O. Pitois, *Eur. Phys. J. E*, 2009, **28**, 293–304.
11. S. A. Koehler, S. Hilgenfeldt, E. R. Weeks and H. A. Stone, *Phys. Rev. E: Stat. Nonlinear, Soft Matter Phys.*, 2002, **66**, 040601.
12. R. A. Leonard and R. Lemlich, *AIChE J.*, 1965, **11**, 18.
13. V. Carrier, S. Destousesse and A. Colin, *Phys. Rev. Stat., Nonlinear, Soft Matter Phys.*, 2002, **65**, 061404.
14. O. Pitois, N. Louvet and F. Rouyer, *Eur. Phys. J. E*, 2009, **30**, 27–35.
15. H. T. Lee, S. J. Neethling and J. J. Cilliers, *Colloids Surf., A*, 2005, **263**, 320–332.
16. N. A. Bennani, A. Fujiwara, S. Takagi and Y. Matsumoto, *Colloids Surf. A*, 2007, **309**, 7.
17. O. Pitois, C. Fritz, L. Pasol and M. Adler, *Phys. Fluids*, 2009, **21**, 103304.
18. F. Rouyer, C. Fritz and O. Pitois, *Soft Matter*, 2010, **6**, 3863–3869.
19. N. Louvet, R. Höhler and O. Pitois, *Phys. Rev. E: Stat. Nonlinear, Soft Matter Phys.*, 2010, **82**, 041405.
20. M. E. Staben, A. Z. Zinchenko and R. H. Davis, *Phys. Fluids*, 2003, **15**, 1711–1733.
21. F. Carn, A. Colin, O. Pitois, M. Vignes-Adler and R. Backov, *Langmuir*, 2009, **14**, 7847.
22. R. M. Guillermic, A. Salonen, J. Emile and A. Saint-Jalmes, *Soft Matter*, 2009, **5**, 4975–4982.
23. A. Britan, M. Liverts, G. Ben-Dor, S. A. Koehler and N. Bennani, *Colloids Surf., A*, 2009, **344**, 15–23.
24. J. Goyon, F. Bertrand, O. Pitois and G. Ovarlez, *Phys. Rev. Lett.*, 2010, **104**, 128301.
25. S. Guignot, S. Faure, M. Vignes-Adler and O. Pitois, *Chem. Eng. Sci.*, 2010, **65**, 2579.
26. S. A. Koehler, S. Hilgenfeldt and H. A. Stone, *Langmuir*, 2000, **16**, 6327–6341.
27. D. Weaire and S. Hutzler, *The Physics of Foams*, Clarendon Press, Oxford, 1999; I. Cantat, S. Cohen-Addad, F. Elias, F. Graner, O. Pitois, F. Rouyer and A. Saint-Jalmes, *Les mousses—Structure et Dynamique*, Belin, Paris, 2010.
28. F. Rouyer, O. Pitois, E. Lorenceau and N. Louvet, *Phys. Fluids*, 2010, **22**, 043302.
29. N. Bennani and S. A. Koehler, *Soft Matter*, 2010, **6**, 3841–3850.
30. R. Meloy, S. J. Neethling and J. J. Cilliers, *Int. J. Miner. Process.*, 2007, **84**, 185–191.
31. I. Ippolito, L. Samson, S. Bourlès and J. P. Hulin, *Eur. Phys. J. E: Soft Matter Biol. Phys.*, 2000, **3**, 227–236.

Conclusions et Perspectives

Certaines des propriétés physiques des mousses présentées ici sont communes aux propriétés physiques d'autres matériaux appartenant à la physique des milieux divisés :

- du point de vue rhéophysique : la mousse est un fluide à seuil dont la réponse mécanique à une sollicitation oscillatoire peut être décrite au premier ordre harmonique par des propriétés viscoélastiques. Ce comportement est similaire à celui des émulsions et pâtes granulaires. De plus, des bandes cisaillement peuvent être observées aux plus grandes déformations.

- du point de vue hydrodynamique : le liquide s'écoule à l'intérieur de la phase continue d'une mousse stabilisée par des interfaces "immobiles" comme dans un empilement de grains solides non-déformables dont la perméabilité est décrite par la loi de Carman-Kozeny qui prend en compte la surface spécifique du réseau de pores.

- d'un point de vue du transport de particules solides à travers la phase continue : la trajectoire de particules denses est guidée par la gravité vers les canaux les plus "verticaux" du réseau de la mousse, leur dispersion est comparable à celle de petits grains à travers un empilement de plus gros grains secs.

Mais, un milieu granulaire constitué de particules solides ne peut pas modéliser une mousse, bien au contraire ! Les trois points précédemment cités correspondent à des particularités parmi l'ensemble des comportements observées dans le cas des mousses et des empilements d'objets (mou ou dur) pour lesquelles les propriétés de contact entre objets et les propriétés des interfaces sont identiques ou n'interviennent pas. En effet, comme cela a été montré tout au long de ce manuscript, la fluidité des interfaces des bulles et leur variabilité rhéologique influencent fortement les propriétés de transport dans une mousse.

Dans l'ensemble des chapites 2 et 3 de ce manuscript, cette mobilité a été variée expérimentalement avec 2 solutions moussantes "modèles" et numériquement en étudiant les écoulements sur une vaste gamme de nombre de Boussinesq ($10^{-3} - 1$). La modélisation de cette mobilité à l'échelle de la mousse n'est pas encore complète, cependant les études à l'échelle locale montrent que l'effet de recirculation de liquide dans les films induite par contrainte de Marangoni doit être prise en compte. Nous avons montré l'importance d'une zone de transition aux coins des sections des bords de Plateau dans laquelle le liquide s'écoule à contre courant et qui affecte la géométrie des canaux ainsi que les conditions limites de l'écoulement. En particulier, cet effet permet de comprendre pourquoi de petites particules sont transportées moins vite dans un bord de Plateau que le liquide alors que pour des interfaces mobiles (écoulement bouchon), on s'attendrait à ce que les particules soient transportées à la vitesse de l'écoulement.

Dans le cas spécifique du verre fondu, là encore la fluidité des interfaces a son importance. En effet nous avons montré que les films fins peuvent être stabilisés par des phénomènes d'évaporation de substances chimiques "surfaces actives" qui induisent des courants Marangoni dans le sens opposé au drainage gravitaire. La thèse d'Helena se termine le 14 novembre 2011 mais le sujet n'est pas clos et nécessite encore des expériences ... J'aimerai poursuivre ce travail en collaboration avec Saint-Gobain Recherche afin de mieux caractériser la corrélation entre le phénomène d'évaporation et la stabilité des films de verre fondu en menant des expériences en atmosphère contrôlée. Ce travail pourra faire l'objet d'un stage de Master deuxième année. Enfin, nous avons pour projet de poursuivre l'étude à l'échelle d'une mousse dans le cadre d'une deuxième bourse CIFRE, afin de pouvoir appréhender la problématique industrielle : peut-on prédire la hauteur d'une mousse au-dessus d'un bain de verre fondu à partir du taux de gaz crée dans le fondu ?

Pendant les trois prochaines années, je m'intéresserai au transport de gouttelettes d'huile dans une mousse aqueuse (projet ANR WOLF - water oil laden foam - porté par Elise Lorenceau). J'adapterai les outils numeriques développés pour les particules solides au cas de goutelettes afin de prendre en compte la fluidité de leur interface ainsi que leur déformabilité. L'intérêt de ces études est de comprendre les mécanismes physiques d'imbibition et de fractionnement de gouttelette d'huile dans une mousse. Ce problème a des multiples applications : récupération du pétrole, décontamination ...

FIGURE 3.7 – (gauche) monocouche de grains comprimés dans une cuve de Langmuir, (milieu) agrandissement d'un pli de flambement (droite) flambement d'une goutte enrobée pendant son séchage.

Un autre sujet d'étude me tient à coeur et concerne les propriétés physiques des interfaces liquide/air décorées de particules solides. Depuis une petite dizaine d'années, à l'instar des émulsions dites de Pickering, de nombreuses équipes de recherche s'intéressent à la stabilisation de mousses par des particules solides [1]. Dans ce cas, la rhéologie des interfaces devient très complexe. En effet, les interfaces forment alors un milieu granulaire à deux dimensions dont les propriétés mécaniques sont largement méconnues. Ainsi, comment ces interfaces se déforment-elles et comment leur rhéologie dépend du taux de couverture en particules, sont des questions ouvertes. Des expériences récentes montrent que de telles interfaces flambent et s'apparentent à une coque solide pour des taux de couverture en grains inférieurs à la fraction surfacique d'empilement compact désordonné [2], alors que des études antérieures modélisent l'arrangement des grains au seuil de flambement par un empilement hexagonal compact [3, 4].

Les interfaces décorées de particules sont donc sujets à une problématique plus fondamentale : peut-on définir une fraction surfacique pour un empilement lâche à deux dimensions ? comment celle-ci dépend des interactions entre grains et donc de leurs propriétés physiques (angle de contact - densité ...). Ce travail est lié à une collaboration avec N. Menon débutée en Juillet 2010 à UMass où j'ai initié des expériences d'empilement granulaire 2D immergé.

Au L.P.M.D.I, des expériences ont débuté au printemps dernier dans le cadre d'un stage de M1. Ces expériences de compression d'interfaces décorées de particules micrométriques hydrophobes ont été menées dans une cuve de Langmuir ou lors du séchage de goutte. Le dispositif de la cuve de Langmuir équipé d'une balance de Langmuir permet la mesure instantanée de

la surpression en surface à l'aide d'une plaque de Wilhemy, de plus, deux cameras permettent la mesure de la concentration surfacique moyenne et locale des grains sur l'interface ainsi que l'observation de la déstabilisation de l'interface (plis de flambement). Les premiers résultats montrent un effet important de la relaxation des pressions de type viscoélastique et des plis de l'interface lorsque celle-ci est rapidement mise sous contraintes. Nous avons pour projet de quantifier de manière systématique la relaxation (temps de relaxation, ajustement des coefficients visqueux et élastiques par un modèle de type Zener) pour différents taux de recouvrement imposés (ϕ_i). Nous chercherons alors à identifier les mécanismes microscopiques qui régissent les comportements visqueux et élastiques aux temps cours et aux temps longs : contacts entre grains, ponts capillaires, dissipations visqueuse dans le fluide sous la monocouche de grains. La mesure de la surpression aux temps long permettra ainsi de déduire la tension de surface d'une telle interface en fonction de la concentration surfacique. Par ailleurs, la fraction surfacique (ϕ_{ic}) à laquelle les plis de flambement ne peuvent plus relaxer permettra de mesurer une fraction surfacique minimum d'empilement de grains à 2D. Nous serons alors à même de comparer cette fraction à celle d'un empilement compact et ainsi de déterminer si il existe des empilements lâches à 2D, et comment la valeur de ϕ_{ic} dépend des contacts entre grains (bulles ou grains solides) et des propriétés de l'interface liquide-air... Enfin les expériences de séchage de gouttes correspondant à des compressions quasi-statiques permettent d'étudier le seuil de flambage dans le cas d'interface courbe.

Bibliographie

[1] D. Weaire and M. Vignes-Adler "New foams : fresh challenges and new opportunities " *Current Opinion in Colloid and Interface Science*,**13** (3) : 141-149 (2008).

[2] M. Berhanu, A. Kudrolli, *Phys. Rev. Letters*,**105** 9, 098002 (2010)

[3] R. Aveyard, J.H. Clint, D. Nees and N. Quirk, *Langmuir*,**16** (23), 8820Ũ8828 (2000).

[4] D. Vella, P. Aussillous, L. Mahadevan, *EUROPHYSICS LETTERS*, **68** 2, 212-218 (2004)